

~~466-13000~~
~~466-36362~~

N.I.

GPO PRICE \$ _____
CFSTI PRICE(S) \$ _____
Hard copy (HC) 3.50
Microfiche (MF) _____
653 July 85

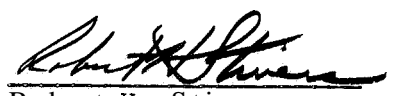
SOLAR-POWERED ELECTRIC
PROPULSION SPACECRAFT

Bi-Monthly Report

NO.2

FACILITY FORM 602
67-39960
(ACCESSION NUMBER)
225
(PAGES)
0489653
(NASA CR OR TMX OR AD NUMBER)
(THRU)
(CODE)
03
(CATEGORY)

HUGHES AIRCRAFT COMPANY
Space Systems Division



Robert H. Stivers
Electric Propulsion Programs

Prepared for JPL under
Contract No. 951144

July 1965

PRECEDING PAGE BLANK NOT FILMED.

TABLE OF CONTENTS

	Page
I. INTRODUCTION	
II. TECHNICAL DISCUSSION	
A. Mission Analysis	A - 1
1. Solar-Electric Spacecraft Performance Analysis	A-1
2. All-Chemical Spacecraft Performance	A-31
3. Performance Comparison	A-35
B. Propulsion System Studies	B-1
1. Scaling Study	B-1
2. Reliability Analysis	B-25
3. Subsystem Layouts	B-41
4. Conceptual Design of Propulsion System	B-57
5. Power Matching Study	B-64
6. Design Verification Hardware	B-88
C. Spacecraft System Design	C-1
1. General Arrangement	C-1
2. Scientific Payload	C-15
3. Retro Propulsion	c-20
4. Thermal Control	c-21
5. Spacecraft Attitude Control	C-22
6. Telecommunication	C-43
7. Structural and Dynamics Analysis	c-44
8. System Analysis	C-51
D. Spacecraft Design Criteria	D-1

I. INTRODUCTION

This is the second bi-monthly report issued under Contract Number 9511.44 with the Jet Propulsion Laboratory. It is essentially a report of progress since the first bi-monthly report issued in May, 1965,

Certain fundamental approaches and basic derivations were included in the first report and are not repeated here,

During this reporting period trade-off studies have continued and several new areas have been investigated. Also a briefing was made to representatives of NASA Headquarters, various NASA centers, and JPL.

During the next two months, the Spacecraft system design, propulsion system design, and mission analysis will be in the final phase preparatory to the reliability and cost analysis **for** the final phase of the contract.

II. TECHNICAL DISCUSSION

A. MISSION ANALYSIS

The main objective of the mission, is to deliver a scientific payload and a reliable telecommunications system into an orbit around the planet Mars. Such a delivery can be accomplished by either an all chemical system or by use of a solar electric powered final stage spacecraft. The purpose then to be fulfilled in this study is a comparison of the chemical and the solar electric mission within the constraints stipulated by the contracting agency.

1. Solar Electric Spacecraft Performance Analysis

As pointed out in the 1st Bimonthly Report, the purpose of the low thrust mission studies is to (1) determine the payload capability of an electrically propelled spacecraft and subsequently compare it to an all chemical vehicle and (2) establish the optimum design points for the propulsion system. It was also stated that although the total mission objective was a Mars Orbiter, the specific role which the ion propulsion system will play in accomplishing this objective must still be decided. The various possible mission profiles for the ion propulsion stage are Optimum Coast Rendezvous, Zero Coast Rendezvous, Minimum Time Flyby, and Flyby. Each of these mission profiles were to be studied for effects of departure date, launch year, hyperbolic excess, flight time, specific impulse, and thrust orientation.

During the first reporting period, the mission analysis was limited to the zero coast rendezvous mission and primarily to the 1971 launch year so that the propulsion and spacecraft system designs could proceed. The 350 day, 1971, zero coast rendezvous profile was chosen as the design model mission. The results of these analyses established the following design points for an electrically propelled spacecraft launched by a SATURN IB/CENTAUR:

1. Hg Bombardment Engine
2. Specific Impulse - 4000 sec.
3. Power Requirement - 48 kW
4. Propellant Weight - 1600 lbs.
5. Thrust Vector thru 50°

good year for flybys

During the last two months the mission analyses have been extended to include the Optimum Coast, Zero Coast, and Flyby mission profiles for the launch years of 1969, 1971, 1732, 1975, and 1977. These missions (with a few exceptions) were studied under the following conditions

1. Departure Date - determine optimum and effect of launch window
2. Hyperbolic Excess - zero
3. Flight Time - 150 days to 500 days
4. Specific Impulse - 3000 sec to 6000 sec
5. Thrust Orientation - optimum

The results of these analyses which were obtained as a direct output of the JPL low thrust variable power trajectory program, are presented in this report in Fig. A.1-1 thru A.1-18. The first fourteen of these figures represent the performance maps for low acceleration, high specific impulse propulsion systems. The use of these maps has been described in the 1st Bimonthly Report and will not be repeated here. However, as stated, these data are completely independent of propulsion system constraints and can be used to evaluate the effectiveness of any low thrust device.

Although a complete analysis of the data presented in Figs. A.1-1 thru A.1-14 is not yet complete, some preliminary but significant conclusions can be drawn at this time. First, although the propellant requirement initially decreases with increasing flight times, in all cases a point is reached where no further advantage is accrued. In fact, in many instances a minimum propellant requirement is seen. The flight time at which this minimum occurs, however, does not necessarily guarantee a maximum payload, since the initial acceleration also decreases with flight time. Second, for a 350 day mission, the initial acceleration levels (and, therefore, power requirements) decrease in the order of Optimum Coast, Zero Coast, and Flyby, the Optimum Coast profile requiring almost twice the initial acceleration than that of a Flyby and one third more than that of a Zero Coast. Third, again considering a 350 day mission, the propellant requirement for the Optimum Coast and Zero Coast profiles is twice that of a Flyby. Finally, there is no apparent

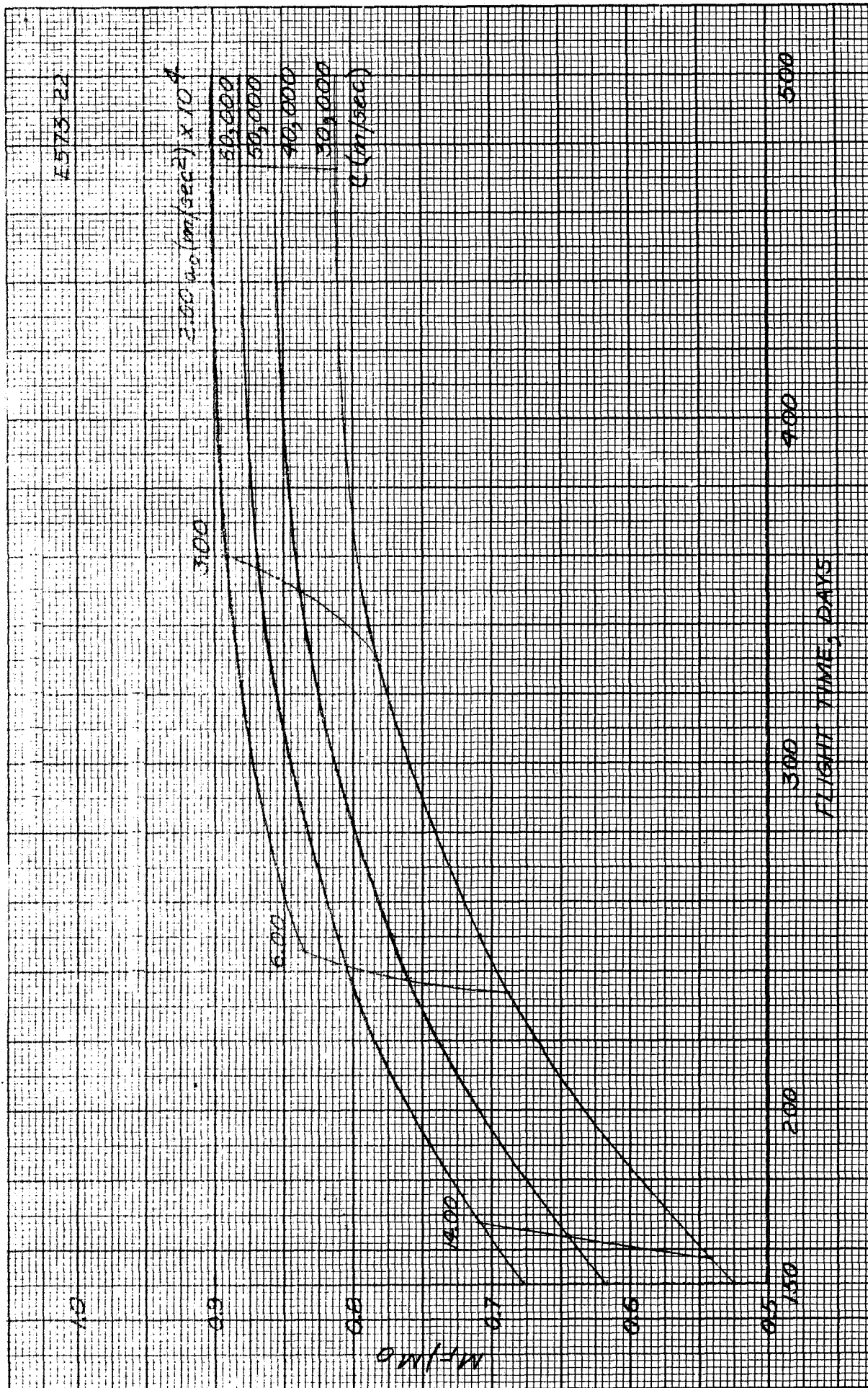


Fig. A.1-1. 1969 optimum coast rendezvous.

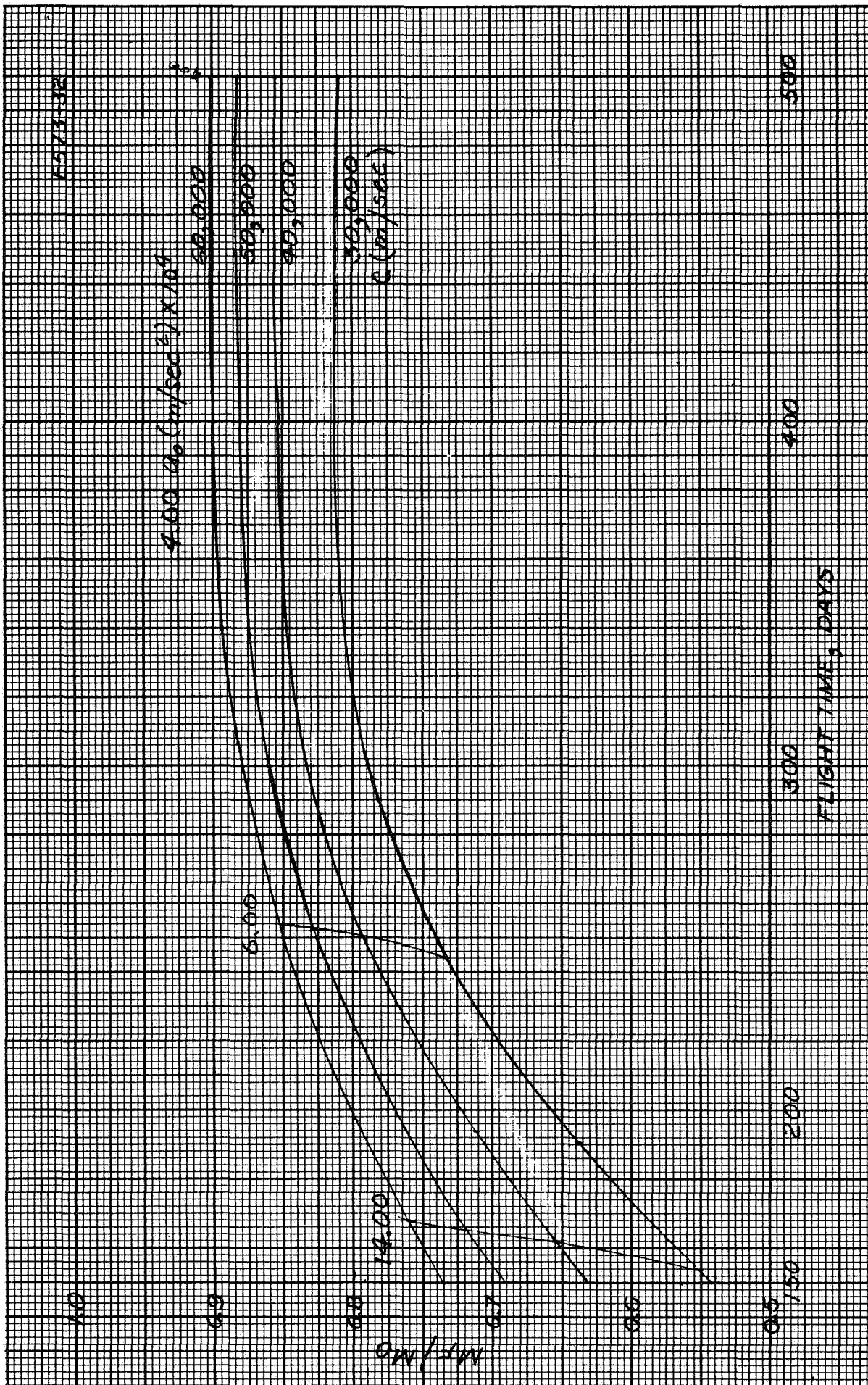


Fig. A.1-2. 1973 optimum coast rendezvous.

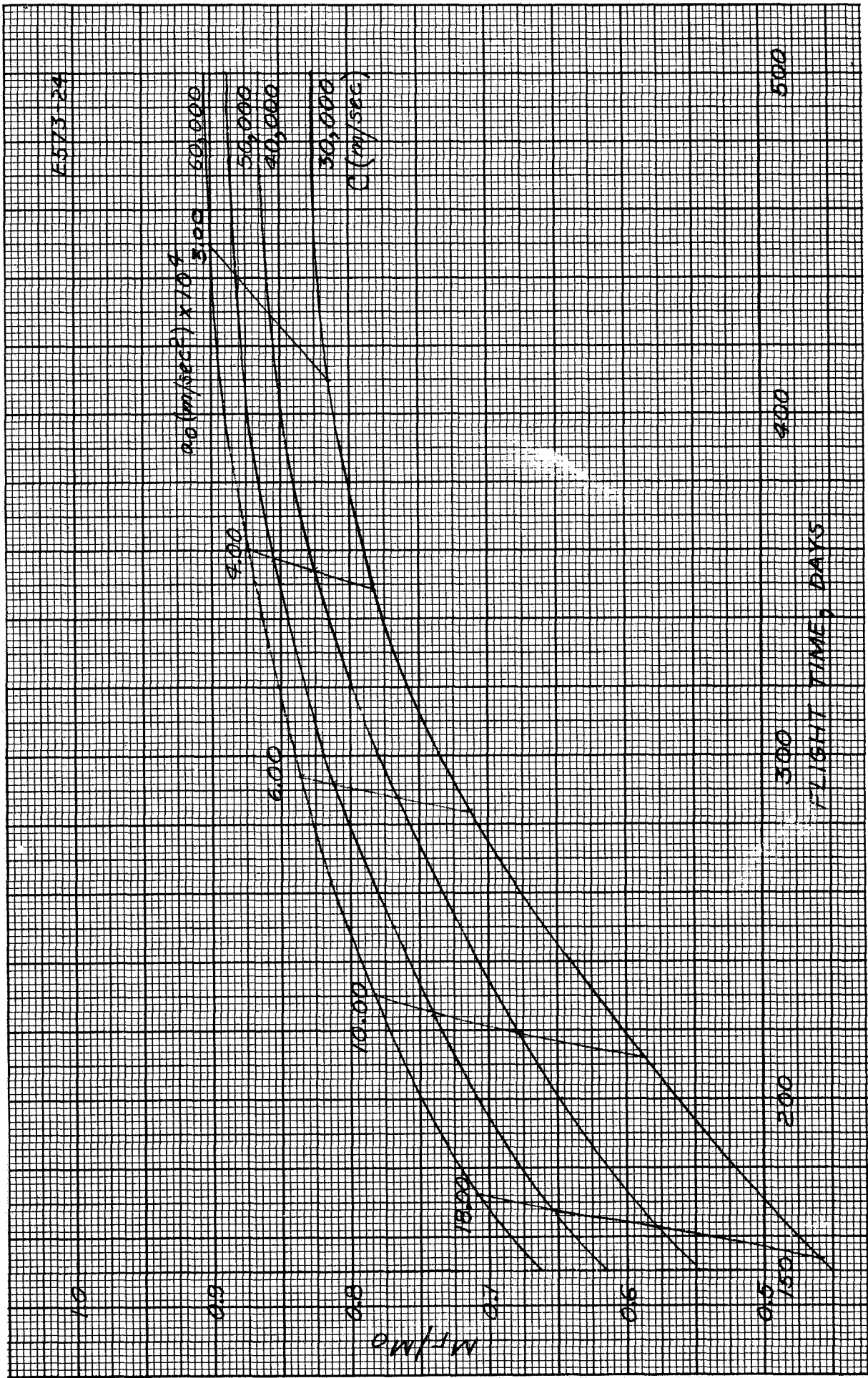


Fig. A.1-3. 1975 optimum coast rendezvous

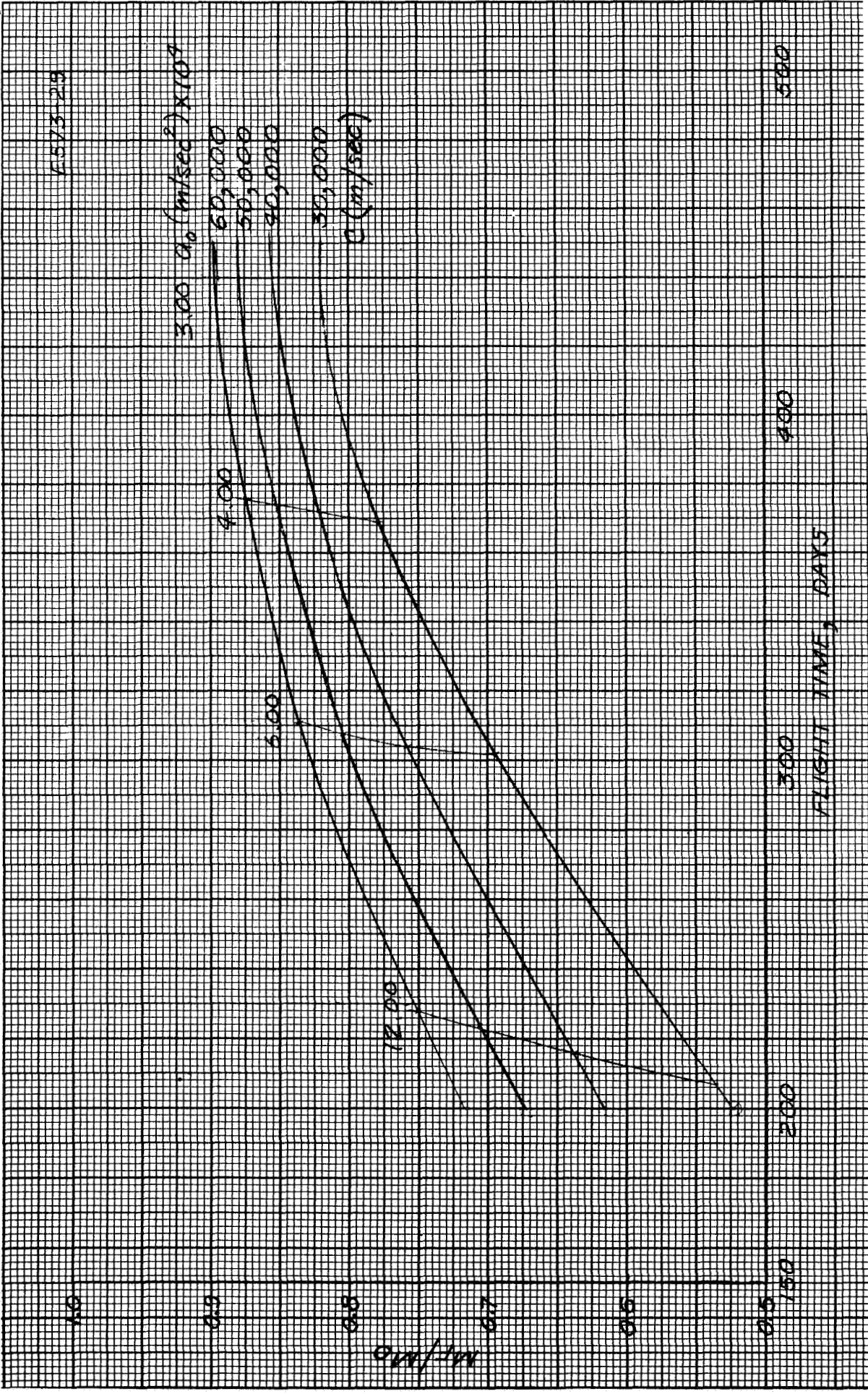


Fig. A.1-4. 1977 optimum coast rendezvous.

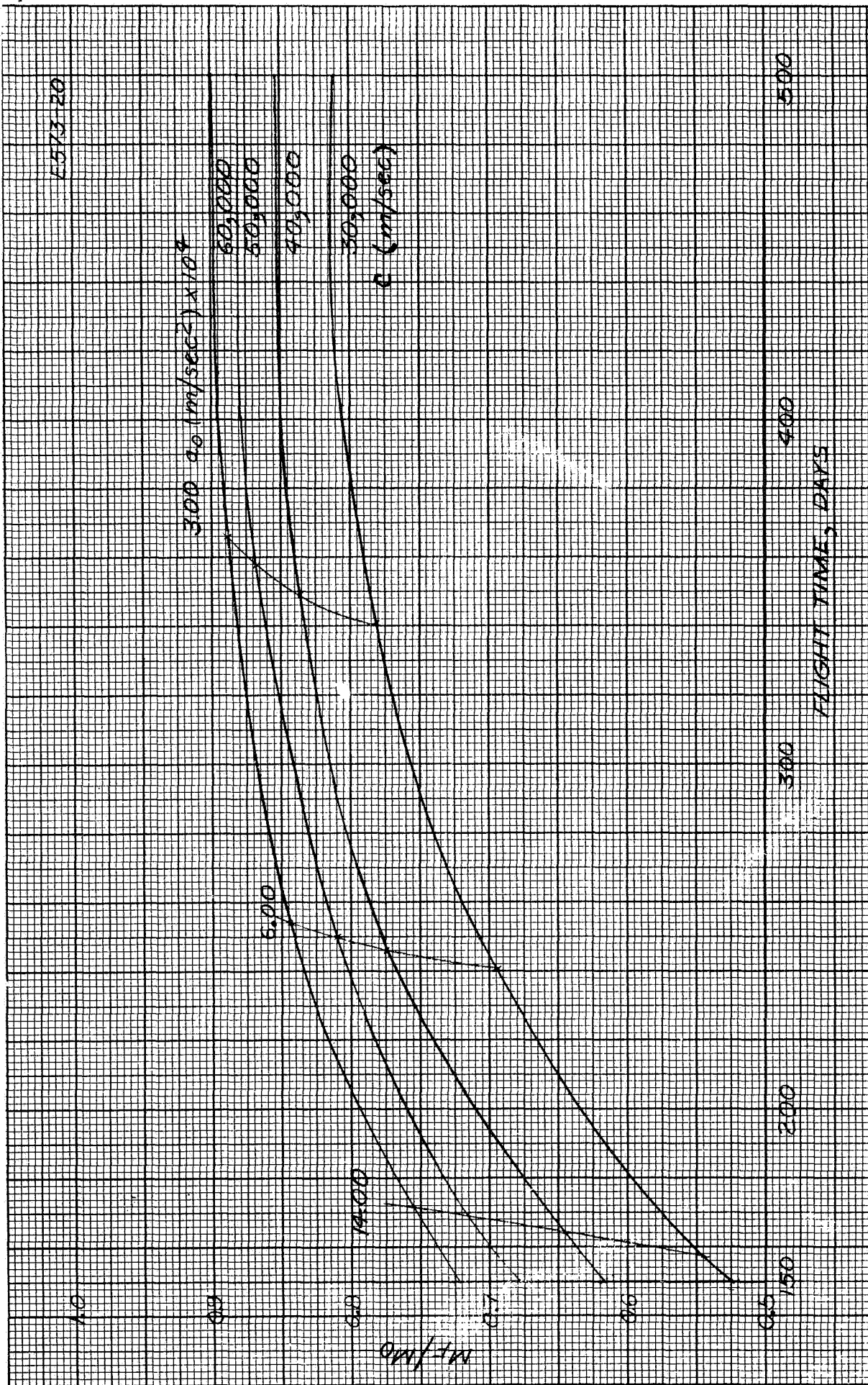


Fig. A.1-5. 1969 zero coast rendezvous.

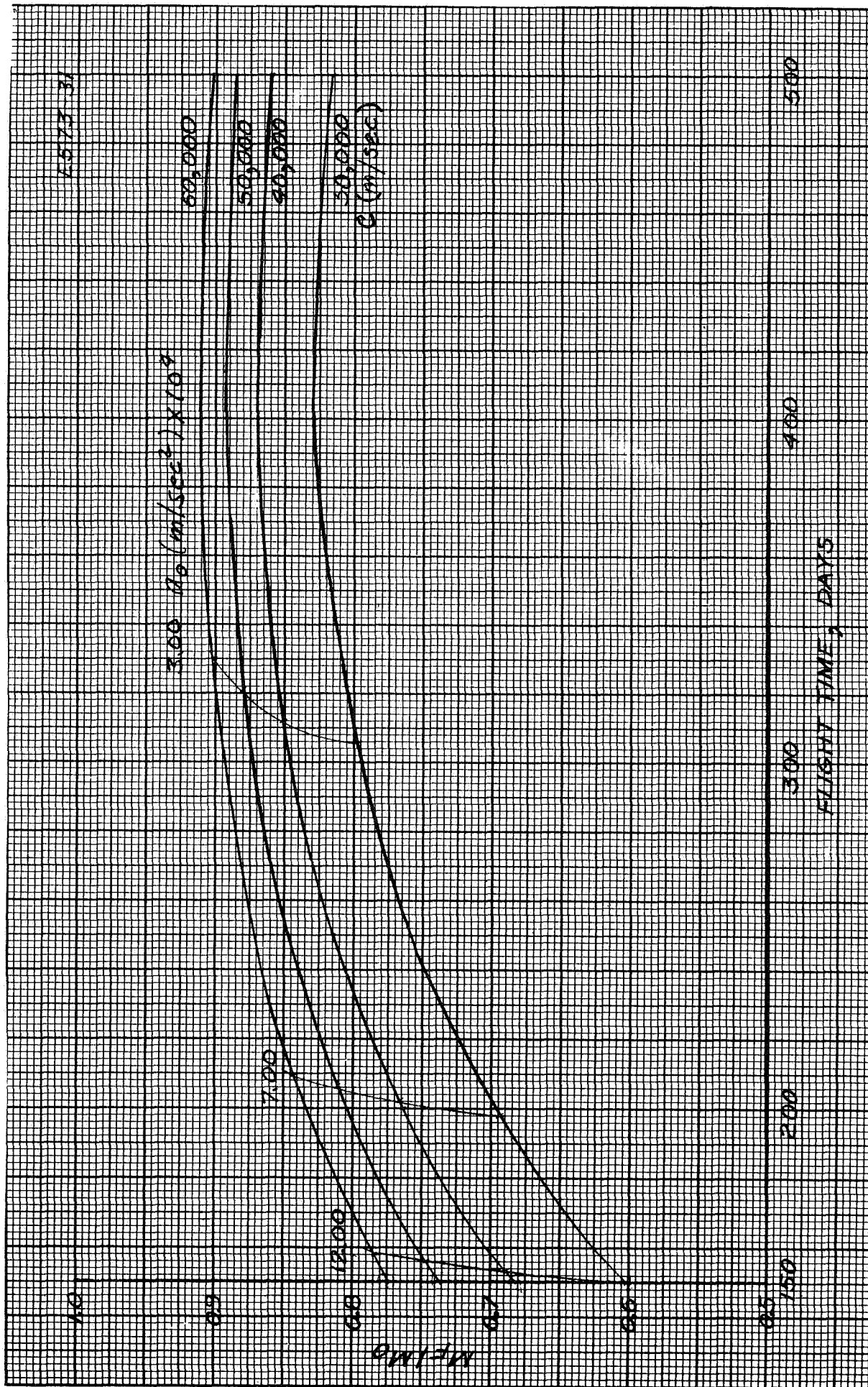


Fig. A.1-6. 1971 zero coast rendezvous.

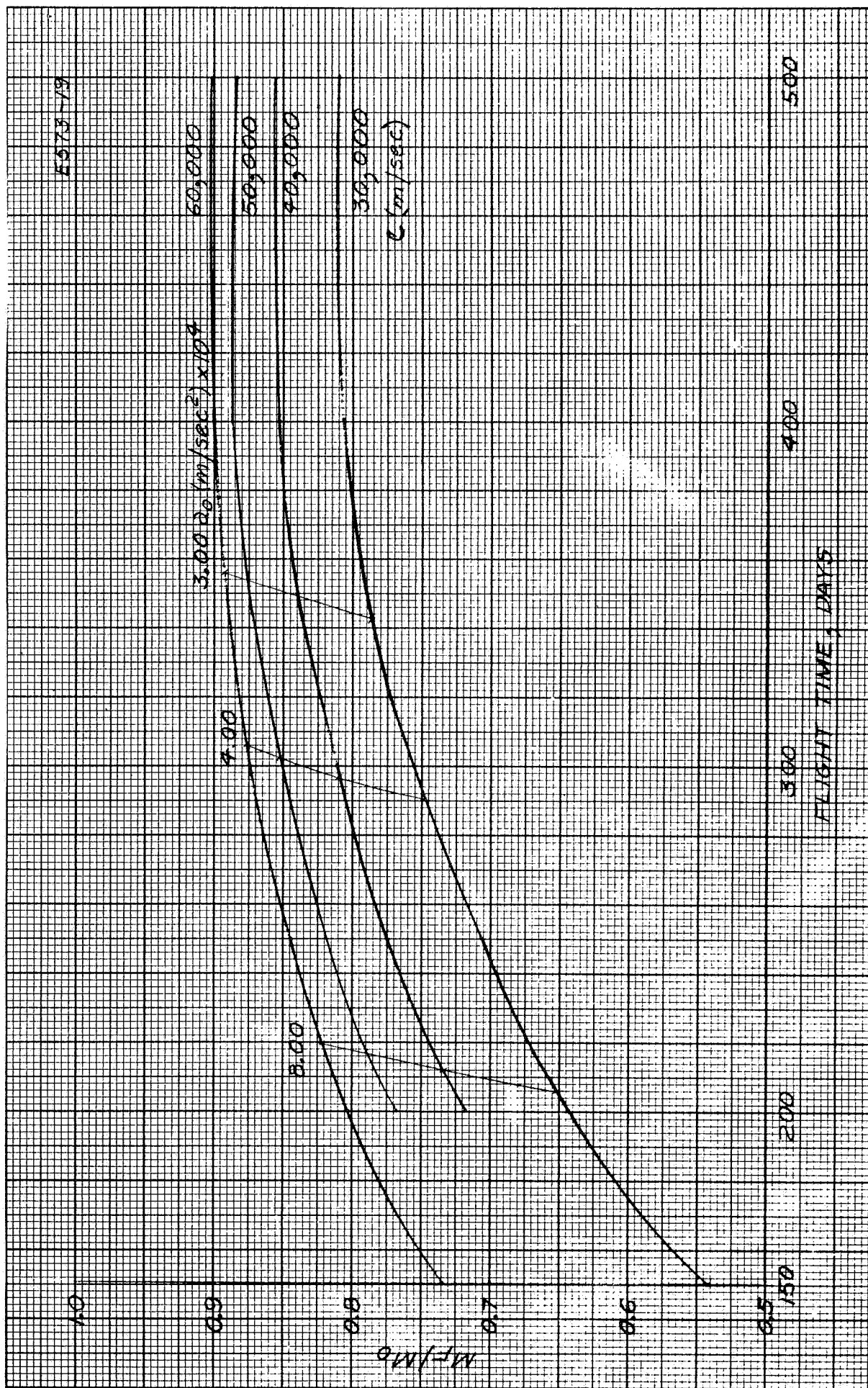


Fig. A.1-7. 1973 zero coast rendezvous

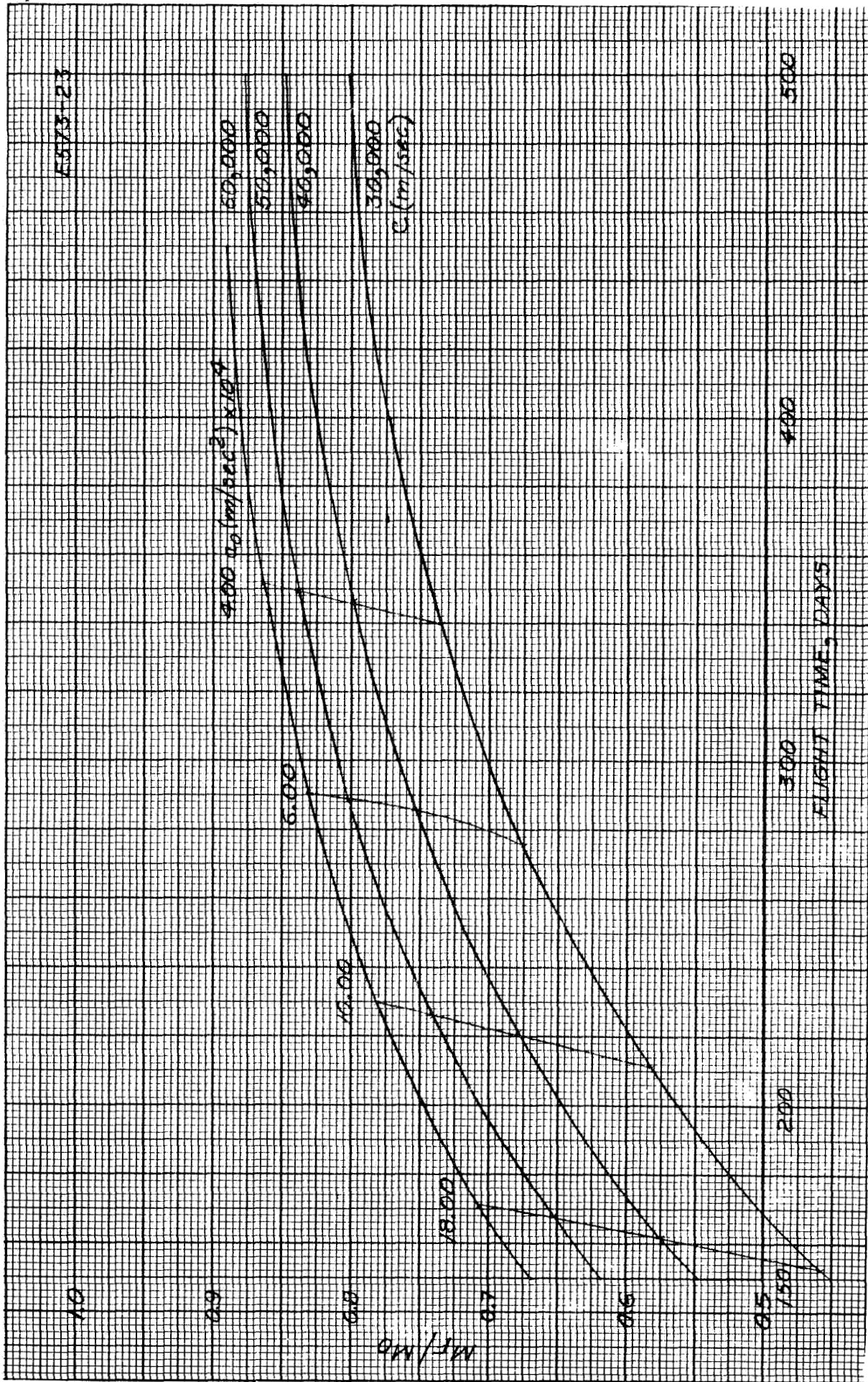


Fig A.1-8 1975 zero coast ren000zvovus

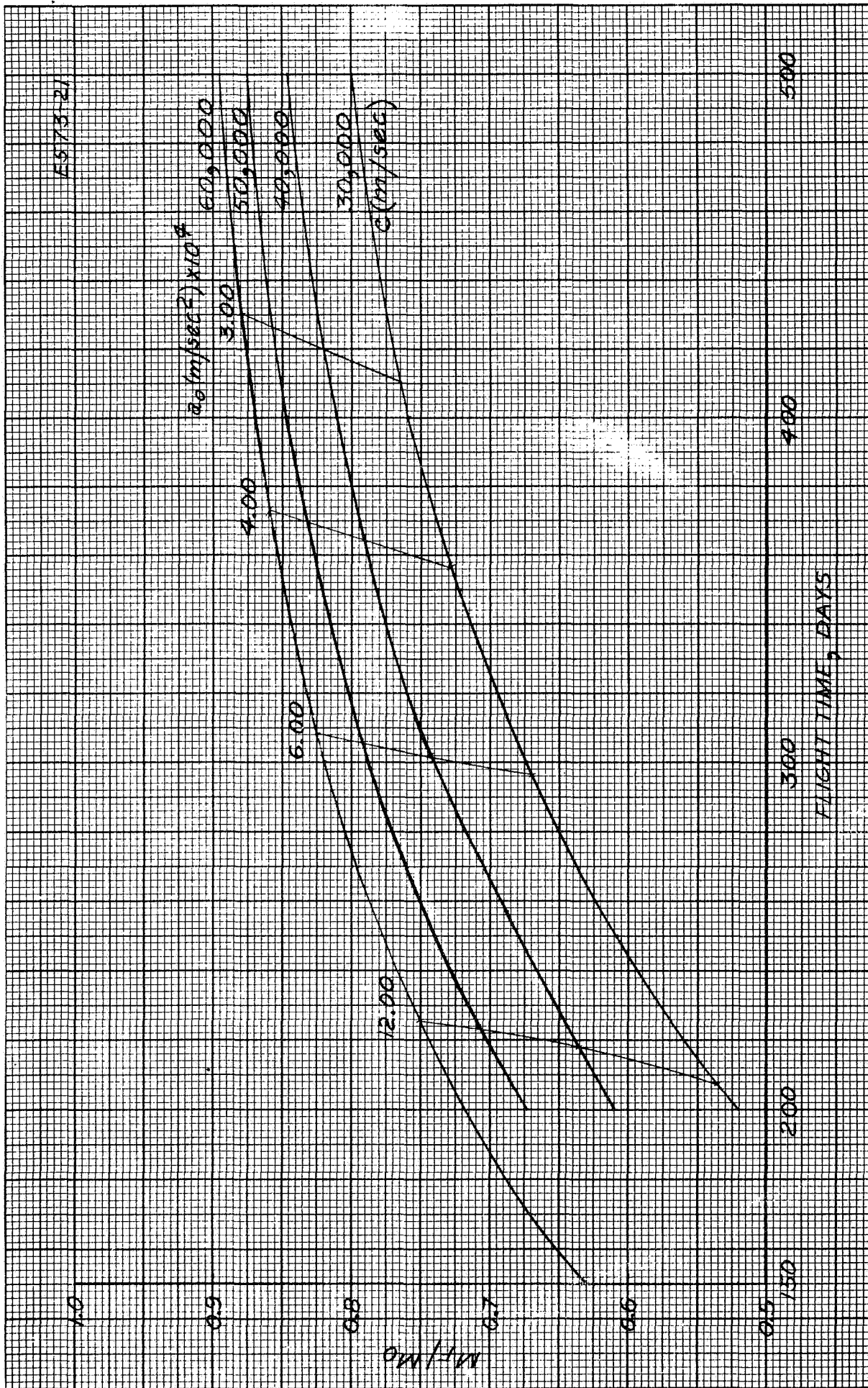


Fig. A.1-9. 1977 zero coast rnp0p2v0us

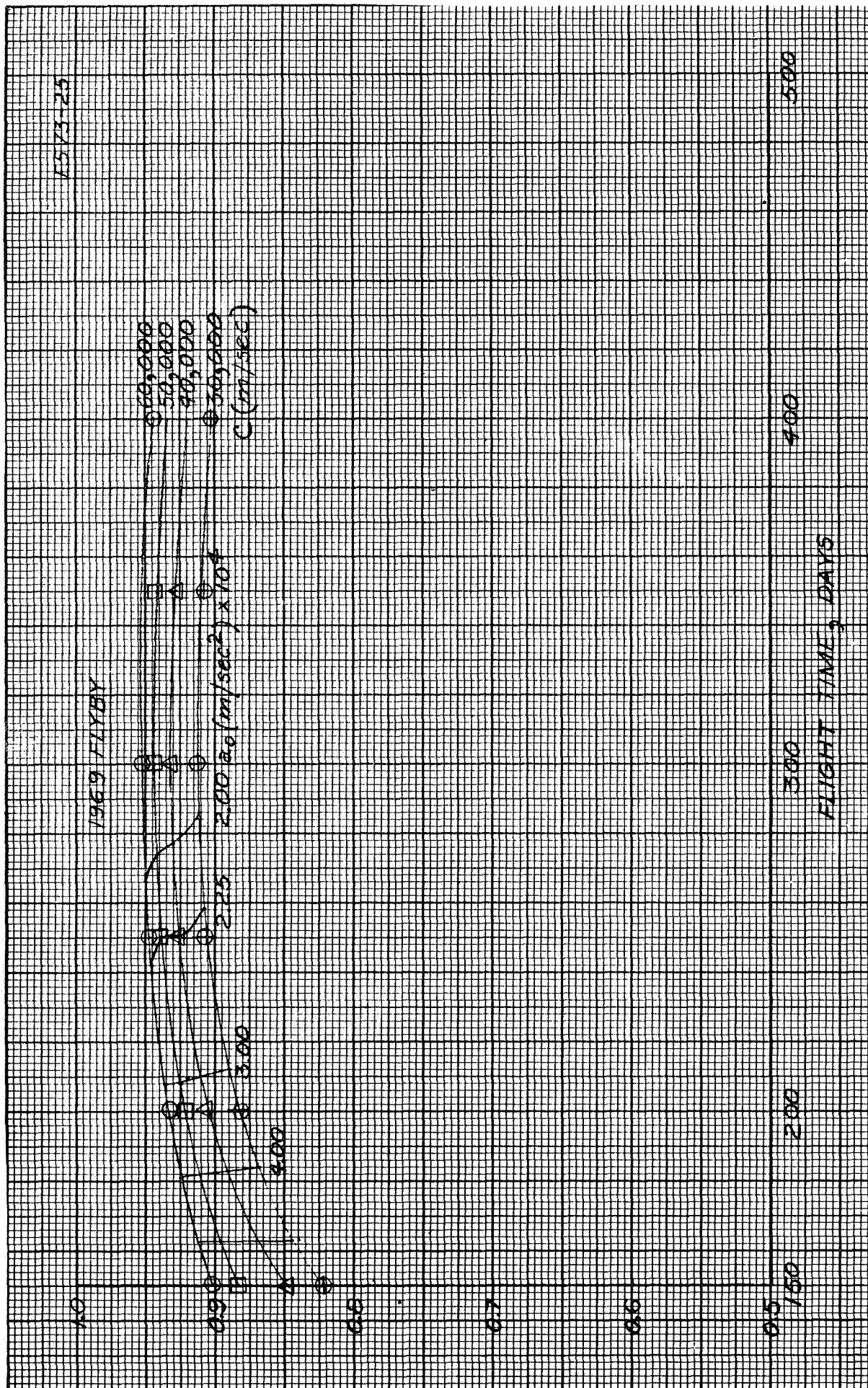


Fig. A.1-10. 1969 flyby.

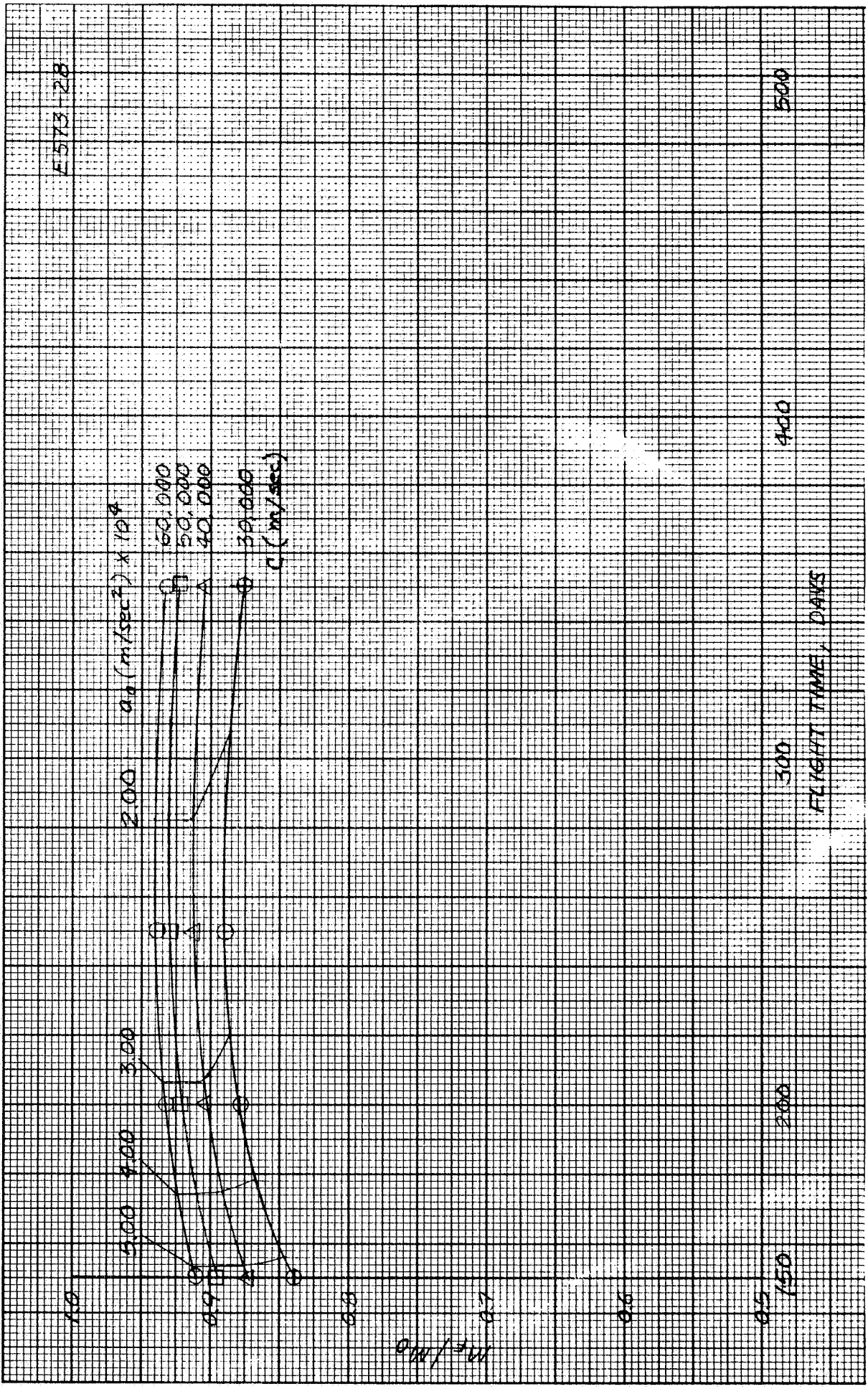


Fig. A.1-11. 1971 flyby.

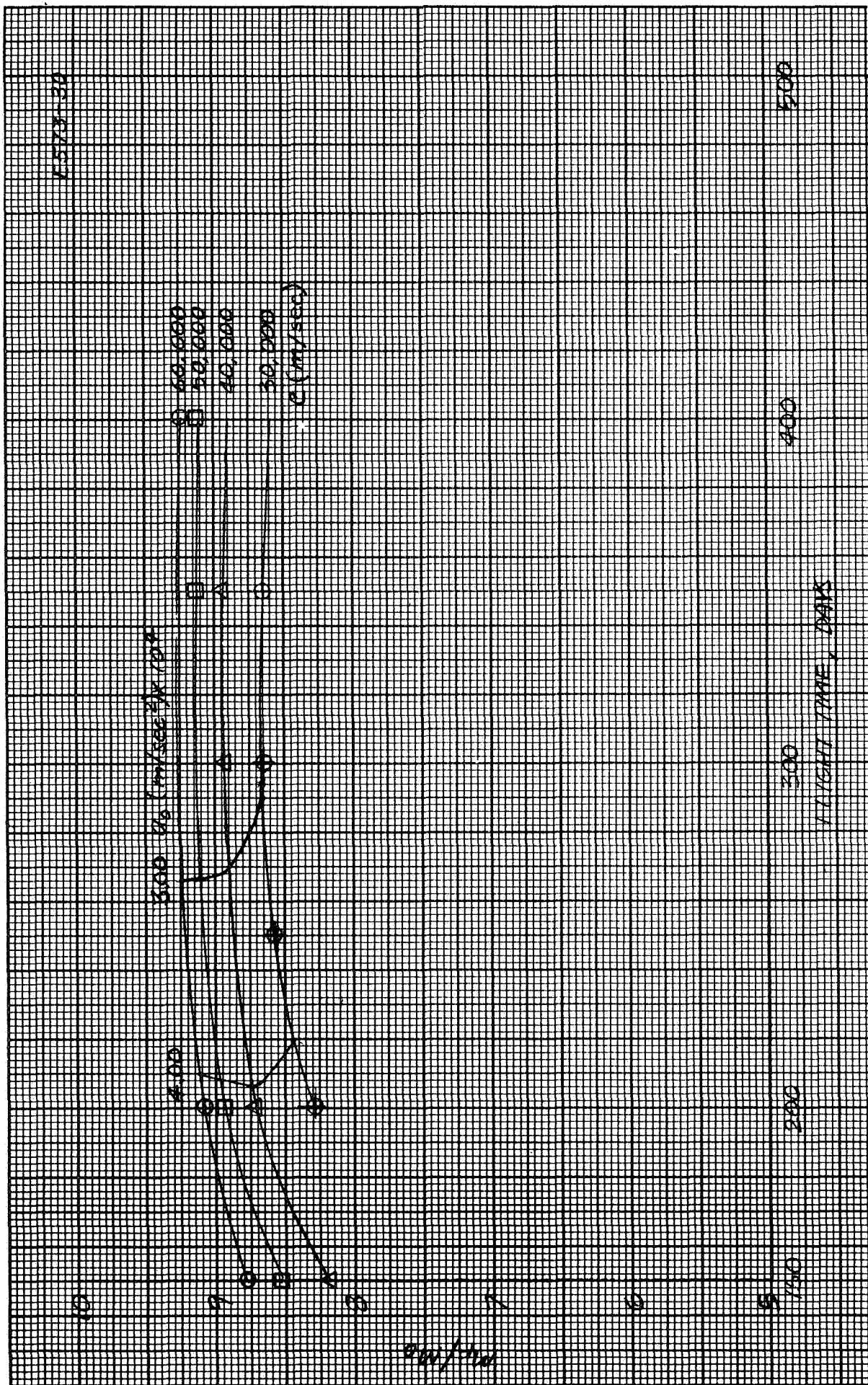


Fig. A.1-12. 1973 flyby.

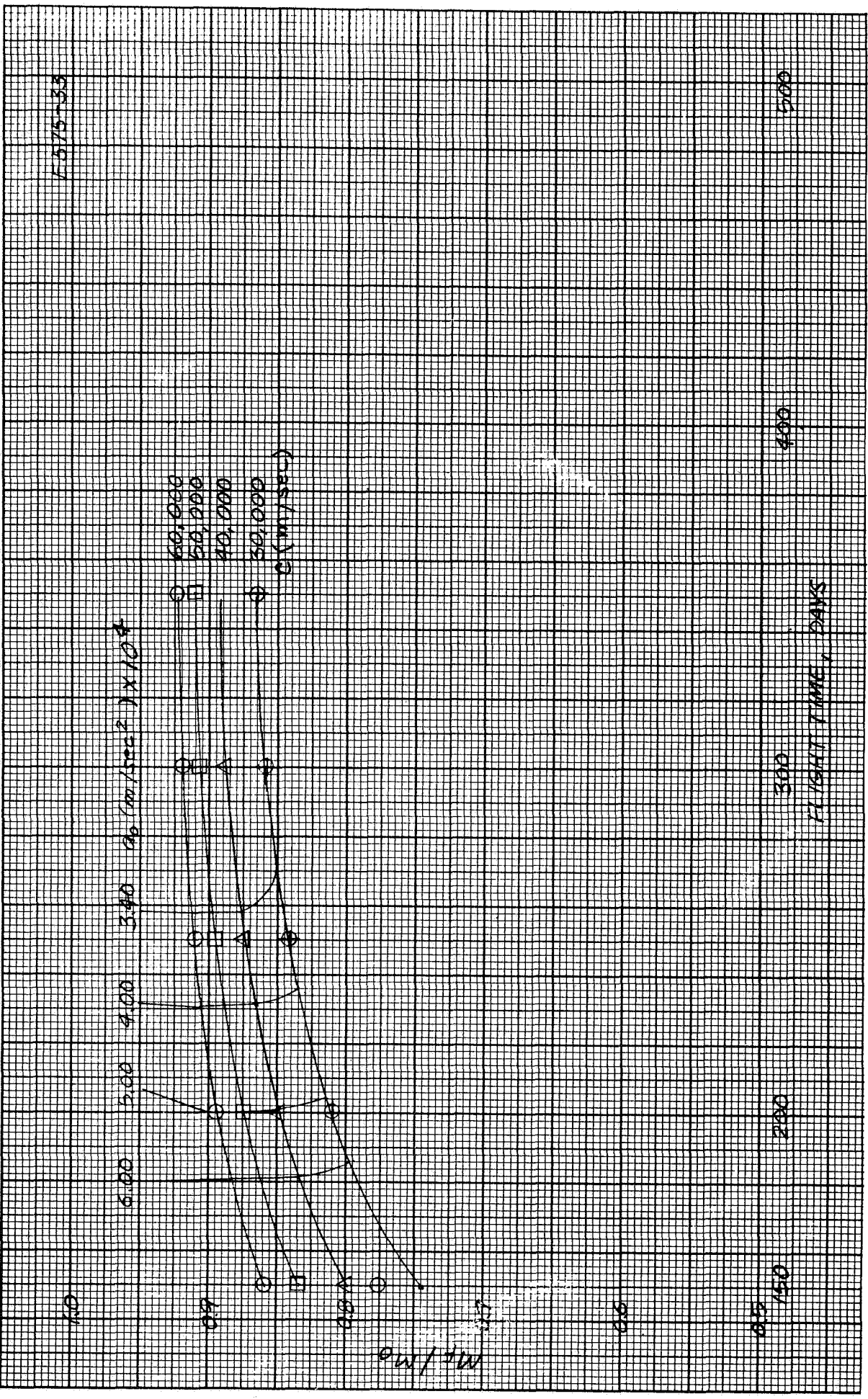


Fig. A. 1-13 1975 flv. v.

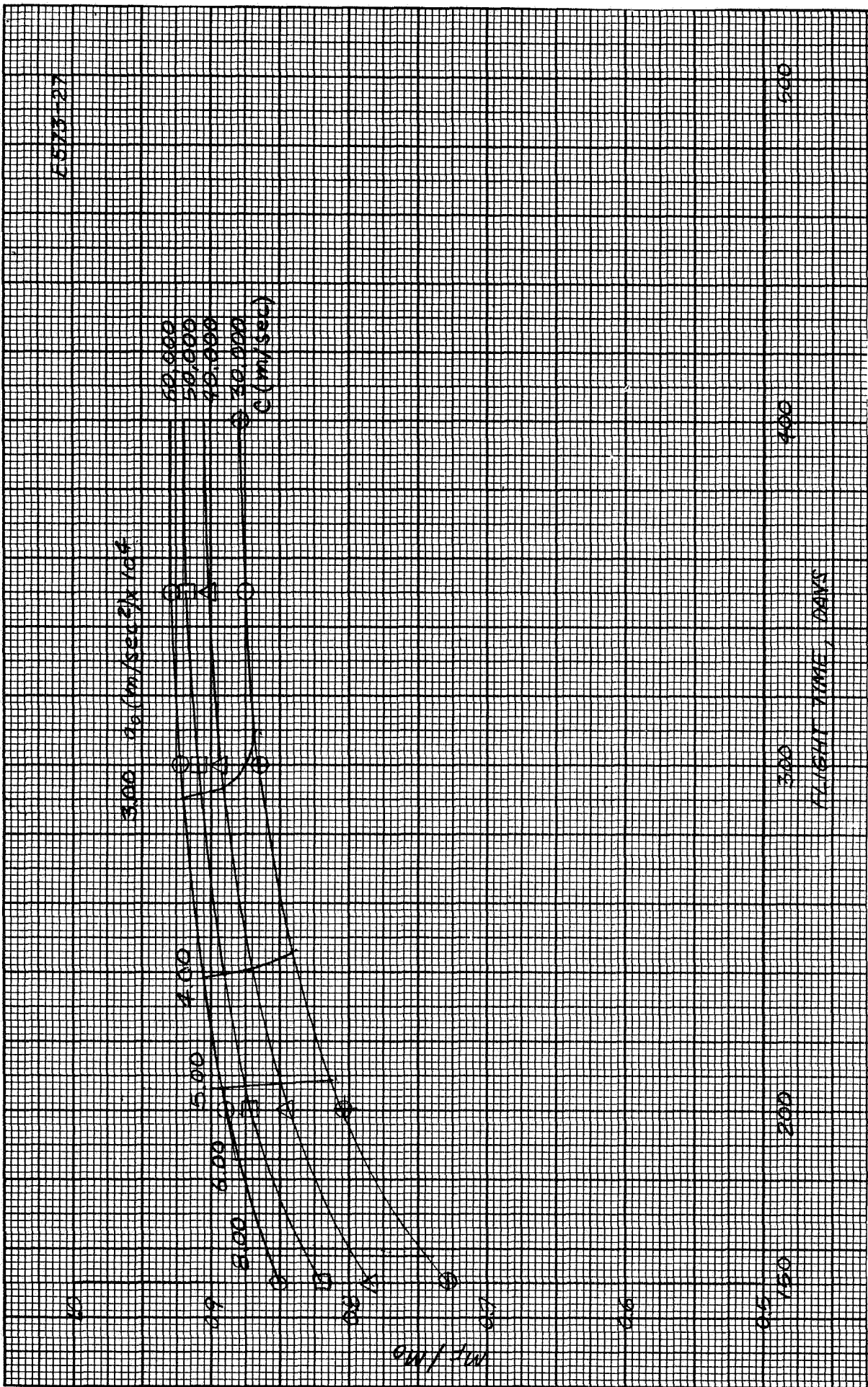


Fig. A.1-14. 1977 flyby.

advantage to the Optimum Coast profile over the Zero Coast. The choice between Flyby and Zero Coast for each launch year must await further detailed analysis..

Figures A. 1-15 thru A. 1-18 present the time histories of the heliocentric angle and thrust vector orientation for several missions namely 1971 zero coast rendezvous and 1973 flybys. The total heliocentric angle (as measured from the initial sun-probe line) through which the spacecraft must travel during a 1971 zero coast rendezvous mission varies from 225° to 290° for flight times between 300 days and 400 days (Fig. A. 1-15). For the 1973 flyby, the heliocentric angle is seen by Fig. A. 1-16 to be approximately 230° .

An important consideration in the spacecraft design is the required thrust vector direction. The variation of thrust angle as measured from the sun-probe line for the two types of mission profiles are shown in Figs. A. 1-17 and A. 1-18. Figure A. 1-17 indicates the effect of flight time on the thrust orientation requirement for the 1971 zero coast mission. The wide variation (40° to 135° for 300 day flight time and 60° to 110° for 350 days) may be undesirable from the spacecraft design point of view, even though these curves might be simulated by two discrete thruster positions (e.g., 60° and 120° for 300 days and 70° and 100° for 350 days). The 400 day mission, on the other hand, appears extremely attractive since the total thrust vector variation is less than 20° total that is, between 70° and 90° . Since this variation is small it could probably be replaced with a constant thrust vector of about 80° thereby eliminating the need for thruster array rotation and deployment. The thrust angles for the 1973 flybys are shown in Fig. A. 1-18. The angular variation ranges from 90° to 20° and is relatively independent of flight time in the cases shown.

The trajectory data presented in Figs. A. 1-1 thru A. 1-14 can now be used to determine the payload capability of ion propulsion systems and their optimum design points. Although results have already been presented (e.g., 1st Bi-monthly Report, for the design model mission) they will be repeated here for completeness.

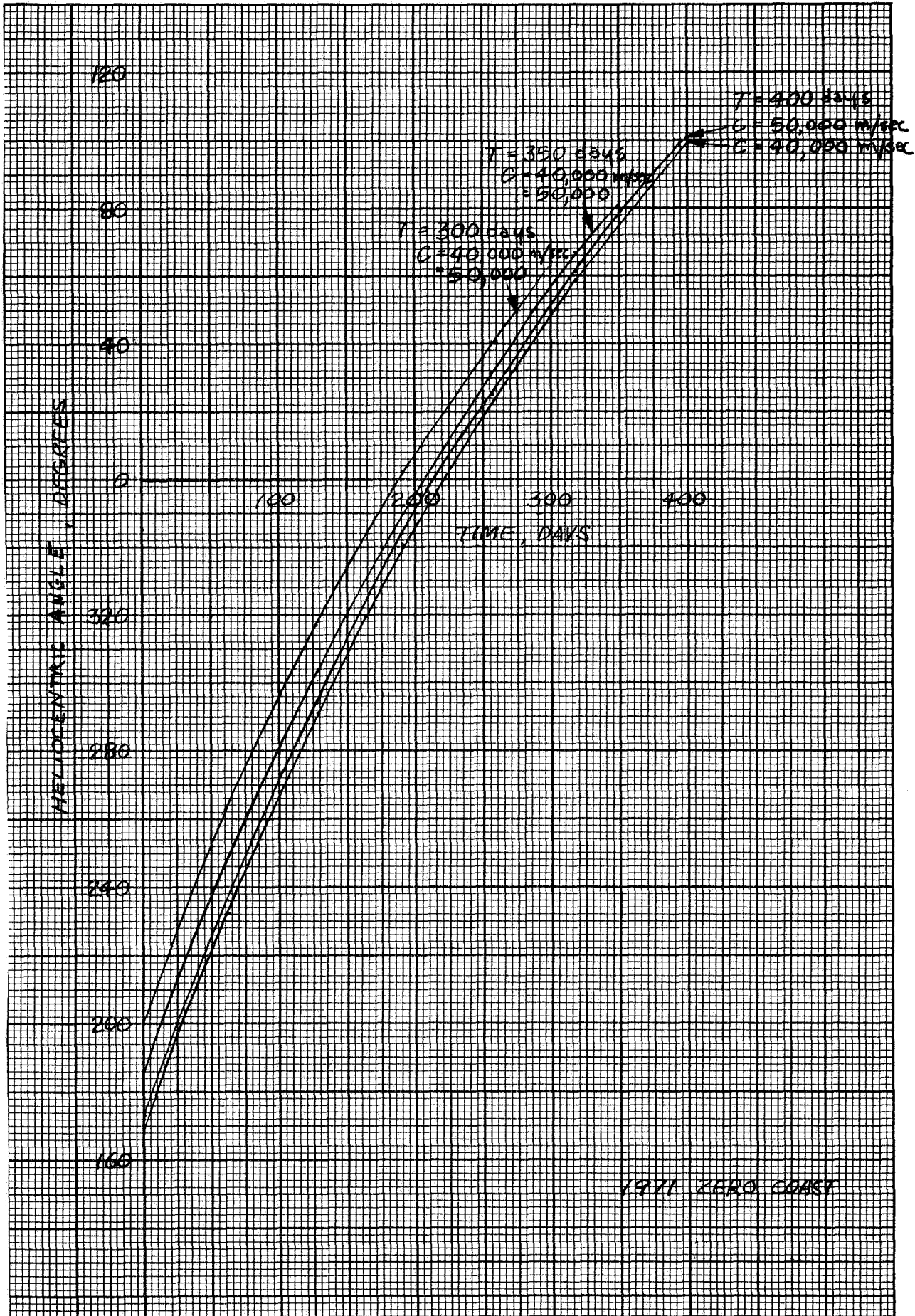
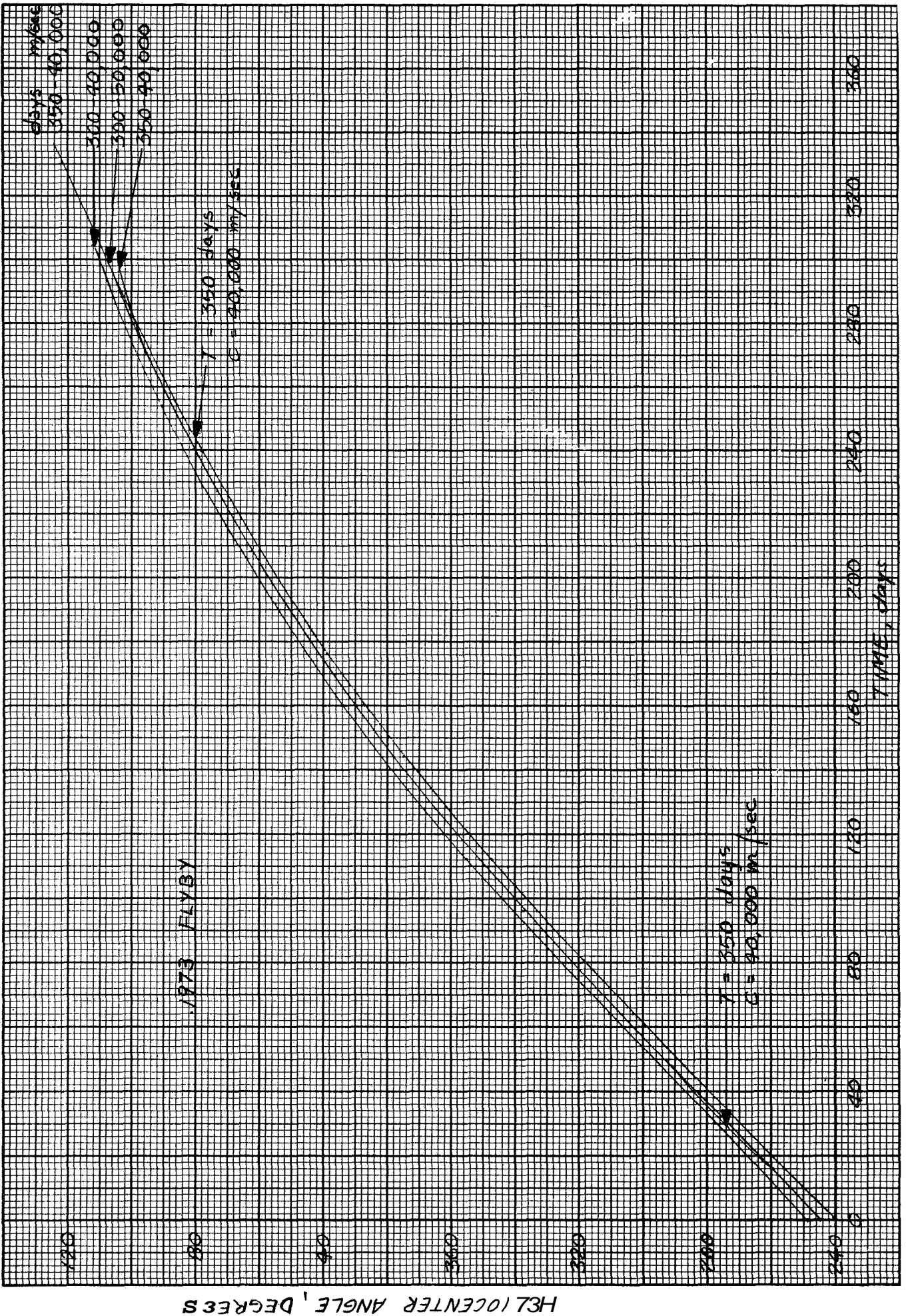


Fig. A. 1-15. Heliocentric angle time profile.

E573-26



A.1-16. Heliocentric angle time profile

E 573-34

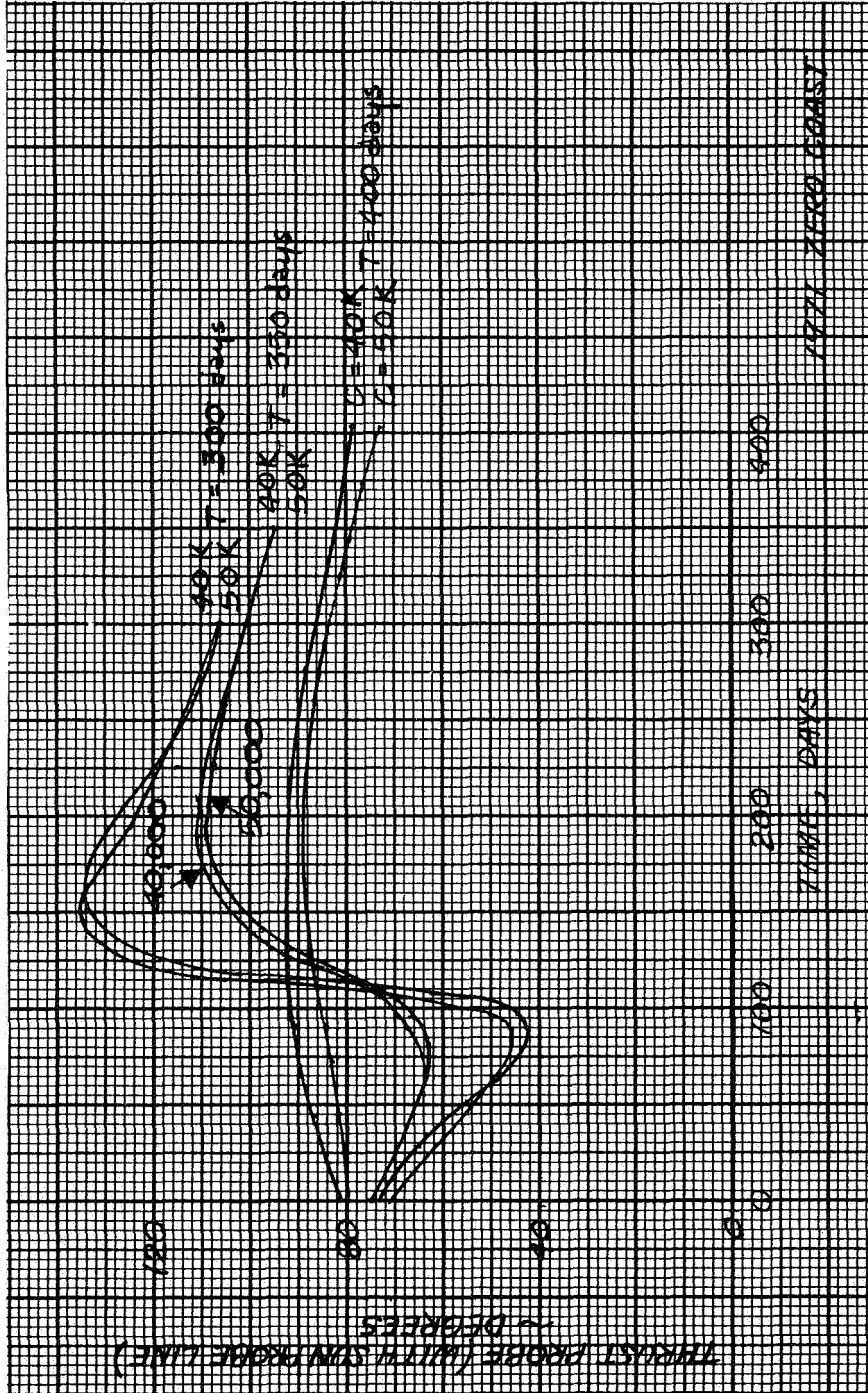


Fig. A. 1-17 Thrust wgle time profile.

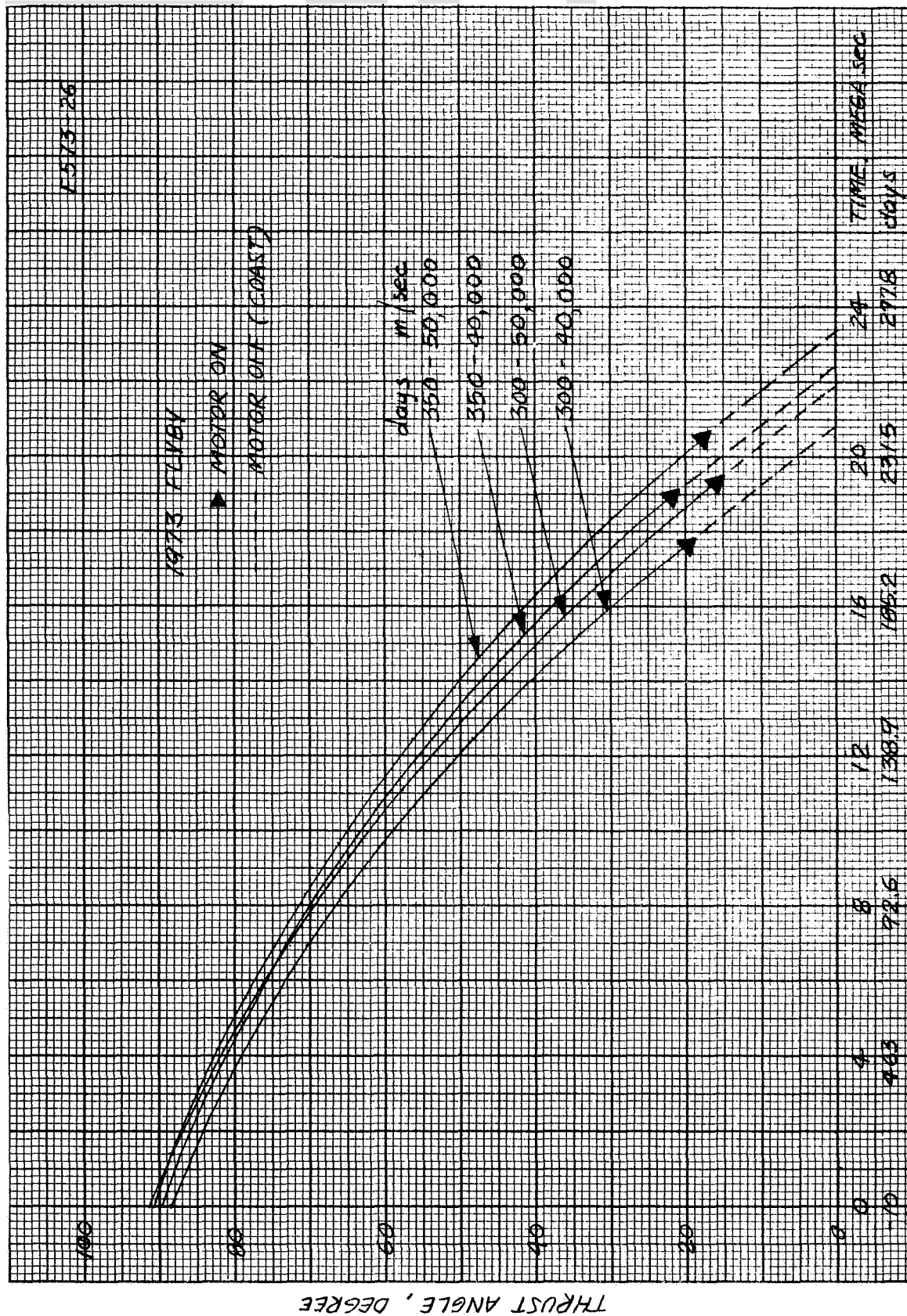


Fig. A. A-18 Thrust angle time θ profil^e

Since **for** the propulsion **system** and spacecraft design a 1971, 350 day, zero coast rendezvous mission was **chosen**, the propulsion system performance was evaluated **for** operating points from 3000-6000 sec I_{sp} and initial acceleration levels of approximately $2.5 \times 10^{-4} \text{ m/sec}^2$ (e.g., see A. 1-6). By moving up the vertical 350 day line on Fig. A. 1-6 to higher values of specific impulse the final-to-initial mass ratio is increased, that is, the required propellant is decreased. However, since the power in the exhaust beam of an electric thruster is proportional to specific impulse, the power **source mass increases** with I_{sp} . Obviously there is a tradeoff then between power **and** propellant and, therefore, an optimum I_{sp} . Optimum I_{sp} is defined **here as** that specific impulse at which the sum of the propulsion system **and** propellant masses are minimized. The total power required by the propulsion system is proportional to the specific impulse divided by the engine efficiency, thus one more effect that must be considered in determining $\{I_{sp}\}_{opt}$ is the variation of engine efficiency with specific impulse.

The total engine efficiency **as** a function of specific impulse for the Hg bombardment thruster is shown in Fig. A. 1-19. These curves are meant to represent ~~state-of-art~~ devices and not ultimate performance capability. In addition, these performance figures are felt to be consistent with 10,000 hr engine life.

With the data in Fig. A. 1-19 and the performance maps shown in Figs. A. 1-6, A. 1-7, and A. 1-8; the optimum specific impulse, payload capability, and the power requirement for a given initial spacecraft weight can be determined for the thruster system.

Figure A. 1-20 presents the payload capability and the optimum I_{sp} for the bombardment engine for the 1971, 350 day, zero coast rendezvous mission. The specific weight of the propulsion system is assumed to be 75 lb/kW. **In** each case the power requirement for a 11,700 lb spacecraft is given. The term payload mass on this figure, as well as those to follow, is defined as that mass placed in some elliptical orbit about Mars less the mass of the electric propulsion system. For the bombardment engine, the maximum payload capability

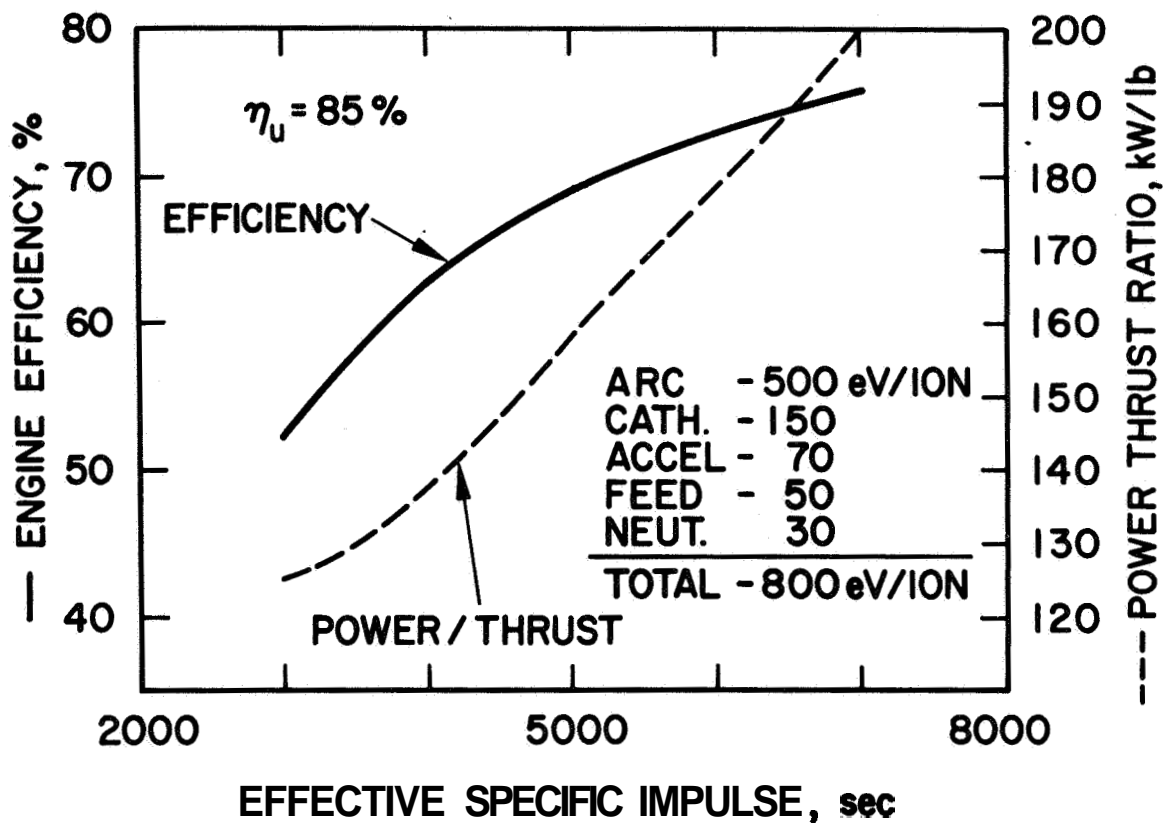


Fig. A. 1-19. State-of-the-art mercury bombardment ion engine efficiency.

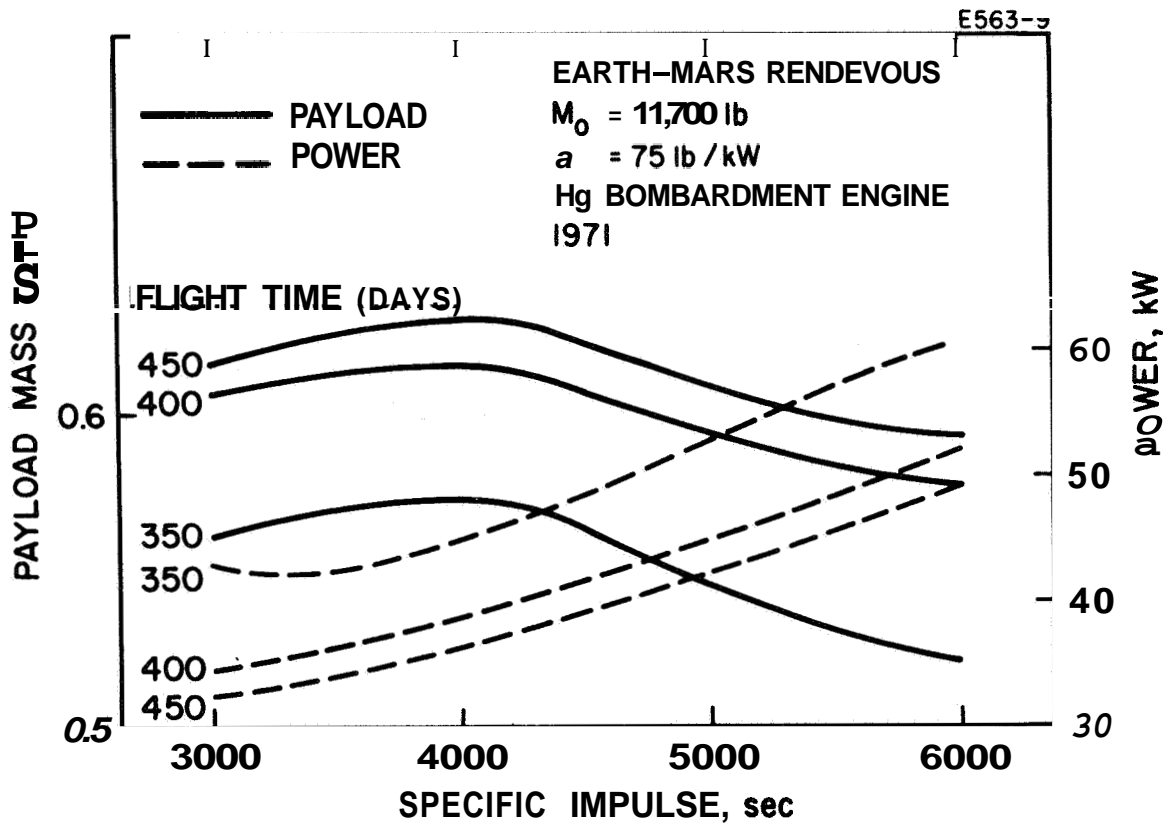


Fig. A. 1-20. Effect of total flight time on ion engine performance.

is about 57% at an I_{sp} of 4000 sec. The payload falls off slightly at $I_{sp} > 4000$ sec. The power requirement at 4000 sec I_{sp} is about 46 kW increasing to 60 kW at 6000 sec I_{sp} . Therefore, even though only a small payload penalty is paid for operating at a specific impulse greater than the optimum, a relatively large increase in power is required. However, operation at 3000 sec I_{sp} provides little or no payload loss while lowering the power requirement to 40 kW.

The effect of total flight time on payload optimum I_{sp} , and power requirement is also shown in Fig. A. 1-20. The optimum specific impulses for the three flight times show, all lie between 3000-4000 sec with the payload mass ratio increasing from 57% for 350 days to 61.5% for 400 days. The power requirement for the 400 day mission is 39 kW. Since the payload capability increases only slightly with longer flight times (e.g., to 63% for 450 days), 400 day flights can be considered optimum from a payload standpoint. Since the 400 day trip also provides the least variation in thrust angle, it appears quite attractive.

The reduction in payload capability for launch years of 1973 and 1975 is given in Fig. A. 1-21. Also presented is the effect of launch year on the system design parameters. The optimum I_{sp} remains in the 3000 to 4000 sec region while the power requirement increases to about 67 kW for the 1975 launch year. The payload mass ratio for 1973 is 47% as compared to 33% for 1975. Again these data are for a 350 day, zero coast rendezvous mission. It is possible that for the 1975 mission, a flyby profile would be more desirable. This possibility will be evaluated.

The penalty paid as a function of launch window is shown in Fig. A. 1-22. As shown; about a 2% loss in payload is sustained if a 30 day launch window is required. For the 30 day launch window, the power requirement increases from 46 kW to 48 kW.

During the course of the propulsion system design (Section B) an estimate of the weight of the propulsion system weight was made. The results of this preliminary evaluation indicated that specific weight of the complete engine system (i.e., less solar array) would be under 15 lbs/kW. Assuming the solar panel specific weight meets its design

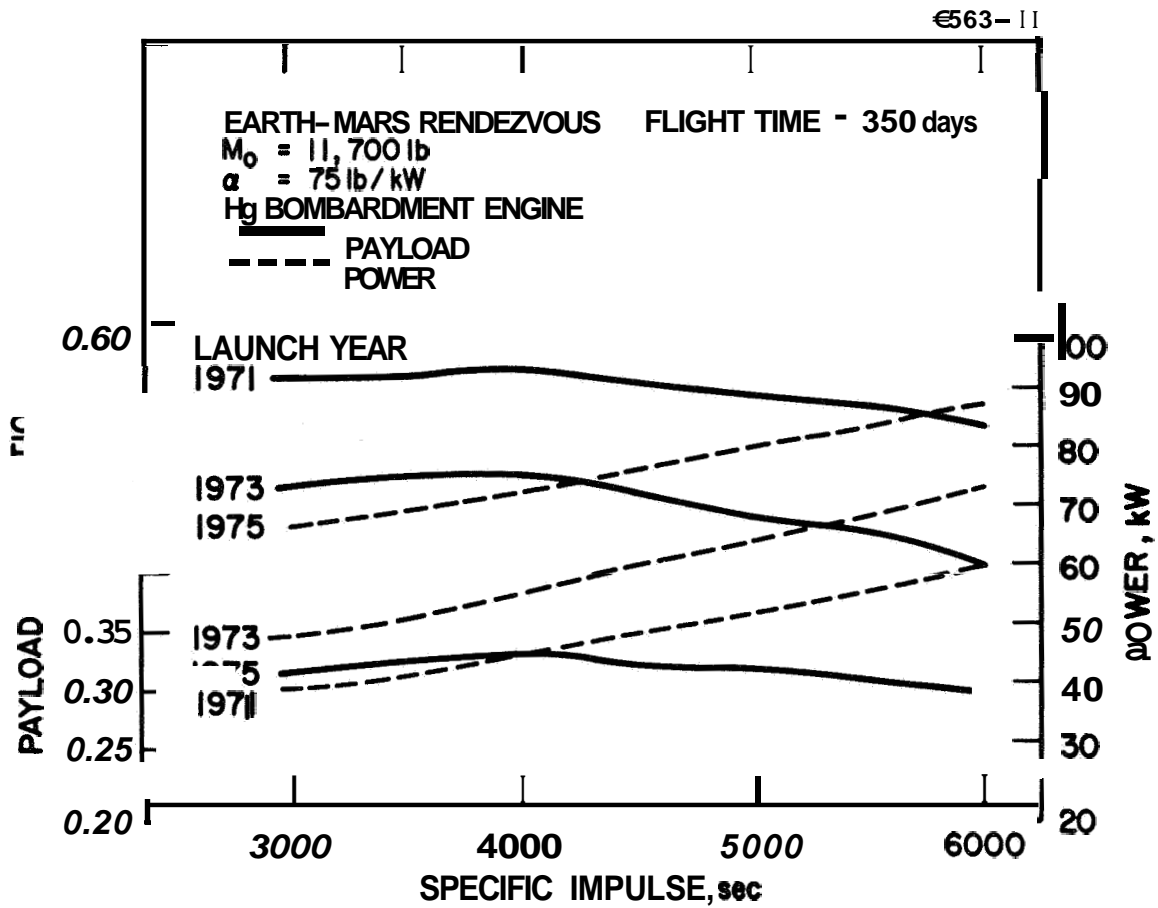


Fig. A. 1-21. Effect of launch year on ion engine performance.

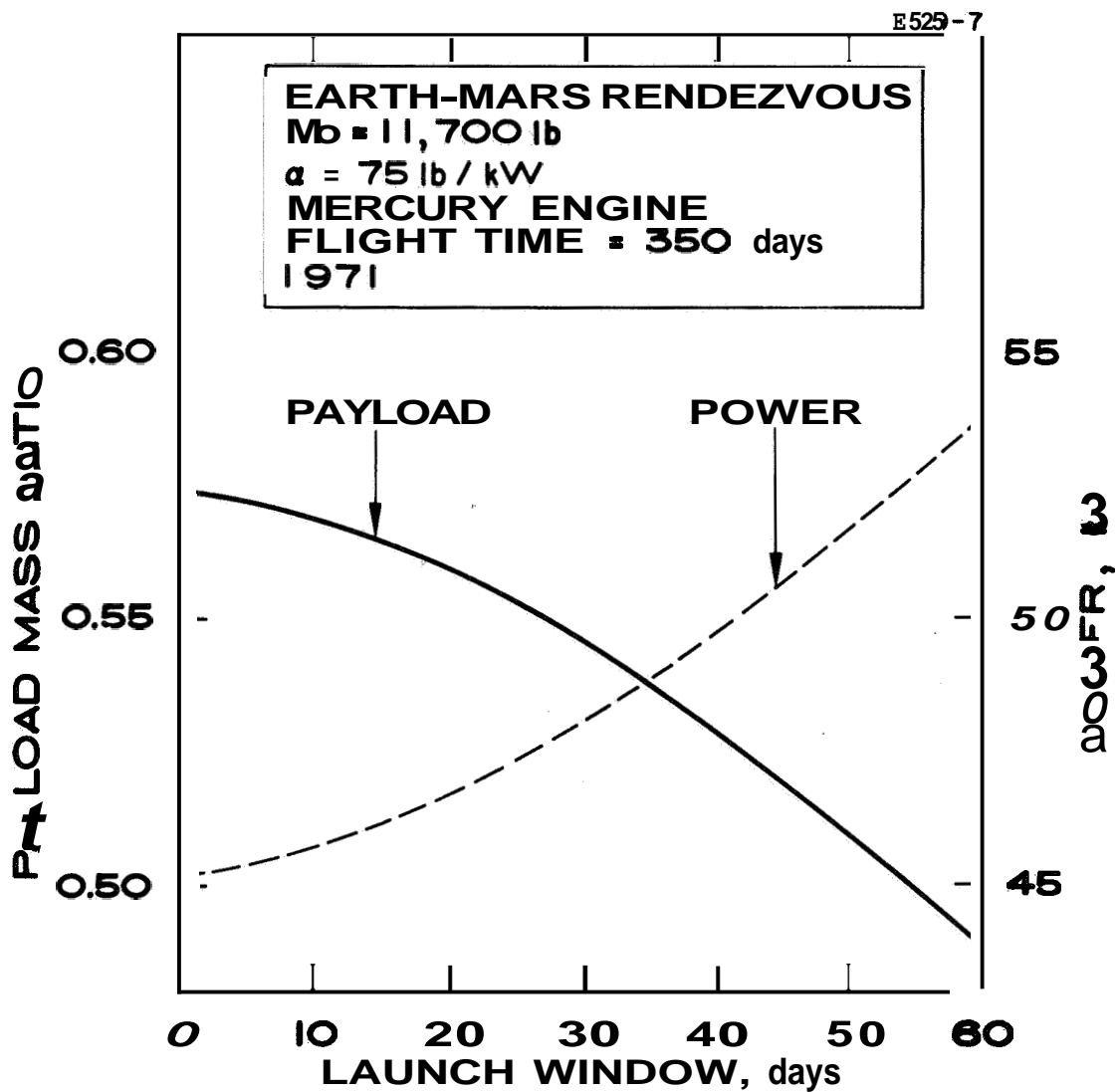


Fig. A. 1-22. Effect of launch window on ion engine performance.

goal of 50 lb/kW, the complete propulsion system will probably weigh less than the 75 lb/kW used in the preceding analyses. Figure A. 1-23 shows the effect of specific weight on ion engine payload capability. As shown, if a specific weight of 65 lb/kW is achievable for the complete propulsion system, the payload ratio increases from 57% to 61% for a 350 day mission and from 61.5% to 65.7% for a 400 day mission.

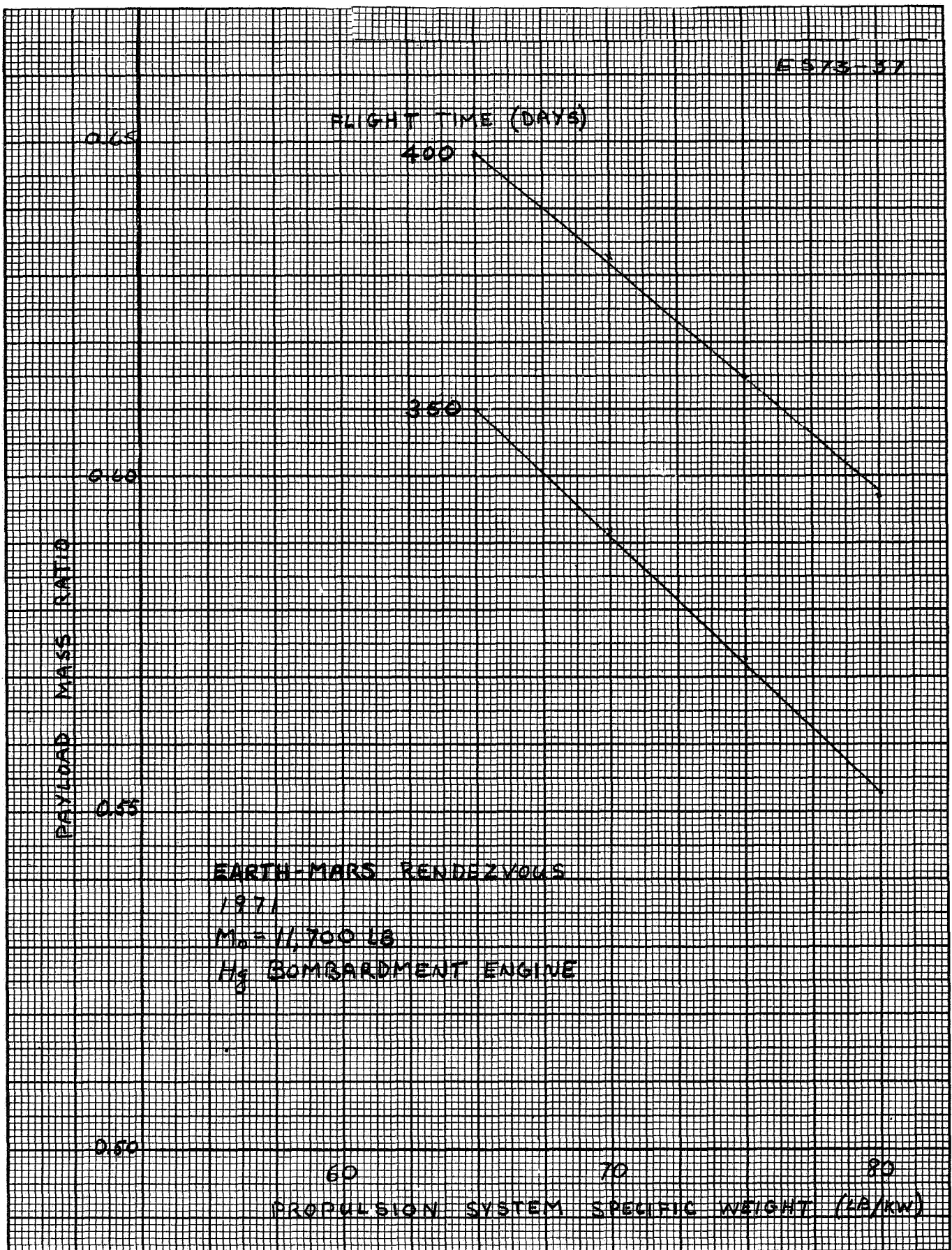


Fig. A-1-23. Effect of specific weight on ion engine performance.

A.2 All-Chemical Spacecraft Performance Analysis

Payload capability of a Mars orbiter using all-chemical propulsion for the 1969 to 1975 launch opportunities utilizing the Saturn 1B/Centaur vehicle, and the 1971 launch opportunity utilizing the Atlas/Centaur launch vehicle were presented in the first "Bi-Monthly Report". Additional results for the 1977 launch opportunity utilizing the Saturn 1B/Centaur launch vehicle (as per the increased scope of contract) are presented here:

The assumptions are identical to those listed in the previous report, namely:

- a. A 1000 pound capsule will be aboard the orbiter using the Saturn 1B/Centaur booster. Capsule separation will take place well before retro application.
- b. The nominal Martian orbit will have a periapsis altitude of 4,000 km. and the apoapsis altitude of 50,000 km.
- c. The retro propulsion system will have a specific impulse of 315 seconds and the dry weight of the propulsion system is taken to be 10 per cent of the entire propulsion system.
- d. An allowance of 3000 meters per second is assumed to provide for midcourse correction and losses due to finite burning time and other causes.

Results for both Type I and Type II trajectories are shown in the attached graphs (Figures A.2-1 and A.2-2). It is noted that the 1977 period will be rather unfavorable for Type I trajectories, because of large declination angles required during the ascent phase. Orbiter mass of 4000 to 4500 pounds may be

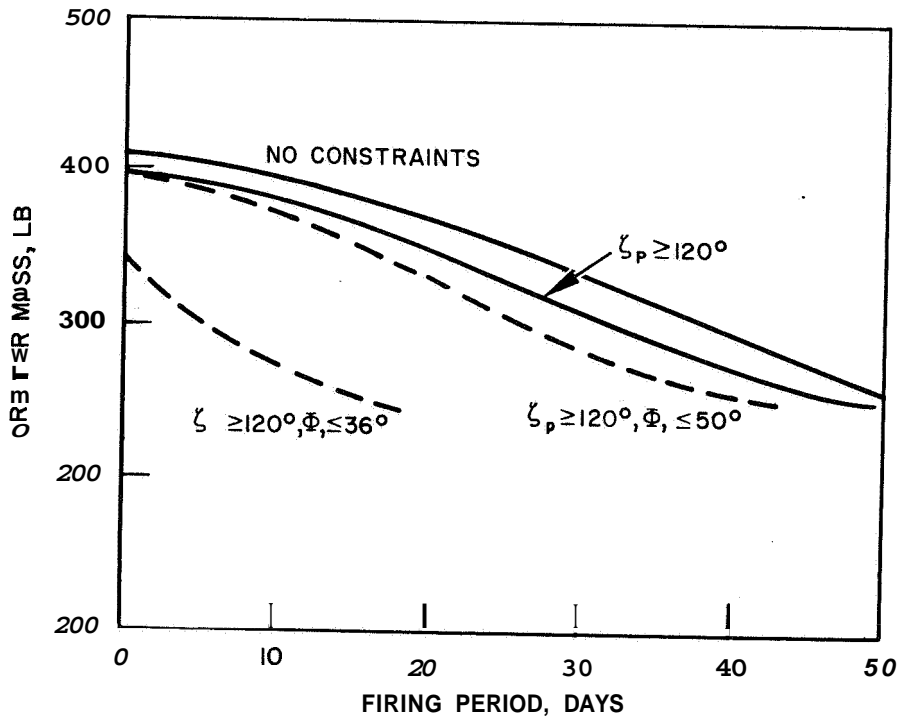
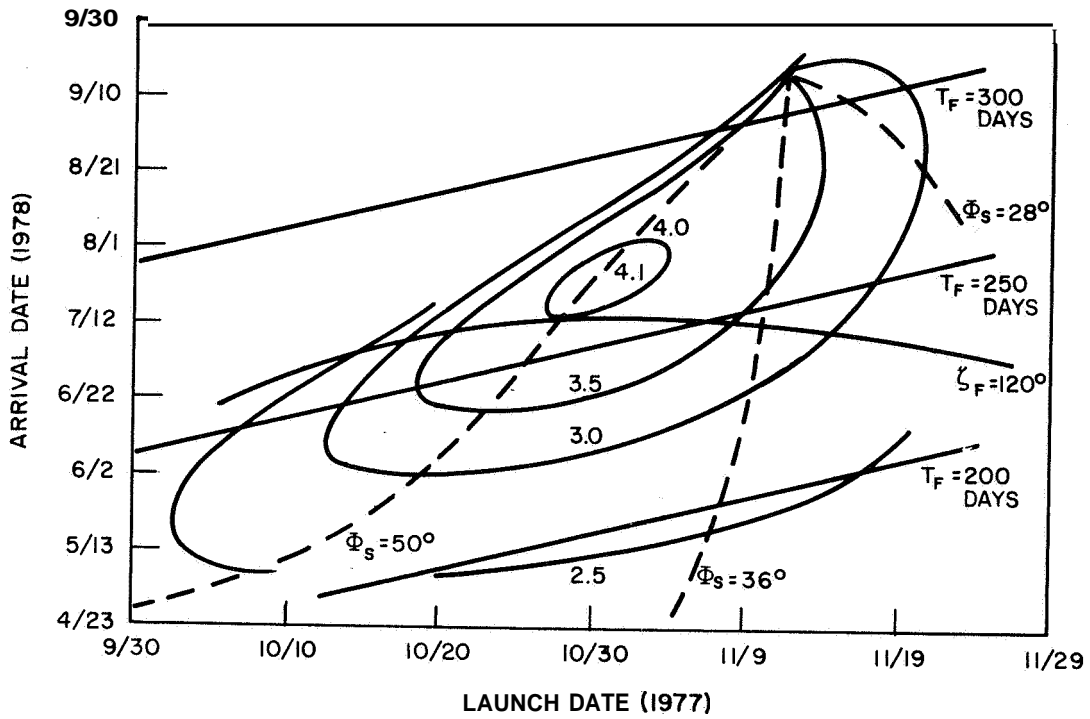


Figure . Mars Orbiter Capability Saturn IB/Centaur Launch Vehicle 1977 Type I

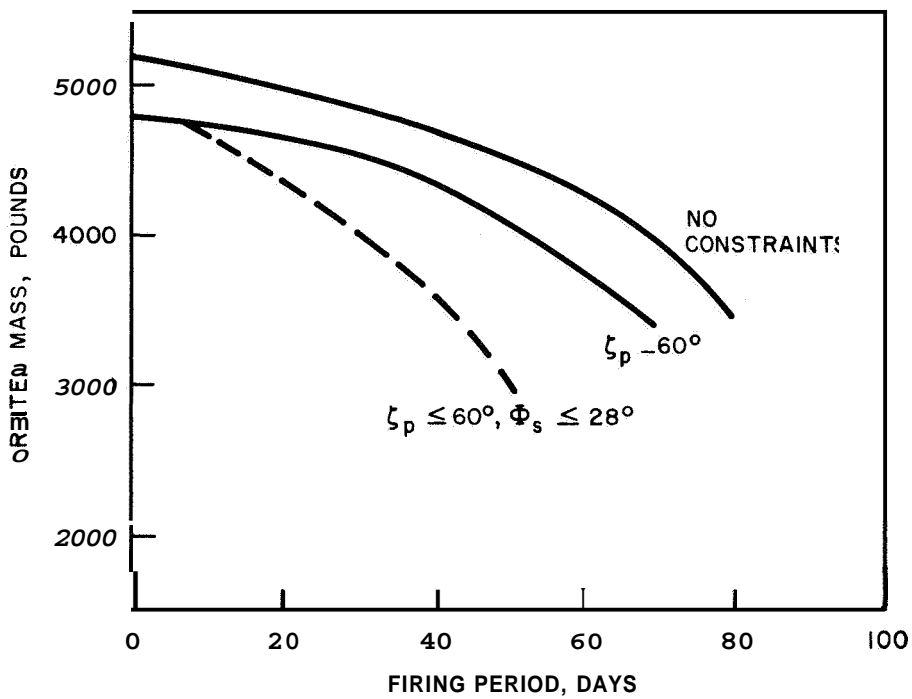
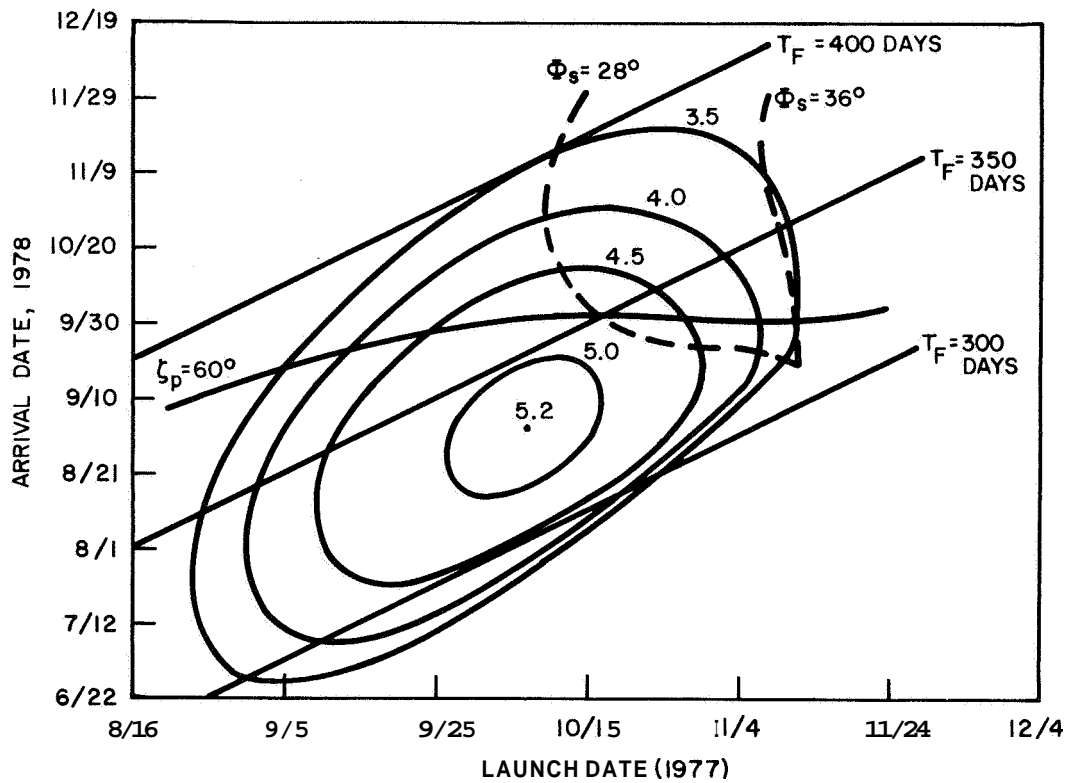


Fig. A.2-2. Mars Orbiter Capability - Saturn IB/Centaur Launch Vehicle 1977 Type II

handled by Type II trajectories for a firing period of thirty days, although the flight time required would be in excess of 350 days.

Additional summary to be appended to Table I of the first Bi-Monthly report is presented below

ORBITER MASS FOR 1977

Traj. Type	Lighting Constraint	No	$60^\circ \geq \zeta_p \geq 120^\circ$	$60^\circ \geq \zeta_p \geq 120^\circ$	Flight Time Days
	Launch Constraint	No	No	$36^\circ \geq \psi_s \geq -36^\circ$	
I	1977	3,370	3,100	2,100	240-200
II	1977	4,850	4,550	4,550	400-350

If the launch declination angle is to be kept below 28° , the value for Type II trajectories will become 4,000 lbs.

A.3 Performance Comparison

Presented in Figure A.3-1 is a comparison of the "best-case" solar-electric powered spacecraft Mars mission capability with that of the all-chemical powered spacecraft for the 1971 launch opportunity. The solar-electric powered spacecraft curve depicts the Mars orbiter weight-capability for a 400 day mission in which the heliocentric transfer phase is accomplished in a zero coast rendezvous mode. The all-chemical spacecraft mission time is 190 days. It is evident that the electric propulsion spacecraft has a useful Mars orbiter weight advantage of at least 1200 pounds over the entire launch window investigated. It should further be noted that these performance numbers are based on a specific weight of 25 lb/KW for the electric engine system (thruster, power conditioning, feed system, and control system) whereas present indications are that a specific weight of about $\frac{1}{2}$ of this value is feasible. (See Section II B)

Similar comparisons for all launch opportunities from 1969 to 1977 are under preparation.

MARS ORBITER WEIGHT CAPABILITY COMPARISON

1971 LAUNCH OPPORTUNITY

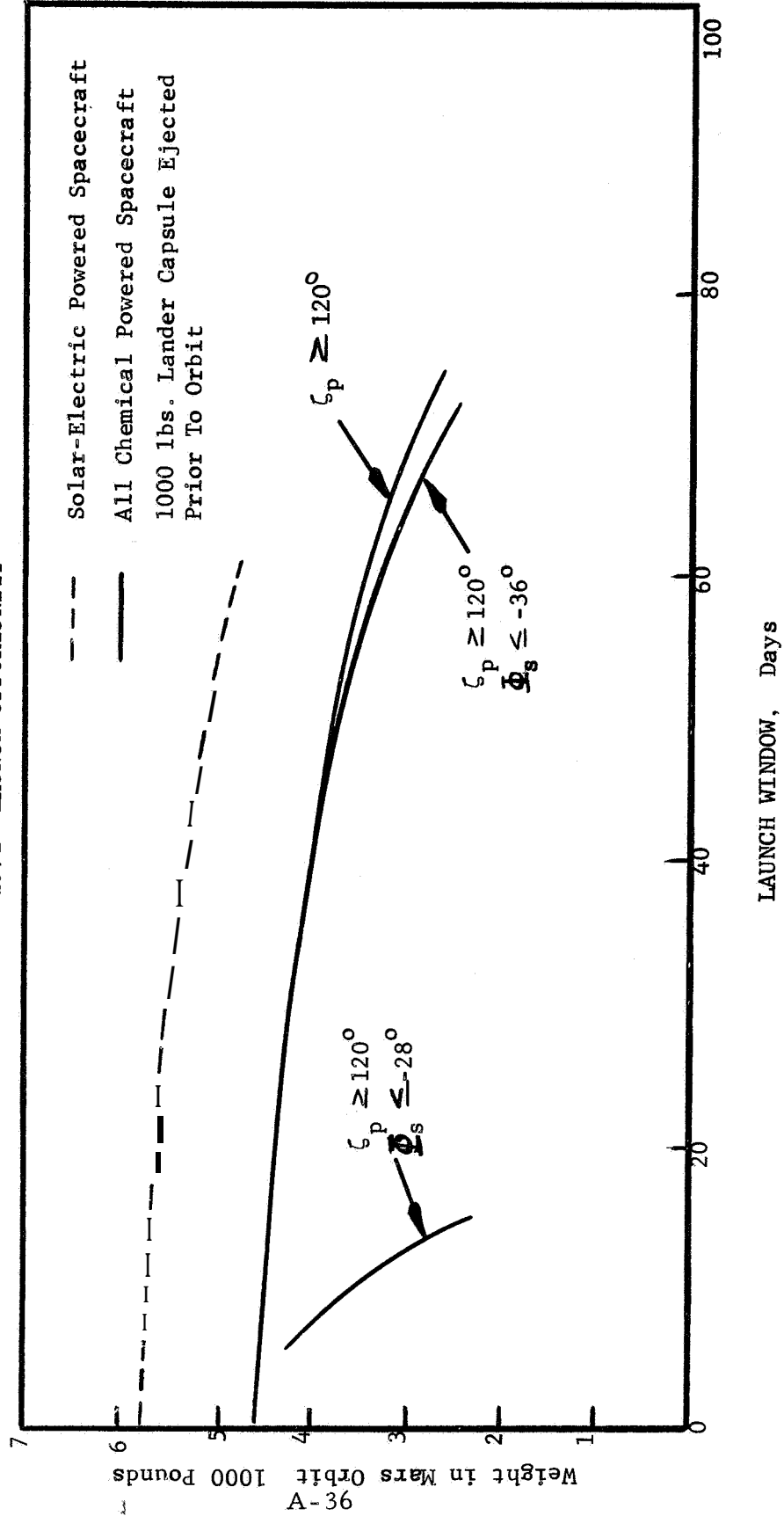


FIGURE A.H-1

B. PROPULSION SYSTEM STUDIES AND HARDWARE

The propulsion system studies which have been performed during this phase of the program have consisted of (1) a study of the effect of power level on the design and operating characteristics of the major propulsion system subsystems, (2) a reliability analysis to determine the optimum thruster module size for a high power propulsion system and to determine the effect of reliability considerations on overall system design, (3) a design layout of each of the major subsystems which would be used to make up a 48 kW ion propulsion system, (4) a conceptual design of a 48 kW ion propulsion system, and (5) a preliminary analysis of the problem of voltage and power matching between solar panel output and engine system. The design verification hardware to be discussed in this report is limited to the Hg bombardment thrusters (both oxide and pool cathodes) and their associated feed systems. The power conditioning and control systems have been described in detail in Ref. 1 and, therefore, will not be repeated here.

1. Scaling Study

In order to determine the optimum engine module size for a high power ion propulsion system, the variation of subsystem characteristics with power level must be determined. Also these scaling studies are used to define the optimum design parameters for subsystems at any power level and guarantee that the interpolation and/or extrapolation of existing data during the design phase is done on a realistic basis.

a. Thruster

In order to establish the relation between power level and engine design parameters the mercury bombardment thruster was scaled over a range of power levels. The factors considered in the study were: (1) perveance, (2) life and (3) mechanical design. The result of the study was to determine, as a function of power level, the optimum thruster configuration for providing a lifetime of at least one year at an I_{sp} of 4000 seconds,

Perveance

A relationship was derived which gives the average current density of a thruster (total beam/diameter squared) as a function of hole size (w) and electrode spacing (d). Reference 2 gives a general equation for the maximum current per hole. Considering countersunk optics (because of the increased

current capability) we obtain the following modified perveance expression, independent of screen electrode thickness.

$$(1) \quad I_H = P_H V_T^{3/2} = 4.4 \times 10^{-9} \left(\frac{1}{.336 + \frac{d}{w}} \right)^2 V_T^{3/2} \text{ amps}$$

V_T is the total accelerating voltage ($V_B + V_A$). The relationship between beam voltage (V_B) and specific impulse is shown in Fig. B. 1-1. At 4000 seconds and 80% propellant utilization, $V_B = 2500$ volts. The maximum allowable total voltage is then determined by assuming an upper limit for the accel/decel ratio:

$$(2) \quad \text{accel/decel} = \frac{V_B + V_A}{V_B}$$

References 3 and 4 indicate that an accel/decel ratio of two is easily attainable. Thus, we allow $2 \times 2500 = 5000$ volts for total accelerating potential and proceed to setup the resulting relationship between beam current and engine geometry. We can see from Fig. B. 1-1 that lower I_{sp} implies less available total voltage. For example, at 3000 seconds the total accelerating voltage would only be $1400 \times 2 = 2800$. This is just about half of what is available at an I_{sp} of 4000 seconds. With such sharp reduction in available voltage, the resulting engine designs for any power level would incorporate much larger diameters than for the 4000 second case.

From **Eq. 1**, the total current of an engine is given by:

$$(3) \quad I_T = \bar{P}_H N V_T^{3/2}$$

where N is the number of holes. \bar{P}_H is the "average" perveance per hole, so noted because of the non-uniform beam distribution associated with a bombardment engine. In other words, the product of N times **Eq. 1** does not necessarily give the engine current but, in general, indicates more current than is actually available. This is because the ion arrival-rate at the center

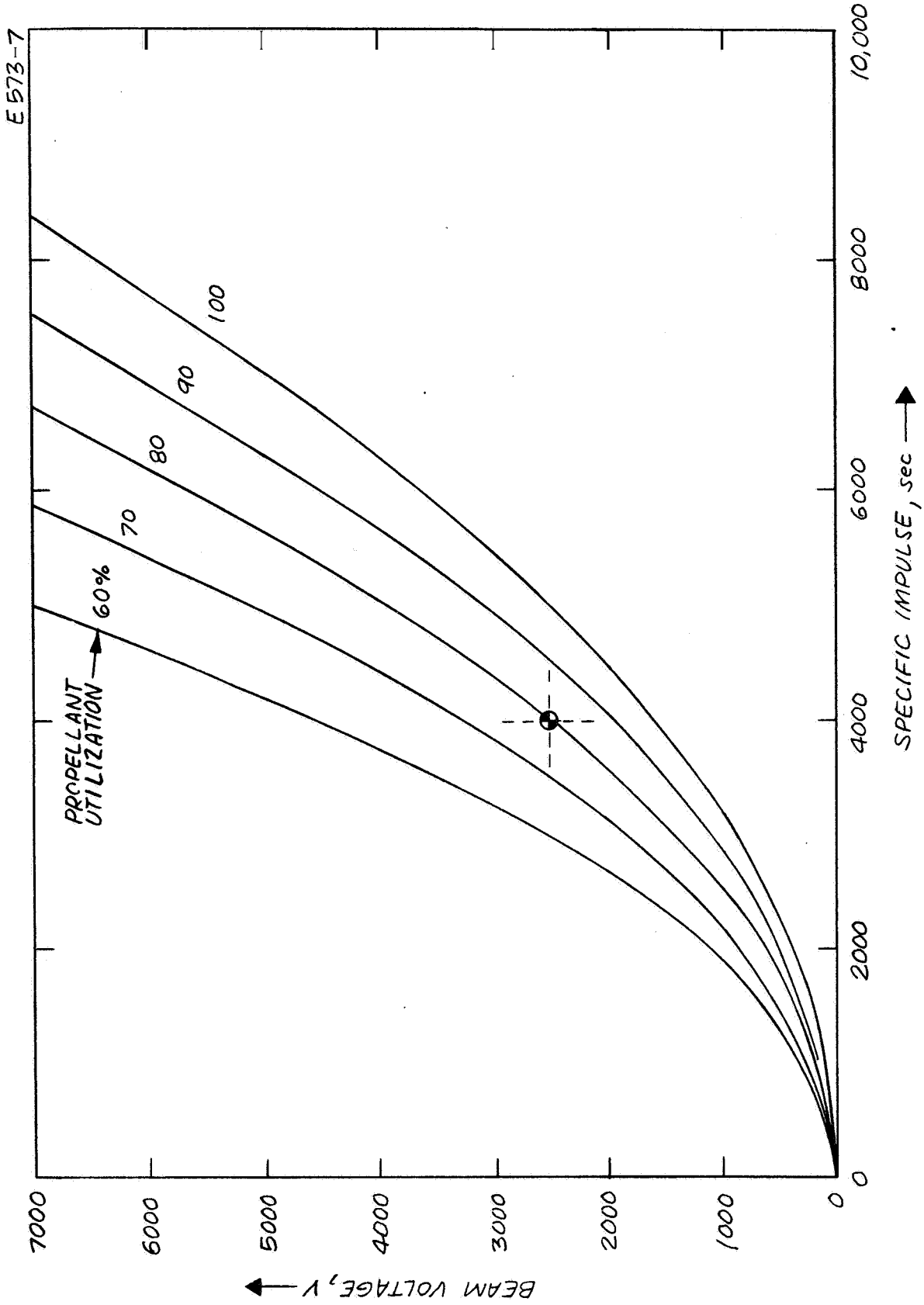


Fig. B. 1-1. Mercury bombardment engine. Beam voltage versus specific impulse for various values of propellant utilization.

will be drawn only at the peak of the current density distribution (center of engine). The remaining regions of the electrode will produce less current per hole.

A typical current density distribution exhibits a peak-to-average ratio of two-to-one {Refs. 5, 6, and 73. Hence:

$$(4) \quad \bar{P}_H = \frac{P_H}{2}$$

Eq. 3 becomes:

$$(5) \quad I_T = \frac{1}{2} P_H N V_T^{3/2}$$

The number of holes (N) of a thruster electrode is given by:

$$(6) \quad N = \left(\frac{D}{w} \right)^2 \gamma$$

where:

γ = ratio of open electrode area to total area = 0.58 for this study
(a typical value for present engines)

D = active engine diameter (cm)

w = hole diameter (cm)

Eq. 5 thus becomes:

$$(7) \quad I_T = \frac{1}{2} (4.4 \times 10^{-9}) \left(\frac{1}{.336 + \frac{d}{w}} \right)^2 \left(\frac{\gamma D^2}{w^2} \right) (5000)^{3/2} \text{ amps}$$

For convenience in expressing current density, we now introduce I_B ; $I_B = 10^3 I_T$ and expresses current in mA. Solving for (I_B/D^2) and evaluating:

$$(8) \quad \frac{I_B}{D^2} = 0.45 \left(\frac{1}{.366 w + d} \right)^2 \text{ mA/cm}^2$$

Figure B. 1-2 is a plot of Eq. 8. The aspect ratio (w/d) is also cross-plotted in Fig. B. 1-2.

If there were no other considerations, the engine size could be selected based on these results. But, so far, we have said nothing about engine life. An engine design selected at random from Fig. B. 1-2 could not be guaranteed to operate for 10,000 hours.

Engine Life

Electrode life considerations were based on the analysis of charge-exchange effects found in Ref. 4. In Ref. 7 it was found empirically that the life of a 1.27 millimeter thick accel electrode of a 10 cm. bombardment engine is given by:

$$(9) \quad t = \frac{3.28}{I_A} \text{ hours}$$

where I_A = accel interception current in amps, It is assumed that Eq. 9 may be extrapolated into a form general enough to predict the life of any electrode of thickness x and effective diameter D . The resulting expression is:

$$(10) \quad t = \frac{3.28}{I_A} \left(\frac{x}{.127} \right) \left(\frac{D}{10} \right)^2$$

Kerslake (Ref. 4) has derived an expression for I_A ;

$$(11) \quad \frac{I_A}{I_B} = 75 (1 - \eta_{\mu}) (l + 1) \frac{o}{\lambda}$$

where:

$$\begin{aligned} \eta_{\mu} &= \text{propellant utilization} \\ I_o &= \text{total mass flowrate} = I_B / \eta_{\mu}, \text{ amps} \end{aligned}$$

*So long as the spacing is greater than 2.5 mm to prevent voltage breakdown (based on the 2000 V/mm criteria in Ref. 8.)

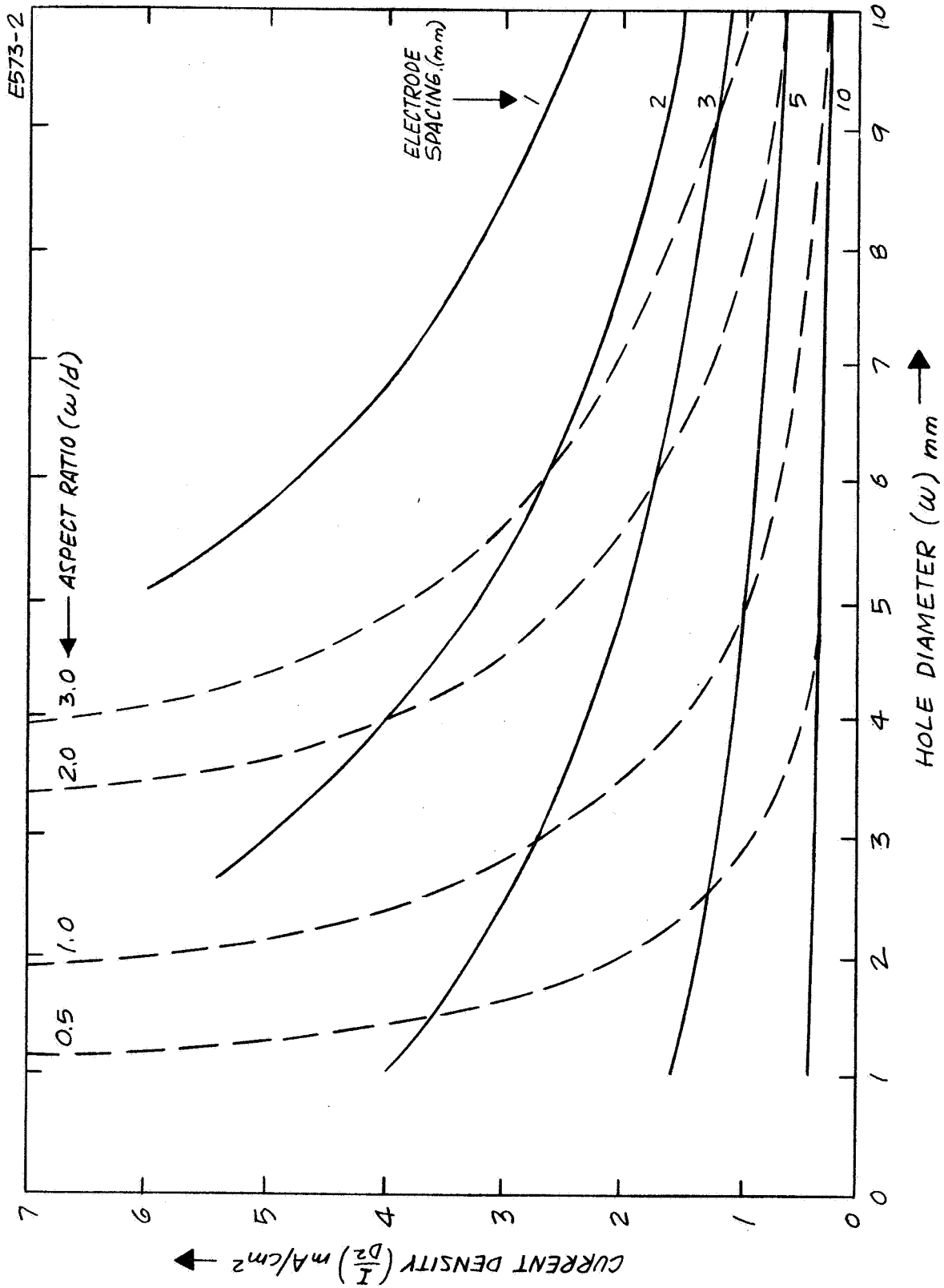


Fig. B. 1-2 Current density versus pole size and electrode spacing (mercury bombardment engine)
 sp = 4000 sec.

- A_o = overall electrode area, cm^2
 ℓ = distance between electrodes, cm .
 ℓ^1 = additional charge-exchange length, cm .

The term ℓ^1 accounts for the charge-exchange occurring downstream from the accel electrode, and is given by:

$$(12) \quad \ell^1 = \frac{1}{1.5} \left[\frac{\beta V_B^{3/2} A_I f}{\eta_\mu I_c} \right]^{1/2}$$

where:

- β = constant = 3.86×10^{-9} mks units
 A_I = electrode open area = $.58 \left(\frac{\pi}{4} D^2 \right)$
 f = function of accel/decel ratio (= 4.5 for a ratio of 2)

Evaluating Eq. 12 results in:

$$(13) \quad \ell^1 = 0.5 \left(\frac{D^2}{I_B} \right)^{1/2} \text{ cm.}$$

Equation 13 expresses the fact that the additional charge-exchange length is a function only of average current density, under the conditions we have specified. It is common to find ℓ^1 somewhat larger than ℓ , indicating that charge-exchange occurs over a distance of more than twice the electrode spacing.

Returning to Eq. 9, we may eliminate I_A by using **Eq. 11**. The resulting expression for electrode life in terms of current density, propellant utilization, and electrode geometry is:

$$(14) \quad t = \left(\frac{.5 \times 10^4}{\ell + \ell^1} \right) \left(\frac{\eta_\mu}{1 - \eta_\mu} \right) \left(\frac{D^2}{I_s} \right)^2 \left(\frac{x}{.127} \right) \text{ hours}$$

where ℓ^1 is given by **Eq. 13**.

Using $\eta_\mu = 80\%$ and defining:

$$(15) \quad j = \left(\frac{I_B}{D^2} \right) \text{ mA/cm}^2$$

Eq. 14 becomes:

$$(16) \quad t = 16. \times 10^4 \left(\frac{x}{l + .5/j^{1/2}} \right) \left(\frac{1}{j^2} \right)$$

We now set $t = 10,000$ hours in Eq. 16 and obtain the relationship between electrode plate separation and accel electrode thickness (at any current density) consistent with a one year life. The quantity l , as used above, represents the distance between electrodes measured from centerlines. Hence:

$$(17) \quad l = d + x/2$$

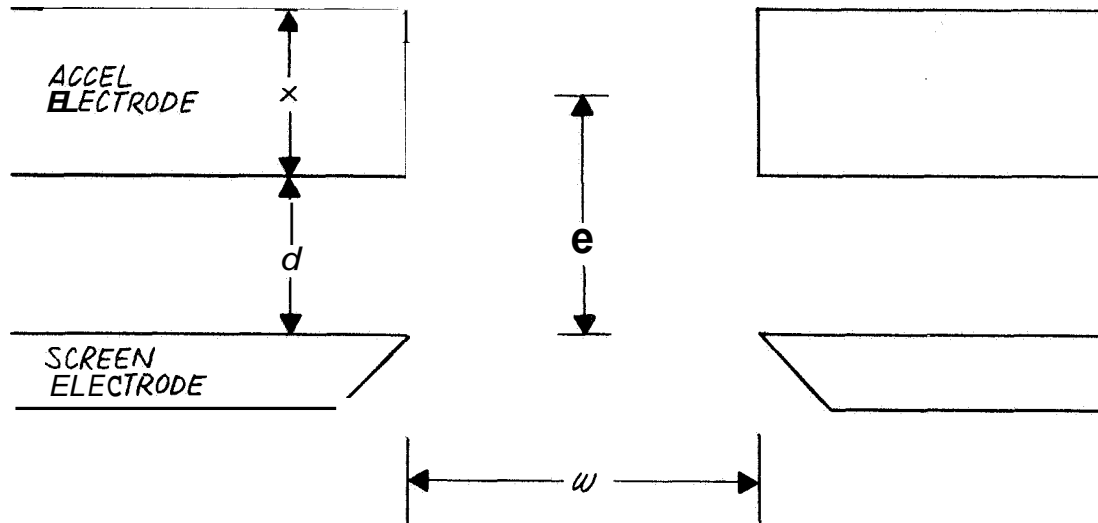
where d is the actual separation between electrode plates (see Fig. B. 1-3). Using Eq. 17 and rearranging, Eq. 16 becomes:

$$(18) \quad x = \frac{dj^2 t \frac{1}{2} j^{3/2}}{16. - \frac{1}{2} j^2}$$

Figure B. 1-4 is a plot of Eq. 18 for various values of j . The thickness requirement increases with plate separation because of the increasing charge-exchange region.

Engine Design

We are now in a position to qualify the results in Fig. B. 1-2 with respect to life. The accel electrode thickness requirements (Fig. B. 1-4) may be superimposed on Fig. B. 1-2, resulting in Fig. B. 1-5. These thicknesses represent the minimum requirement such that the electrode will survive a year of operation at the indicated current densities. Therefore, at this point we must eliminate certain regions of Fig. B. 1-5 from consideration for potential design on the basis that accel thickness cannot be made arbitrarily large. The criteria used is that the thickness cannot exceed half the hole diameter. Otherwise, direct beam interception is expected. This consideration forms one of the boundaries of the "design region" indicated in Fig. B. 1-5. This boundary is the inclined straight lines, which represents the locus of points where $x = w/2$.



x = accel thickness

I = separation (measured at center)

d = distance between electrodes

w = hole diameter

$$I = d + \frac{x}{2}$$

Fig. B. 1-3. Definition of electrode geometrical parameters.

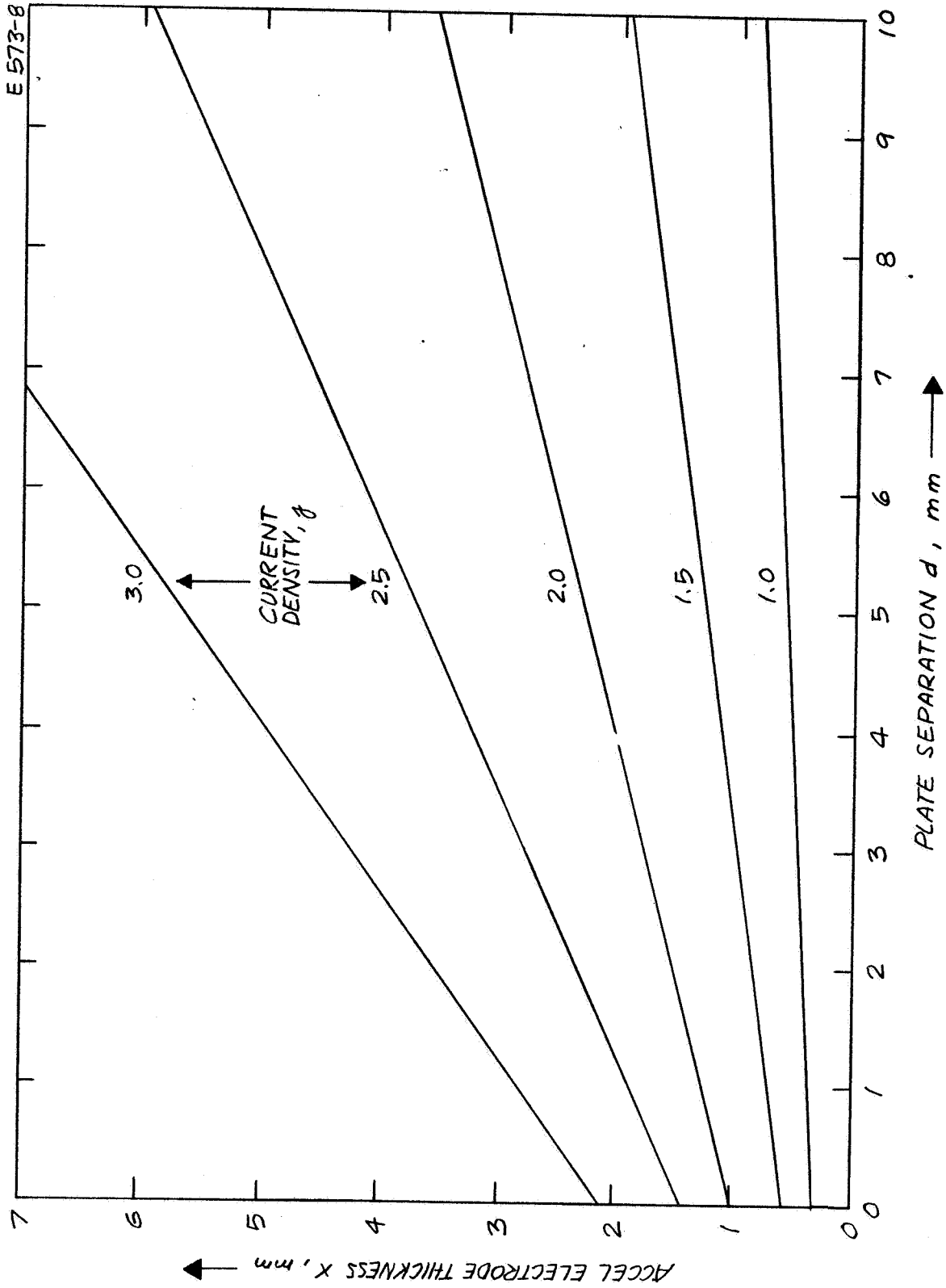


Fig. B. 1-4. Accel electrode thickness required for one year life and current density $I_{sp} = 4000$ sec.

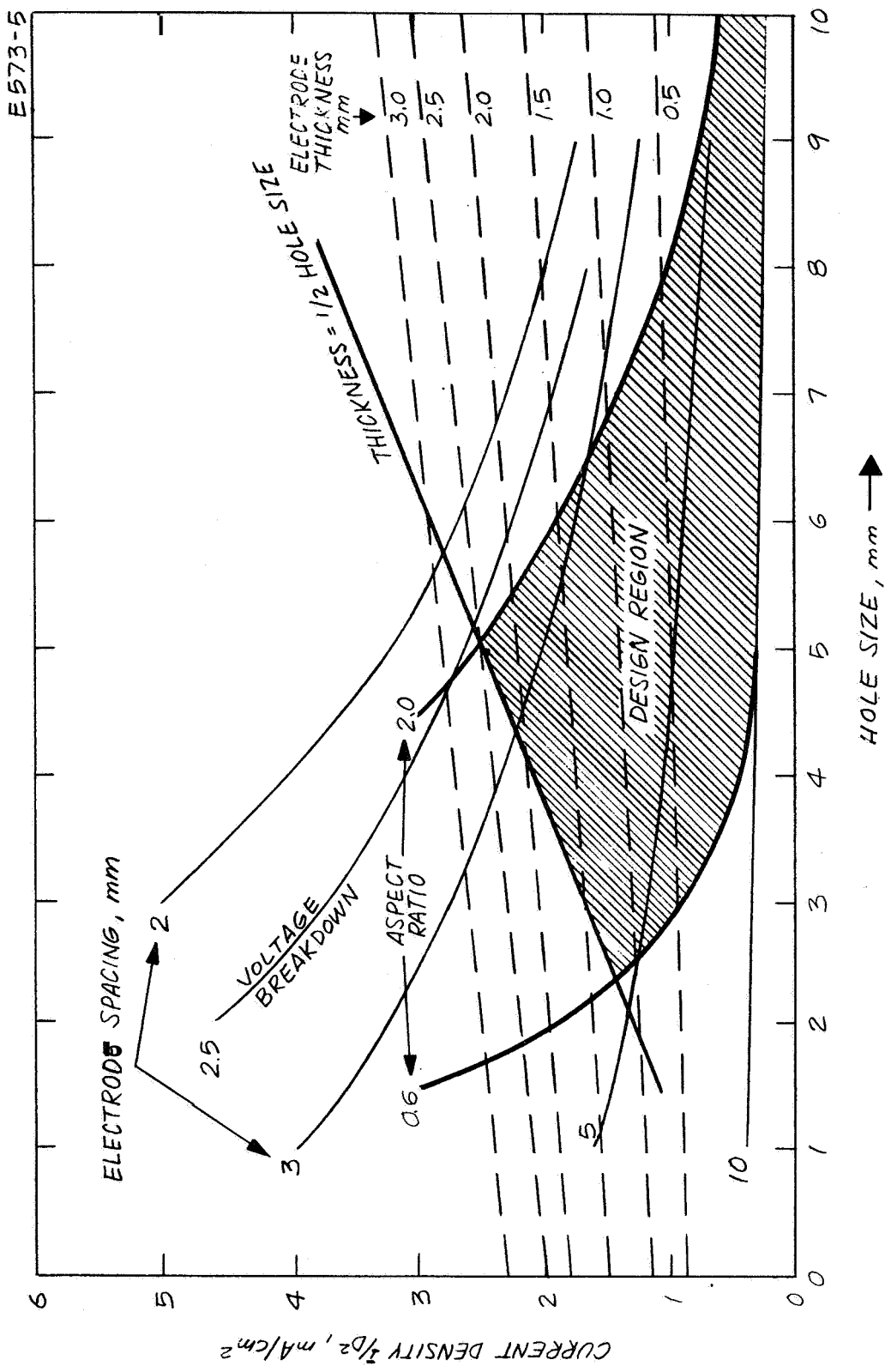


Fig. B. 1-5. Mercury bombardment engine design range defined by optics and life considerations
 $I_{sp} = 4000$ sec.

The remaining boundaries of the "design region" are defined by limitations on aspect ratio (ratio of hole size to electrode spacing, w/d). The allowable range of aspect ratio is chosen as 0.6 (Ref. 8) to 2.0 (Ref. 9). Thus, the region of allowable combinations of design parameters becomes completely defined (Fig. B. 1-5). Any point within the region represents a set of parameters (electrode spacing, thickness, hole size) which can produce the indicated current density, while at the same time guaranteeing a one year life.

The final step is to determine the engine size (effective diameter, D) necessary to produce the beam current required for various power level modules. To do this, plots of total engine power vs. engine diameter are constructed for various hole sizes and electrode spacings (Fig. B. 1-6).

These curves are obtained from the relationship:

$$(19) \quad P = \left(\frac{j}{10^3} \right) \left(\frac{V_B}{10^3} \right) \frac{D^2}{\eta_P} \quad \text{KW}$$

where j is obtained from Fig. B. 1-5 for any combination of hole size and electrode spacing. The beam voltage (V_B) is obtained from Fig. B. 1-1. η_P is the power efficiency of the engine ($\eta_P = 75\%$ at 4000 seconds).

At first glance, Fig. B. 1-6 indicates that any size engine from some minimum diameter to 100 cm diameter may be selected for a given power level thruster module.. This is indeed the case, since any engine design selected from Fig. B. 1-6 has already been qualified with respect to optics and life (see Fig. B. 1-6). Therefore, if one wanted the smallest possible engine configuration (regardless of any other considerations) engine designs from curve "A" (Fig. B. 1-6) would be selected to deliver the required power level. It is felt, however, that one additional factor should be considered; namely, mechanical implementation.

Mechanical Aspects

A primary aspect of mechanical implementation is the number of holes which must be drilled in the electrode plates. It will now be shown that the number of holes may be minimized for any power level by a proper design selection, without unduly increasing engine size. The number of holes in an electrode is calculated from Eq. 6.

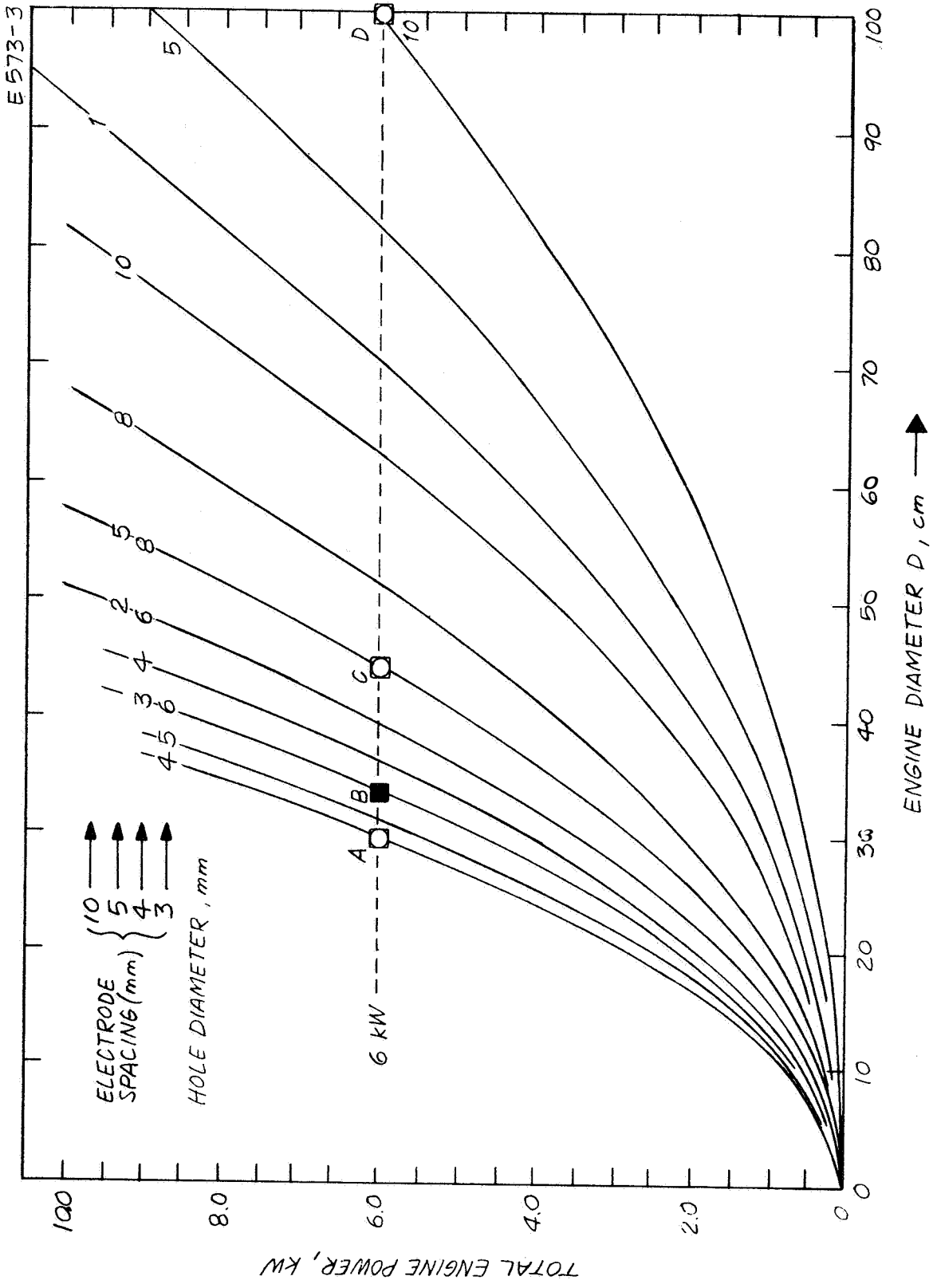


Fig. B.1-6. Potential design parameters for 6 kW mercury ombarelement thruster module, I = 4000 sec.

The physical dimensions necessary to solve for the number of holes are obtained from Fig. B. 1-6 once a power level is established. For this discussion 6 kW is used. The engine defined by curve "A" has the following specifications:

diameter = 30 cm
hole size, w = 0.4 cm

Therefore, the number of holes in "A" is:

$$(20) N_A = (.58) \left(\frac{30}{.4} \right)^2 = 3260 \text{ holes}$$

Similarly, we may calculate the number of holes in engines "B", "C", and "D". The results are presented in Table B. 1-1

TABLE B. 1-1

Thruster Parameter for Various 6kW Designs

Engine	Diameter (cm)	N	d (mm)	D/d
A	30	3260	3	100
B	35	1860	3	116
C	45	1830	4	112
D	100	5800	10	100

Although these calculations are detailed for a 6kW power level, the results are general.

The result of calculating N indicates:

- 1) Increasing the effective diameter from 30 cm (engine A) to 35 cm. (engine B) reduces the required number of holes by almost 50%.
- 2) Further increase in effective diameter does not appreciably reduce the required number of holes any further (engine C).

3) Continued increase in effective diameter above 45 cm.

actually increases the required number of holes (engine D). Therefore, engine B would be selected as opposed to engine A on the basis of the advantage in mechanical implementation, even though a slight increase in size is required.

One other mechanical aspect requires attention: thermal distortion of the electrode plates. Reference 10 indicates that with a center support, the ratio of electrode diameter to spacing may be 100. Table B. 1-1 lists values of this ratio for the different engines. Although it is desirable to maintain this ratio as low as possible, Table B. 1-1 indicates that there is no appreciable difference in this value among engines A through D. This result is also true at other power levels. Hence, no new criteria arises from considering thermal distortion. Engine B still remains as the preferred choice for the 6 kW example cited above.

Carrying out the above calculations for other power levels results in the same conclusion. The best engine design for any power level lies on curve "B" in Fig. B. 1-6. Regardless of the power level required, the electrode spacing will be 3 mm. and the hole diameter 6 mm. The power level will thus explicitly determine the thruster diameter, D. Figure B. 1-6 may now be replaced with Fig. B. 1-7: A direct relationship between power level and engine size. Also shown in Fig. B. 1-7 are the corresponding engine weights associated with the various thruster sizes. This power vs. weight relationship is used in the reliability study to optimize the thruster module power level.

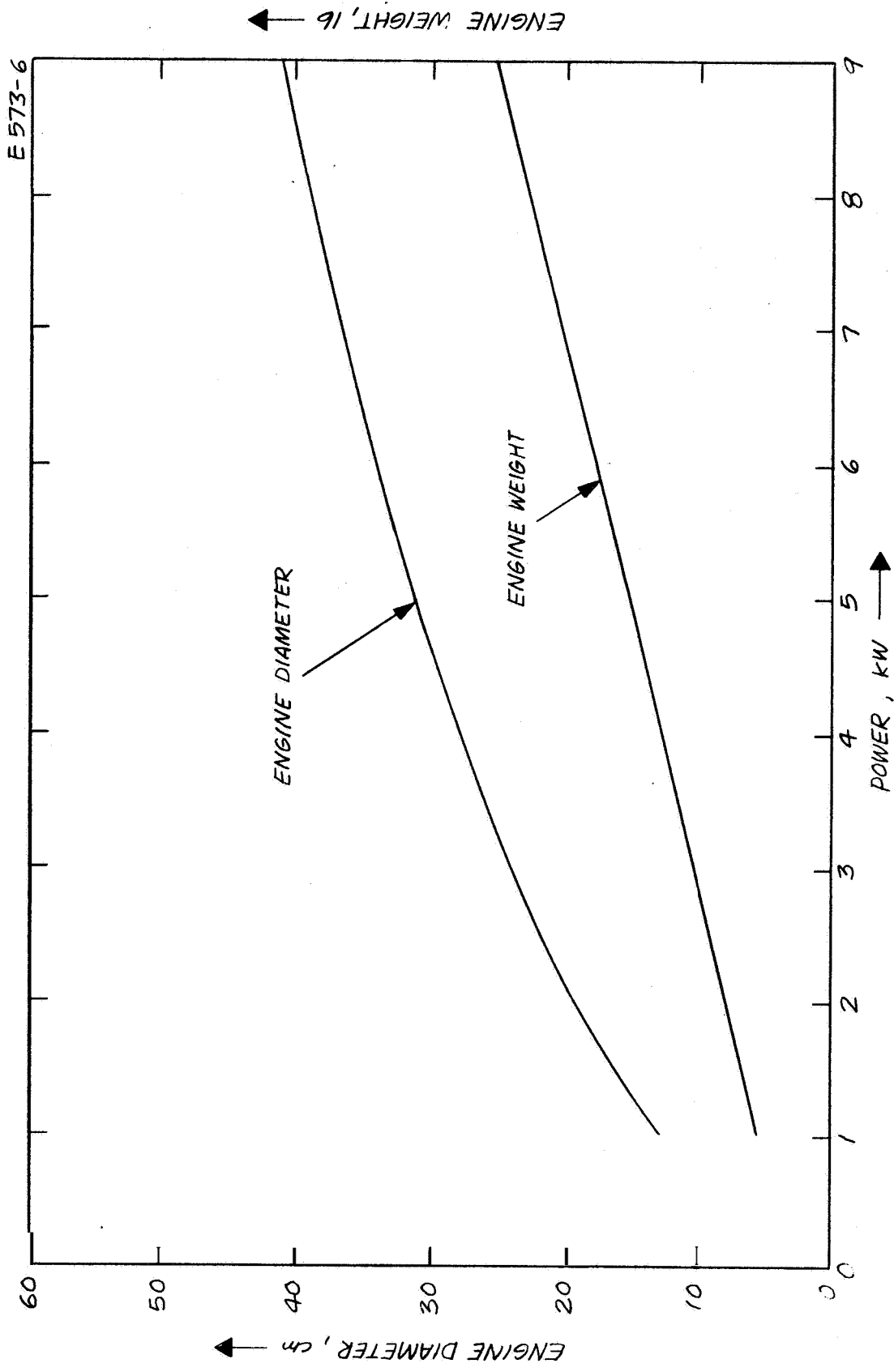


Fig. B. 1-7. Mercury bombardment engine size and weight for $I_{sp} = 4000$ sec

b. Feed System

To determine the relation between engine module power level and feed system design parameters, it is first necessary to establish what feed system components are affected. Each thruster module requires the following feed system elements: (1) vaporizer, (2) flow meter, (3) isolator, (4) solenoid valve and (5) plumbing. The propellant reservoir is not included in the above list because the total amount of propellant required is a constant for the 48 KW system. The way in which the propellant is stored (number and size of tanks used) is independent of the number of thruster modules chosen. For example, one tank could feed several engines, or several tanks could feed one engine. The only items applicable to the scaling considerations: at this time, are those which might effect the selection of the number of thruster modules. Separate scaling studies of the propellant storage system have already been carried out (Ref. 12).

The requirement that each thruster module have a complete duplication of the above five components arises directly from the operating characteristics of the feed system module. Flow control is produced by a change in vaporizer temperature. Since each thruster requires separate flow control, one vaporizer could not properly supply control for more than one thruster. Similarly, one flow meter is required per thruster, since individual flow control can only be provided in response to individual signals from the flow meters.

Duplication of high voltage isolators and solenoid valves is required to allow thruster modules to be separately switched in and out of a central propellant storage system (consisting of one or many tanks). See, for example, the system layout in Fig. B.4-2. The only way in which this solenoid valve and high voltage isolator could be eliminated is if **each**, thruster module had its own propellant storage tank. This would be a highly inefficient scheme: since standby engines **would** require standby fuel. In addition, there are other factors negating a scheme of this type.

The basic feed system module is shown in Fig. B.3-2. The thruster module, and a propellant storage tank are shown for illustration. The

feed system component maximum weights are given in Table B. 1-2. These weights are independent of the power level of the engine module over the range of interest. Therefore, the feed system weight per engine module (excluding the storage system) is a constant. The total feed system weight (again, excluding the storage system) is, of course, a direct function of the number of engine modules because of the one-to-one relationship between engine modules and feed system components.

TABLE B. 1-2

FEED SYSTEM COMPONENT WEIGHTS

Component	Weight, lb.
Vaporizer	1.0
Flow Meter	1.0
Isolator	1.0
Solenoid Valve	0.5
Plumbing	<u>0.5</u>
TOTAL	4.0

c. Power Conditioning and Controls

A comparison of the conventional and multi-module approach to power conditioning was made during the first study period (e.g., see Ref. 11). On the basis of these analyses, the multi-module concept was chosen for the solar-electric propulsion system being designed for the JPL program. The design philosophy of the multi-module circuit concept (discussed in detail in Ref. 1) is simply to construct a high power system using many low power modules. This circuit concept has many unique system characteristics and functional advantages that are important in the design of a solar powered electric propulsion system. A salient design advantage of this approach is the inherent ability to increase the power ratings of the supplies associated with the power conditioning system without requiring a major circuit re-design such as would be the case with a conventional circuit approach. Power conditioning systems ranging in power from 1.0 to 6.0 kilowatts can be built from basic 100 and 200 watt inverter building blocks by simply adding the modules in series so that the sum of the inverter power ratings equals the power required by the supply. The only circuit modification necessary would be to change the turns ratio of the module output power transformer to obtain the designed supply output voltage.

Figure B.1-8 shows the effect of scaling on the characteristics of the main beam supply, assuming a 200 watt inverter module as the basic building block. The output voltage versus the main beam power curve is shown to indicate the required turns ratio of the module output power transformer. Also, the efficiencies of both full wave center tap and full wave bridge rectifier circuits are presented. As shown, there is only about a one-percent penalty in power efficiency in scaling the power from a 1 kilowatt beam to a 4 kilowatt beam. The third graph shows the main beam supply weight and number of modules required for various main beam power levels.

The effect of power scaling on the module voltage output, power efficiency and weight characteristics of the arc discharge supply is presented in Fig. E.1-9. Again employing the 200 watt inverter module in the initial design analysis phase both ac and dc series adding were considered

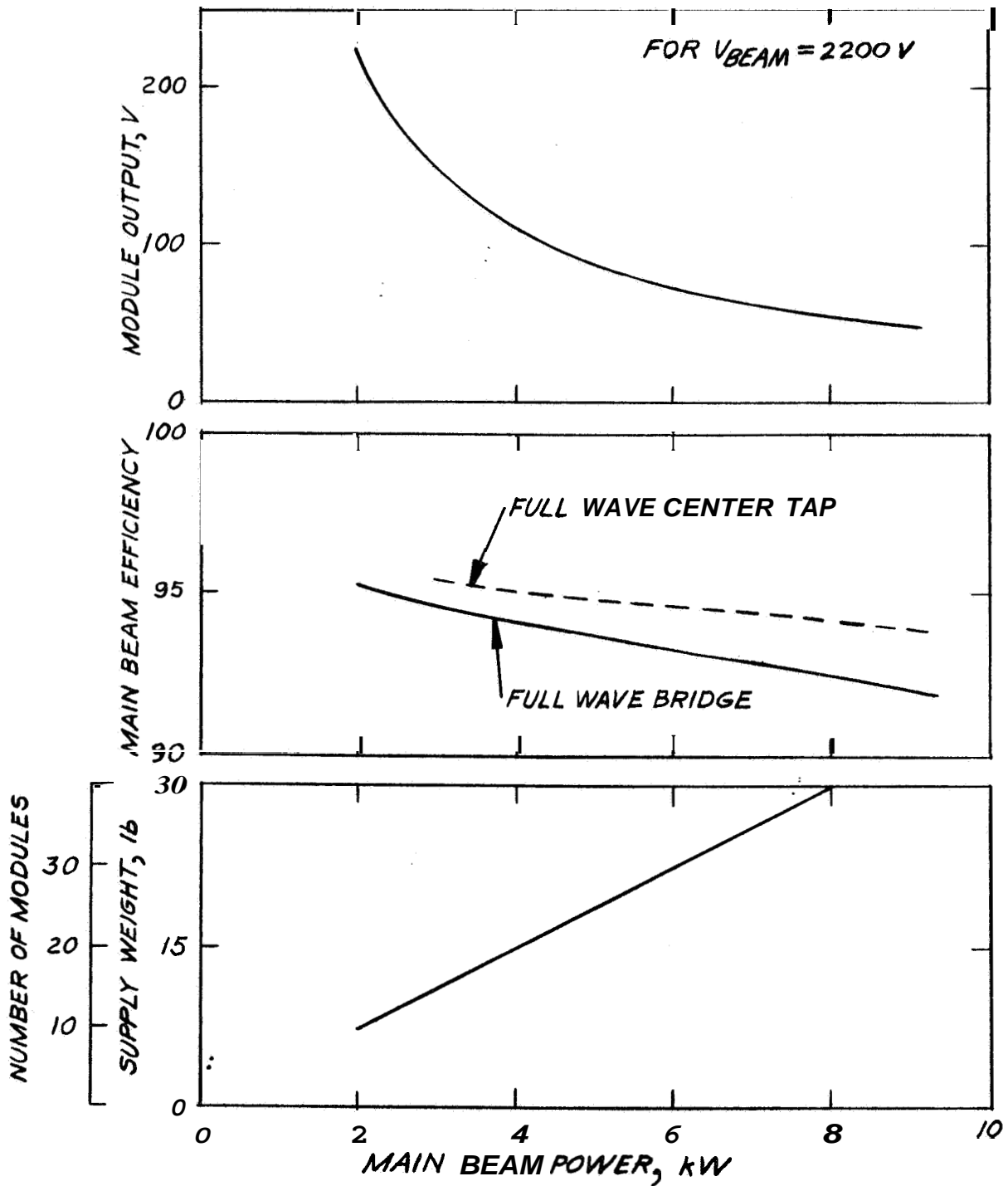


Fig. B. 1-8. Main beam parameter study (employing 200 W inverter module).

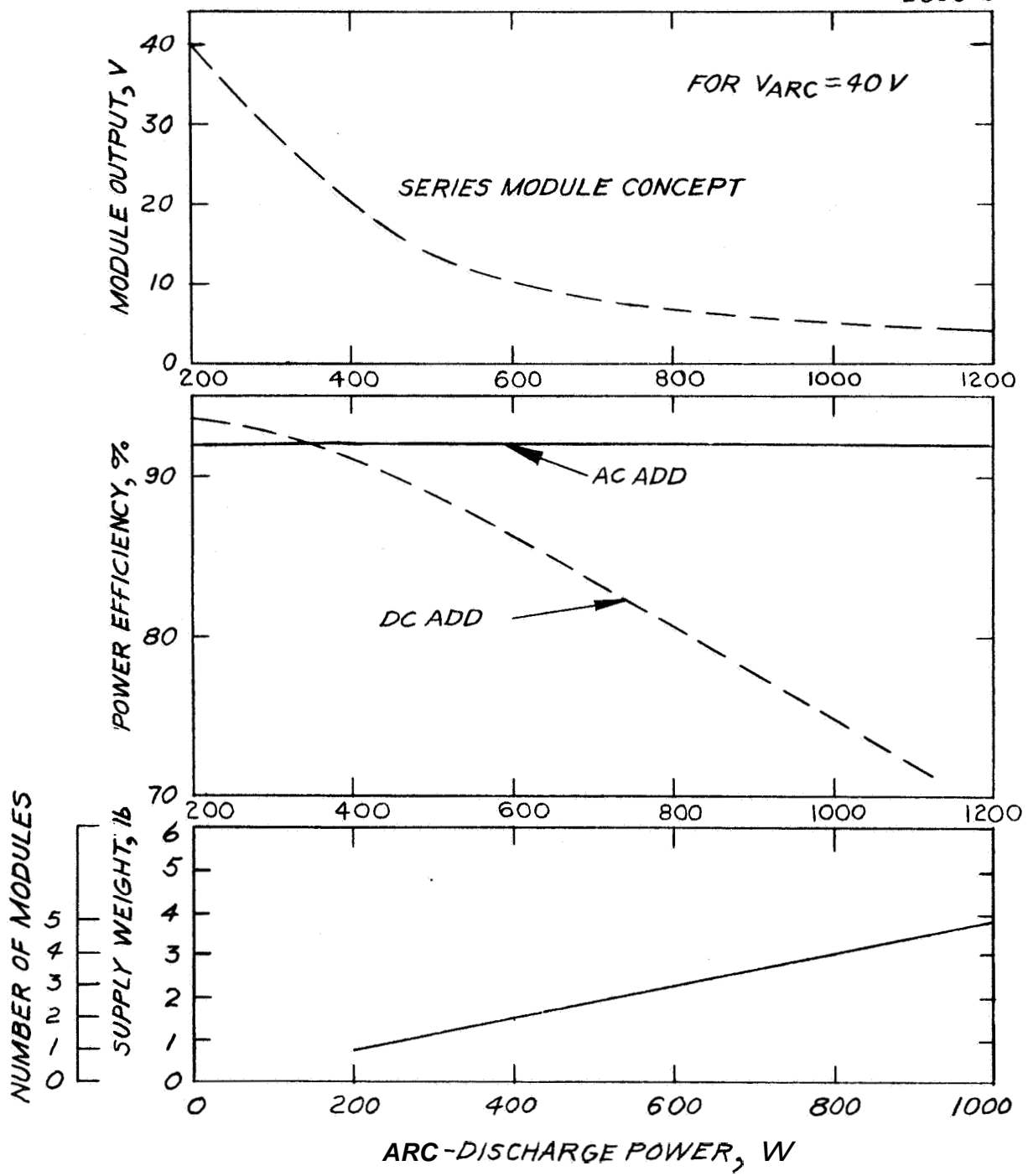


Fig. B. 1-9. Arc discharge parameter study (employing 200 W inverter modules).

for the discharge supply. Figure B. 1-9 shows that the degradation in power efficiency is quite severe at the high power levels with the dc adding technique. For this reason, ac adding becomes the only practical method of power scaling the arc-discharge supply, even though circuit operation is somewhat more complicated.

The low voltage supplies are essentially not affected by scaling in the power range under consideration. At the higher power levels, however, the inverter capacity of the magnet supply would have to be increased to 200 W.

For the accelerator supply, the number of modules required is primarily governed by the overload current capability of the system during startup. It is estimated that the accelerator supply will require a startup current transient capability of 20 percent of the normal main beam current. For example, the accelerator supply for the 1.4 kW engine requires three 100 W inverter modules (two operating, one in standby). When power scaling to larger engine systems, the increase in overload current transient capability is obtained partially by using an inverter transistor with higher current rating, and partially by increasing the number of inverter modules.

The total efficiency and weight of a 48 kW power conditioning system is shown in Fig. B. 1-10. These data assume that the large system is made up of individual ion engines and their associated power conditioning systems of power ratings from 1 to 6 kW. It is seen that, although the over-all power efficiency decreases, the total system weight is reduced considerably as the basic engine unit power level increases. It should be noted, however, that these data are based on the use of 100 and 200 W modules, thereby penalizing somewhat the lower power engine systems.

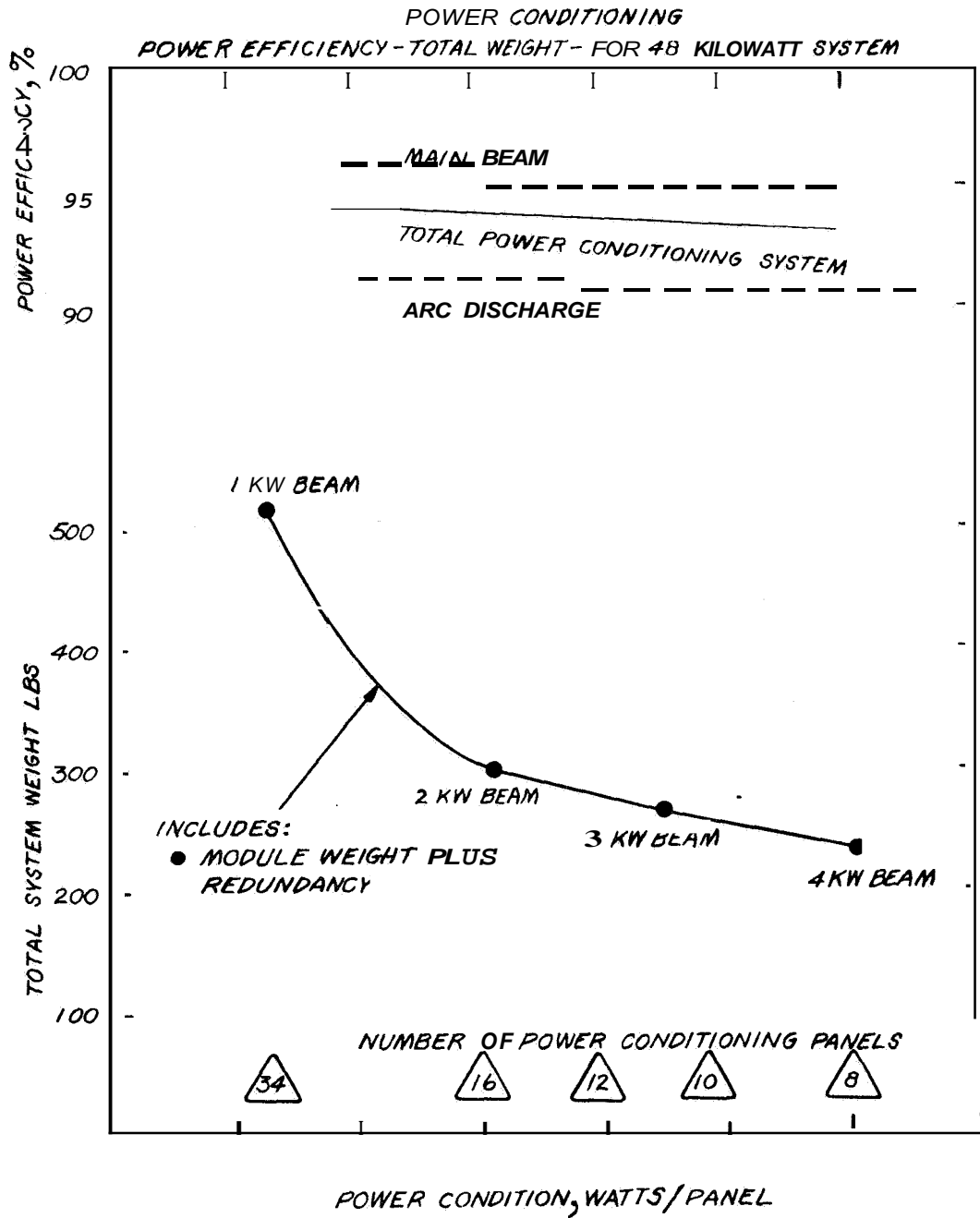


Fig. B. 1-10. Power conditioning efficiency-weight parameter study.

REFERENCES

1. Ion Engine Modular Power Conditioning and Control System, Phase I Progress Report, Contract JPL 951144.
2. N. B. Kramer, "Ion Optics for the Electron Bombardment Engine", RL Research Report #324, February, 1965.
3. W. R. Kerslake and E. V. Pawlik, "Additional Studies of Screen and Accel Grids for Electron Bombardment Ion Thrusters", TN-D 1411.
4. W. R. Kerslake, "Charge-Exchange Effects on the Accelerator Impingement of an Electron Bombardment Ion Rocket", TN D- 1657.
5. P. D. Reader, "Experimental Performance of a 50-Cm Diameter Electron-Bombardment Ion Rocket", AIAA No. 64-689, September, 1964.
6. P. D. Reader, "Experimental Effects of Propellant Introduction Mode on Electron-Bombardment Ion Rocket Performance, TN - 2587.
7. P. D. Reader, "Investigation of a 10-Cm Diameter Electron Bombardment Ion Rocket", D-1163, 1962.
8. W. R. Kerslake, "Accelerator Grid Tests on an Electron-Bombardment Ion Rocket", TN-D 1168.
9. H. J. King, "Performance of 20-Cm Reverse Feed Thrustor with Flower Cathode", IPD, June, 1965.
10. P. D. Reader and W. R. Mickelsen, "Experimental Systems Studies of Large Modules and Arrays of Electrostatic Thrustor", AIAA, 64-503, July, 1964.
11. Solar Powered Electric Propulsion Spacecraft, Bi-Monthly Report No. 1, May, 1965, JPL Contract 951144.

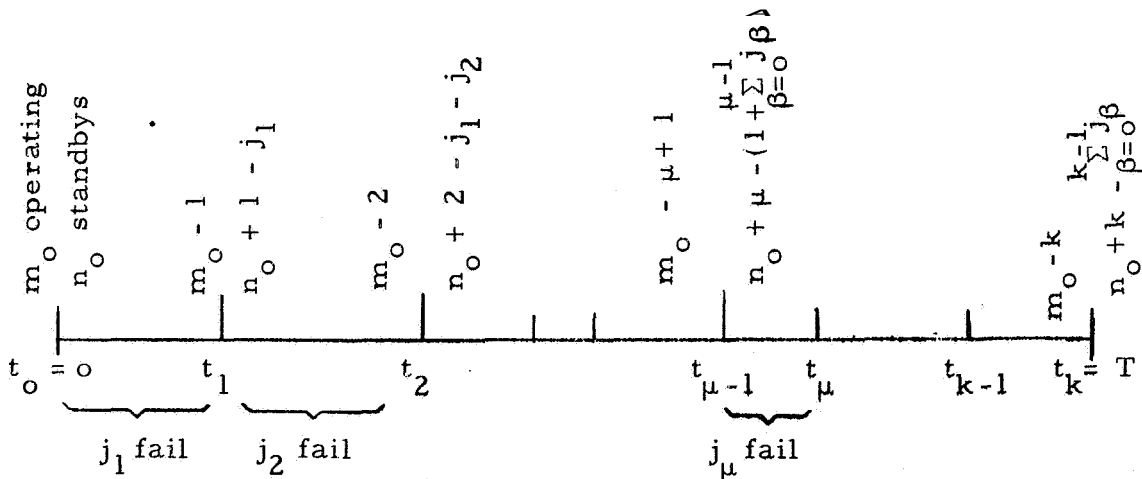
2 Reliability Analysis

The reliability analysis of a standby redundant configuration¹, with m_o modules operating and n_o in standby, has been extended for application to the solar-electric propulsion system conceptual design. Due to the decrease in available power and increase in output voltage of the solar panel, engine and power conditioning modules will be shut down during the course of the mission. In each case the modules and their respective subsystems will be designed such that disconnected modules can be reinstated. From a reliability point of view the shut down modules can then be considered as standbys.

a. Standby Redundancy With Shutdowns

The reliability of a system consisting initially of m_o operating and n_o standby modules must now be calculated with the added condition that at certain times t_μ , $\mu = 1, 2, \dots, k-1$ one of the operating modules becomes a standby.

As shown in the diagram below, the total mission time T has been partitioned by the times t_μ where $t_o = 0$, $t_k = T$. The points in between ($\mu = 1, 2, \dots, k-1$) correspond to times when an operating module becomes a standby. If j_μ failures occur during $(t_{\mu-1}, t_\mu)$ and there are m_o operating and n_o standbys at $t = 0$, there will be $(m_o - \mu + 1)$ operating and $n_o + \mu - (1 + \sum_{\beta=0}^{\mu-1} j_\beta)$ standbys at $t = t_{\mu-1}$. Let the



random variable J_μ , $\mu = 1, 2, \dots, k$ denote the exact number of failures during $(t_{\mu-1}, t_\mu)$. Also define $\Pr(J_\mu = j_\mu)$ to be the probability that exactly j_μ failures occur during $(t_{\mu-1}, t_\mu)$. The mission reliability which is defined as the probability that the mission is successful to time T , equals the product of the probabilities of success in each interval $(t_{\mu-1}, t_\mu)$ where $\mu = 1, 2, \dots, k$. Moreover, the probability of success during a given interval is defined as the probability that the number of failures does not exceed the number of standbys. Hence

$$(1) \quad \Pr(\text{success in } (0, t)) = \Pr(J_1 \leq n_0) = \sum_{j_1=0}^{n_0} \Pr(J_1 = j_1)$$

and

$$(2) \quad \Pr(\text{success in } (t_{\mu-1}, t_\mu)) = \Pr\left[J_\mu \leq n_0 + \mu - \left(1 + \sum_{\beta=0}^{\mu-1} j_\beta\right)\right], j_0 = 0$$

$$= \sum_{j_\mu=0}^{L(\mu)} \Pr(J_\mu = j_\mu)$$

where

$$(3) \quad L(\mu) = n_0 + \mu - \left(1 + \sum_{\beta=0}^{\mu-1} j_\beta\right), j_0 = 0$$

therefore

$$(4) \quad \text{Mission Reliability} = \prod_{\mu=1}^k \left[\sum_{j_\mu=0}^{L(\mu)} \Pr(J_\mu = j_\mu) \right]$$

To determine $\Pr (J_{\mu} = j_{\mu})$ the statistics of the failures must be assumed. As in all classical reliability theory the Poisson Distribution with constant failure rate will be used. The failure rate λ for the system depends on the number m_o of modules of which it is composed. For simplicity this function, $\lambda (m_o)$ is taken to be linear, i. e.

$$(5) \quad \lambda (m_o) = \lambda_p + m_o \lambda_c$$

This relationship gives the system failure rate during the first interval $(0, t_1)$. However, as modules are shut down only a fraction of the system is operating. For example, during $(t_{\mu-1}, t_{\mu})$ only the fraction $(m_o - \mu + 1) / m_o$ is operating. Thus the failure rate during this interval is

$$(6) \quad \lambda_{\mu} = (\lambda_p + m_o \lambda_c) \frac{m_o - \mu + 1}{m_o}$$

In terms of the Poisson Law and failure rate λ_{μ} , the formula for $\Pr (J_{\mu} = j_{\mu})$ is

$$(7) \quad \Pr (J_{\mu} = j_{\mu}) = \frac{e^{-\lambda_{\mu} \Delta t_{\mu}} (\lambda_{\mu} \Delta t_{\mu})^{j_{\mu}}}{j_{\mu}!}$$

where

$$(8) \quad \lambda_{\mu} = (\lambda_p + m_o \lambda_c) \frac{m_o - \mu + 1}{m_o}$$

$$(9) \quad \Delta t_{\mu} = t_{\mu} - t_{\mu-1}$$

In summary, the reliability of a system in which,

- 1) m_o modules are operating initially
- 2) n_o modules are in standby initially
- 3) one operating module becomes a standby at each time t_{μ} , $\mu = 1, 2, \dots, k-1$

- 4) the mission lasts from time $t_0 = 0$ to time $t_k = T$
 5) failures are Poisson distributed

is given by the formula

$$(10) \quad {}_0n_0(t_0, t_1, \dots, t_k) = \prod_{\mu=1}^k \left[\sum_{j_{\mu}=0}^{L(\mu)} \Pr(J_{\mu} = j_{\mu}) \right]$$

where

$$(11) \quad L(\mu) = n_0 + \mu - (1 + \sum_{\beta=0}^{\mu-1} j_{\beta}), \quad j_0 = 0$$

$$(12) \quad \Pr(J_{\mu} = j_{\mu}) = \frac{e^{-\lambda_{\mu} \Delta t_{\mu}} (\lambda_{\mu} \Delta t_{\mu})^{j_{\mu}}}{j_{\mu}!}$$

$$(13) \quad \lambda_{\mu} = (\lambda_p + m_0 \lambda_e) \frac{m_0 - \mu + 1}{m_0}$$

$$(14) \quad \Delta t_{\mu} = t_{\mu} - t_{\mu-1}$$

b. Application to Thruster Arrays

A weight-reliability study has been performed to determine the optimum thruster module size for a solar-electric propulsion system. The optimization procedure consists of finding the initial number of operating and standby modules which, for a desired system reliability, minimizes the percent increase in thruster array weight. For a given initial power level, the optimum module size is thus defined.

Before proceeding with the optimization study formulas for the turn off times, t_μ , and the weight penalty function, G_{m_o, n_o} , will be developed.

Turn Off Times

For a thruster array consisting of m_o initial modules operating the turn off times, t_μ , are determined from solar panel power curve, $P(t)$, shown in Fig. B. 5-6. If P is the available power at $t = 0$, then the time, t_1 , for first switching is found from the equation

$$(1) \quad P(t_1) = \frac{m_o - 1}{m_o} P_o$$

Just before the second switching time t_2 there are $m_o - 1$ engines operating hence t_2 can be found from

$$(2) \quad P(t_2) = \frac{m_o - 2}{m_o - 1} P(t_1) \\ = \frac{m_o - 2}{m_o - 1} \cdot \frac{m_o - 1}{m_o} P_o = \frac{m_o - 2}{m_o} P_o$$

Thus, it can be seen that t_μ is defined by

$$(3) \quad P(t_\mu) = \frac{m_o - \mu}{m_o} P_o; \quad \mu = 1, 2, \dots, k-1$$

Percent Weight Increases

The weight, W , of a thruster array consisting of m_o modules can be written

$$(4) \quad W(m_o) = W_p + m_o W_c$$

where W_p = weight of those items dependent on engine size
 W_c = weight of those items independent of engine size

The weight of a thrustor system with m_o operating and n_o standby modules is then

$$(5) \quad W_{m_o, n_o} = (W_p + m_o W_c) \left(1 + \frac{n_o}{m_o}\right)$$

The weight penalty incurred to increase system reliability to some desired level by employing a modularized system with redundancy is given by the quantity G_{m_o, n_o} , where

$$(6) \quad G_{m_o, n_o} = \frac{W_{m_o, n_o} - W_{1,0}}{W_{1,0}}$$

With C defined by $C = W_p/W_c$, the weight penalty can be written as

$$(7) \quad G_{m_o, n_o} = \left(m_o + n_o - \frac{n_o}{m_o} - 1\right) \frac{C}{C+1} + \frac{n_o}{m_o}$$

Optimum Module Size

The procedure for determining the optimum engine module size based on a weight-reliability criterion may be summarized in the following manner. A desired system reliability, \bar{R} and a range for m_o are chosen. For each value of m_o in its range the set of times t_{μ} are found from equation (3) and the smallest value of n_o is determined such that

$$(8) \quad R_{m_o, n_o}(t_o, t_1, \dots, t_k) \geq \bar{R}$$

From the set of operating and standby module pairs (m_o, n_o) generated, the one is chosen which makes the percent increase in system weight, G a minimum.

The above optimization procedure was carried out by computer for all combinations of the values of $R_{1,0}$, λ_p/λ_c , and C shown in Table B.2-1. Typical results from these computer runs are presented in Figs. B.2-1, B.2-2, B.2-3 and B.2-4.

TABLE B.2-1
Values of Parameters Used
In Reliability Study

$R_{1,0}$	λ_p/λ_c	C
0.5	0.1 1 10	0.07
0.6		0.05
0.7		0.03
0.8		0.01
0.9		0.003

The optimum number of operating and standby modules are shown in Fig. B.2-1 as a function of the reliability of an unmodularized system. These curves are for $\lambda_p = \lambda_c$ and various values of C . Their behavior varies from widely oscillatory ($C = 0.003$) to almost constant ($C = 0.07$). Because modules are counted as standbys when they are turned off, the optimum number of standbys is relatively insensitive to the number operating and to $R_{1,0}$.

The effects of C , $R_{1,0}$, and λ_p/λ_c on weight penalty are shown in Figs. B.2-2, B.2-3 and B.2-4, respectively. Figure B.2-2 shows that after an initial drop the weight penalty remains approximately constant for small values of C . Therefore, for systems where C is small, little penalty is paid when large numbers of modules are employed. As C increases, however, the curvature, at the minimum of the G curves, increases and a more serious weight penalty is incurred if the optimum module size is not employed. Figure B.2-3 presents the weight penalty for increasing the system reliability to at least 0.97 as a function of the initial number of operating modules

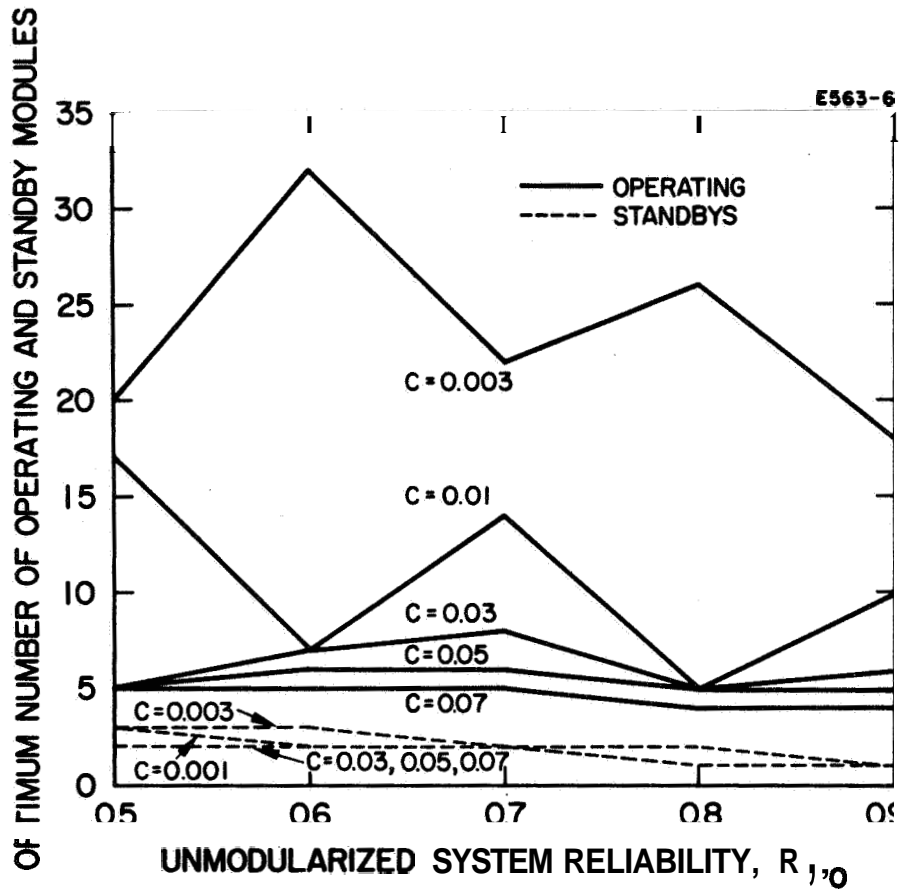


Fig. B. 2-1. Optimum number of modules to obtain 0.97 system reliability.

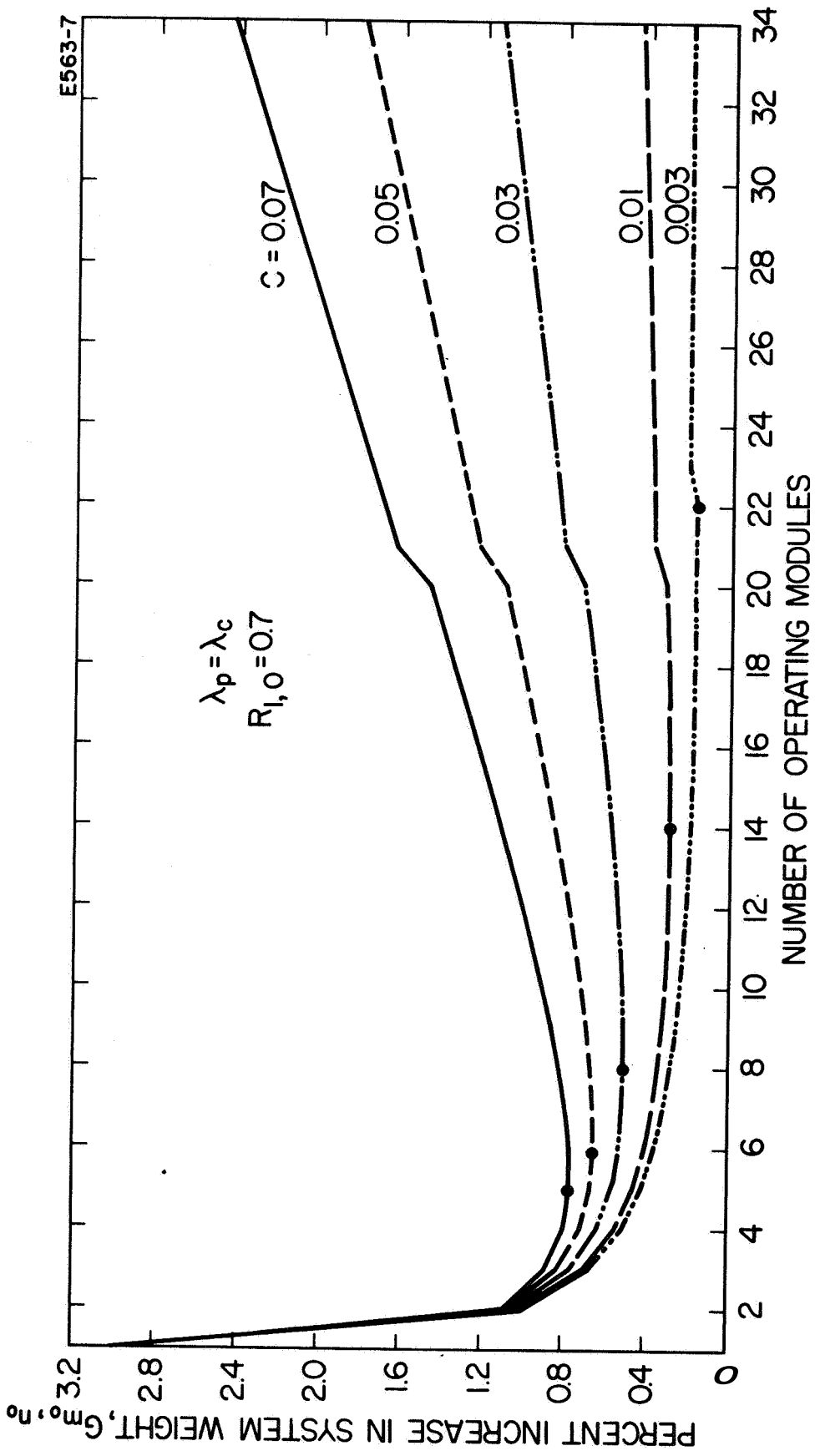


Fig B.Z-Z Weight penalty to obtain 0.97 system reliability.

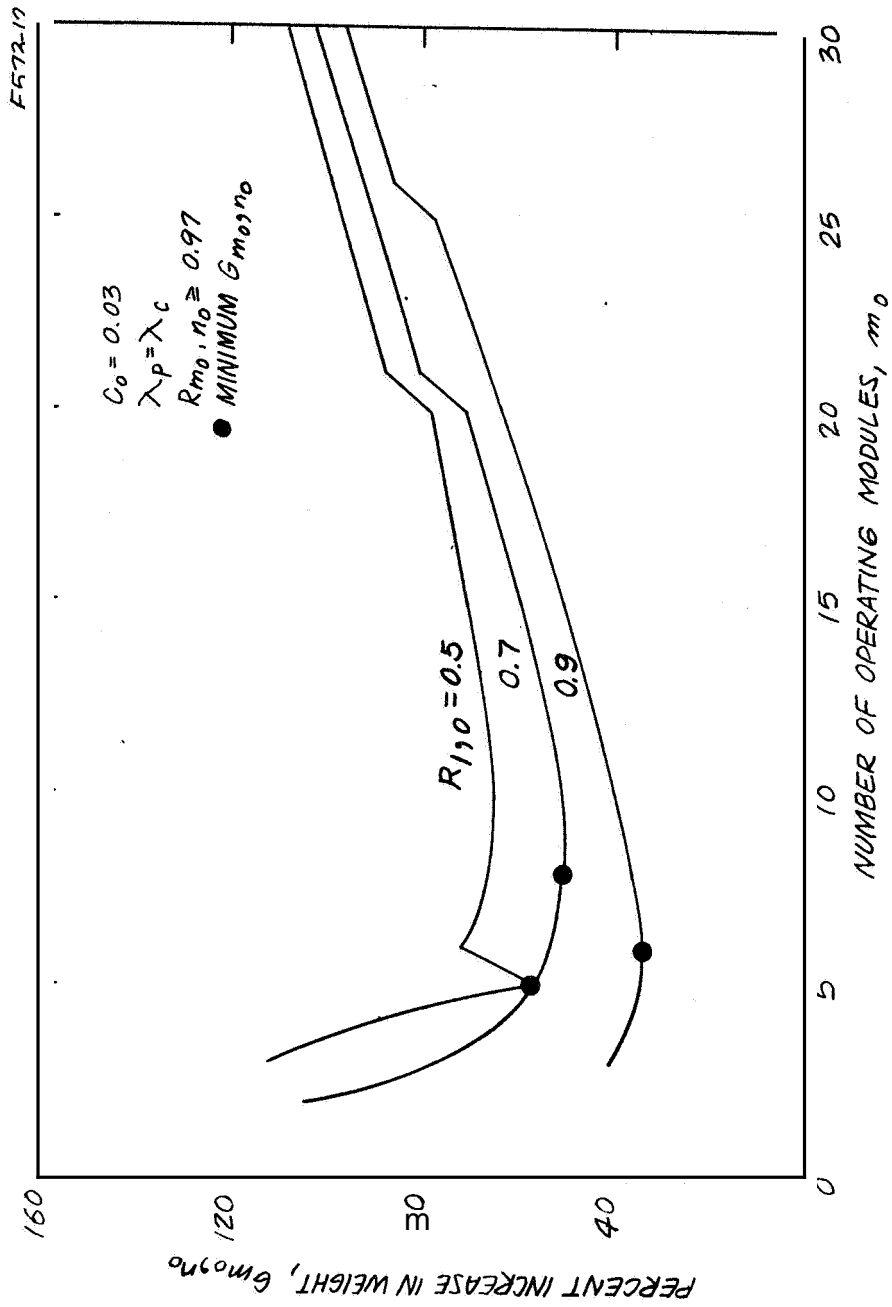


Fig. B.2-3. Effect of $R_{1,0}$ on weight penalty.

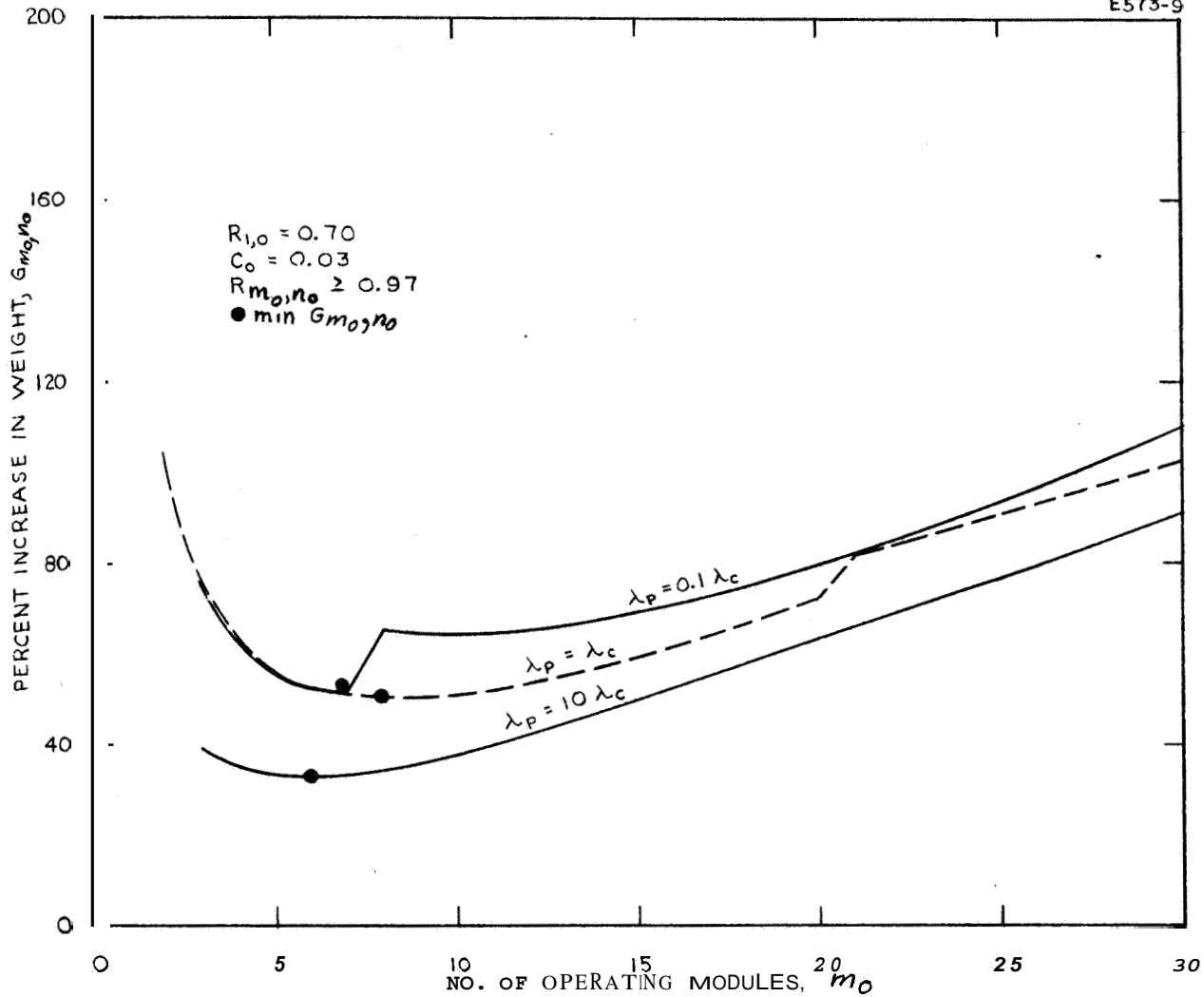


Fig. B. 2-4. Effect of A_p/λ_e on weight penalty.

for various values of $R_{1,0}$. A general conclusion indicated by these curves is that the lower the value of the reliability of an unmodularized system, the more significant the weight-reliability optimization. The sensitivity of G_{m_0, m_0} on the ratio λ_p/λ_c is shown in Fig. B.2-3. Although the weight penalty is dependent on A_p/λ_c , a variation of two orders of magnitude in this parameter has almost no effect on the location of the optimum m_0 point.

In order to determine the optimum module size (from a weight-reliability standpoint) for a given propulsion system, it is now necessary to define values for the parameters C , λ_p/λ_c , and $R_{1,0}$. The magnitude of C for present day Hg bombardment engines can be found by considering the scaling studies presented above. For example, W_p and W_c can be derived from the data presented in Figs. B. 1-7 and B. 1-10 and Table B. 1-2 for the thruster, power conditioning and controls, and feed system, respectively. Using these data the ratio of W_p/W_c was found to be on the order of 0.03. The ratio λ_p/λ_c is more difficult to establish since virtually no information is available on the failure rates of ion thrusters. However, since failure rate data is available on power conditioning and feed system components and since a ratio rather than absolute values are involved, a reasonable estimate can be made. For the system presently under consideration, a ratio of one was assumed. (It should be noted that the optimum module size is relatively insensitive to the value of A_p/λ_c .) The parameter $R_{1,0}$ is the most difficult to establish since it assumes a knowledge of the failure rate of the thrust device. Since this information is not available, a relatively conservative value of 0.7 was chosen for the reliability of an unmodularized system.

It is now possible, by considering Fig. B.2-1, to define the optimum number of operating and standby modules. Figure B.2-1 shows that in order to increase the engine system reliability to greater than 0.97, the thruster array should be composed initially of eight operating modules with two in standby. (The system reliability for this combination is actually 0.9.) Therefore, since

the initial power to the system is 48 kW, the individual thruster module is a 6 kW device.

c. Application to Power Conditioning System

The reliability of a 1 kW and a 4 kW main beam supply has been analyzed. It has been shown that, due to their modularized design, standby redundancy can provide significant reliability increases with small weight penalties.

The 1 kW beam supply consists of ten 100 watt modules. Since the input voltage from the solar array increases (at the points of maximum power transfer) with time, modules are switched out to bring the output voltage back to its initial value. For a 350-day mission, two modules are switched off—the first at 140 days and the second at 290 days. The reliability of the 10 module (1 kW) beam supply is shown as a function of single module reliability in the two lower curves of Fig. B.2-5. The lowest curve applies when it is assumed that the switched off modules cannot be returned to the system. The upper curve applies when the switched off modules are assumed to be standing by and capable of replacing an operating module that fails. The two top curves of Fig. B.2-5 show how the beam supply reliability can be made as close to 1 as desired by beginning the mission with extra modules in standby. With one initial standby, the supply reliability is greater than 0.97 for all values of module reliability above 0.955. With two initial standbys, the supply reliability is greater than 0.9977 for all values of module reliability greater than 0.950. It is important to realize that the penalties in beam supply weight are only 10% and 20% for the one and two initial standby configurations, respectively.

The 4 kW beam supply consists of twenty 200 watt modules. The parametric study of its reliability is summarized in Fig. B.2-6 in terms of the same type curves used for the 1 kW supply,

A comparison of the two sets of curves (Fig. B.2-5 vs Fig. B.2-6) reveals that (1) due to the larger number of operating modules in the 4 kW supply, the curves of Fig. B.2-6 are lower than

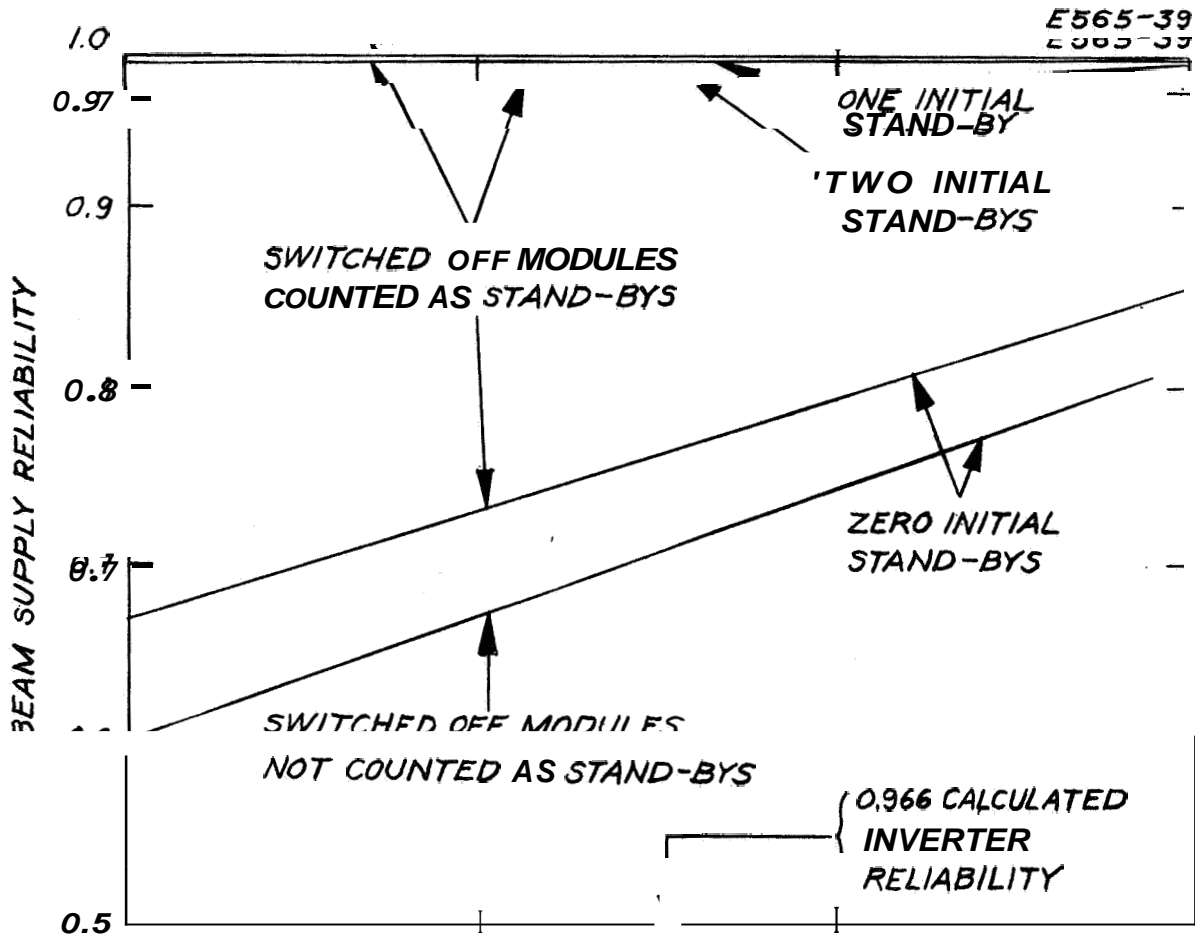


Fig. B. 2-5. Reliability of 1 kW beam supply.

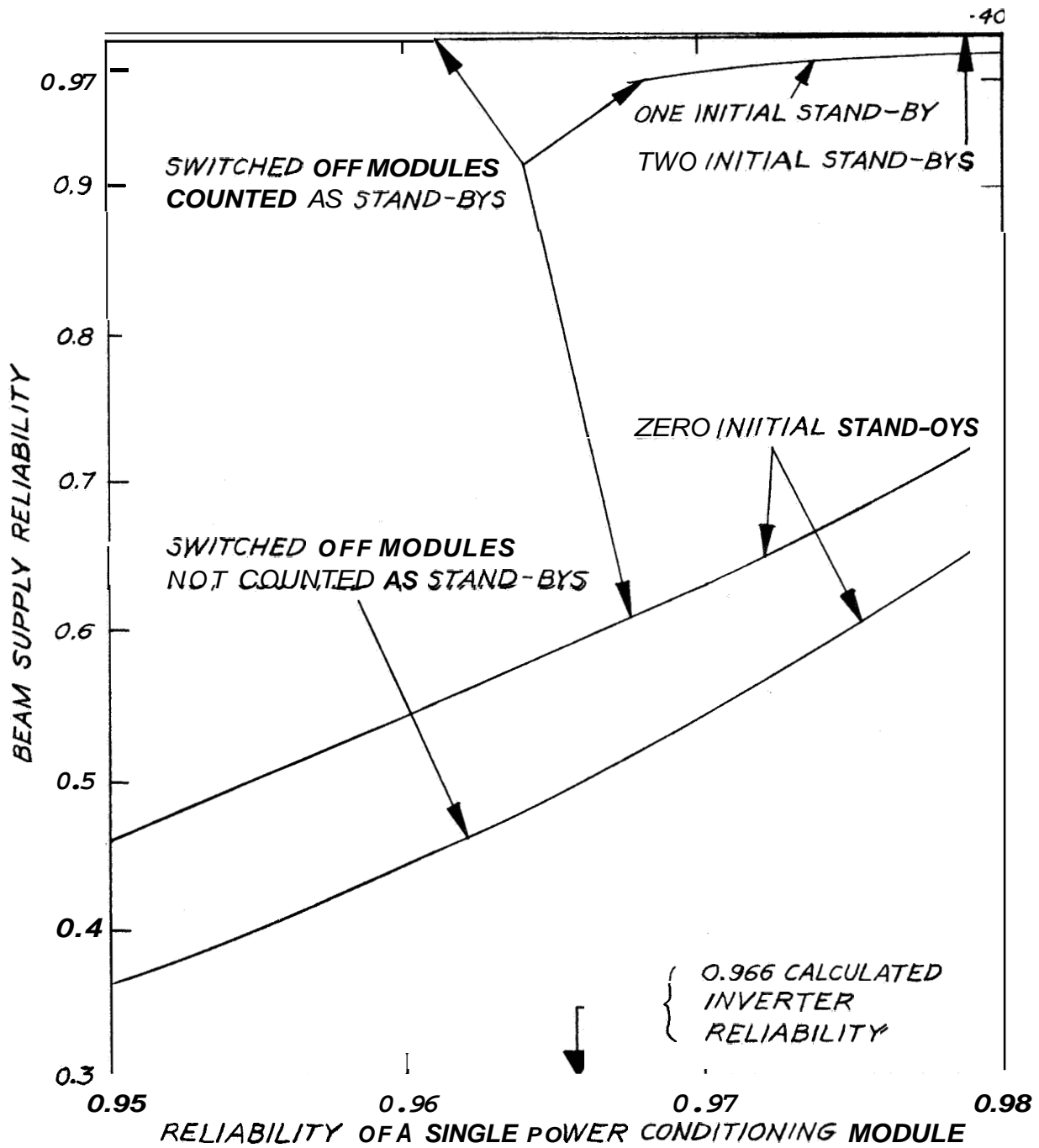


Fig. B. 2-6. Reliability of a 4 kW beam supply.

those of Fig. B.2-5, and (2) with two initial standbys, the 4 kW supply has a reliability greater than 0.9951 for all module reliabilities above 0.950. Accordingly, it is seen that for the 4 kW supply high reliability is achieved with only a 10% increase in weight.

The merits of the modularized beam supply are now apparent. This design permits voltage control by switching modules on and off and lends itself to the use of standby redundancy.

REFERENCES

1. J. H. Molitor, K. R. Pinckney and R. L. Seliger, "Effects of Reliability Considerations on the Design of Electric Thruster Arrays," AIAA 65-68, January 1965.

3. Subsystem Layouts

Eased on the reliability considerations discussed above a 6 kW engine module was chosen as the building block for the 48 kW propulsion system. By using the results of the scaling studies (e.g., Section B-1), it is now possible to provide a preliminary layout of each of the major propulsion subsystems.

a. Thruster

This discussion summarizes the key design parameters leading to the completed design of the 6 kW thruster module (Fig. B.3-1). As derived in Section B.1.a, an engine size is defined by specification of the thruster module power level (Fig. B.1-7). Since the module power level has been established at 6 kW, an engine diameter of 35 cm has been chosen (e.g., see Fig. B.1-7).

Design parameters associated with the thruster optics are: electrode spacing, electrode thickness, hole size and hole distribution. Section B.1.a has shown that (independent of power level) the electrode spacing and hole size should be 3 and 6 mm, respectively. In addition, Fig. B.1-5 shows that the associated minimum accel electrode thickness, to assure one year operation, is 1.5 mm. The screen electrode may be somewhat thinner, and has been chosen to be 1.0 mm. The hole distribution (distance between centers) is defined by the ratio of open area to total electrode area. (γ). It may be shown that for $\gamma = .58$ the above specifications led to a distance of 7.5 mm between centers. In a hexagonal array, consider a triangle with vertices at the centers of three adjacent holes. The open area within this triangle is equal to 1/2 the area of one hole. The area of the triangle is:

$$A_t = \frac{1}{2} \ell^2 \sin 60^\circ \text{ cm}^2$$

where ℓ is the distance between centers. The area of half a hole is:

$$A_h = \frac{1}{2} \frac{\pi}{4} (0.6)^2 \text{ cm}^2$$

Solving $A_h/A_t = 0.58$ for ℓ yields 7.5 mm. Electrolytic tank studies have shown that the diameter of the accelerator hole should be 0.75 that of the screen aperture. This allows the electrode a greater margin on life as limited by charge exchange erosion. The optics will not be effected if the accel holes are reduced to 4.5 mm, since the ratio of accel thickness to hole size is still under one half ($1.5/4.5 = 0.33$). The above design specifications for the 6 kW thruster module are summarized in Table B.3-1.

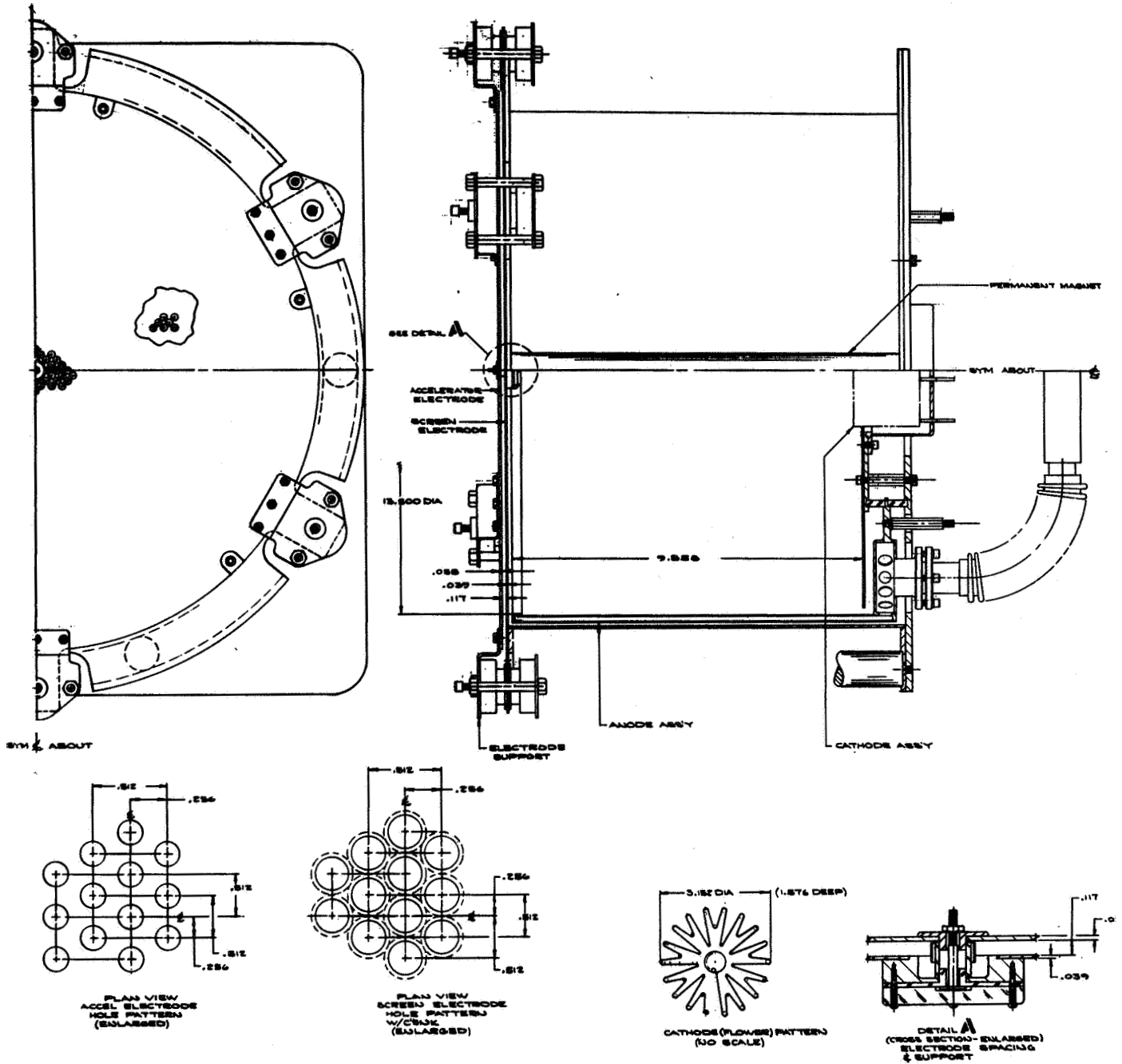


Fig. B.3-1. Detailed design of thruster module - 35 cm mercury bombardment ion engine.

TABLE B. 3-1
 Thrustor Design Specifications

Active thrustor module diameters	35 cm
Accel electrode (molybdenum)	
Hole size	4.5 mm
Distance between centers	7.5 mm
Thickness	1.5 mm
Screen Electrode (molybdenum)	
Hole size (countersunk)	6.0 mm
Distance between centers	7.5 mm
Thickness	1.0 mm
Electrode Spacing	3.0 mm

It should also be noted that one electrode center support is specified in the module design. As discussed in Section B.1.a, this is to reduce thermal distortion problems.

The arc chamber diameter is already defined (equal to the engine effective diameter). The arc chamber depth is specified as 25 cm. In conjunction with the reverse feed propellant distribution concept (being developed by HRL) these arc chamber dimensions should minimize the beam profile non-uniformity.

The 35 cm engine uses an oxide coated thermionic cathode of the HRL flower configuration. Based on the rated electron output of present flower cathodes, it is expected that the over-all dimensions of a cathode for the 35 cm engine will be 8 cm (diameter) and 4 cm (depth),

The magnetic field of the 35 cm engine will be derived from four permanent magnets (1 in. in diameter) mounted 90° apart, around the periphery of the engine.

A detailed design drawing of the 6 kW thrustor module appears in Fig. B.3-1.

b. Feed System and Tankage

Figure B.3-2 shows the layout for a 6 kW module feed system (thruster also shown for comparison). A two hundred lb. mercury propellant reservoir is included, in addition to the hardware specified in Section B.1.b (vaporizer, isolator, etc.).

Actually, in the 48 kW system, there is not exactly one propellant tank per engine module. It is shown in Sections B.1.b and B.4.a that the number of tanks can be independent of the number of thrusters. For the 48 kW system, the number of tanks specified is eight (Ref. 11), whereas the number of engines specified is ten: eight operating and two in standby (see Section B.2.b). Thus, a 6 kW feed system module would theoretically have associated with it less than one full tank (8/10 of a tank). However, for convenience in describing a complete 6 kW module (weight, etc.) we consider each module to include one 200 lb. propellant reservoir (Fig. B.3-2).

As described in Section B.1.b, the feed system component specifications are independent of thruster module power level (within the range of interest: one to ten kW). Hence there is no need to further specify the parameters of these components beyond what is described in Reference 11 (except for weight, listed in Section B.1.b).

Figure B.3-2 indicates a comparison between the component sizes and the distances involved in the integrated system. Thus, the distance required between reservoir and thruster (containing the feed system components plus plumbing) is about the same dimension as the diameter of the reservoir itself (30 cm). The integrated system (feed system and thruster) results in a compact configuration,

c. Power Conditioning and Controls

A block diagram of a multi-module power conditioning and control system for a 6 kW, 35 cm, Hg bombardment (oxide cathode) engine is shown in Fig. B.3-3. As shown in Fig. B.3-3, dc adding techniques are used in the main beam and accelerator electrode supplies. On the other hand, ac adding techniques are employed in the arc discharge, magnet, and heater circuits. The diagram **also** shows the engine control systems and control feedbacks required to start up and maintain the ion engine at its design operating point.

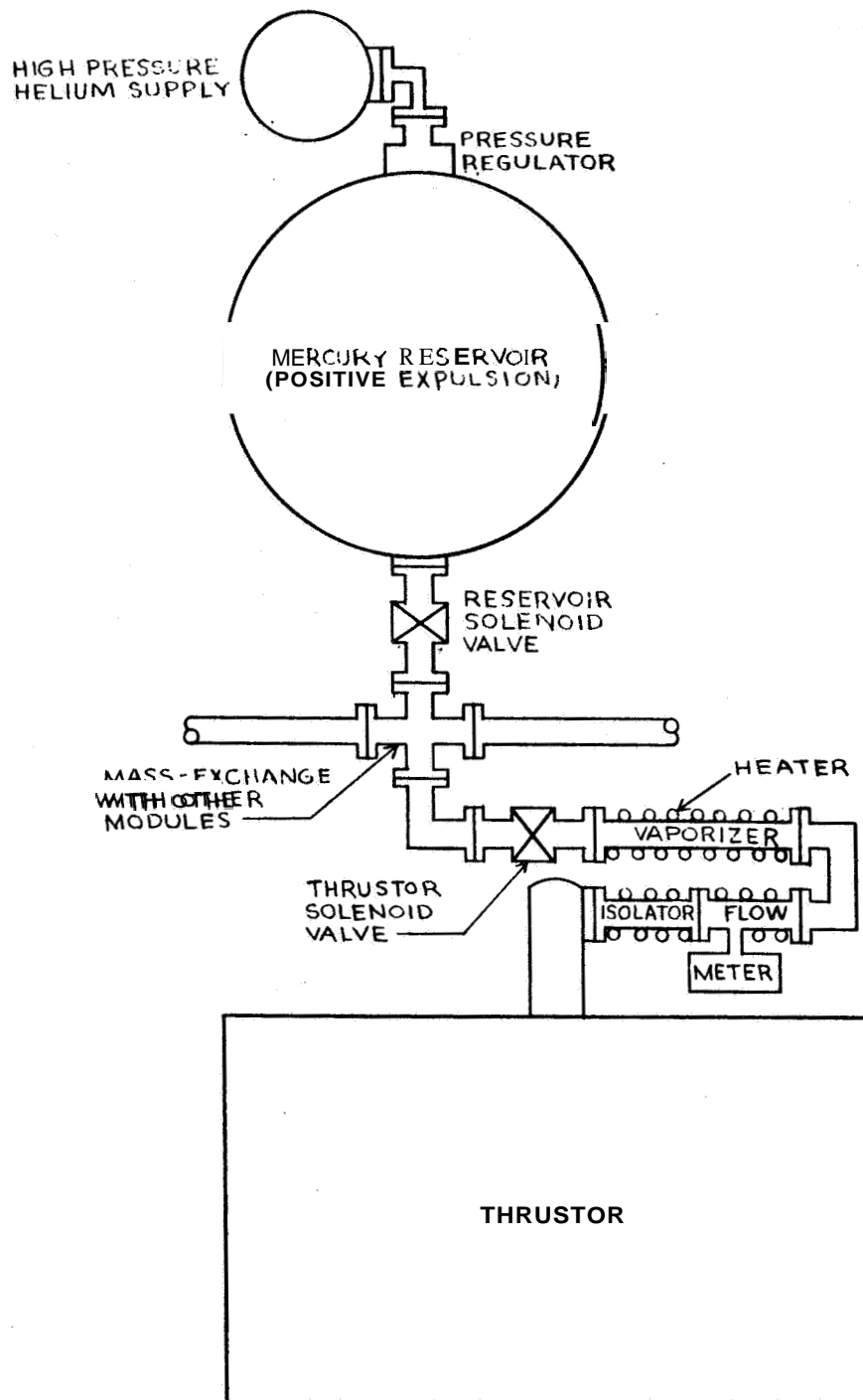


Fig. B. 3-2. Basic feed-system module with capability of mass-exchange with other modules.

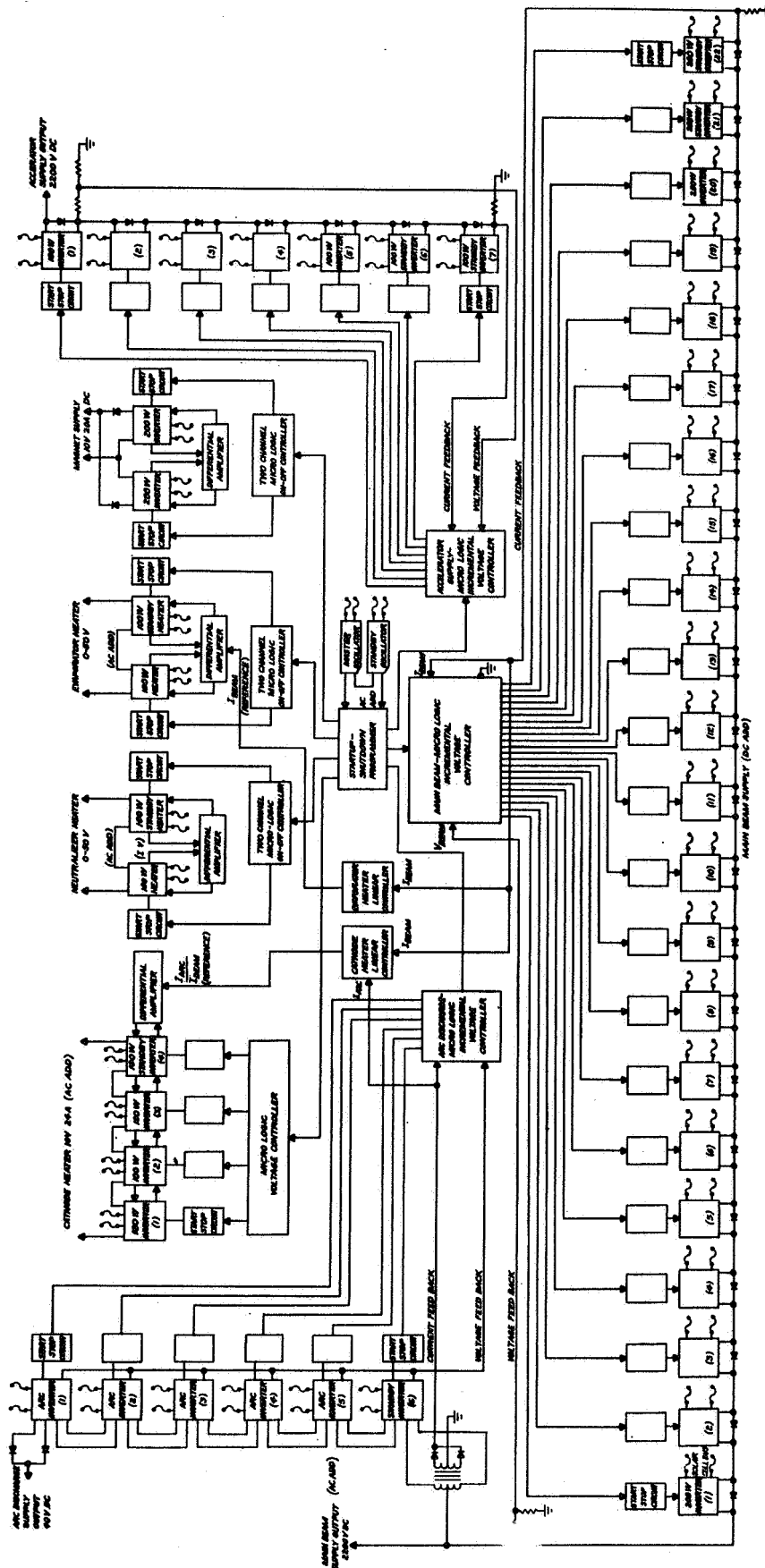


Fig. B. 3-3. 6 kW Hg Torr tube filament engine modular power conditioning system block diagram.

The individual power supply and control system circuitry associated with each block shown in Fig. B. 3-3 has been given in detail in Ref, 1. Therefore, only the general (but quantitative) characteristics of the over-all power conditioning as well as the control system philosophy is repeated here,

The distribution of power among the various power supplies is presented in Table B. 3-2 for a 6 kW, 4000 sec I_{sp} , Hg bombardment engine (oxide cathode). This table indicates the minimum power rating and voltage requirement for each supply.

A detailed breakdown of a power conditioning system for the 6 kW engine is shown in Table B. 3-3. This table gives the number of modules required for each supply and their various operating characteristics. As shown, the 6 kW power conditioning system would require a total of 47 inverter modules, would weight 35 lb and would have an over-all power efficiency of 93.5%. The specific weight of the complete system is, therefore, only 6 lb/kW.

TABLE B. 3-2

Power and Voltage Requirements for a 6 kW, 4000 sec I_{sp} , Engine

Power Supply	Power Distribution, %	Power Requirement, W	Voltage, V	Type
Main Beam	71.0	4000	+2200	dc
Discharge	16.5	920	40	dc
Cathode heater	4.3	240	0 - 10	ac or dc
Magnet	3.0	170	0 - 10	dc
Accel-electrode	2.0	110	-2200	dc
Vaporizer heater	0.6	34	0 - 50	ac or dc
Isolation	0.6	34	Solar Panel Bus	
Neutralizer	1.0	55	0 - 50	ac or dc
Control Master Oscillator	1.0	50	28	ac
Solenoid			Solar Panel Bus	

TABLE B. 3-3

Six Kilowatt Ion Engine Power Conditioning System

Function	Power, W	Module Rating	Min. No. Mod. (Low Line)	Standby	Tot. No. Mod.	Wt. Mod., lbs	Tot. Wt.	Eff.	Loss Mod., W (Low Line)	Tot. Loss, W	Tx. Type	Inv. Type	Inv. Freq., kc (Hi Line)	Mod. Out.	
Main Drive	4000	200	20	2	22	0.75	17.25	0.93	14.0	280	2N2581	Self Osc.	10	110 VDC	
Accelerator	500	100	5	2	7	0.50	3.5	0.93	7.0	35	DTS423	Self Osc.	10	440 VDC	
ARC	900	200	1		6	0.	4.0	0.92	8.0	72	DTS423	Driven	4	40 VDC	
Cathode	300	100	3	1	4	0.50	2.0	0.92	24.0	24	2N2581	Driven	4	10 VAC	
Neutr. Htr.	60	100	1	1	2	0.50	1.0	0.92	6.0	6	DTS423	Self Osc.	4	50 VAC	
At Ground Potential operated directly from solar cell bus															
Isolation Htr.															
Evaporation Htr.	50	100	1	1	2	0.50	1.0	0.92	5.2	5.2	DTS423	Self Osc.	4	50 VAC	
Magnet	120	200	1	1	2	1.50	3.0	0.92	16.0	16.0	2N2581	Self Osc.	10	10 VDC	
Master Oscillator Micrologic	100	100	1	1	2	1.0	2.0	0.90	10.0	10.0	DTS423	Self Osc.	10	28 VAC Regulated	
	6050 W		37	10	47		35.0			448.2 W					
$\text{lbs/k.W} = \frac{35}{6} \approx 6.0$ (Includes redundancy but not supporting structure or controls)															
Efficiency = $\frac{6050}{6448} \approx 93.5\%$															

Power Supplies

Main Beam Supply: As shown in Table B. 3-2 the main beam supply must furnish 4000 W of power at +2200 V dc. Table B. 3-3 and Fig. B. 3-3 show that twentytwo **200** W inverter modules will be dc added in series to supply this power. Each inverter module will operate in a self-oscillating mode, Two of the inverter units will operate as standbys. The inverter inputs are connected in parallel, their outputs in series. At the start of the mission solar cell bus voltage will be 75 V. At the end of the mission solar cell bus voltage will be 100 V. To compensate for solar cell bus voltage rise, power conditioning modules will be switched out during the mission., This mode of operation will generate effectively 5 more standby inverter modules, As shown in Fig. B. 3-3 each inverter module is fused at the input and employs a by-pass diode in the output circuit. If an inverter module short circuits, the fuse opens, If the inverter stops oscillating or a transistor malfunctions, the by-pass diode prevents an opening of the inverter output series circuit. The main beam supply will employ a micro-logic incremental voltage regulator, The regulator system monitors beam output voltage and automatically adds or subtracts inverter modules to maintain the **2200** V output. The voltage regulation is controlled to one module output voltage increment which will be approximately $\pm 2.5\%$. Each inverter module will have individual micro-logic start-stop circuits to start or stop inverter oscillation. The start-stop circuit will also be used for arc protection. In the event of sustained engine arc, all inverters will be automatically stopped to prevent inverter transistor damage.

Arc Discharge Supply: Table B. 3-2 shows the arc discharge supply must furnish **920** W of power at 40 V dc at main beam potential. As shown in Table B. 3-3 and Fig. B. 3-3, **6**, 200 W inverter modules will be ac added in series and the output rectified to supply this power. The ac adding technique is employed to minimize rectification power losses. Five inverter systems will be operating with one inverter in the standby status. To effect ac adding, the inverter frequencies are synchronized together at 4000 cps. Two master oscillator modules (one operating, one in standby) are used to supply the drive power to the inverter modules, Micro-logic incremental voltage regulator system

will be employed to maintain a 40 V output. The arc discharge output voltage will be directly related to the number of modules operating and will have 0, 8, 16, 24, 32, 40, 48 V output. Individual inverter start-stop circuits are also employed. In the event of a sustained current overload or arc, all inverters will be automatically stopped to prevent inverter transistor damage,

Accelerator Supply: The accelerator supply must furnish 110 W of power at -2200 V dc (e.g., see Table B. 3-2). Table B. 3-3 and Fig. B. 3-3 show that seven (five operating and two standby) inverter modules will be dc added in series to supply this power. The excess power capacity is required for the engine start-up. It is estimated that the accelerator supply, when initially turned on, will have a current overload transient of 20% of the normal main beam current. A micrologic voltage regulator system will be employed to maintain the 2200 V output. Seven output voltage combinations are possible (0, 440, 880, 1320, 1760, 2200, 2640, and 3080 V) by switching in or out inverter modules. Here again, micrologic circuitry is employed for arc and overload current protection.

Cathode Heater Power: The cathode heater supply must furnish 240 W of power at 10 V, ac. Four 100 W inverter modules (three operating and one standby) will be ac added to supply this power. Micrologic circuitry will be employed to start-stop the inverter modules and to automatically start the standby inverter on the advent of an operating module malfunction,

Low Voltage Supplies: Two low voltage ac heater supplies (evaporator and neutralizer) and one low voltage dc magnet supply are required by the ion engine. (The magnet supply may be eliminated if permanent magnets are used.) As shown in Fig. B. 3-3 each supply has one inverter module operating with one module in standby. The supplies are added in series. A two station incremental voltage regulator is employed to monitor output voltage and to automatically start-up the standby inverter module in the event the operating module malfunctions.

Engine Controls

Since the ion engine control system must be considered to be an integral part of the power conditioning system, its effect on circuit design will be discussed. The control system must provide the necessary logic for ion engine startup, restart, and shutdown, as well as establishing and maintaining the

engine design operating point, To accomplish these latter two functions a combination of both digital and linear control techniques are employed, The control philosophy consists of operating the ion engine at a fixed point by employing digital incremental voltage regulator circuits to hold constant the main beam, accelerator, and arc discharge voltages. Linear control techniques are then used to control the heater temperatures of the cathode, vaporizer and neutralizer supplies.

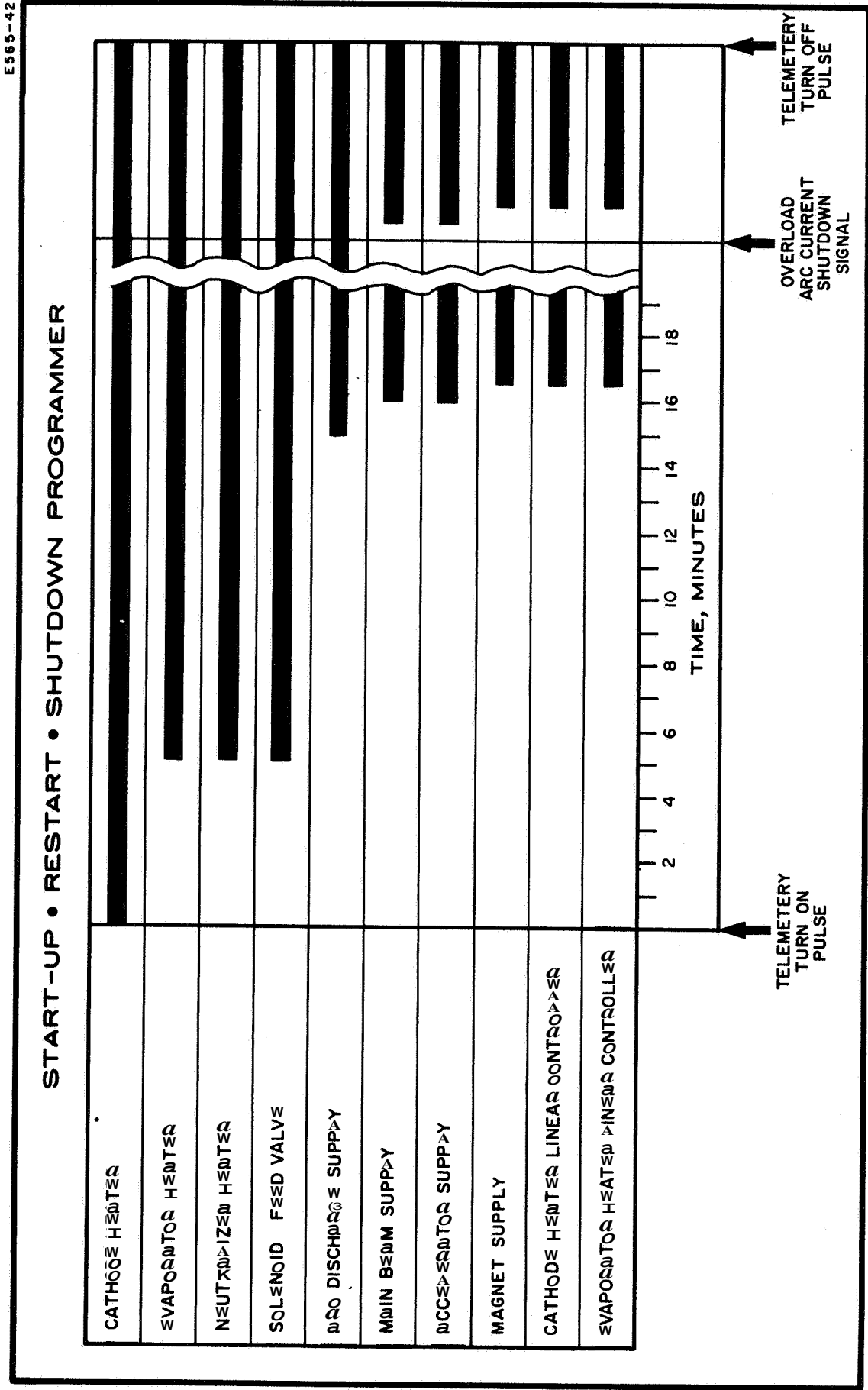
As shown in Fig., B.3-3 the ion engine control circuitry consists of:

1. Micro-logic startup-shutdown programmer
2. Micro-logic incremental voltage controllers
3. Linear heater controllers employing voltage and current feedback.

Startup-Shutdown Programmer: The micro-logic Startup-Shutdown Programmer provides the sequence logic for starting, restarting, and shutting down an ion engine system. The time sequence for turning on and off the power conditioning supplies and controllers is given in Table B.3-4. As shown, a telemetry signal turn-on pulse is required to initiate an ion engine start-up sequence. The first supply activated is the cathode heater, A time delay of 5 min is allowed for the cathode heater to come up to rated temperature, During this 5 min period, the startup current of the cathode heater supply magnetic modulator is limited by a series reactor, Five min after startup the evaporator, the neutralizer heaters are turned on, In addition the mercury solenoid feed valve is opened. A 10 min period is then allowed for the evaporator heater to come up to rated temperature, At the 15 min mark the arc discharge supply is turned on. At the 16 min mark the high voltage main beam and accelerator supplies are also activated, Finally, at the 16.5 min mark the magnet supply is turned on and the ion engine beam current established. Also, at this same time the cathode and evaporator heater linear controllers are activated,

This same circuit logic would provide restart in the event of arc shutdown. The main beam, accelerator, and arc discharge supply output currents are continually monitored. If current overload or arc occurs in any one of these three supplies or if a loss of arc discharge current occurs, an automatic shutdown of all three circuits is initiated, When this occurs, the arc current is extinguished and ion engine restart is required. However, in this case,

TABLE B. 3-4.



the startup procedure is much simpler and faster. As shown in Table B.3-3, the magnet supply and cathode and evaporator linear controllers would be turned off at the time the arc shutdown signal was initiated. Thirty sec after shutdown the high voltage supplies would be turned on, followed in 30 sec by the turn on of the magnet supply. When beam current is reestablished, the cathode and evaporator linear controllers are again activated,

Incremental Voltage Controllers: A micro-logic Incremental Voltage Controller is associated with each of the power supplies. The main beam supply micro-logic incremental regulator system will automatically switch in or out inverter modules to maintain an essentially constant output voltage. The incremental regulator circuit will compensate for any variations in solar cell input voltage which affects the supply output voltage. In addition the incremental regulator circuit will compensate for any changes in supply output voltage caused by a module failure. In the event of a module failure, the voltage drop in the output circuit will be detected and a standby inverter module will automatically be started to compensate for the voltage drop.

In the case of the accelerator, arc discharge, and heater and magnet supplies the micro-logic circuitry is used primarily as a malfunction monitor. If a gross voltage change is detected as a result of a module failure, a standby inverter module system is automatically substituted.

Linear Controllers; The modular form of the power conditioning system affords the opportunity of creating an extremely versatile means for maintaining an engine operating point. The linearly controlled regulators with their high gain differential amplifiers are ideal summing points to which the ion engine process parameter can be fed for closed loop control. By utilization of the concept, undesired interactions among supplies are eliminated so that closed loop system response is only that which is inherently designed into each of the interconnecting loops.

The primary engine process parameters that must be controlled for optimum system performance are beam current I_B and propellant utilization efficiency η_u . Since under fixed operating conditions the beam current is directly related to mercury flow rate which in turn is related to evaporator

heater temperature, the regulation of beam current can be achieved by comparing actual I_B to a desired I_{B0} reference and using the difference signal to control evaporator heater temperature.

To assure that the beam current actually achieved is that corresponding to a desired propellant utilization efficiency an additional constraining control loop must be incorporated to hold η_U constant. Since the utilization efficiency is a direct function of the ratio of arc current to beam current and since both are monotonic non-decreasing functions (with non-equal slopes) of cathode temperature, regulation of η_U can be achieved by comparing I_{arc} and I_{beam} currents and controlling cathode heater power to give the desired ratio.

To discuss the unconditional stability of the process controlled by the above loops the Process State Transition Diagram, Fig. B. -3-4, will be utilized. The plots of I_B and I_A versus cathode heater temperature, showing that the transfer gain for I_{beam} is less than that for I_{arc} , are representative of the experimental data available and it is noted that for any given neutral flow rate a unique cathode temperature (hence cathode power) exists for a fixed I_{arc}/I_{beam} ratio. Travel to the right is in the direction of an increased ratio. It is immediately seen that the process is stable with either a positive or negative cathode temperature step input, since a ratio greater than that set by the loop scaling constant causes a decrease in cathode power while a smaller ratio causes an increase in cathode power. Because of the relative magnitudes of the cathode and evaporator, essentially no disturbance flow rate would occur. Hence for constant flow rates the process is stability fixed at State I,

Now consider that a step increase in mercury flow rate, H_g^0 , is applied to a process initially at State I. The sudden increase of propellant in the arc chamber causes an increase in both I_{beam} and I_{arc} so that the process is placed at State II. For sake of discussion, it is assumed that at this flow rate, H_g^0 , the desired I_{arc}/I_{beam} ratio is slightly to the left of the T_o line, however the desired ratio location does not inherently change the stability considerations. Again, because of the relative time constants of the cathode and evaporator the cathode power reduction carries the process to the desired I_A/I_B ratio at State III, hence η_U is set at the new beam current level.

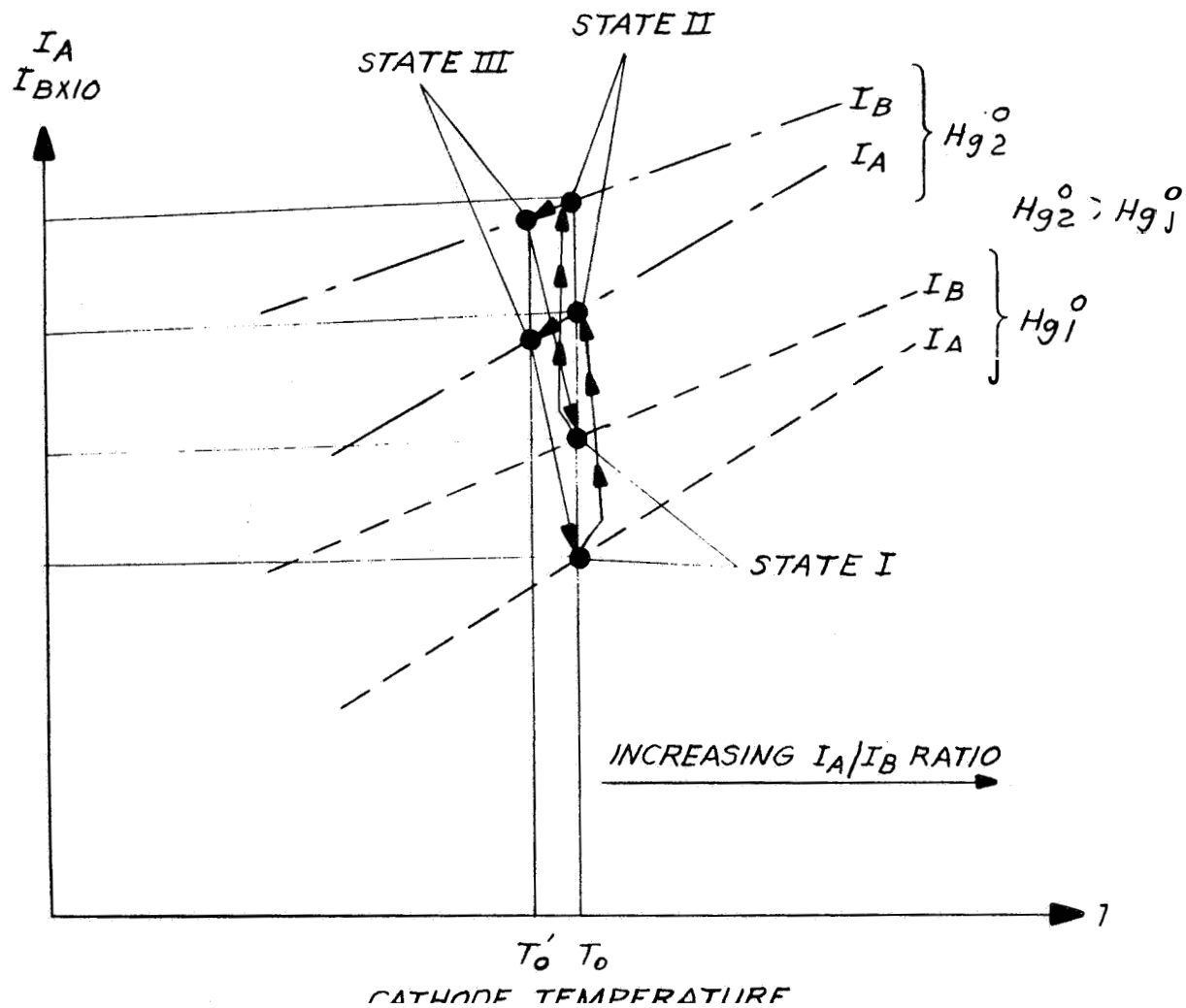


Fig. B. 3-4. Process state transition diagram.

The excess beam current is sensed and the evaporator power is reduced, hence the process is returned along the path between State III and State I, i. e. , the beam control loop causes a downward movement due to decrease flow and the I_a/I_b ratio loop causes a movement to the right because of the need to increase the cathode temperature to hold the ratio constant.

Hence the process control method chosen to hold the beam current and the propellant utilization efficiency at the desired design center values is shown to be unconditionally stable.

4. Conceptual Design of Propulsion System

The trajectory and mission studies which were performed to determine typical design points for the ion propulsion system have led to the choice of a 1971 zero coast Mars rendezvous as the model design mission. Assuming a Saturn IB/Centaur launch vehicle, the following propulsion characteristics have been established:

Thrustor	-	Hg Bombardment Engine
Specific Impulse	-	4000 sec
Power (total)	-	48 kW
Propellant Weight	-	1600 lb

Furthermore, based on reliability considerations it was shown in Section B. 2 that the optimum combination of operating and standby engines for the 48 kW propulsion system is 8 and 2, respectively,

A conceptual drawing of a complete ion propulsion system (exploded view) which satisfies the design constraints which have been discussed above is shown in Fig. B. 4- 1. It consists of 10 thruster modules. Initially, 8 of these would be operating and 2 would be in standby to satisfy the reliability considerations. The thruster array shown is based on a 6 kW, 35 cm, Hg bombardment (permanent magnet) engine operating at low current density (e. g. $2-3 \text{ mA/cm}^2$) and is somewhat less than 5 ft x 7 ft. More detailed discussion and illustration follows, and is divided into the areas of; (1) thruster and feed system, (2) Power conditioning and controls and, (3) System weight itemization.

The conceptual design of the thruster-feed system array is shown in Fig. B. 4-2. Half the array is shown. There are a total of ten 35 cm engines and 8 200 lb Hg storage reservoirs. Each tank has a separate solenoid valve as does each engine. (See Fig. B. 3-2 for further identification of the sub-module components.) A basic feature of this design is the capability for cross-coupling between fuel tank modules and thruster modules, provided by the one additional solenoid valve. In other words, any number of the 8 Hg storage tanks may be used to feed simultaneously

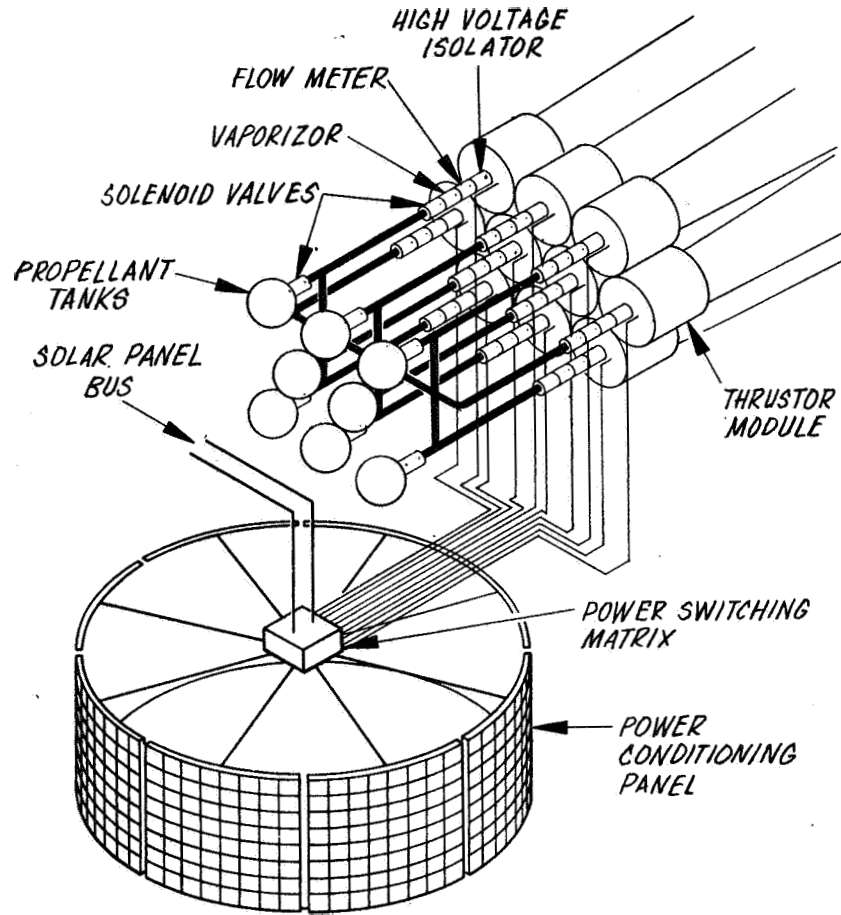


Fig. B.4-1. Conceptual drawing of 48 kW ion engine system.

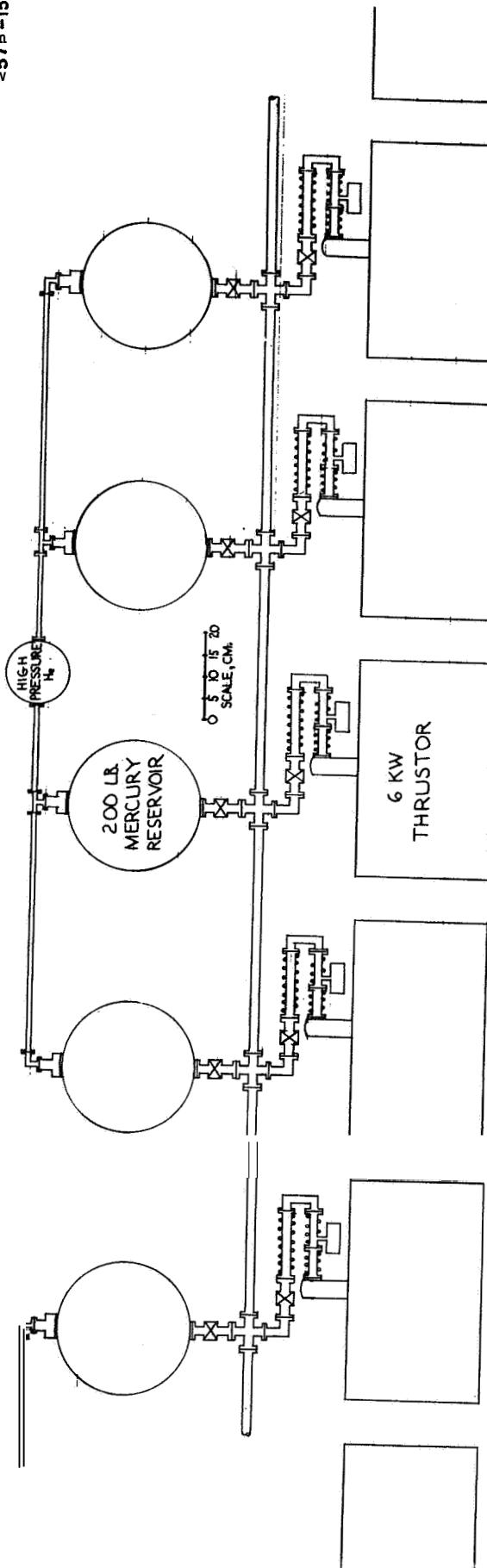


Fig. B. 4-2. Detailed layout of 48 kW feed system and thruster array.

any number of the 10 thrusters. The number of engines operating and the number of tanks operating are completely independent. This feature is desirable for two reasons; engine switching and reliability of propellant supply.

Engine switching is required because the propulsion system employs the standby thruster module concept (in order to raise thruster system reliability). It may be necessary to turn off an engine at random, switching in a standby to replace it. The cross-coupling design allows the fuel which is at first available to the original operating engine, then to become available to the standby.

Engine switching is also a requirement of solar cell power matching, which requires the beam current to be reduced as a function of time. Because of this, at discrete points in the mission complete thruster units are turned off. Therefore, an increasing number of standbys become available. The complexity in determining beforehand which engines will be operating at any given time thus becomes enormous. The cross-coupling design eliminates this requirement.

Although engine switching could be accomplished with only one propellant tank, the use of multiple tanks is highly desirable for other reasons. First, it is unlikely that the positive expulsion bladder of a single tank could support, under launch conditions, the large amount of propellant required for the mission (1600 lb). Therefore, in sizing the tankage, operational limitations on the expulsion system must be considered. Present work in this area has involved tanks of 50 lb capacity so that extrapolation to capacities greater than 200 lb would be subject to question.

Next, multiple tanks are desirable for reliability of propellant storage. If one tank failed, (for example, due to meteoroid puncture) the multiple-tank arrangement allows that tank to be isolated from the propulsion system in such a way that thruster performance continues undisturbed. The punctured tank could be immediately isolated by its own solenoid valve, limiting the propellant loss to that remaining in the defective reservoir. To conserve propellant further a slightly more elaborate

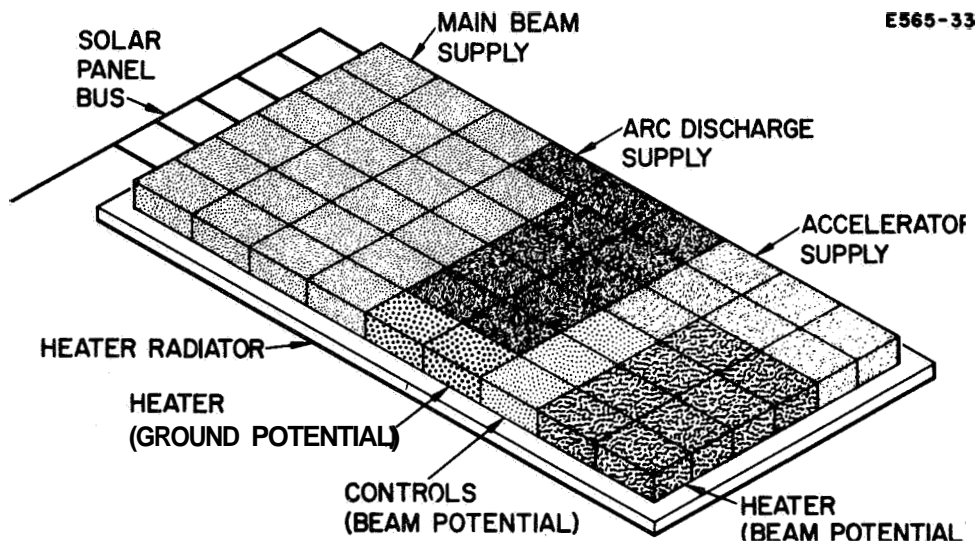
scheme may be employed. For example, upon a signal that a particular mercury reservoir was leaking, all other tanks would be shut off until all fuel in the leaky tank was utilized. The punctured tank could then be isolated and the other tanks reopened, thus maintaining continuous supply to the operating thruster modules.

Finally, the pressurization of the eight mercury reservoirs is accomplished with only two high pressure helium supplies. In Fig. B.4-2 one high pressure supply is shown with its associated four mercury tanks.

The power conditioning system consists of eight panels of modules, one panel consisting of the power supplies required for a single thruster. Each panel is approximately 2.5 ft by 3.5 ft and is designed in a flat panel for radiation cooling. The eight panels are shown forming a cylinder about 8 ft in diameter which slips over the spacecraft structure. A power switching matrix provides switching between the power conditioning panels and thruster modules. Again extra power conditioning panels could be provided to increase system reliability. However, the reliability of each panel can be made arbitrarily high by increasing the number of power conditioning modules per panel, as shown in Fig. B.4-3.

As shown, each power supply is made up of a number of low voltage, low power modules strung in series such that the required thruster voltage and power is obtained. By placing a number of extra modules in series with those required, the reliability of the individual supplies can be increased to any desired level. The high voltage high power beam supply is shown consisting of twenty-three 100 V, 200 W modules. Other supplies shown are the high voltage, low power accelerator supply, the arc discharge supply, and the various heater and control supplies.

As indicated the 48kW system may be approximately considered to be composed of separate 6 kW engine systems, each with its own feed system and power conditioning. It is of interest, therefore, to tabulate the components of a 6 kW mercury bombardment engine system. Table B.4-1 shows the weights broken down into the four major subsystems. The total 6 kW system weight is shown, to be 68 lb for a specific weight of 11.5 lb/kW. Although items such as cabling, piping, and thruster redundancy are not included, the indications are that the complete 48 kW engine system will come well within the 25 lb/kW goal.



E565-33

Fig. B.4-3. Conceptual drawing of a 6 kW power conditioning system.

TABLE B.4-1

6 kW Mercury Bombardment Engine System

THRUSTOR		POWER CONDITIONING	
Accel Electrode	4 lb	Main Beam Supply (23)*	18 lb
Screen Grid	2	Accel Supply (7)	3.5
Shell	6	Arc Supply (11)	5.5
Permanent Magnet	3.5	Heater Supplies (10)	6
Miscellaneous	<u>2.5</u>	Master Oscillators (2)	<u>2</u>
Total	18.0 lb	Total ("No. of Modules)	35.0 lb
FEED SYSTEM		CONTROL SYSTEM	
Mercury Reservoir (200 lb Propellant Capacity)	10.5	Micro-Logic (1 Equivalent)	<u>2</u>
Isolator	1	Total	2.0 lb
Vaporizer	1		
Flow Control	1		
Plumbing	<u>0.5</u>	TOTAL WEIGHT	69.0 lb
Total	14.0 lb	SPECIFIC WEIGHT	11.5 lb/kW

5. Power Matching Study

A major problem in designing a solar electric propulsion system is the utilization of the maximum available power from the solar panels. In order to guarantee this utilization, the thruster and power conditioning systems must be designed and programmed to provide the proper load at all times to the constantly varying power and voltage outputs of the solar array.

a. General Considerations

Maximum Power Transfer from A Non-Linear Source

For the circuit shown in Fig. B. 5-1, in which

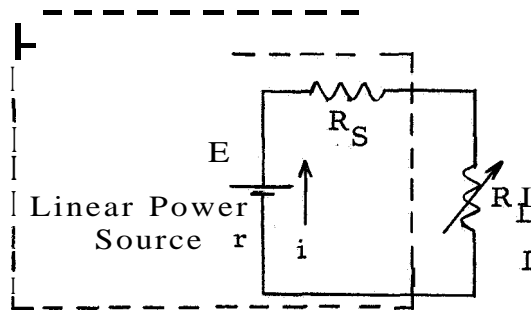


Fig. B. 5-1

Linear Power Source

$$(1) \quad E = (R_S + R_L) i$$

$$(2) \quad P_L = i^2 R_L$$

battery E and resistance R_S represent a typical voltage supply with linear internal resistance (R_S), it is well known that when R_L is adjusted to equal R_S maximum power $P_L (= i^2 R_L)$ is transferred to the load (R_L). However, since a solar panel is a non-linear source, this more complex problem of maximum power transfer from a non-linear supply (i.e., one for which the above representation as a battery and linear resistance is not possible), has been studied.

A two terminal source is specified if its terminal characteristic (V vs I) is given. The following analysis and comparison of linear and non-linear sources is made using their terminal characteristic curves. The V - I characteristic for the linear source is a straight line determined completely by the two constants E and R_S . A non-linear source is defined to be any source whose terminal

Characteristic I_s is not a straight line. A circuit representation similar to that of Fig. B. 5-1 can be used for the non-linear source provided that the internal resistance R_S is allowed to depend on the current, I . (Fig. B. 5-2)

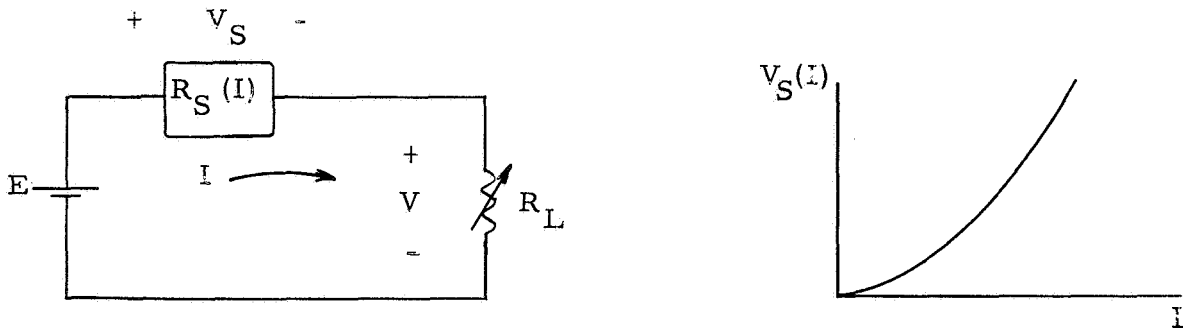


Fig. B. 5-2 Representation of A Non-Linear Source

The curve $V_S(I)$ may be calculated directly from the V-I characteristic and the equation

$$(3) \quad E = V_S(I) + V(I)$$

It must be noted that the voltage $V_S(I)$ can not be measured physically and that for the linear source $V_S(I) = R_S I$, where R_S is a constant. The problem of obtaining maximum power transfer is now setup mathematically and solved for a general non-linear V-I curve. In the special case when the V-I curve is linear the results reduce to the well known condition $\bar{R}_L = R_S$.

The problem is to find the R_L for which $P_L = I^2 R_L$ is a maximum subject to the condition

$$(4) \quad E - V_S(I) - I R_L = 0$$

The maximum P_L can be found by the method of Lagrange multipliers as follows:

$$(5) \quad g(I, R_L) = I^2 R_L - \lambda (E - V_S(I) - I R_L)$$

where λ is a Lagrange multiplier. The conditions for P_L to be maximum are that

$$(6) \quad \frac{\partial g}{\partial I} = \frac{\partial g}{\partial R_L} = 0$$

Applying these conditions to Eq. 5 gives

$$(7) \quad 2 I R_L + \lambda \frac{\partial V_S}{\partial I} + R_L = 0$$

$$(8) \quad I^2 + \lambda (I) = 0 \quad \text{or} \quad \lambda = -I$$

Therefore

$$(9) \quad 2 I R_L - I R_L - I \frac{\partial V_S}{\partial I} = 0$$

or

$$(10) \quad \bar{R}_L = \frac{\partial V_S}{\partial I} \quad I = \bar{I}$$

where \bar{R}_L is the load resistance necessary for maximum power transfer. This result means that for maximum power transfer the load should be adjusted to equal the slope of the V_S vs I curve at the value (\bar{I}) of I at maximum power transfer. (This value of I is obtained from Eq. 4 with $R_L = \frac{\partial V_S}{\partial I}$.)

Checking this result for the linear source, i. e., $V_S = R_S I$, we see that $R_L = \frac{\partial V_S}{\partial I} = R_S$ follows immediately.

Since a V - I curve is usually given for a non-linear source and not V_S vs I , we find \bar{R}_L in terms of $V(I)$ by differentiating Eq. 3.

$$(11) \quad \frac{\partial V_S}{\partial I} = - \frac{\partial V}{\partial I}$$

Combining Eqs. 10 and 11, we have

$$(12) \quad R_L = \left. \frac{\partial V}{\partial I} \right|_{I = \bar{I}}$$

Thus, \bar{R}_L is the negative slope of the V vs I curve at $I = \bar{I}$. A second geometric interpretation of \bar{R}_L can be obtained in terms of the $V-I$ curve as follows: The maximum power transfer point on the $V-I$ curve can be found by drawing a family of constant power hyperbolas, $VI = \text{constant}$, on the $V-I$ plane (Fig. B.5-3)..

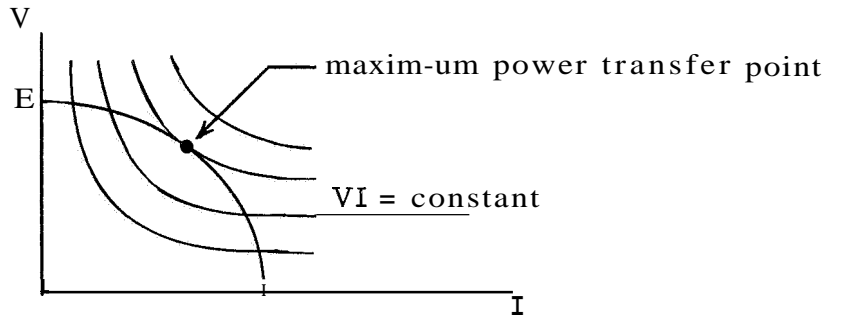


Fig. B.5-3 Location of Maximum Power Transfer Point

It is clear that one hyperbola in the family will be tangent to the $V-I$ curve and that the point of tangency is the maximum power transfer point. Thus, the slope of the $V-I$ curve at \bar{I} must equal the slope of the hyperbola at \bar{I} . Hence

$$(13) \quad \frac{\partial V_S}{\partial I} = \frac{\partial}{\partial I} \left[\frac{\text{constant}}{I} \right]$$

But a hyperbola, $V = \text{constant}/I$ has the property that the slope of its tangent at any point equals the negative of the slope of a chord from the origin to the point. That is, if $V = \text{constant}/I$ then

$$(14) \quad \frac{\partial V}{\partial I} = - \frac{\text{constant}}{I^2} = - \frac{V}{I}$$

Therefore, \bar{R}_L is the slope of the chord from the origin to the maximum power point on the V-I characteristic of the non-linear source (Fig. B. 5-4).

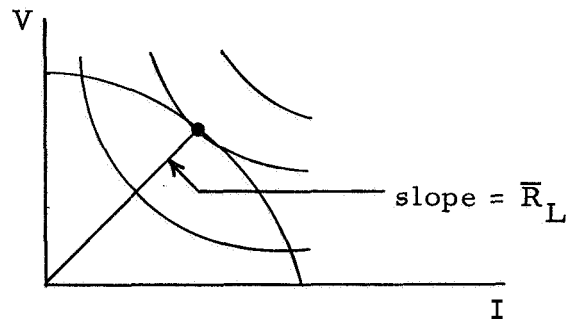


Fig. B. 5-4 Interpretation of \bar{R}_L

Power Matching Theory for A Solar-Electric Propulsion System

The electrical properties of the solar cell array have been given in terms of a terminal I-V characteristic (Fig. B. 5-5) which is non-linear and varies continuously with time. At any fixed time the solar array is a non-linear source of the type considered in the preceding section,

From the earlier analysis, it is seen that the operating point for maximum power transfer is known (I_{S_o}, V_{S_o}) and the value of the load resistance necessary to operate at this point is $R_{S_o} (= V_{S_o} / I_{S_o})$. As time increases during the mission the I-V curve changes and the point (I_{S_o}, V_{S_o}) of maximum power transfer moves. Plots of V_{S_o} , R_{S_o} , and $P_{S_o} (= V_{S_o} I_{S_o})$ are shown as functions of time in Fig. B. 5-6.

From these curves, it is seen that

- 1) The resistance R_{S_o} appearing at the source terminals must be continuously varied in time to achieve transfer of the maximum available power from the source to the load.
- 2) if R_{S_o} is adjusted for maximum power transfer the terminal voltage V_{S_o} is an increasing function of time.
- 3) The maximum available power P_{S_o} from the supply is a decreasing function of time.

Since the load is specified to be a 48 kW electric thruster array, some of the power conditioning objectives can be specified. First, the voltage and current out of the solar array must be transformed to new values corresponding to the operating points of electric thrusters. Second, the load resistance that the engines present to the source must be either adjusted or transformed continuously

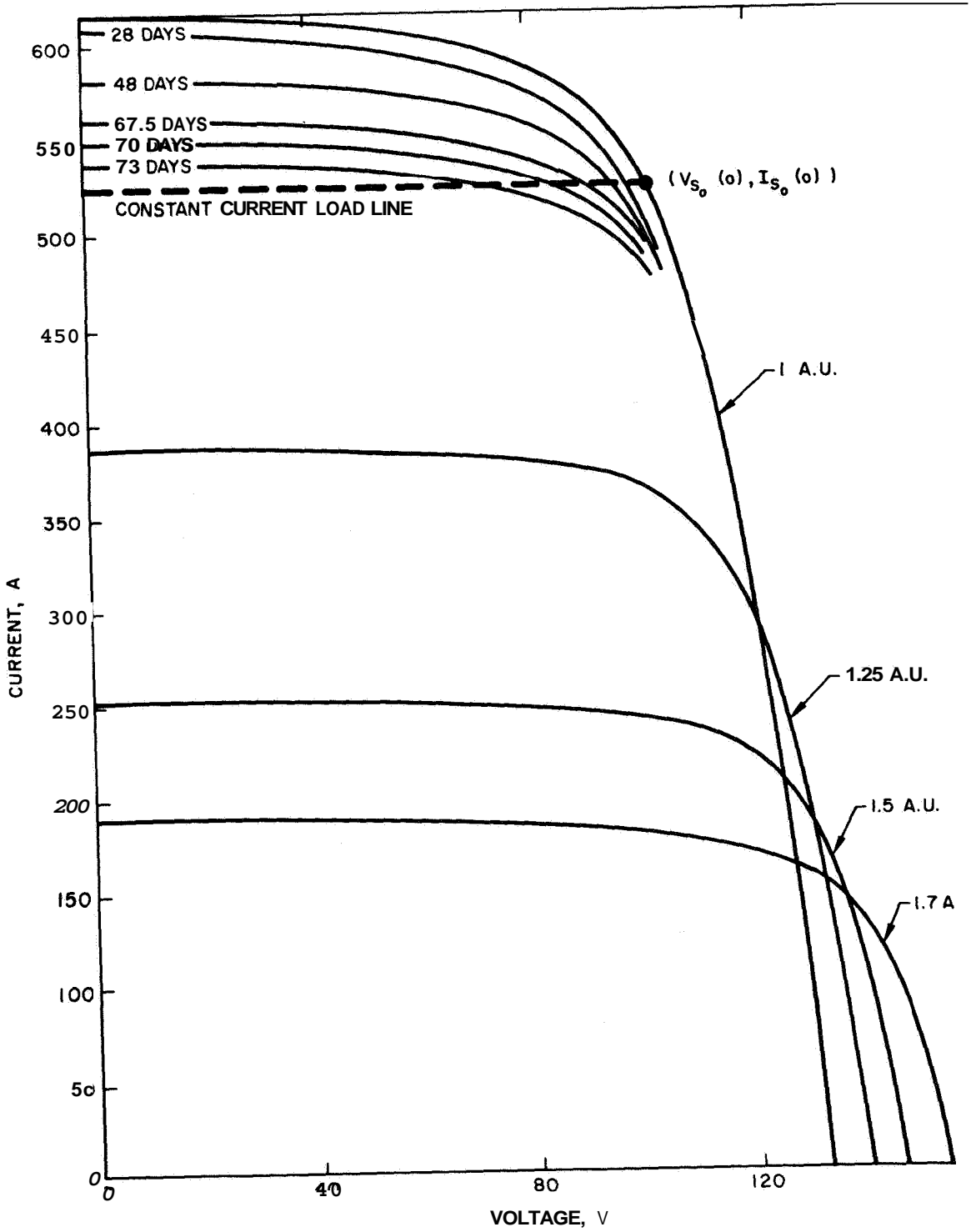


Fig. B. 5-5. Array IV characteristic 50 kW saturn/centaur (preliminary).

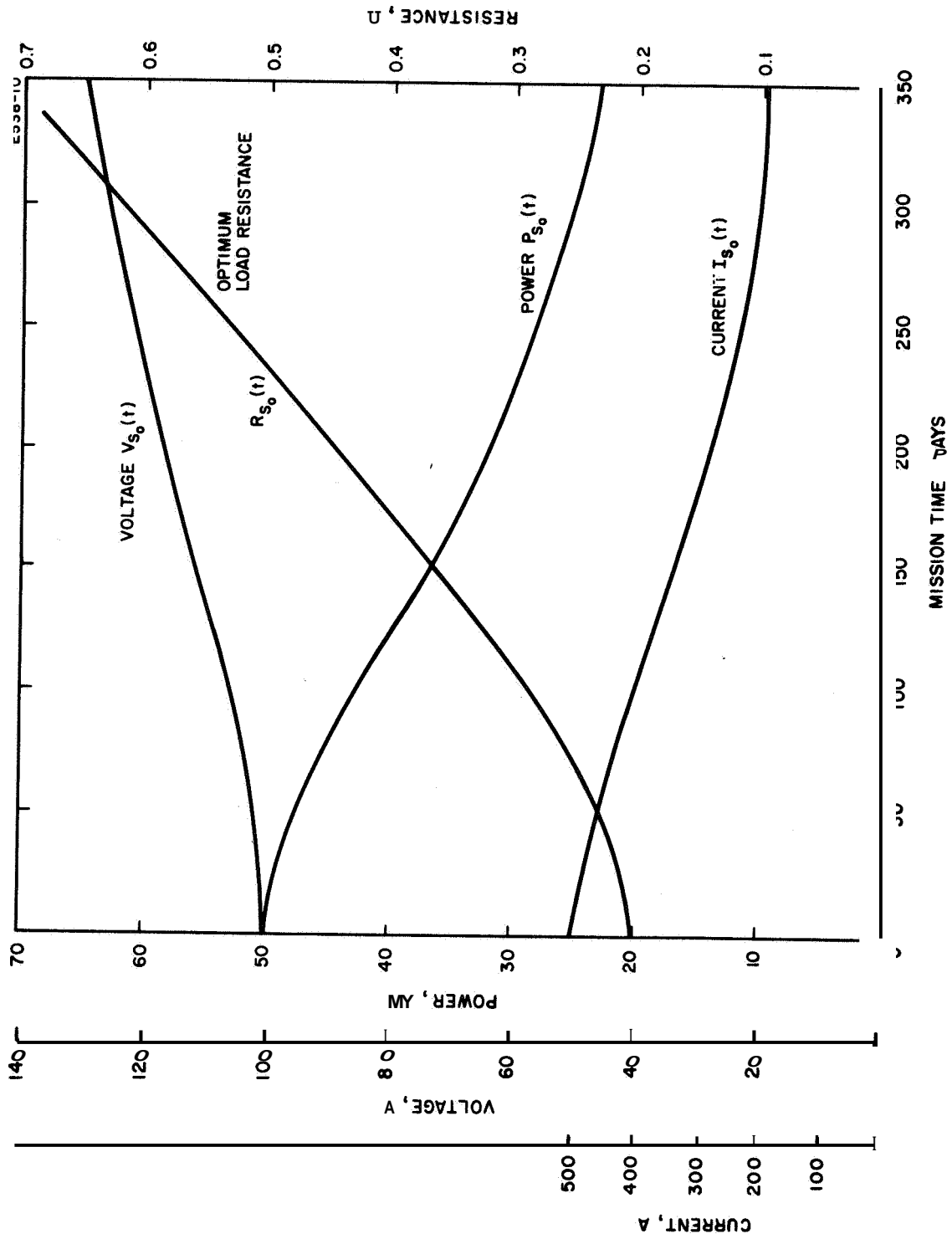


Fig. B. 5. 6 Solar array electrical output characteristics.

into the value $R_{S_0}(t)$ if maximum power transfer is to be achieved. The advantages of a power conditioning system that could keep the engines at their optimum operating points and simultaneously present the correct resistance ($R_{S_0}(t)$) to the source at each instant of time are obvious. To see the extent to which the power matching problem can be solved by today's power conditioning designs, it is useful to assume that the power conditioning system is simply an ideal transformer with turns ratio $1:n$. The following analysis of the power matching problem for the solar-electric system is based on the circuit of Fig. B.5-7

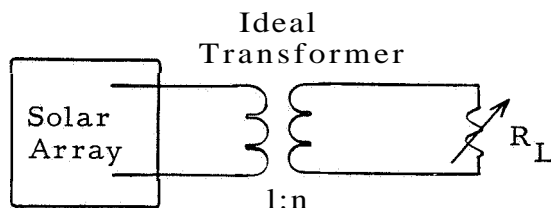


Fig. B. 5-7 Propulsion System Model (Electrical)

The applicability of this model to actual power conditioning and engine system designs is shown after some preliminary results and obtained.

Effect Of Time Varying Characteristics: The first situation studied is the effect of the time varying solar cell characteristics on the voltage, current and power to the load. Since 90% of the power to the load is to the beam supply (70%) and arc supply (20%) and both are operated as flow limited devices, it is reasonable to assume that the I-V characteristics of the load will be lines of constant current. The load line (as reflected through the transformer) is also a constant current line. If the system is initially at the maximum power transfer point $(V_{S_0}(0), I_{S_0}(0))$, at a later time t_1 the system will be at the point (V_{S_1}, I_{S_1}) which is the intersection of the load line and the t_1 source characteristic. The result is that the current in the load doesn't vary but the voltage and power decrease as shown in Fig. B. 5-8. The reason for the sharp decrease in power after 50 days is that the load resistance no longer matches $R_{S_0}(t)$. The penalty in power paid when $R_S \neq R_{S_0}$ for the $t = 175$ day source characteristic is shown in Fig. B. 5-9. Notice that the penalty for the non-linear solar cell source is more severe than for a linear source.

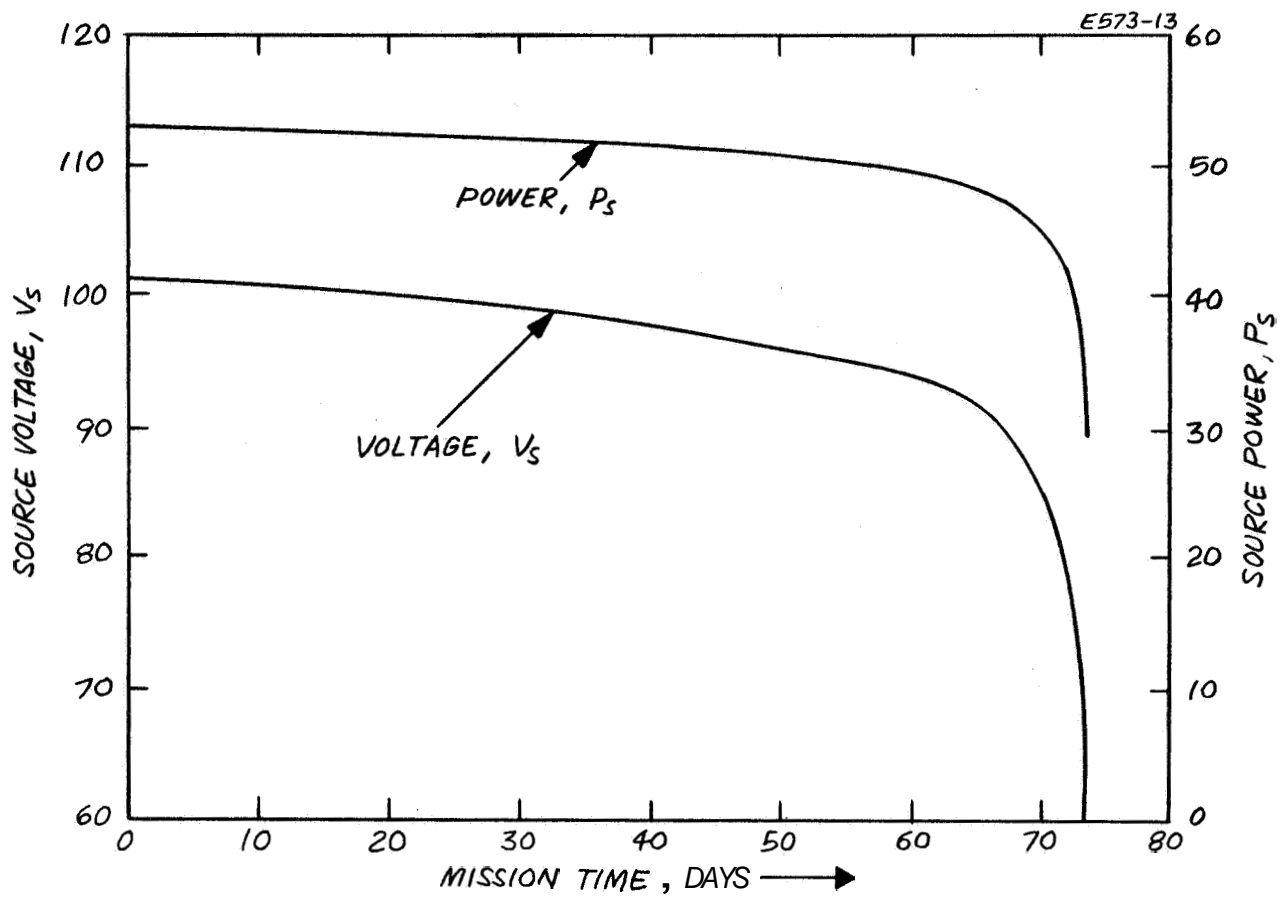


Fig. B. 5-8. Penalty in power transferred due to mismatched load.

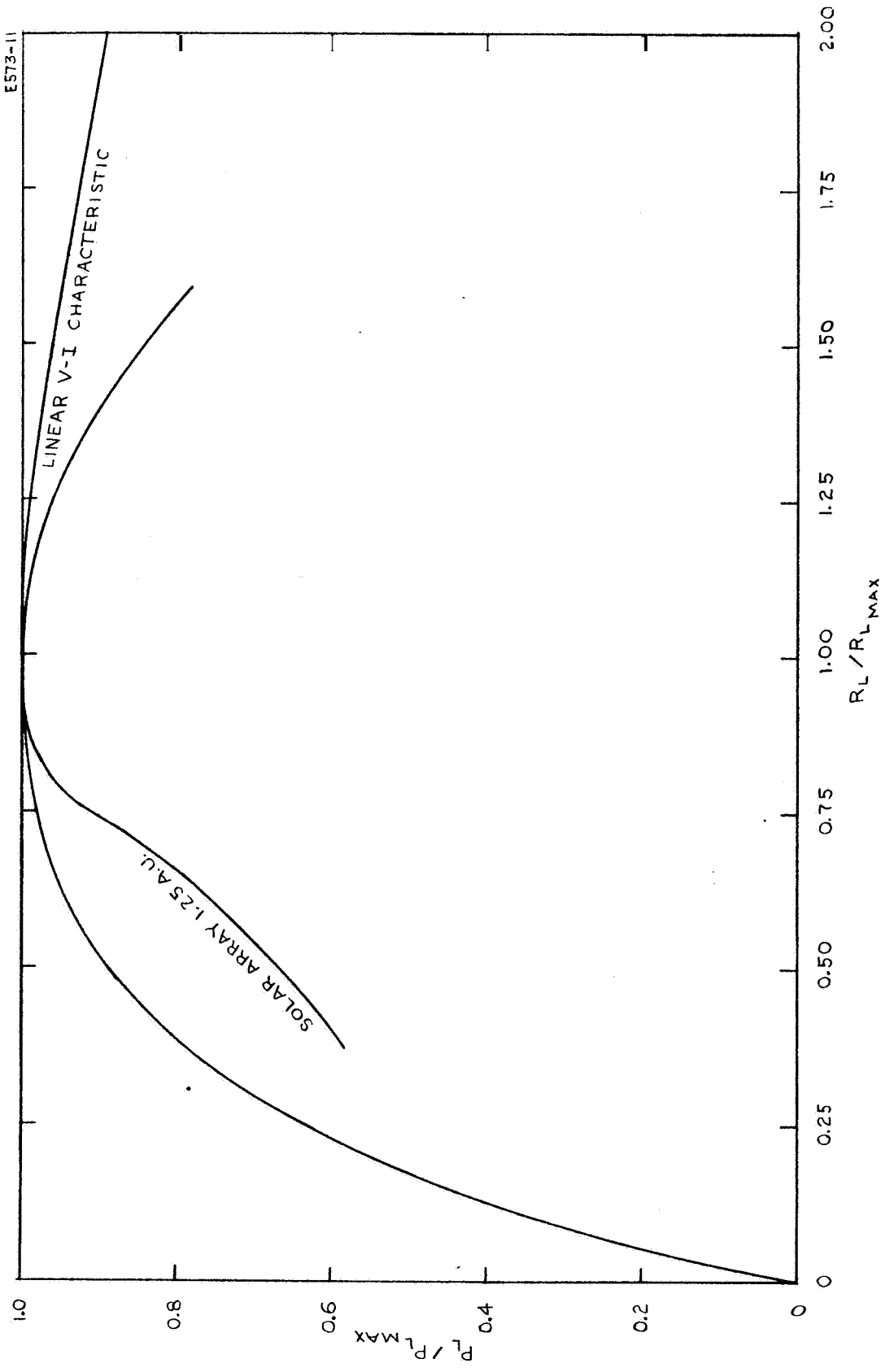


Fig. B.5-9. Penalty in power transferred due to mismatched load

Various things can be done before the mismatch condition gets too serious. Still assuming a constant current load, one can a) adjust n (to n_1) so that the load voltage is correct and vary R_L so that the reflected resistance matches $R_{S_o}(t_1)$. These adjustments are consistent with the transformer equations

$$(15) \quad V_{S_o}(t_1) = \frac{1}{n_1} V_L$$

$$(16) \quad R_S(t_1) = \frac{1}{n_1^2} R_L$$

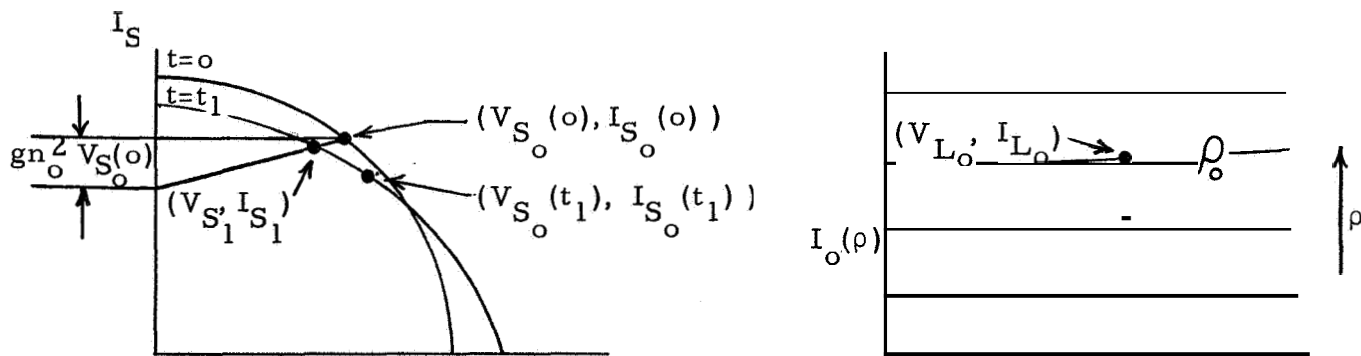
b) adjust n so that the source current is $I_{S_o}(t_1)$ i. e., use the equation

$$(17) \quad I_{S_o}(t_1) = n_1 I_{L_o}$$

and allow the load voltage to vary to

$$(18) \quad V_L(t_1) = n_1 V_{S_o}(t_1)$$

Notice that in both cases the adjustments given allowed a condition to be placed on V_L or I_L and maximum power transfer to be achieved simultaneously. The case of non-constant current load characteristics is analyzed next and the adjustments required for situations as above are investigated.



Non-Constant Current Load: Assume that the load I-V characteristics is a straight line with slope g and current intercept I_o which depends on an adjustable flow parameter ρ (Fig. B.5-10). (We shall see later that ρ is physically related to the boiler and arc heater temperatures.) Equation 19 represents the load characteristic for any ρ .

$$(19) \quad I_L(V_L) = I_o(\rho) + g V_L$$

Suppose that the system starts operating at the maximum power transfer point, $(V_{S_o}(o), I_{S_o}(o))$ (Fig. B.5-11), and that n is adjusted so that the load is at a desirable operating point (V_{L_o}, I_{L_o}) . This point (V_{L_o}, I_{L_o}) lies on a line of constant ρ . Throughout this analysis ρ is held constant and equal to ρ_o . The current intercept, $I_o(\rho_o)$ on the load characteristics can be found in terms of the initial source point $(V_{S_o}(o), I_{S_o}(o))$ from Eq. 19 and the transformer equations

$$(20) \quad V_{L_o} = n_o I_{S_o}(o)$$

$$(21) \quad I_{L_o} = \frac{1}{n_o} V_{S_o}(o)$$

to be

$$(22) \quad I_o(\rho_o) = \frac{1}{n_o} I_{S_o}(o) - g n_o V_{S_o}(o) = I_o$$

With $\rho = \rho_o$ (constant) it follows that the load line reflected through the transformer is also straight. Its equation is

$$(23) \quad I_S - n I_o + g n^2 V_S$$

which represents a one parameter family of straight lines whose current intercept increases like n and slope increases like n^2 . This family covers the first quadrant ($I_S > 0, V_S > 0$) in the sense that given any point (I_S', V_S') in the first quadrant the quadratic Eq. 23 has a positive solution n . This means that by adjusting n maximum power transfer can be obtained at any time. For $t = t_1$ n must be adjusted to the value of the positive root of the quadratic

$$(24) \quad g n^2 V_{S_o}(t_1) + n I_o - I_{S_o}(t_1) = 0$$

Rewriting Eq. 24 with I_o put in explicitly because it depends on g , gives

$$(25) \quad g n^2 V_{S_o}(t_1) + n \left(\frac{1}{n_o} I_{S_o} - g n_o V_{S_o} \right) - I_{S_o}(t_1) = 0$$

We see that for $g = 0$

$$(26) \quad n = \frac{I_{S_o}(t_1) n_o}{I_{S_o}(o)}$$

and the load current $I_L(t_1)$ is

$$(27) \quad I_L(t_1) = \frac{1}{n} I_{S_o}(t_1) = \frac{I_{S_o}(o)}{n_o} = I_{L_o}$$

As should be expected, with $g = 0$, maximum power transfer and constant load current occur simultaneously. For the case $g \neq 0, \rho = 0$ maximum power transfer can be achieved but both I_L and V_L must be changed. This may be argued as follows: With $g \neq 0$ any adjustment that allows $I_L(t_1) = I_{L_o}$ also forces $V_L(t_1) = V_{L_o}$ and therefore $P_L(t_1) = P_{L_o}$. But this is impossible because the power available is a decreasing function of time.

The difference $| I_L(t_1) - I_L(o) |$ is now calculated for "small" g . To specify what "small" g means more precisely, dimensionless variables are introduced. Let

$$(28) \quad I_S^* = I_{S_o}(t_1) / I_{S_o}(o)$$

$$(29) \quad V_S^* = V_{S_o}(t_1) / V_{S_o}(o)$$

$$(30) \quad n^* = n/n_o$$

Upon substitution, Eq. 25 becomes

$$(31) \quad -I_S^* + n^*(1-\epsilon) + \epsilon n^{*2} V_S^* = 0$$

where

$$(32) \quad \epsilon = \frac{g}{I_{S_o}/n_o^2 V_{S_o}} = \frac{g}{I_{L_o}/V_{L_o}}$$

The condition $g \ll I_{L_o}/V_{L_o}$ or $\epsilon \ll 1$ is now what is meant by g "small". The behavior of n^* for small ϵ is found by substituting an expansion

$$(33) \quad n^*(\epsilon) = n_o^* + n_1^* \epsilon + n_2^* \epsilon^2 + \dots$$

in Eq. 31 and equating coefficients of ϵ^n for $n = 0, 1, 2, \dots$. Substituting yields

$$(34) \quad I_S^* = (n_o^* + \epsilon n_1^* + \epsilon^2 n_2^*) (1-\epsilon) + \epsilon V_S^* (n_o^{*2} + 2\epsilon n_o n_1^*) + (\quad) \epsilon^3 + \dots$$

Setting the coefficient of $E^0 = 0$ gives

$$(35) \quad I_S^* = n_o^*$$

Setting the coefficient of $E^1 = 0$ gives

$$(36) \quad n_1^* = n_o^* - n_o^{*2} V_S^*$$

Setting the coefficient of $E^2 = 0$ gives

$$(37) \quad n_2^* = n_1^* (1 - 2 V_S^* n_o^*)$$

Thus,

$$(38) \quad n^*(E) = I_S^* t^E (I_L^* - V_S^{*2}) + E^2 (\quad) t \dots$$

Now consider

$$(39) \quad \Delta I_L = | I_L(t_1) |_{g \neq 0} - I_L(0) |$$

$$= | \frac{1}{n_1} I_S(t_1) - \frac{1}{n_o} I_S(0) |$$

$$(40) \quad \frac{1}{n_1} = \frac{1}{n_o^*} = \frac{1}{n_o^* I_S^*} [1 + \epsilon (1 - V_S^* I_S^*) + \dots]^{-1}$$

$$= \frac{1}{n_o^* I_S^*} [1 - \epsilon (1 - V_S^* I_S^*) + \dots]$$

Hence,

$$(41) \quad \frac{I_{S1}}{n_1} = \frac{I_{S_o}(0)}{n_o} [1 - \epsilon (1 - V_S^* I_S^*) + \dots]$$

and

$$(42) \quad \Delta I_L = \epsilon (1 - V_S^* I_S^*) \frac{I_{S_o}(o)}{n_o} t \dots$$

The corresponding voltage change is

$$(43) \quad \Delta V_L = |V_L(t_1)|_{g \neq 0} - V_{L_o} = \frac{\Delta I_L}{g} = \frac{\epsilon}{g} (1 - V_S^* I_S^*) \frac{I_{S_o}(o)}{n_o}$$

or

$$(44) \quad \Delta V_L = (1 - V_S^* I_S^*) n_o V_{S_o}$$

From **Eqs.** 42 and 44, it is seen that the change in the load current is of order ϵ and the change in voltage is of order 1.

Specification of V_L or I_L and maximum power transfer can be attained simultaneously provided that ρ is not held constant. Suppose that maximum power transfer and constant I_L are required. Then the applicable equations are

$$(45) \quad I_{S_o}(t_1) = n I_o(\rho) + g n^2 V_S(t_1)$$

$$(46) \quad I_{S_o}(t_1) = n I_{L_o}(o) = \frac{n}{n_o} I_{S_o}(o)$$

which must be solved for n and ρ ,

b. Application of Power Matching Theory to Conceptual System Design

The problems of voltage and power matching analyzed in section 5a is now reviewed and restated in terms of the engine and power conditioning parameters. Although no attempt is made to solve all of these problems now, a brief preliminary analysis is made of the voltage matching and regulation possible using a modularized beam supply under the assumption that maximum power transfer is being achieved. Applying Transformer Model to Conceptual Design

The power conditioning conceptual design includes the use of modularized d-c inverter systems.* With the possibility of switching modules in and out these d-c inverters essentially act as discrete turns ratio d-c transformers which couple the primary solar cell power to the various system loads. The effective turns ratio of a modularized inverter depends directly on the number of modules that it contains. In the problems which require a continuous turns ratio, m for matching, a study must be made of the penalties paid in voltage and power matching when m is discrete.

The possibility of adjusting the load, R_L was the other key to being able to maintain power matching and the correct engine operating points. Due to the modularized engine system design, the load can be varied in discrete increments. There is also the possibility of varying the load resistance continuously by controlling the propellant flow rate (and therefore the beam current).

The discrete voltage matching and continuous load resistance variation possible with the present system design make the conditions assumed in the matching theory realistic. A trade off study must now be made to find the optimum degree of power and voltage matching attainable. Such a study would include (1) finding the best number of inverter modules in each power supply and (2) weighing the complication

* A more detailed description of a beam inverter system is given in the section that follows.

of varying beam current continuously (to maintain maximum power transfer) against the penalty of not being power matched continuously.

Voltage Control with a Modularized Beam Supply

The schematic diagram of a multi-module beam supply is shown in Fig. B. 5-12 with the definition of the parameters pertinent to its analysis. The philosophy of this design is to provide a relatively high power system by using many low power modules. As shown in Fig. B. 5-12 all of the modules have the solar cell bus as a common input. With the individual transformers providing isolation between modules, their outputs are connected in series to yield the required high voltage of a main beam supply. By switching in or out modules a means of non-dissipative voltage control and regulation is accomplished.

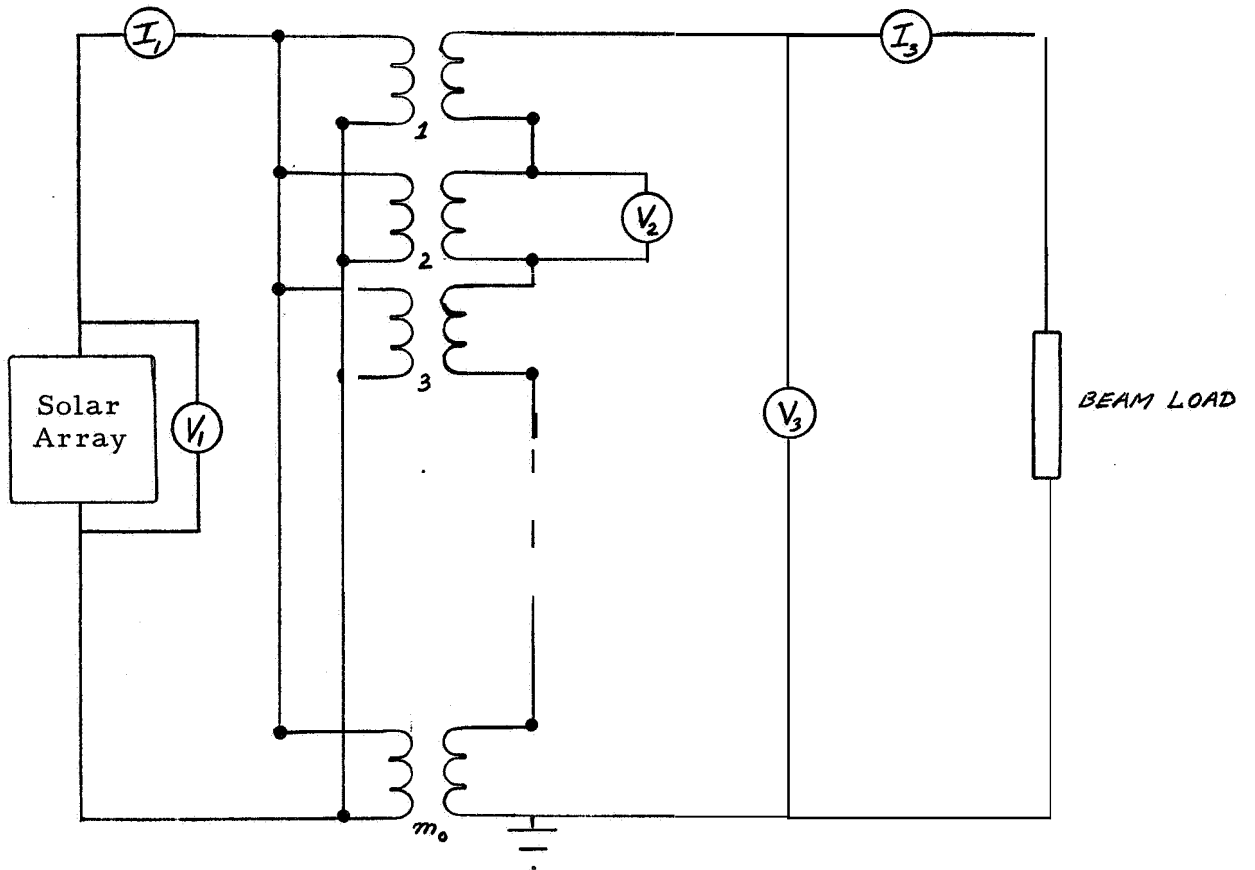
It will be shown in the analysis that the amount of regulation and control available depends on: (1) the number of modules employed, (2) the power rating of the module and (3) the required beam voltage.

The precise situation to be analyzed is as follows: the load to the solar array is assumed to be varied (e.g., varying beam current) so that maximum power transfer is maintained. The thrusters are to be run at constant specific impulse, i.e., at constant beam voltage. Because the solar cell bus voltage increases in time, at the maximum power transfer points beam supply modules are switched out to provide regulation.

As a typical example, consider a 4 kW beam supply (used in a 6 kW Hg bombardment ion engine). Suppose that the engine is to be run at a constant specific impulse of 4000 sec. which corresponds to a main beam voltage of 2200 volts. Assuming that the modules are rated at 200 watts, the number of modules operating initially (m_o) and the turns ratio of each module (n) are determined as follows:

$$m_o = P_3/P_2 = 4000/200 = 20$$
$$n = m_o V_1/V_3 = \frac{20.75}{2200} = 0.68$$

where the initial solar cell voltage, V_1 , is assumed to be 75 volts.



- m_o = number of modules operating initially
 $V_{1,2,3}$ = solar cell, module, beam voltages
 $P_{1,2,3}$ = solar cell, module, beam power
 n = module turns ratio

Fig, B.5-12

Schematic of Modularized Beam Supply

As the mission proceeds, the solar cell voltage V_1 increases to about 96 volts at 350 days. To try to maintain constant beam voltage, V_3 modules are switched off. In Fig. B.5-13a, a typical curve of bus voltage V_1 at maximum power transfer is shown for a 350-day Mars mission. Figure B.5-13b shows the voltage output (V_1/n) of each module,

In Fig. B.5-14a, the module turn off sequence is given. The switching times are calculated so that V_3 returns to 2200 volts when a module is turned off.

Based on this switching scheme the module and beam voltages are determined as shown in Table B.5-1.

TABLE B.5-1

Mission Time (Days)	Module Output Voltage (V_2)	Number of Modules Operating Initially (m_0)	Main Beam Voltage $V_3 = V_2 m_0$
0	110	20	2200
100	115.6	20 19	2315.6 2200
150	122	19 18	2322 2200
200	129.5	18 17	2329.5 2200
280	137.5	17 16	2337.5 2200
350	141.5	16	2260

The regulation of the beam voltage is shown in Fig. B.5-14b. The largest voltage deviation from the required value of beam voltage (2200 volts in this example) occurs just before the last module is switched. If a total of k modules are switched, the change in voltage, ΔV , is given by

$$(46) \quad \Delta V = \frac{1}{m_0 - k + 1} V_3(t_k)$$

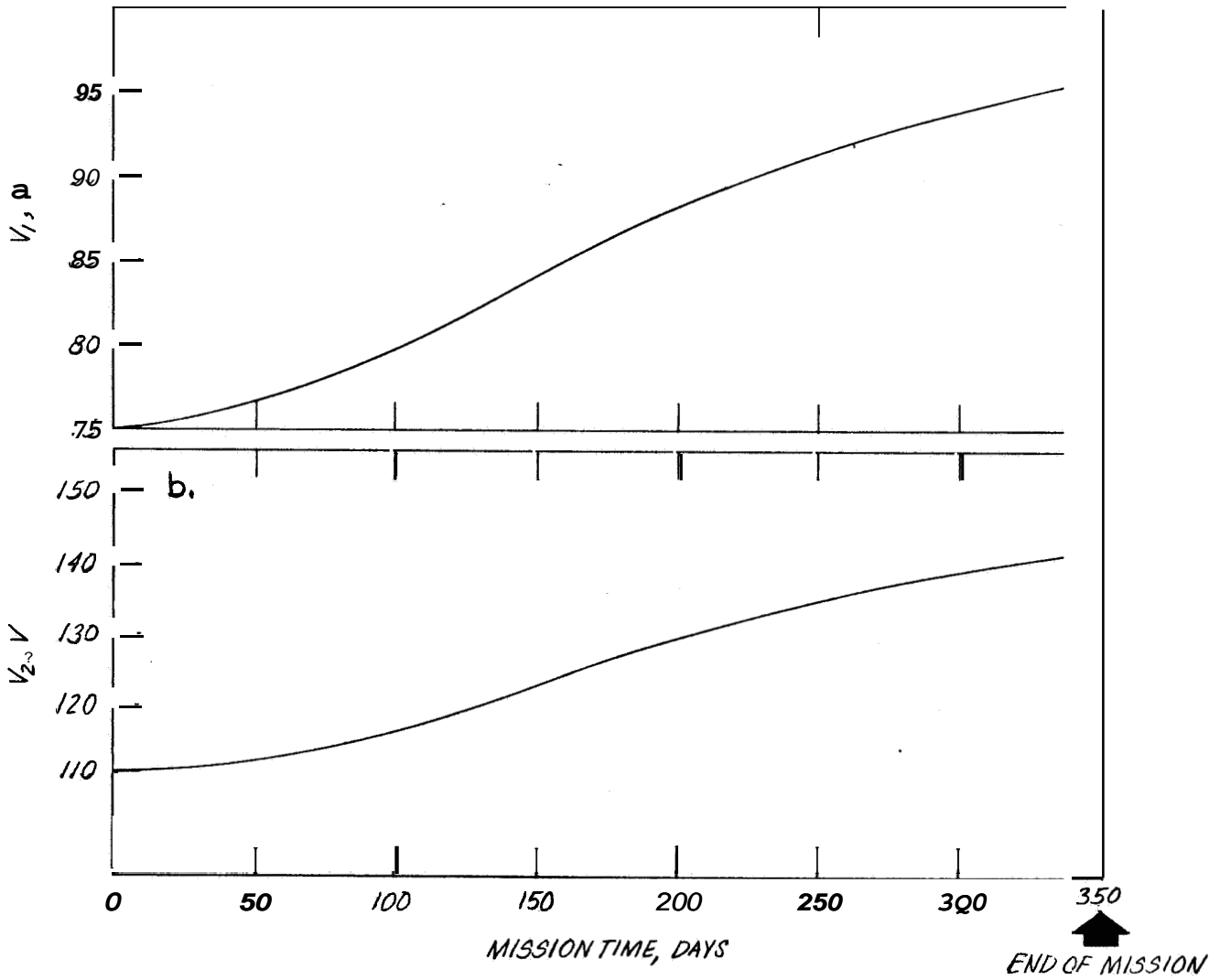


Fig. B.5-13. Solar panel bus voltage versus mission time.

E 573-17

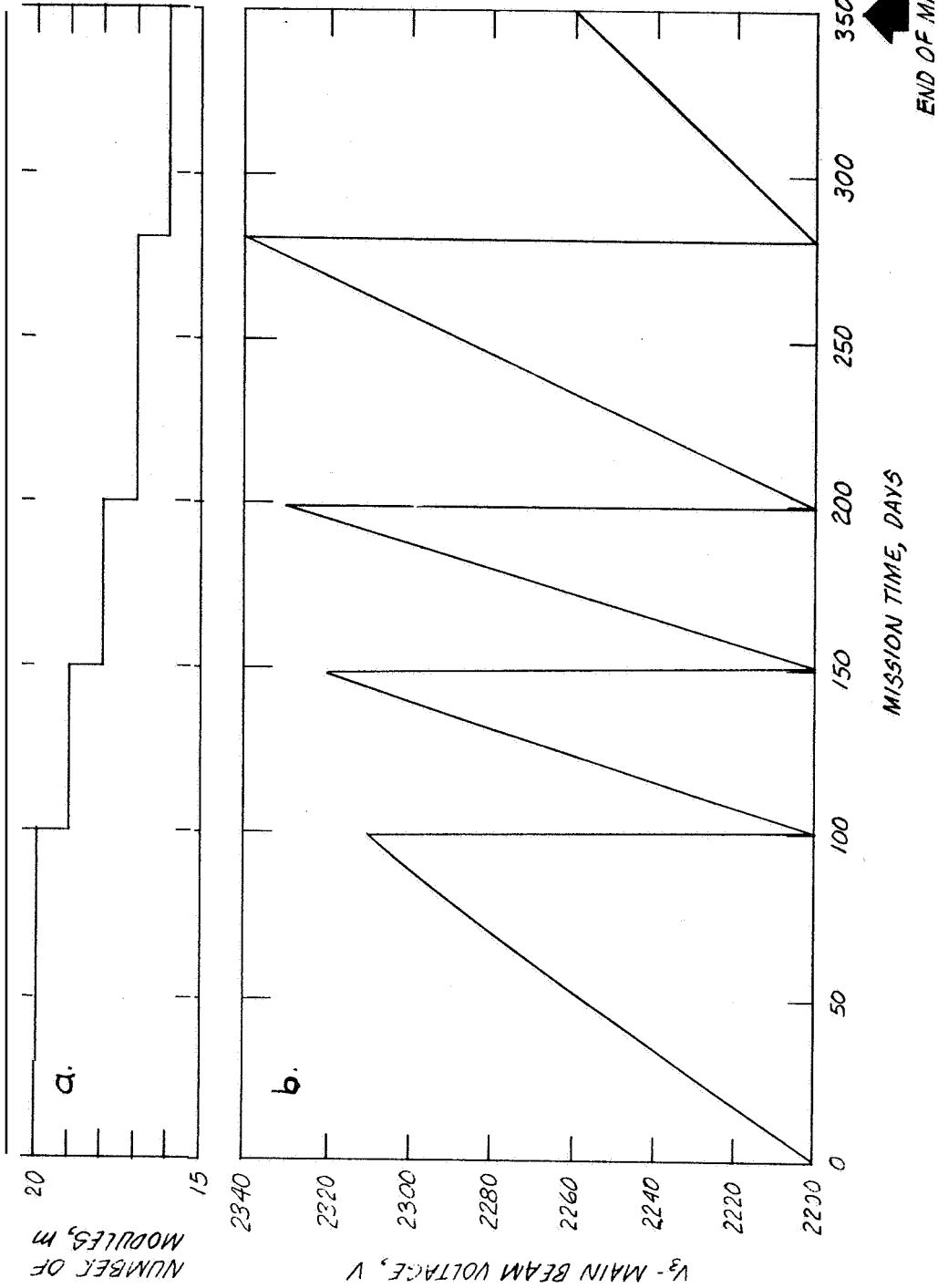


Fig. B. 5-14. Switching sequence for beam supply modules.

where m_o is the initial number of modules operating and t_k is the switching time for the last module. For fixed m_o and k the percentage voltage regulation is constant. It should be noted, however, that for an ion engine load, the maximum ΔV may be more critical than the percentage regulation. To limit ΔV for a given value of V_3 , it is seen that a restriction is placed on the number of initial modules, m_o .

A study is made next of the dependence of beam voltage variation on the power rating of the inverter modules and the total beam supply power.

As seen above, the maximum beam voltage deviation, ΔV , depends on the number of initial modules m_o . But m_o is just the ratio of the beam power to inverter module power (P_3/P_2). In Fig. B. 5-15, a family of curves is given showing the maximum variation in beam voltage with beam power for inverter modules rated at 100, 150 and 200 watts.

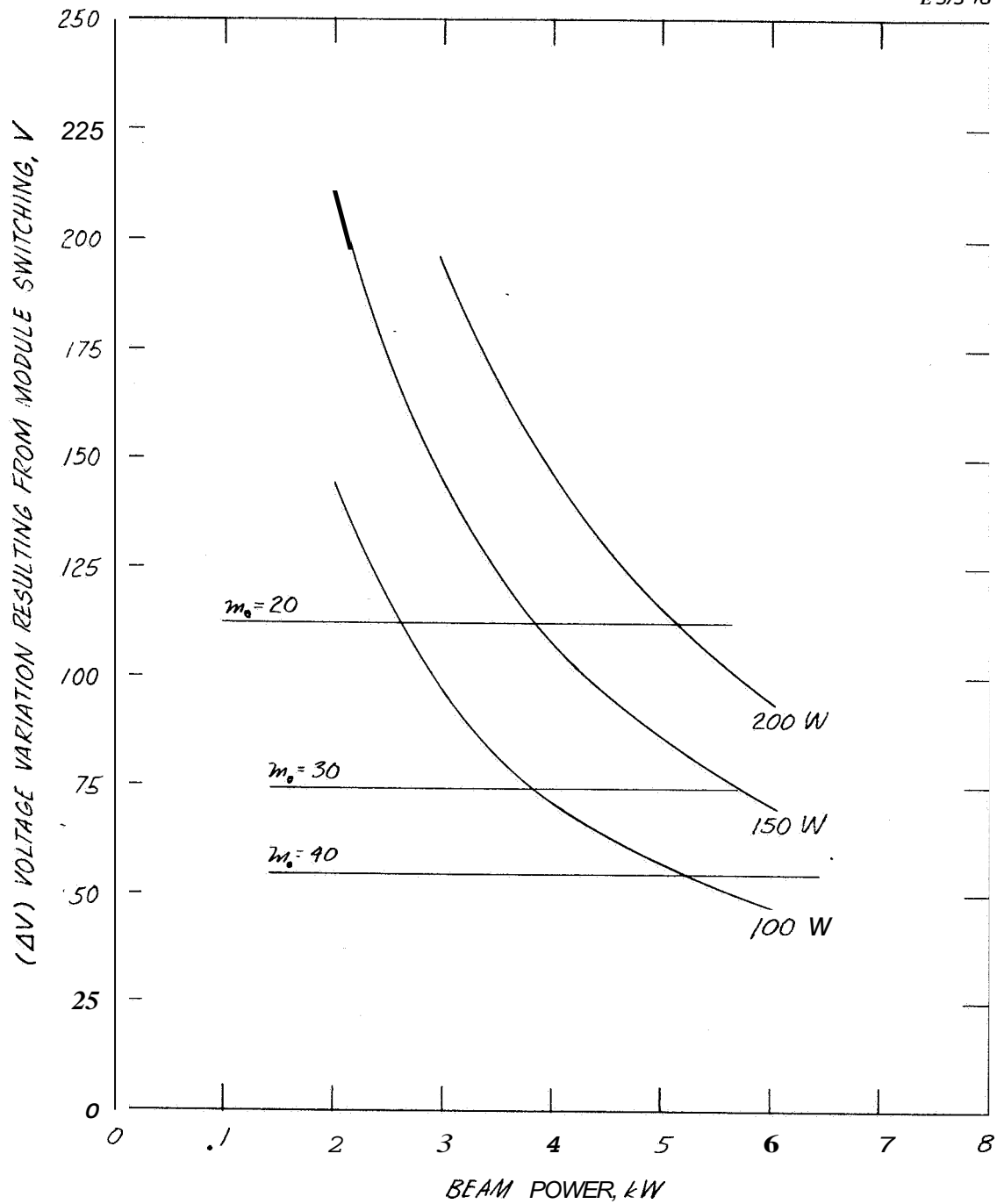


Fig. B. 5-15. Dependence of maximum beamvoltage variation on total beam power and module power rating.

6. Design Verification Hardware

A 20-cm diameter thruster has been designed and operated to verify the thruster performance characteristics used in the study program. At the inception of the program, state-of-the-art performance was determined as

- 1) power and propellant efficiencies attained by Reader (Ref. 1) with a cross-feed 20-cm thruster using a thermionic cathode
- 2) ion-optical performance attained at HRL with countersunk-screen optics at optimum spacing (Ref. 2 and 3)
- 3) LeRC brush cathode then under life test
- 4) a flash evaporator feed system.

It was calculated that a design based on the above would produce a 1 to 1.5 kW beam at 4000 to 5000 sec effective specific impulse with a power to thrust ratio of approximately 140 kW/lb and meet the requirements of weight and electrode lifetime. Assuming the design to be sufficiently close to those under life test at LeRC, the cathode life projections would be applicable here.

The actual results obtained during this test program have exceeded the performance specifications and indicate this thruster to be equal to or better than others reported in the current literature. Specific accomplishments are:

- 1) source energy per ion
in the discharge < 350 eV/ion
in discharge & cathode heater < 425 eV/ion
- 2) beam current > 1 A at $I_{sp} \approx 4000$ sec
- 3) operation at accel-decel ratios as high as 6
- 4) demonstration of a propellant-limited operational mode which reduces design requirements on the vapor flowmeter
- 5) demonstration of good performance characteristics for the "flower cathode" in this thruster. Currents up to 10 A were drawn (from a nominal 5A design) from a cathode that had been run, exposed to air, then run again.

These data have been obtained using a "flower-type" oxide cathode developed at HRL during the contract period. The first of these cathodes has undergone a 700-hour life test with no observable deterioration in performance.

Outstanding progress has been made with the liquid-mercury cathode (Ref 4) at HRL during this same period under a program supported by LeRC*. At the time the above state-of-the-art mercury thruster was proposed, the liquid-mercury cathode had demonstrated equal efficiencies but was subject to an instability problem at high power levels. This problem has since been traced to the thermal design and rectified, thus making the liquid-mercury cathode a very competitive device for this application. Typical near-optimum operating parameters for a present state-of-art 20-cm diameter thruster with liquid-mercury cathode are::

- 1) source energy per ion ≈ 650 eV/ion
- 2) mass utilization $> 80\%$
- 3) beam current ≈ 700 mA
- 4) mass utilization $> 95\%$ at ≈ 800 eV/ion.

A thruster life test with this cathode has passed the 400-hour point as this report is written, while the cathode itself has now been operated for more than 700 hours without any indication of performance deterioration. Also, inspection of the nozzle cone has shown no trace of erosion, making a life prediction of $> 10,000$ hours for this cathode appear very safe.

a. Oxide-Cathode Thruster
Thruster Design

The thruster design (Figs, B6-1 & 2) was based on results obtained by Reader (Ref. 1) who has investigated various propellant injection modes. In the design used here, propellant was introduced through a narrow annular channel at the downstream end of the anode and directed toward the cathode in a reverse or counterflow direction. The length of the channel was optimized, leading to a source energy per ion approximately 20% below the cross-feed geometry used by Reader (Ref. 1), as will be seen below,

Since this **was** an experimental design, mechanical flexibility was not compromised at the expense of minimum weight. This thruster weighs 15 lbs. but could be reduced to approximately 50% of this weight if desired in a future design,

Ion Optics

For expediency the mechanical design of the ion-optical system was not changed from the LeRC thruster supplied under contract NAS 3-6262. The screen apertures, however, were countersunk from the plasma side to provide

* Contract NAS 3-6262

M 4027

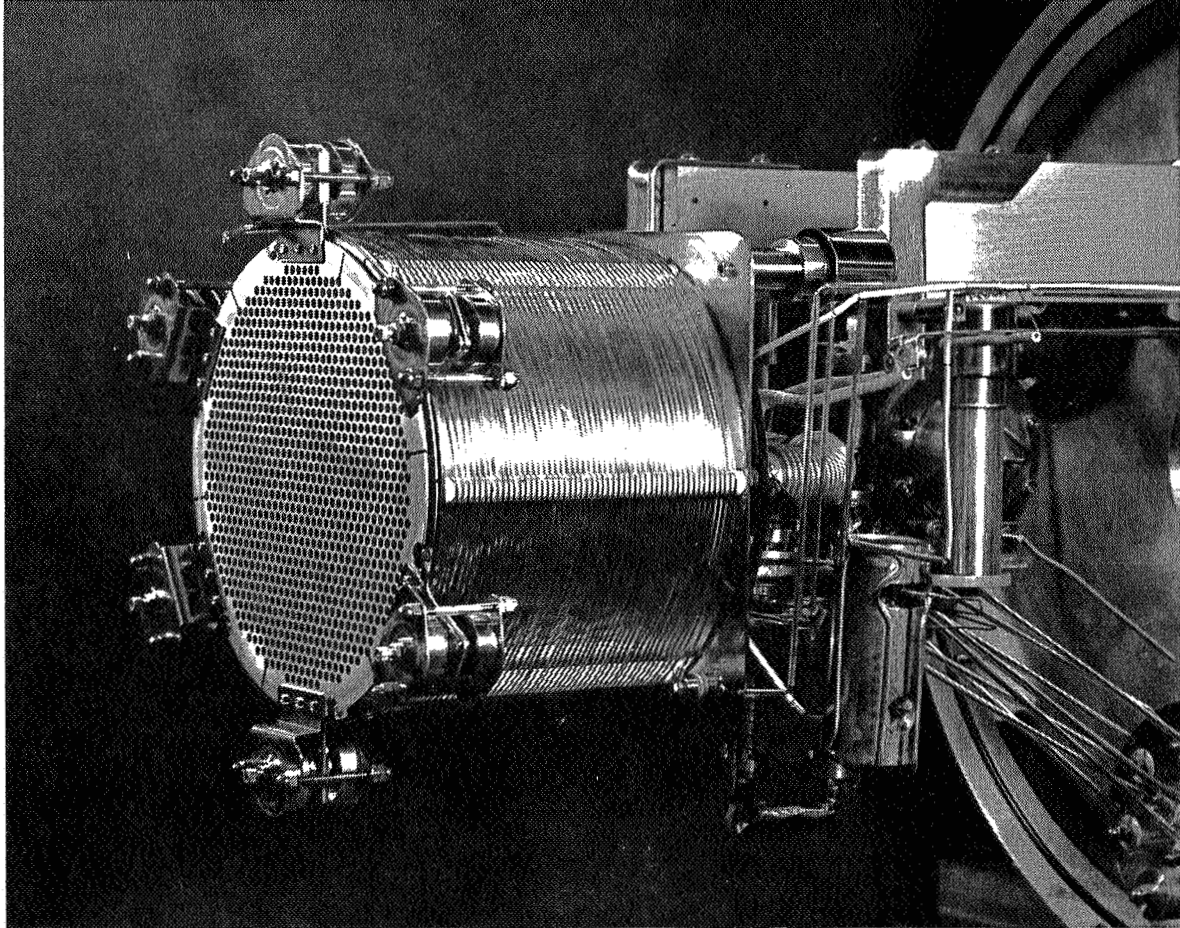


Fig. B. 6-1. Photograph of 20 cm thruster used for performance testing.

M 4028

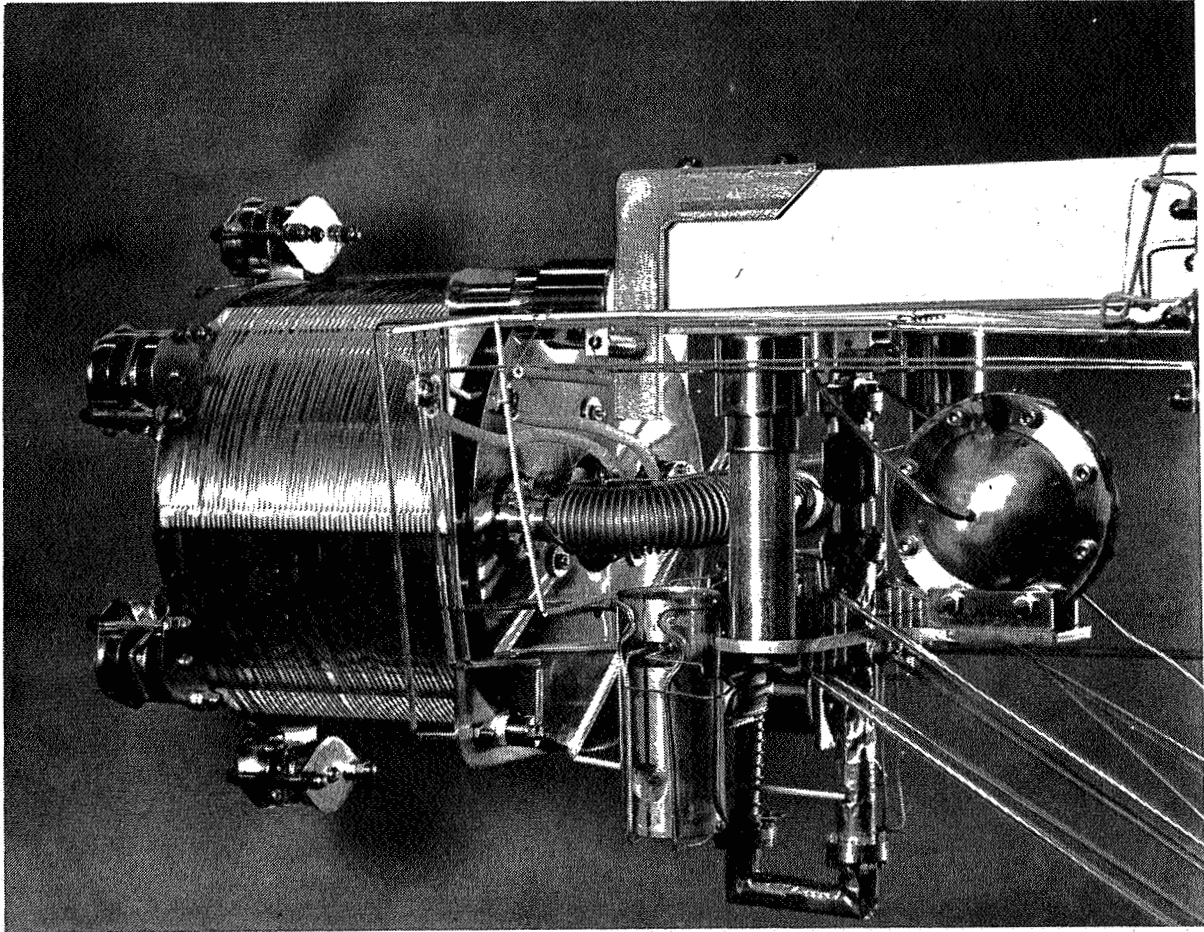


Fig. B. 6-2. Photograph of 20 cm thruster used for performance testing.

perveance-density matching to the plasma (Ref. 3), and the interelectrode spacing was reduced to increase the perveance.

The calculated perveance of the array is

$$P = 6.05 \times 10^{-6} \text{ perv,}$$

$$\begin{aligned} \text{thus for } V_{\text{total}} &= 6 \text{ kV} \\ I_{\text{max}} &= (6.05 \times 10^{-6}) (6000)^{3/2} \text{ A} \\ &= 2.78 \text{ A} \end{aligned}$$

This is the current that could be carried if the plasma was uniform across the diameter of the discharge chamber. The maximum measured current at this voltage (see Table B.6-1) was 1.25 A, indicating that the average current density in the optical array is 0.45 times the peak current density, which presumably occurs at the center.

Extrapolating this ratio to the proposed 35-cm diameter thruster operating at 2A beam current, the maximum current density expected through the central aperture is 9 mA/cm². This value is consistent with projected electrode lifetimes of greater than 10⁴ hours at mass utilizations of 90%.

Oxide Cathode

The oxide coated cathode is low in temperature, efficient in terms of watts per ampere, and simple in construction. Past achievements show that neither self-poisoning nor heater failure need be serious problems and that, given a sufficient supply of Ba, BaO, the cathode life can be very long indeed. Ordinarily, Ba, BaO is consumed through evaporation. In ion thrusters, sputtering removes the coating at a much faster rate. During a 334 hour run, one of Kerlake's (Ref. 5) cathodes lost 1.7 x 10⁻² g/cm² of oxide. With a monolayer density of 4 x 10¹⁴ atoms/cm², this constitutes a removal rate of one monolayer every 4 sec. From the ion current density at the cathode surface, which is estimated to be 5 mA/cm², the sputtering rate can be determined to be 3 x 10⁻³ atoms/ion. This is quite high in comparison with that of metals (10⁻⁵ to 10⁻⁴ atoms/ion). This high rate is in approximate agreement with the sputtering rate of barium on tungsten, obtained by Ptushinskii (Ref. 6). During a lifetime of 10,000 hours, therefore, one may expect sputter losses of the order of 0.5 g/cm² (this corresponds to a layer of 0.5 cm thickness).

Unfortunately, oxide layers cannot be made arbitrarily thick. The current flow through the oxide heats the layer, arcs occur, and the surface begins to flake,

Beck (Ref. 7) and Pike (Ref. 8) have studied this Joule heating and have derived the following heat balance relation:

$$P_H + J^2 R \cong CT^4 + J \left(\phi + \frac{2kT}{e} \right)$$

where

P_H \equiv heater power transmitted through coating

$J^2 R$ \equiv Joule heating of coating

CT^4 \equiv heat radiation

$J \left(\phi + \frac{2kT}{e} \right)$ \equiv heat removed by emitted electrons.

Since J varies exponentially with T , the term CT^4 can be considered constant under constant heater power. Thus it is obvious that the above equation can be balanced only when

$$J \leq \frac{1}{R} \left(\phi + \frac{2kT}{e} \right) \cong \frac{\phi}{R}$$

The coating resistance R per unit area can be expressed in terms of a volume resistivity ρ and the coating thickness t

$$R = \rho t$$

Experience shows that at 1100°K, the resistivity of oxide coatings is typically of the order of 100 Ω -cm. Thus, for an emission current density of the order of 0.5 A/cm² the maximum tolerable coating thickness

$$t_{\max} = \frac{\phi}{\rho J}$$

becomes approximately 2×10^{-2} cm. This is much too small for a lifetime of 10,000 hours under ion bombardment.

Figure **B.6-3** shows the oxide cathode configuration which we call the "flower" cathode where large Ba, BaO storage is combined with a sufficiently thin coating. The basic idea behind this design is that, regardless of how large the actual cathode surface, the total number of energetic ions impacting on the cathode is determined by the front area of the cathode facing the plasma. This is expected to be true because most of the ion generation is distributed throughout the whole volume of the discharge chamber. In other words, the relative number

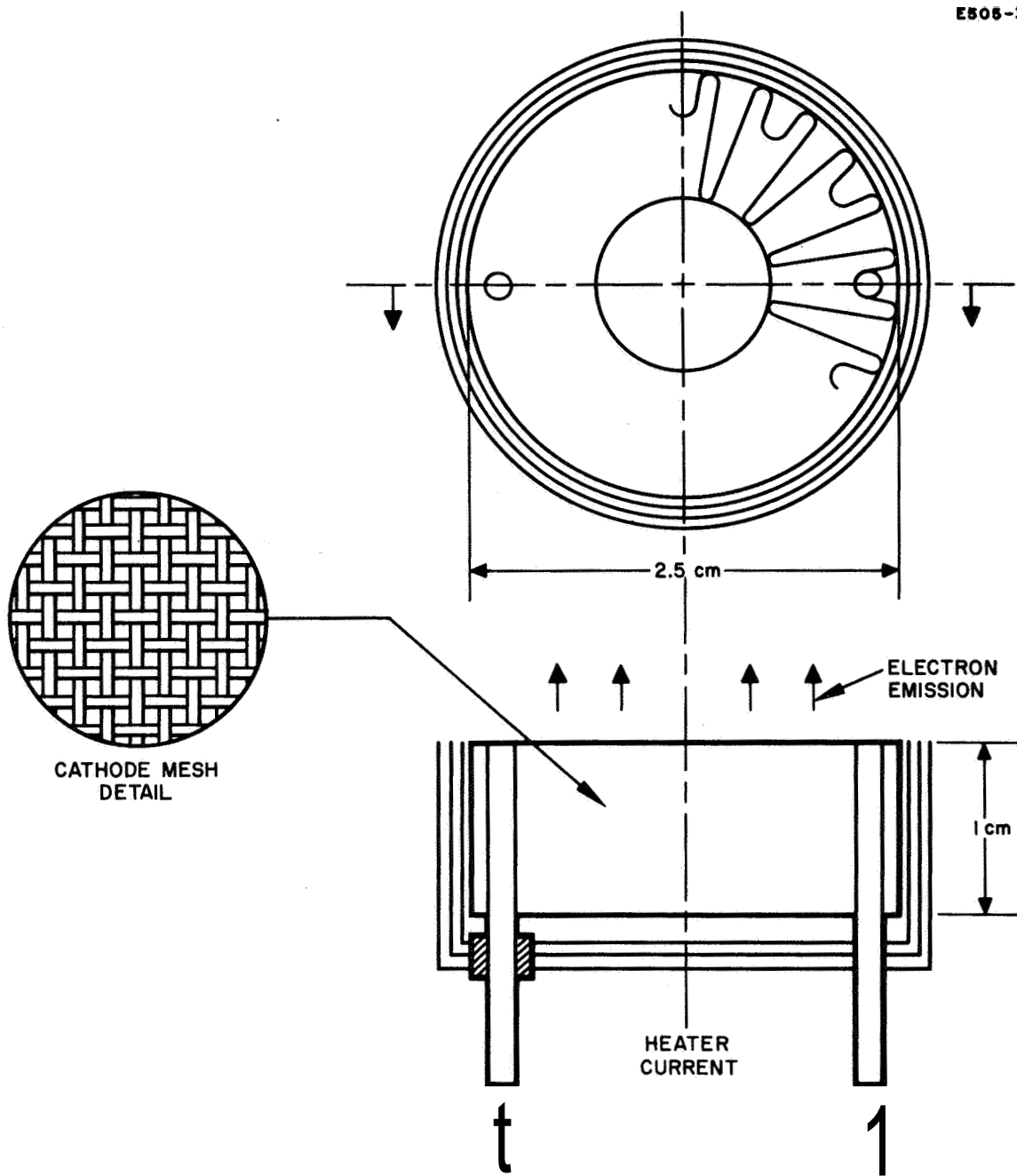


Fig. B. 6-3. Flower shaped oxide cathode design.

of ions generated in the immediate vicinity of the cathode is relatively small. In a folded geometry of the type shown in Fig. B.6-3, the density of the plasma inside the folds is expected to adjust itself to the rate of ion arrival available from the main plasma volume; it will therefore be lower in the immediate vicinity of the cathode surface within the folds than in the rest of the discharge chamber. As a consequence, the ratio of the ion current density bombarding the cathode surface to the ion current density available in the discharge chamber at the frontal area of the cathode is expected to be of the order of the ratio of frontal cathode area to total cathode surface area. With a ratio of 10:1, which is quite practical, the oxide cathode coating thickness required for 10,000 hour life can therefore be reduced from the 0.5 cm value calculated above, to a value of 0.05 cm. Because of the additional storage available between the individual wires of the cathode mesh, the thickness can be reduced by another factor of two, so that the ultimate thickness becomes 2.5×10^{-2} cm. This is quite satisfactory from a point of view of Joule heating, particularly since the average electron current density is also low because of the large total surface area. Finally, in a folded geometry of the type shown in Fig. B.6-3, a large fraction of the sputtered active material is not lost but is redeposited on the useful cathode surface. The above life estimate of 10,000 hours may therefore be quite conservative.

Success with this design is critically dependent upon whether or not the plasma penetrates the individual cathode spaces. Sufficient electron emission will be obtained only if the plasma sheath follows the individual cathode surfaces. Qualitatively, one may argue that this occurs when the distance between neighboring folds is considerably larger than the plasma sheath width. The plasma sheath width may be estimated to be equal to the Debye length. The latter is (in cgs units)

$$\lambda_D = \left[\frac{kT}{2 \pi n e^2} \right]^{1/2}$$

where

kT \equiv thermal energy of ions

n \equiv plasma density

e \equiv electron charge.

With a plasma density of 5×10^{11} particles/cm³ and a thermal ion energy equal

to 30 eV, the Debye length is approximately 10^{-2} cm. As shown in Fig. B.6-3, the separation between cathode folds is of the order of 2×10^{-1} cm so that the plasma should be able to penetrate these folds easily.

The cathode shown in Fig. B.6-3 has a total emitting area of 100 cm^2 and a frontal area of 6 cm^2 . Assuming operation at 5 A, the average emission current density would be approximately 0.05 A/cm^2 .

All tests reported here use this cathode configuration. Excellent performance has been obtained and no "hot spot" formation has been observed, in contrast to observations with thickly coated oxide cathodes. A photograph of a flower cathode in the thruster is shown in Fig. B.6-4.

A cathode life test has been conducted to demonstrate the long term capabilities of this cathode design. The cathode shown here was scaled down by a factor of four and installed in a 10-cm diameter thruster. The test lasted 700 hours approximately 20% with beam extraction, Extraction time has been limited because automatic restart circuitry was not available at the beginning of the test to accommodate high voltage overloads. The test was terminated by accidental exposure of the cathode to line voltage which destroyed the unit.

The performance during the life test is summarized in Fig. B.6-5. The slow change in heater power required at the onset of the test is attributed to thermal emissivity changes on the cathode surface (blackening) due to pump oil contamination and to variations in discharge current. This effect has been observed on other cathodes in this test facility before, The significant fact is that once stabilized, the heater power shows no sharp upward trends.

Feed System for Oxide-Cathode Thruster

The feed system consists of a pressurized reservoir which feeds liquid mercury through a shutoff valve to a vaporizer. The rate of vaporization is controlled by the temperature of the unit and is, to first order, independent of the driving pressure up to some limiting pressure. The vapor flow is monitored by a flowmeter and conducted to the thruster through an isolator which electrically isolates the thruster from the feed system.

With the exception of the valve and flowmeter all components of the feed system have been designed and tested at JPL (Ref. 9). One set of components was delivered to HRL in early June for inclusion in the prototype feed system.

The valve used is that developed for use in the SERT I flight test. It is

M 4031

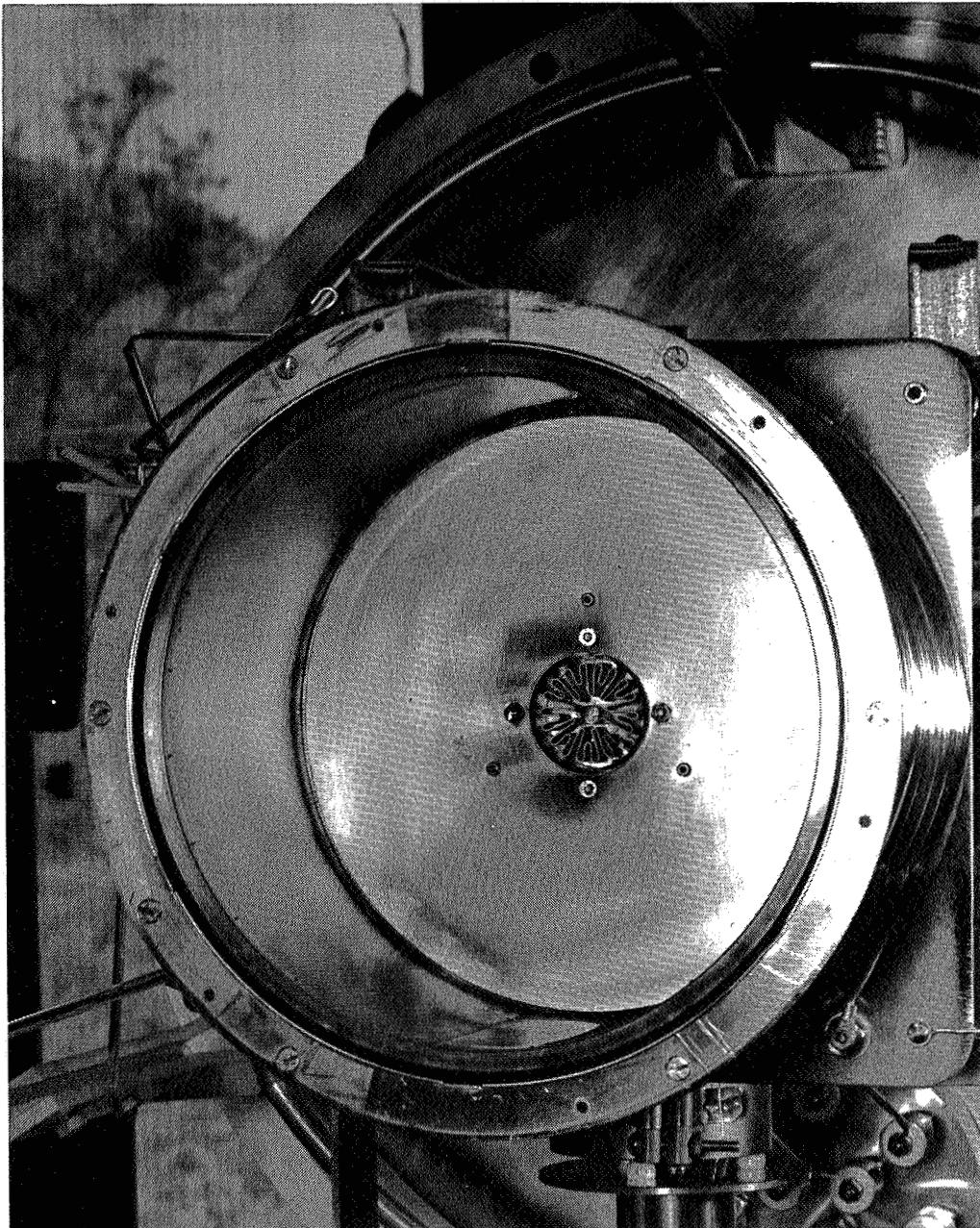


Fig. B. 6-4. Flower cathode in discharge chamber.

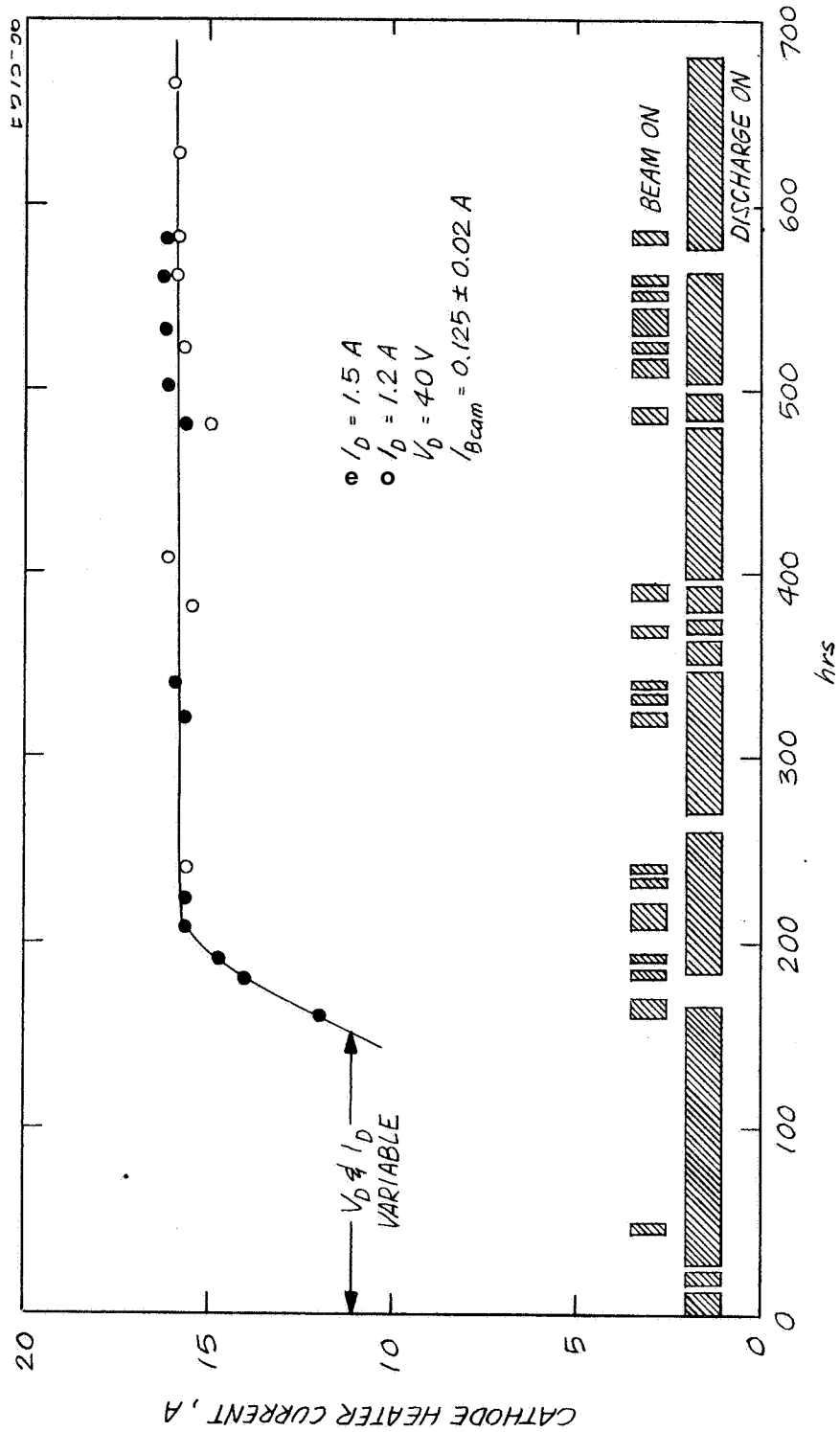


Fig. B.6-5. Flower cathode heater current during life test in 10 cm thruster.

compatible with mercury and has passed flight qualification tests. Operating power is approximately 1 watt,

The flowmeter is basically a pressure sensor followed by a calibrated orifice. The pressure sensor used here is based upon the Townsend mode of discharge, which is obtained by limiting the discharge current in a cold-cathode discharge to less than approximately 10^{-6} A by means of series resistors. At this current level, the electric field between cathode and anode is identical to the vacuum field, since the space charge is not yet significant. As a result, the breakdown potential is identical to the operating potential and is a function of pressure. Figure B.6-6 shows a Paschen curve for mercury; it can be seen that the breakdown potential varies linearly with pressure (for constant distance, d) over a wide pressure range. The linearly rising branch begins at $pd \cong 2$ Torr cm. Under all flow conditions, therefore, operation should be restricted to pd values above this limit. With a discharge gap 10-cm long and a required flow rate range of 10:1, the pressure varies between 0.2 and 2 Torr above the flow restriction. A typical calibration curve is shown in Fig. B.6-7

The feed system was assembled and tested at HRL. It was found that the vaporizer would not hold back the required mercury head, probably due to leakage past the internal welds. A HRL-designed vaporizer was substituted to expedite testing and proved satisfactory. Two runs were performed with the complete thruster-feed system assembly (see following section). A photograph of the assembled system is shown in Fig. B.6-8.

Thruster Test Results

Three test runs were conducted. The first lasted 25 hours and was primarily designed to establish the propellant efficiency, power efficiency and stability of the thruster at the design point of 500 mA beam current. During this run the mercury reservoir temperature was maintained constant to one degree centigrade so that the average flow rate could be accurately established by a weight loss measurement,

The second run lasted approximately six hours and was designed to investigate the maximum power handling capabilities of the thruster and its stability at up to twice the design beam current. During the course of the two runs a number of other parametric studies were also conducted.

The third run was to determine the feed system performance in con-

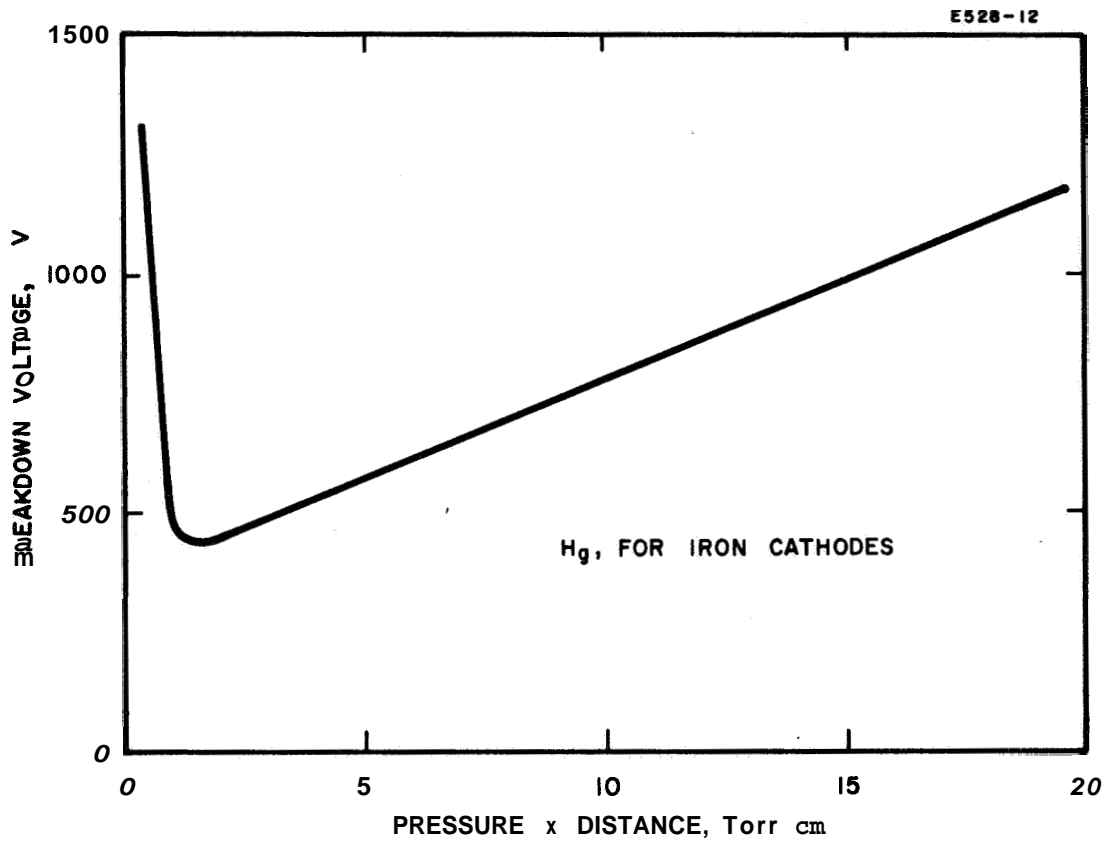


Fig. B. 6-6. Paschen characteristics for mercury.

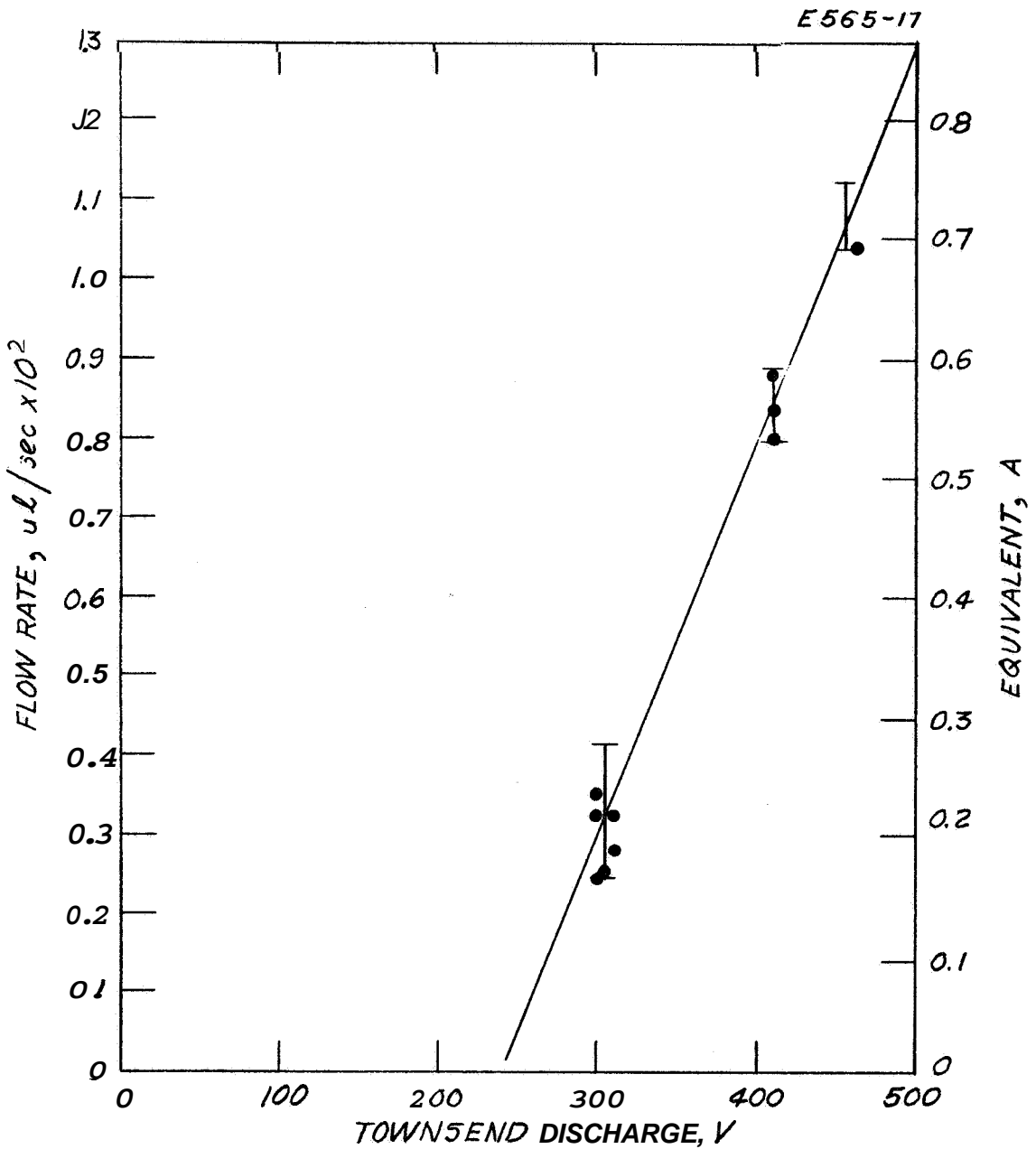


Fig. B. 6-7. Flowmeter calibration.

M 4107

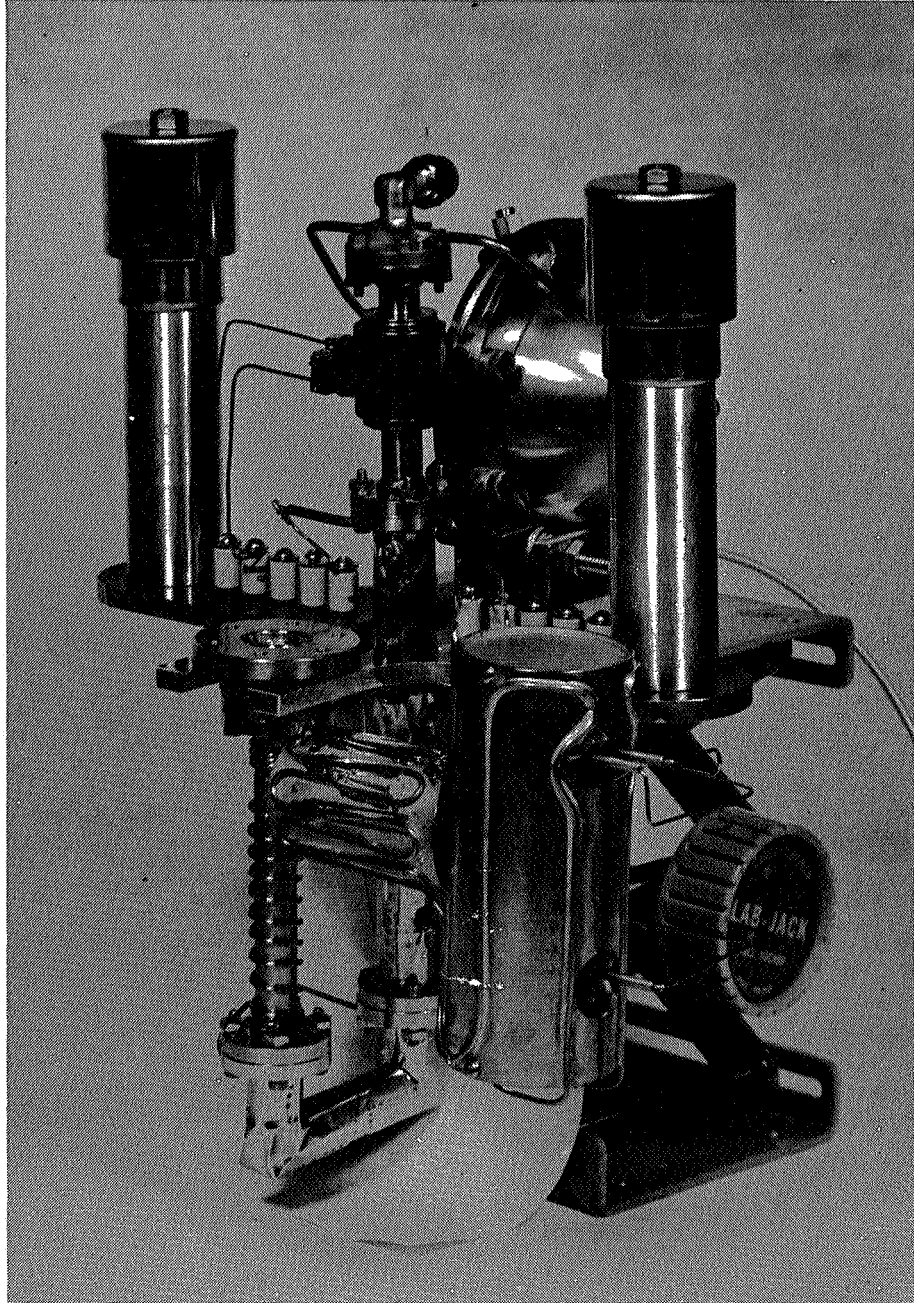


Fig. B. 6-8. Assembled feed system.

junction with the thruster. It was established that the beam current could be controlled by the vaporizer temperature but that the time constant was very long due to the change of vaporizer design. The feedback loop between beam current and vaporizer heater was closed and found to perform adequately. The components were, however, too delicate to withstand high voltage arcing. A more rugged system is presently being constructed.

25 Hour Data Point

The operating point held during the 25-hour period is given as data point one in Table B.6-I. Data point two is a comparable point acquired during the second run. The important factors are:

The design current of 500 mA was easily attainable at the desired I_{sp} of 4000 seconds.

Only 385 eV/ion were expended in the arc. This is 25% lower than that quoted by Reader (Ref, 1) for a cross-feed thruster operating at 2.5 kV beam voltage with $\eta_m = 80\%$. This gives a P/T of 135 kW/lb at $I_{sp} = 4000$ seconds.

The thruster operated stably and reproducibly at this point, on one occasion going for more than 2 hours without arc-out.

The cathode heating power corresponded to < 200 eV/ion; data point 2 shows that it could be brought below 150 eV/ion.

The propellant flow rate was established by first operating the reservoir at several fixed temperature points in an auxiliary vacuum station to determine the rate of change of mercury vapor flow with temperature ($\approx 3.5\%$ per $^{\circ}\text{C}$) then obtaining one absolute point for the complete feed system by weighing the reservoir before and after the 25-hour run. The correction required reduced the propellant efficiency to less than the 90% calculated from the pre-calibration.

High Current Operation

Data points 2 through 8 of Table I indicate thruster performance as the beam current was raised. The thruster handled 1 A of beam current very well at an accel-decel ratio of three with no neutralizer an. Approximately 2-1/2 hours of time were accumulated at beam currents greater than 900 mA. The test was voluntarily terminated with a 10 minute run at 1.25 A as the power rating of the surge resistors was being exceeded by a factor of four, the arc current

meter was off scale and the cathode rating was being exceeded by a factor of two.

Propellant efficiency measurements are not quoted at the higher ranges because the linearity of the feed system calibration has not been demonstrated above 800 mA. The temperature readings taken during the run indicate that if the calibration could be extrapolated to 1.00 A, the propellant efficiency would rise as the beam current rises to approach 100%.

The source energy per ion expended in the arc remains consistently low up to the highest recorded beam current with values as low as 310 eV/ion being recorded. Power to thrust ratios of 125 kW/lb at specific impulses in the 4000 to 5000 sec range at input power of 2.5 kW make this a very useful module for the missions presently under consideration.

TABLE B.6-I

20-cm Thrustor Operating Points with HRL Oxide Cathode

Data Point	1	2	3	4	5	6	7	8
'Beam (kV)	2.5	2.5	3.2	2.0	2.0	1.6	2.0	2.0
V _{Accel} (kV)	3.0	3.0	3.1	4.0	4.0	4.0	4.0	4.0
'Beam (mA)	520	511	744	930	1000	1000	1000	1250
'Accel (mA)	3.3	2.0	3.3	4.9	4.9	4.8	6.4	8.2
I _{Hg} ^o (mA)	630	595	810	-	-	-	-	-
'Disch (V)	40	40	50	50	50	50	50	50
'Anode (A)	5.0	5.5	7.6	6.0	6.2	6.5	8.7	10.2
'Heater (cath.) (V)	4.2	3.5	3.0	3.5	3.5	4.0	4.3	4.3
'Heater (cath.) (A)	24	21.5	19.0	22.0	22.0	24.0	25.0	25.0
B _{Screen} (G)	12	10	12	13	13	13	17	14
η _{mass} (%)	82.5	86	93	-	-	-	-	-
Source Energy/Ion (eV/Ion)								
a) Discharge only	385	430	444	322	310	325	438	410
b) Disch. + Cath. Heater †	585	578	500	405	387	421	543	495
I _{sp, eff} (sec)	4000	4300	5100	-	-	-	-	-
P/T ‡ (kW/lb)	135	135	145	130	121	105	126	126
Thrust (mlb)	12	12	18.6	18.6	20	20	20	25
P _{total} (kW)	1.6	1.6	2.7	2.4	2.5	2.1	2.6	3.2

*
$$\frac{'Disch \cdot 'Disch}{I_{Beam}}$$

†
$$\frac{I_{Disch} \cdot 'Disch + 'Heater \cdot 'Heater}{I_{Beam}}$$

‡ P/T & P_{total} do not include 100 W magnet power (which raises value by ≈ 8 kW/lb)

Performance of Ion Optical System

The first test was run with a screen to accelerator spacing of .125" and the second with .100". The closer spacing gave consistently lower accel current readings (see data points 1 and 2). The accel currents for increasing beam current are given in Table II (Tank pressure $\approx 5 \times 10^{-7}$ Torr).

TABLE B.6-II

Beam (mA)	I _{Accel} (mA)	Accel Interception (%)
350	0.8	0.23
430	1.8	0.42
500	2.0	0.40
650	2.9	0.45
930	5.9	0.63
1000	6.4	0.64
1250	8.2	0.66

The perveance was somewhat difficult to measure exactly because the interception currents rapidly exceeded the capabilities of the accel supply as the perveance was approached. Considering the voltage at which arc-out occurred to represent the practical perveance point, the perveance line shown in Fig. B.6-9 was obtained. This is comparable to the best data obtained with the 10-cm thrust and countersunk optics.

It was possible to operate the thruster at accel-decel ratios as high as 6 to 1. The collector current falls as the ratio is increased and the interception current remains constant up to a ratio of approximately four. Presumably direct interception occurs at this point. The maximum tolerable ratio may be a function of the position of the operating point with respect to the perveance line since an over-focussed beam should withstand the defocussing effect of a high accel-decel ratio better than one which is just on the perveance limit to begin with.

Discharge Chamber

Very efficient discharge chamber operation was observed. This is attributed to the unique reverse-feed mechanism of propellant introduction. It was established that with all other parameters constant the discharge current (hence the beam current) increased with increasing cathode temperature or

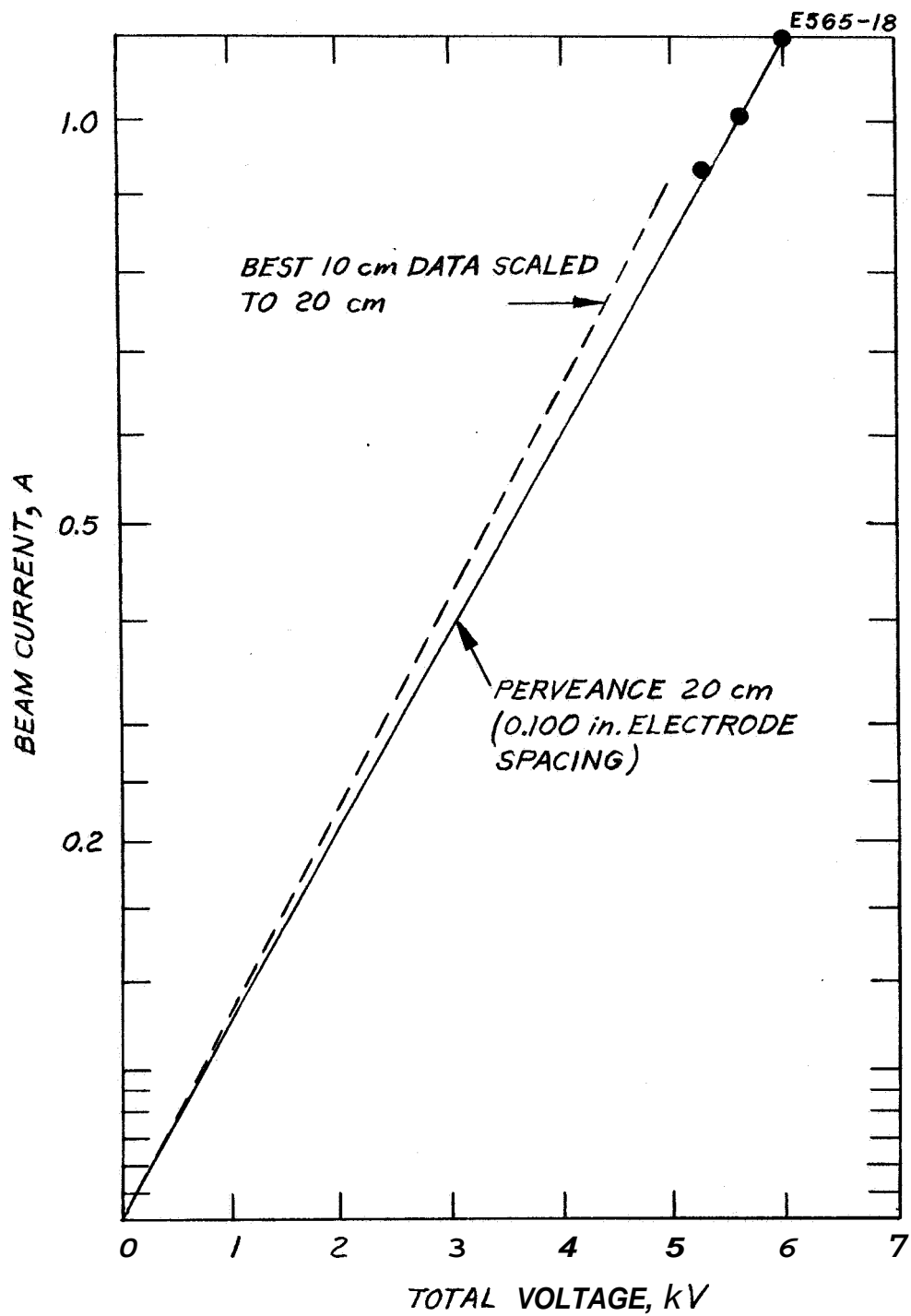


Fig. B. 6-9. Perveance of 20 cm diameter ion optical system.

discharge voltage and that a broad maximum existed with magnetic field strength. The variation with discharge voltage may be attributed to the change in ionization cross-section with voltage and the increasing proportion of Hg^{++} above 40 V.

Control

During the 25-hour run it was established that the thruster would operate in a propellant-limited mode. The six operating points shown in Fig. B.6-10 indicate a direct relationship of

$$I_{\text{Beam}} = .81 I_{\text{Hg}}^0$$

The feasibility of the feed system control loop was demonstrated with the laboratory feed system by sensing the beam current and feeding this signal back to a magnetic amplifier in the mercury reservoir heater. Stable operation was achieved. It was also established that the discharge current is a direct function of cathode temperature for constant propellant flow-rate (see Fig. B.6-11).

The application of these parametric studies to thruster control is discussed above.

b. Liquid-Mercury Cathode Thruster

The life of thermionic cathodes for mercury electron-bombardment thrusters can be made very long, as explained in Sec. 6-a, but it is inevitably limited by sputtering erosion.

The liquid-mercury cathode approach (Ref. 4), on the other hand, completely eliminates this problem by operating the discharge in an arc mode, using a surface of liquid mercury as the cathode, and by utilizing the removal of mercury atoms from this cathode by the discharge as the expellant feed mechanism. Since the mercury surface is continuously replaced, the lifetime expected from this cathode is not limited by sputtering of the electron-emitting material. To provide a gravity-independent equilibrium position for the liquid surface, the mercury is forced through a small orifice and held in position in a pool-keeping structure by surface tension forces and arc pressure. As an additional advantage,

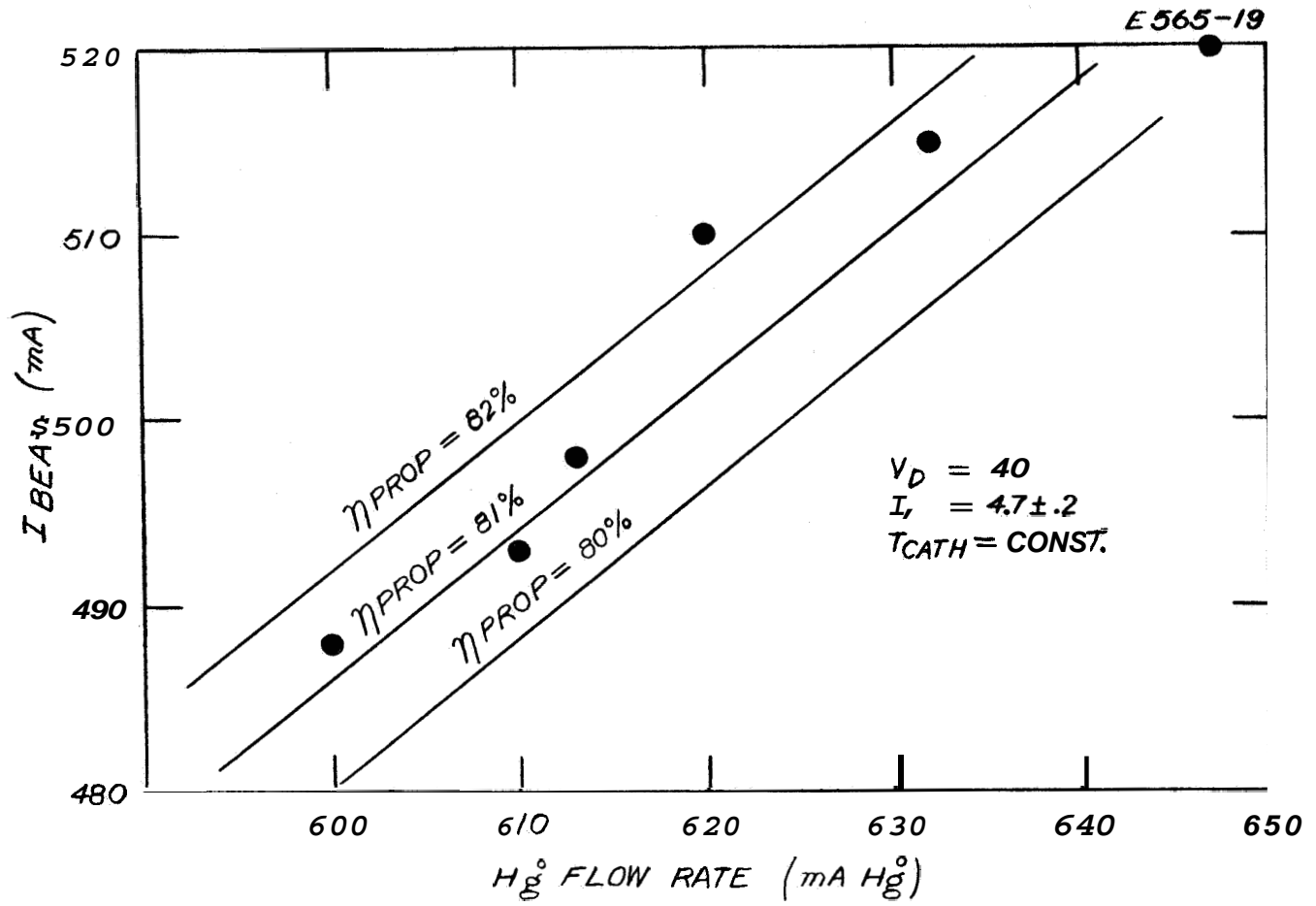


Fig. B. 6-10. Beam current versus neutral flow rate.

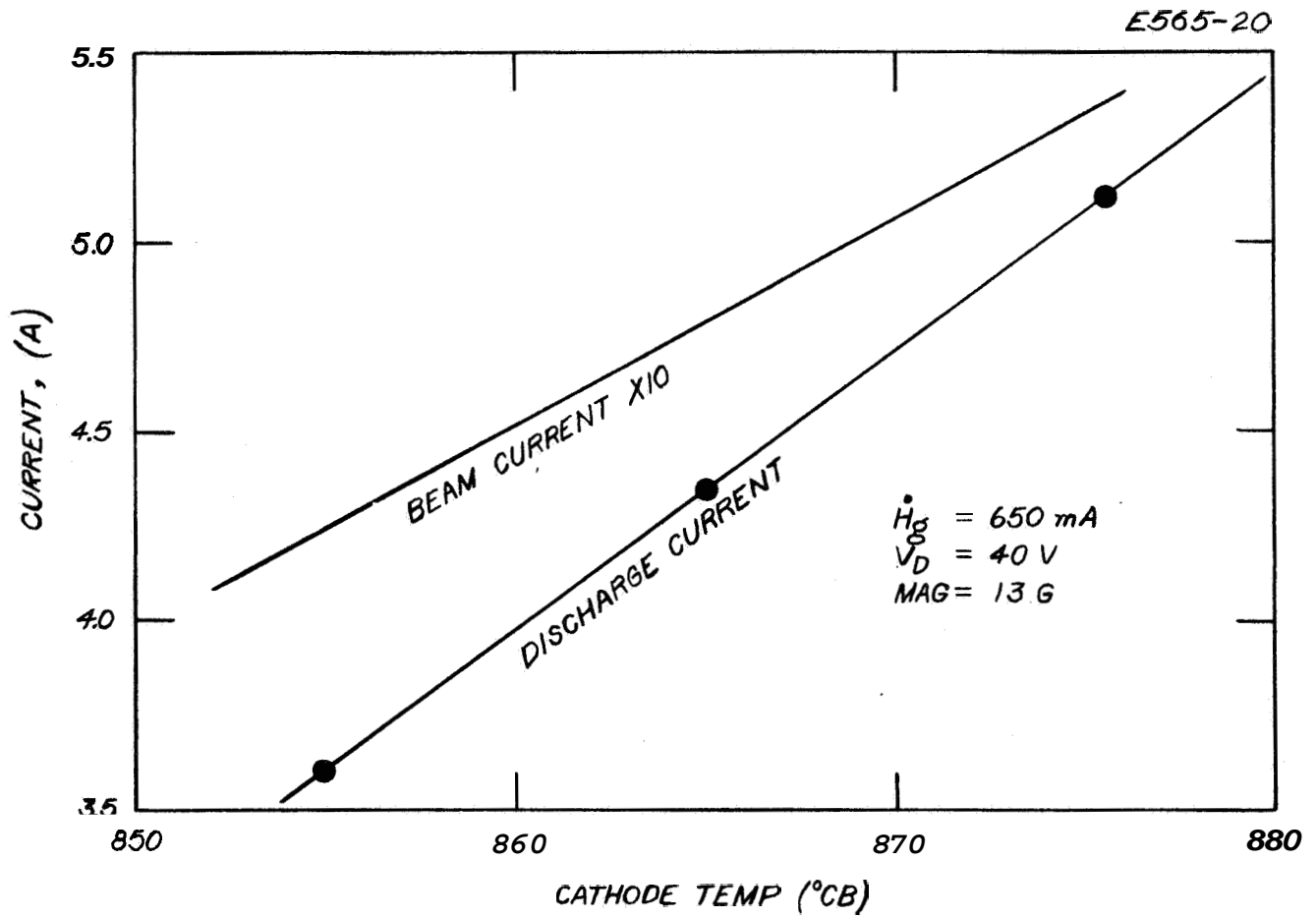


Fig. B.6-11. Discharge and beam current as function of cathode temperature.

no separation between liquid and vapor phases is required in the propellant feed system.

The bombarding ions cause a heat **flux** into the cathode which is proportional to the discharge current and which was measured to be of the order of 2 W/A. Unless efficiently removed, this small quantity of heat raises the local temperature adjacent to the arc spot sufficiently to cause excessive mercury evaporation into the discharge chamber. Continued improvement in the thermal design of the cathode has increased the maximum heat rejection temperature permissible at a prescribed mass utilization as well as the maximum current handling capability of a single cathode. It has been demonstrated that the cathode can be conduction cooled and the excess power radiated to space by the addition of no more than 1/2 kg of radiator mass per kilowatt of thruster power.

In addition to the development of optimized liquid-mercury cathodes, a continuing program is underway to increase the overall efficiency of the thruster. It has been established that performance is sensitive to both the magnitude and shape of the magnetic field as well as to the discharge chamber geometry. Improvements in field and chamber geometry have reduced the power-to-thrust ratio to 174 kW/lb at an effective specific impulse of 5700 sec ($\eta_{\text{mass}} = 81\%$) during recent months. The state-of-art trade-off between mass utilization and source energy per ion in the discharge is shown in Fig. B.6-12; further improvements are anticipated.

A 20-cm diameter thruster incorporating a water-cooled liquid-mercury cathode is presently undergoing life test. More than 400 hours of beam extraction (600 mA beam current) have been accumulated at the time of this writing, and the cathode itself has been operated for more than 700 hours, without any indication of performance deterioration. Also, visual inspection of the pool-keeping structure after this operating period has shown no trace of erosion, making a life prediction of > 10,000 hours for this cathode appear very safe.

The test point maintained during the first 150 hours of the thruster life test is given in Table B.6-III.

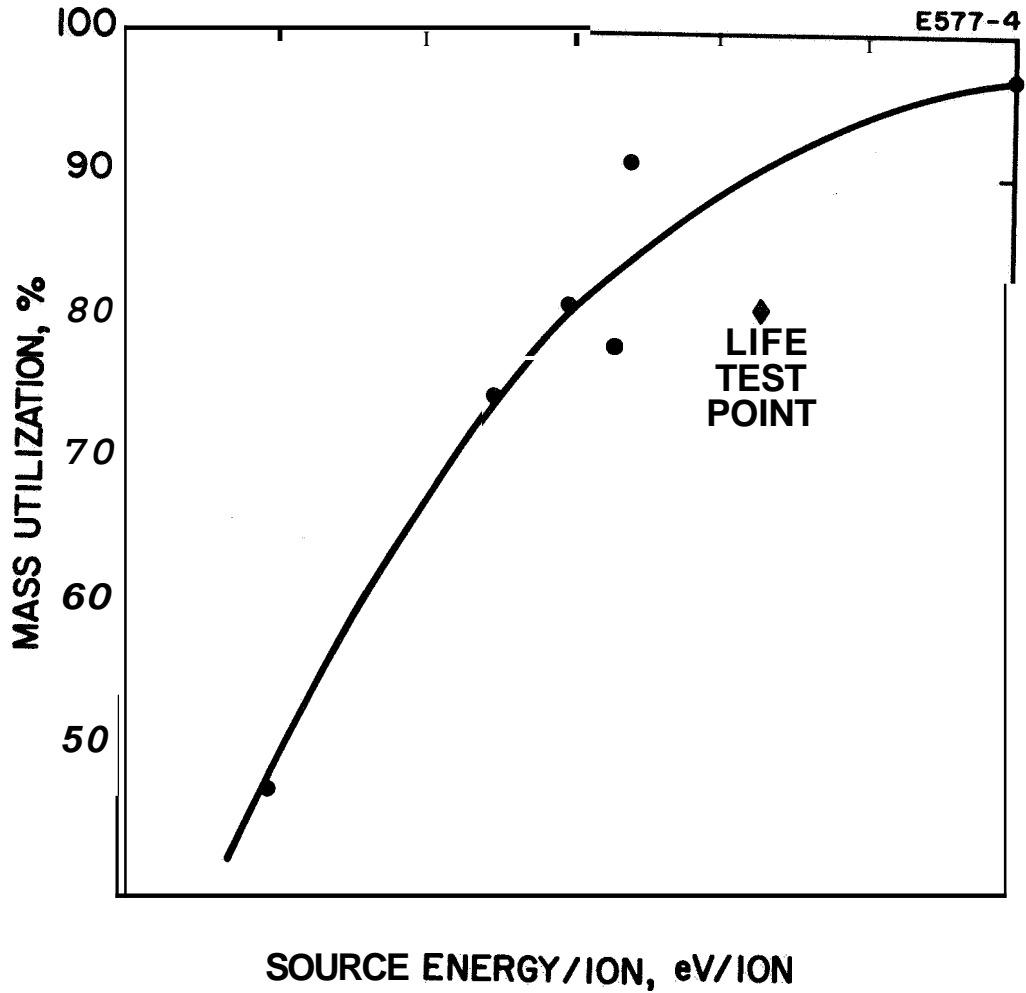


Fig. B. 6-12. Mass utilization versus source energy per ion for 20 cm diameter electron bombardment thruster with liquid mercury cathode.

TABLE B.6-III

20-cm Thrustor Performance with Liquid-Hg Cathode (150-hour average)

Beam Current	595 mA
Beam Voltage	6.2 kV
Accelerator Current	2.9 mA
Accelerator Voltage	2.0 kV
Discharge Current	13.7 A
Discharge Voltage	31.0 V
Magnetic Field (at Screen)	25 G
Cathode Heating Power	n. a.
Source Energy per Ion	$\frac{\text{Discharge Power}}{\text{Beam Current}}$ 714 eV/ion
Mass Utilization	81%
Power Efficiency [*]	90%
Total Thrustor Efficiency	73%
Effective Specific Impulse	6370 sec
Thrust	{ 96 mN { 21.4 mlb
Power/Thrust [*]	{ 43 kW/N { 192 kW/lb

* Excludes magnet power since electromagnets were used only as an experimental convenience.

REFERENCES

1. P. D. Reader, "Experimental Effects of Propellant Introduction Mode on Electron Bombardment Ion Rocket Performance", NASA TND-2587 Jan. 65
2. N. B. Kramer, HRL RR#324
3. H. J. King, Quarterly HRL Report #1, Contract NAS 3-6262
4. W. O. Eckhardt, J. A. Snyder, H. J. Kipg and R. C. Knechtli, "A New Cathode for Mercury Electron-Bombardment Thrustors", AIAA Paper #64-690
5. W. R. Kerslake, AIAA Paper #64-683.
6. Yu. G. Ptushinskii, Radio Eng. Electron (USSR) 2, (No. 12), 46 (1957)
7. A. H. W. Beck, ~~et al.~~, Proc. Inst. Elec. Eng. B106, 372 (1959)
8. H. A. Pike, MIT Lincoln Laboratory Technical Report 356 (1964)
9. T. Masek, JPL, private communication

C. SPACECRAFT SYSTEM DESIGN

All spacecraft conceptual designs considered during this study period are based on the design mission profile which assumes launch during the 1971 opportunity. The solar-electric propulsion spacecraft is boosted to escape velocity by a Saturn 1B/Centaur launch vehicle in a direct ascent, after which the solar array is deployed, the electric propulsion system activated, and the heliocentric transfer accomplished in a zero-coast rendezvous mode. Just prior to Mars approach, the electric propulsion system is jettisoned including the solar array (with the exception of the inboard panel in each quadrant) and the lander capsule ejected before firing the retro rockets to achieve a Mars orbit with a peri-apsis altitude of 4,000 KM and an apo-apsis altitude of 50,000 KM.

C.1 General Arrangement

Three spacecraft arrangements have been developed, all of which include the Boeing "Folding Modular Type" solar array (although the Boeing "Roll-Out" solar array concept will be considered at a later date). Each arrangement evolved from a series of iterations concerned with sub-system integration involving structural considerations, center of gravity constraints, stowed and deployed solar cell array configurations, variable thrust vector orientation, and shroud envelope considerations,

Major components considered in the arrangements presented include the following:

- (a) Lander capsule (1,000 lb. "Discoverer" type)
- (b) Ion propulsion system employing H, electron bombardment thruster units.

G. G. station of the spacecraft and a dual retro-rocket system is located at the forward end of the spacecraft just aft of the lander capsule.

Prime disadvantage of this arrangement is that the ion engine exhaust beam divergence half angle is limited to 5° if the spacecraft base structure is not to be violated. Even with this restriction, the main solar panel hinge length must be reduced in two places.

Of prime importance in all of the general arrangements under consideration is the amount of ion beam divergence. In Figures C.1-1 and C.1-3 are indicated the solar panel areas affected by beam divergence half angles of 15° and 30° for the deployable engine configurations. If (as is presently indicated) 99 percent of the exhaust ions are contained within a 30° half angle only about 1% of the solar panel area is affected. For the "body-fixed" engines configuration (Figure C.1-5), however, any divergence half angle greater than 5° wipes out part of the base structure, including solar panel base hinge lines. Consequently, it appears that spacecraft designs involving non-deployable engine arrays will restrict the thrust vector orientation variation which in turn may require a modification to the design mission profile. These factors are presently under detailed investigation.

A preliminary weight breakdown applicable to all the previous configuration is presented in Table C.1-I.

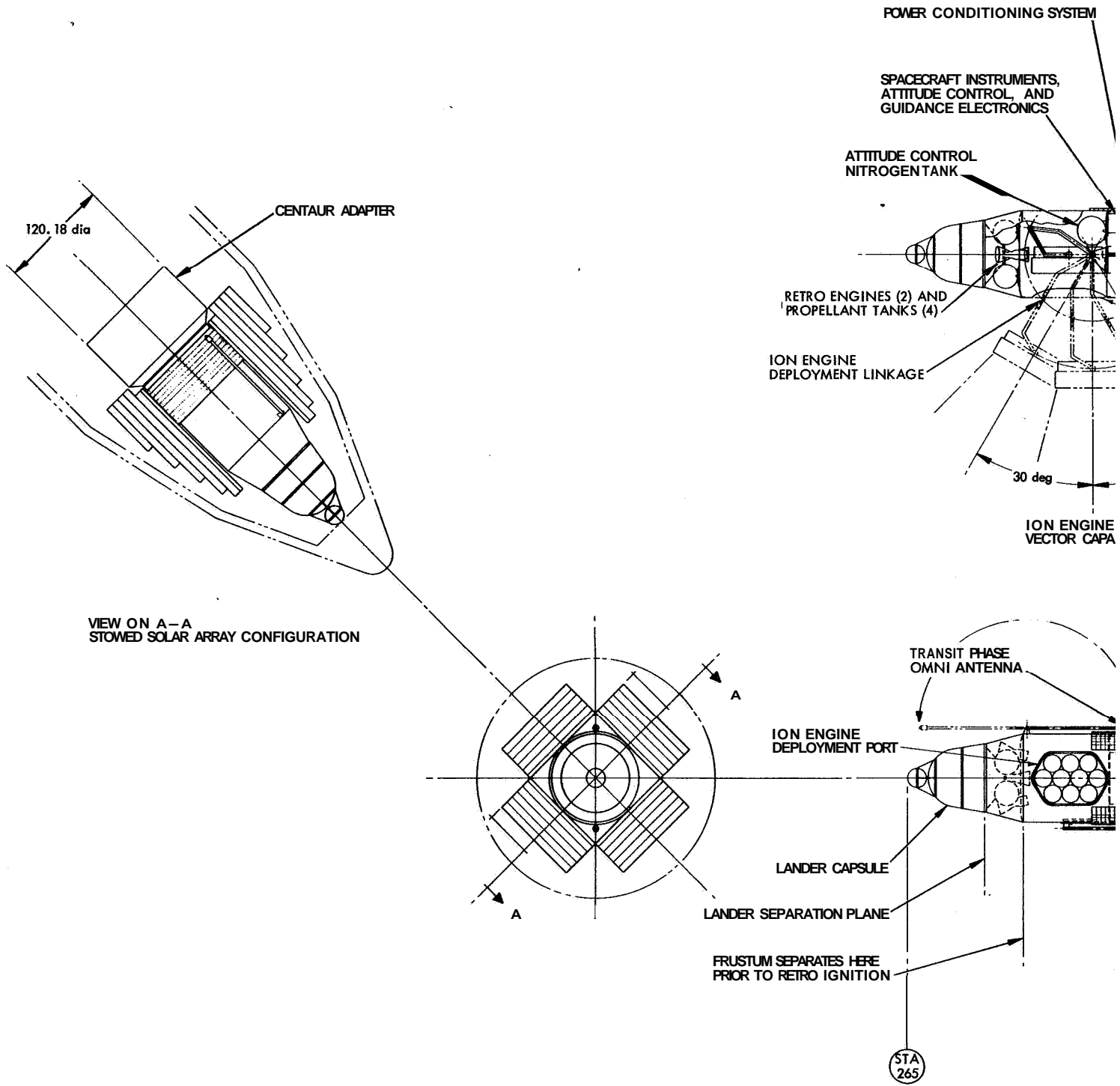
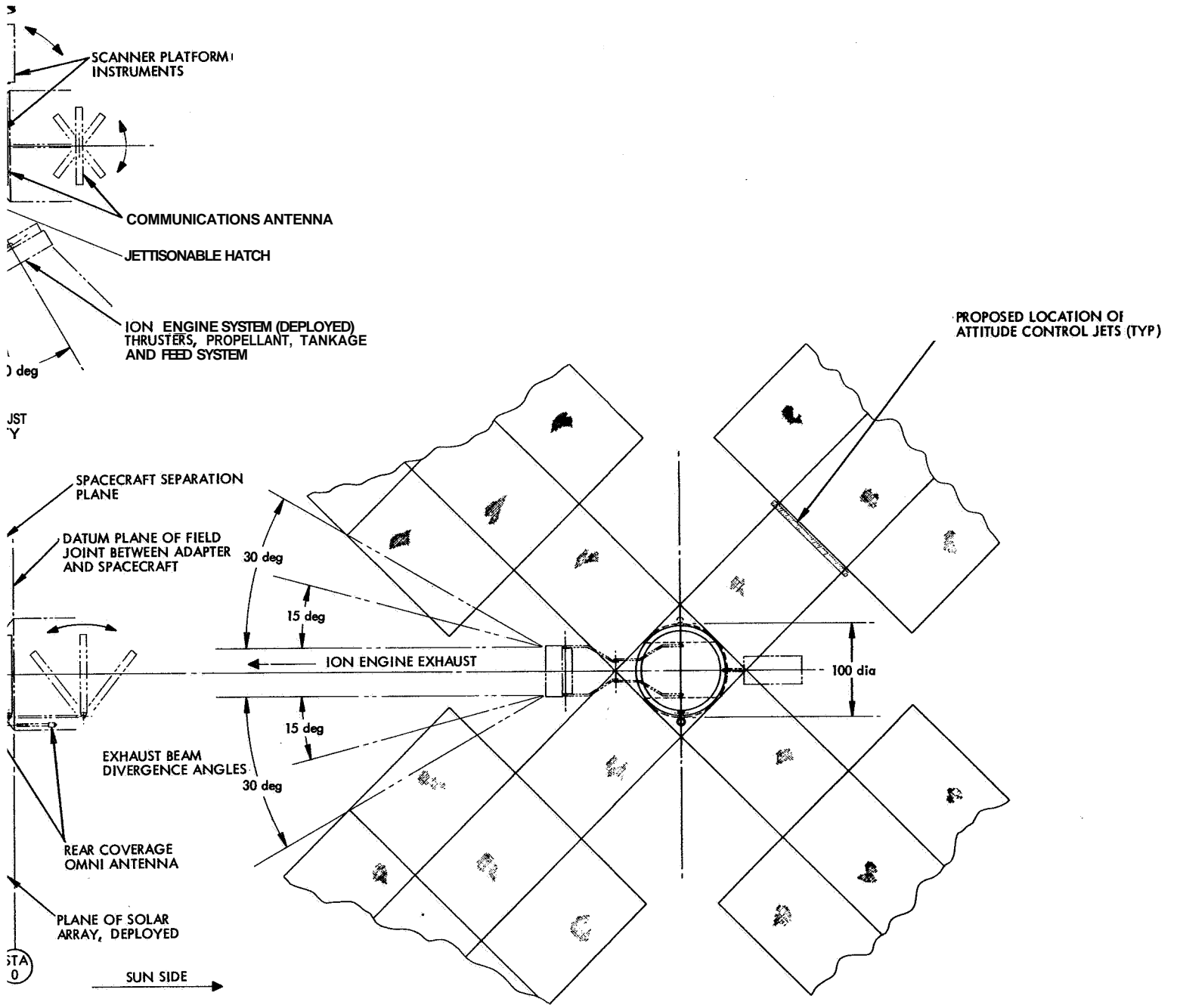
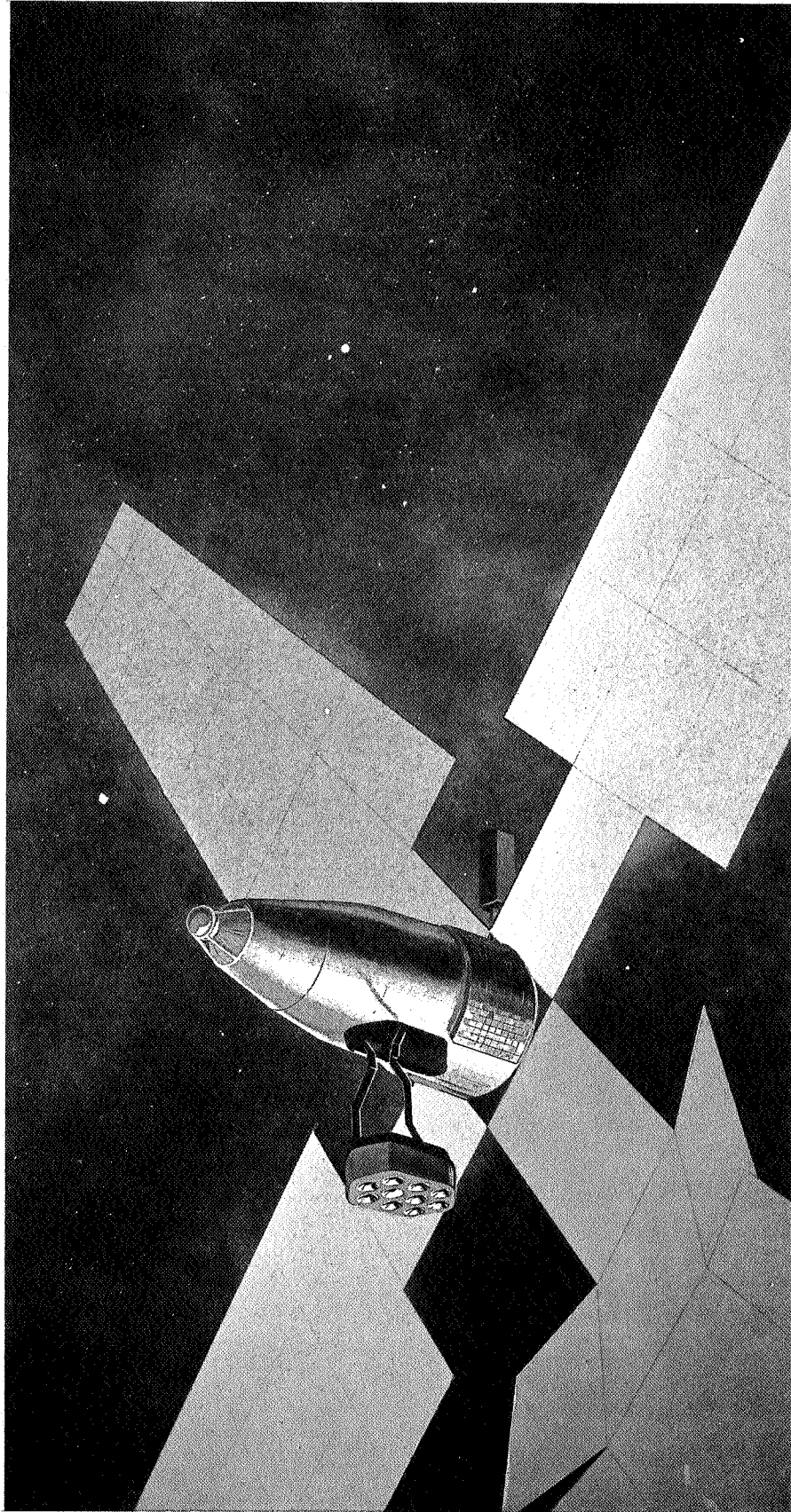


FIG. C.1-1. Solar-Electric Propulsion Spacecraft Utilizing Rectangular Panel 50 kw Solar Array and Deployable Thrustor Array.





Panel Solar Array Concept

TABLE C.1-1
 SOLAR-ELECTRIC PROPELLED MARS ORBITER SPACECRAFT WEIGHT BREAKDOWN

	Wt.	Lbs.
PAYLOAD		1525
o Orbiter	478	
o Lander	100	
o Data Automation System	80	
TELECOMMUNICATIONS		200
GUIDANCE AND CONTROL		324
ELECTRIC PROPULSION SYSTEM		5236
o Solar Array	2640	
o Power Conditioning	413	
o Thrusters (including controls)	475	
o Propellant and Tankage	1708	
RETRO-ROCKET		286
STRUCTURE		800
AUXILIARY POWER		60
ELECTRICAL HARNESS		250
SPACECRAFT-CENTAUR ADAPTER		800
		<u>9481</u>

ENGINE DE

SPACECRA
ATTITUDE
GUIDANC

LANDER CAPSULE SEPA

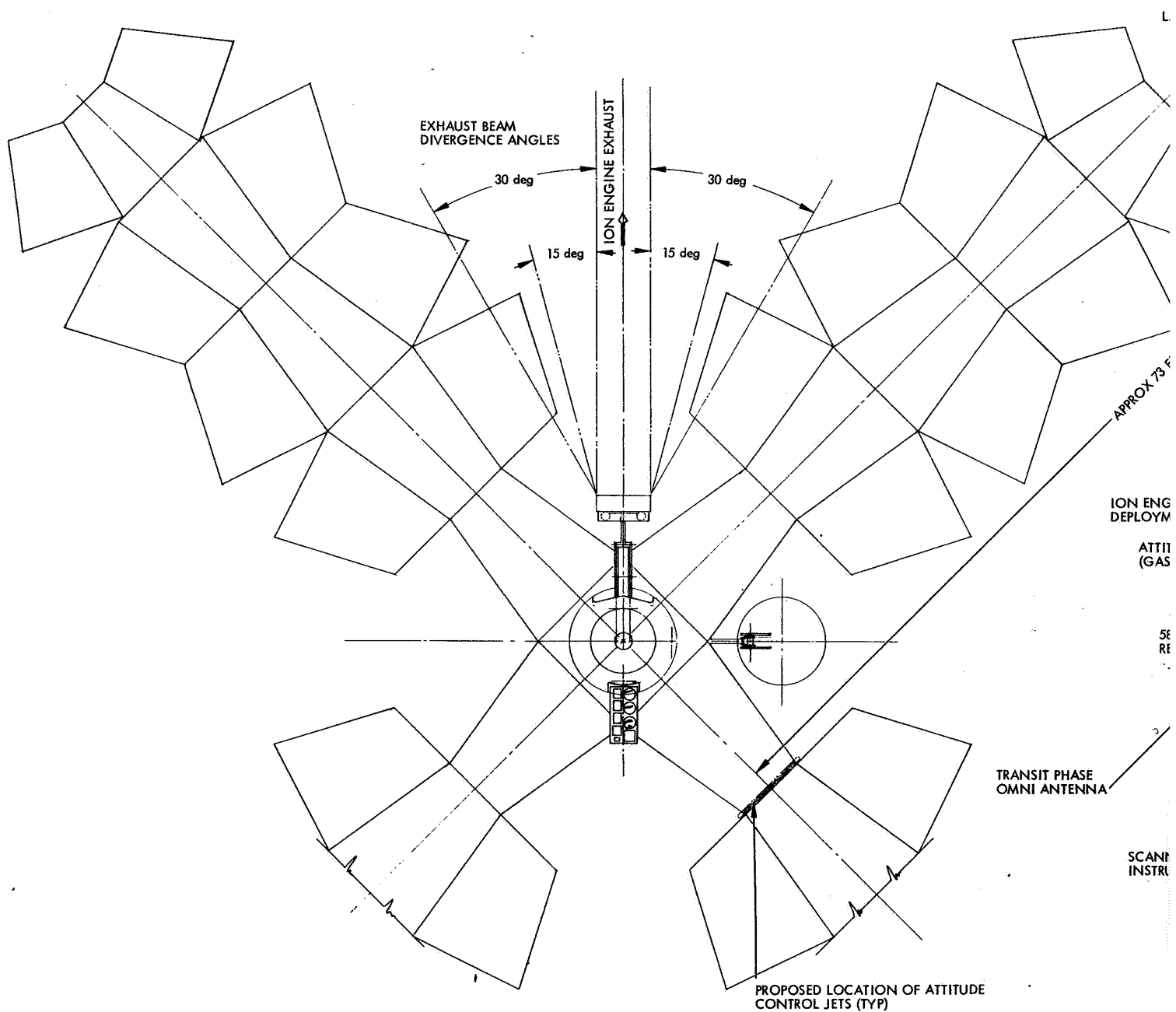
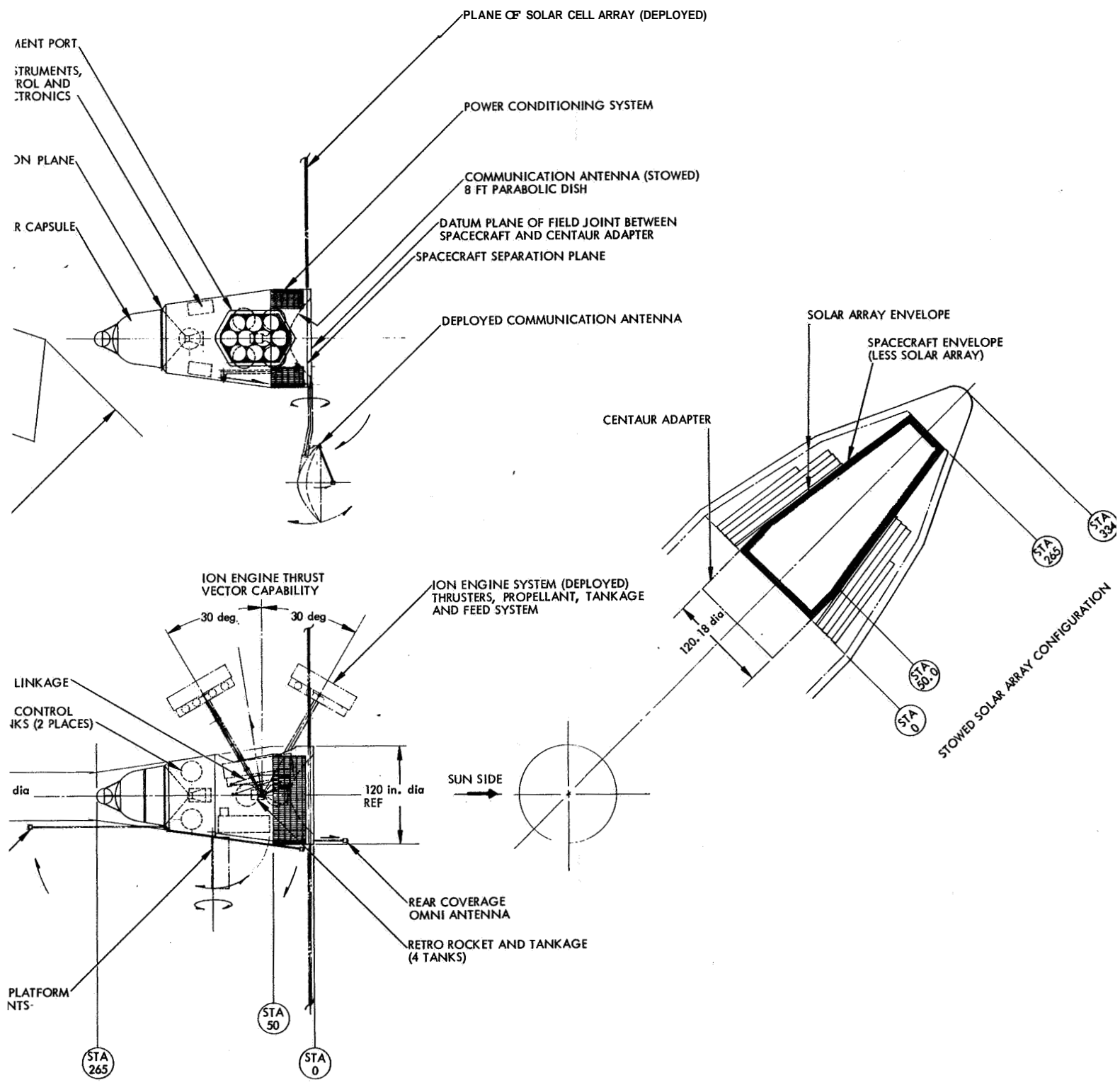


Fig. C. 1-3. Solar-Electric Propulsion Spacecraft Utilizing Trapezoidal Panel 50 kw Solar Array and Deployable Thruster Array.



C-8

- (c) Boeing "Folding Modular Type" solar array system.
- (d) The HAC multi-module power conditioner,
- (e) A liquid-propellant retro-rocket system.
- (f) A cold gas (nitrogen) attitude control system,
- (g) A maximum diameter planar array or parabolic communication antenna.
- (h) Independently oriented **Mars** scanner platform,

One of the most predominant factors influencing **the** general arrangement considered herein is the provision for a thrust vector orientation variation of 60 degrees (as required for the design mission profile) during the heliocentric transfer. **All** three of the conceptual designs presented include a gimbaled and translatable thruster array to accommodate spacecraft center-of-gravity shifts during transit; while two of them (Figure C 1-1 and C.1-3) require the thruster array to be deployed prior to thrusting.

In Figures C.1-1 and C 1-2 is presented a conceptual design of a solar-electric propulsion spacecraft which utilizes the rectangular panel "Folding Modular **Type**" solar array concept and restricts the spacecraft envelope to a 100 inch diameter circular cylinder in the stowed position, Figure C.1-1 depicts both stowed and deployed positions of **all** components, while Figure C.1-2 illustrates an artist's rendition of a perspective view of the spacecraft with all major components deployed.

The primary spacecraft structure is assumed to be of shell-type construction **with** an opening in the side to permit deployment of the electric thruster array. (Figure C.7-2 represents an alternate structural

arrangement under consideration, utilizing a truss type frame in lieu of the shell type construction).

The main solar array hinge lines are located at the base of the spacecraft which locates the entire spacecraft on the shade side of the solar array.

The nitrogen tank for the attitude control system is mounted at the deployed center-of-gravity station of the spacecraft to minimize the C. G. shift with gas expenditure.

The seven foot diameter planar array communication antenna and the planet scanner platform are deployed through the spacecraft base.

A dual liquid retro-rocket system is located at the forward end of the spacecraft just aft of the lander capsule,

The power conditioner is located at the base of the spacecraft adjacent to both the solar array and the ion engine system.

In Figures C.1-3 and C.1-4 is presented a conceptual design of a solar-electric propulsion spacecraft which utilizes the trapezoidal panel "Folding Modular Type" solar array concept and restricts the spacecraft envelope to a 120 inch diameter right circular cylinder from the spacecraft base (station 0) to station 50, tapering forward to a 58 inch diameter at spacecraft station 265.

The spacecraft structure, as in the previous arrangement, is assumed to be of shell-type construction with one opening in the side to permit deployment of the electric thruster array, and another for deployment of the Mars scanner platform.

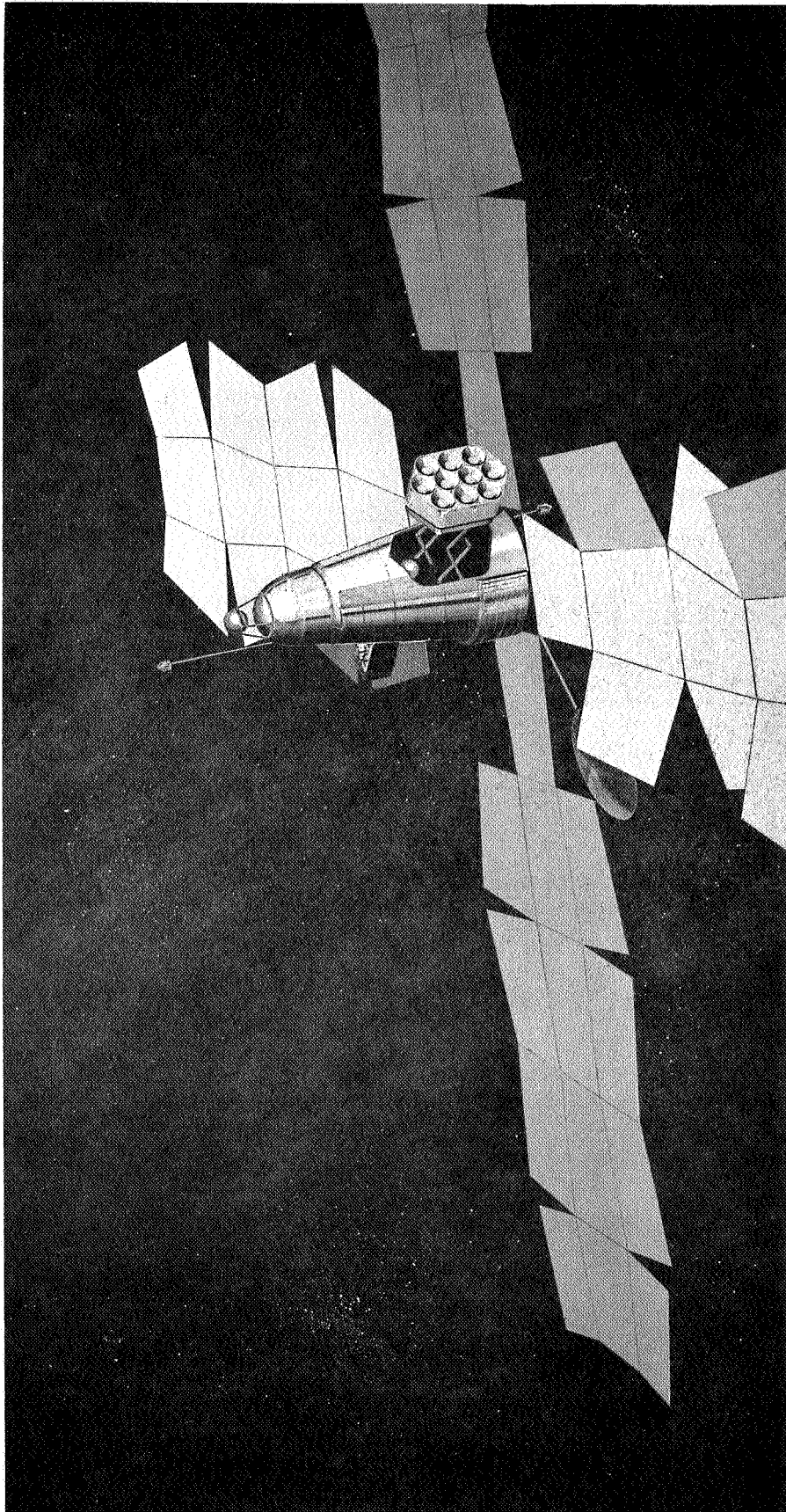


Fig. C.1-4. Trapezoidal Panel Solar Array Concept.

An eight foot diameter parabolic communication antenna is deployed through the base of the spacecraft,

As in the previous arrangement, the main solar array hinge lines are located at the base of the spacecraft which locates the entire spacecraft on the shade side of the solar array.

Dual tanks for the attitude control gas are mounted at the forward end of the spacecraft just aft of the lander capsule,

A single, centrally mounted, liquid retro rocket system (with four tanks) is located close to the base of the spacecraft,

The power conditioner, as with the previous configuration, is located at the base of the spacecraft adjacent to both the solar array and the ion engine system,

It should be noted that the trapezoidal shaped solar array panels utilize the available stowed configuration envelope more efficiently than the rectangular shaped solar array panels, and thereby result in an arrangement requiring 12 less panels and hinges. Also, the 120 inch diameter permits utilization of a larger diameter communication antenna.

In Figure C.1-5 is presented a conceptual design of a solar-electric propulsion spacecraft utilizing the rectangular panel solar array concept and restricting the spacecraft to the 100 inch diameter envelope, but having a "body-mounted" ion engine system (deployment not required). Again, a shell type construction is assumed with an opening in the side to permit unobstructed passage of the ion beam. The seven foot diameter planar array communication antenna and the Mars scanner platform are deployed through the spacecraft base. A single tank for the attitude control gas is mounted at the deployed

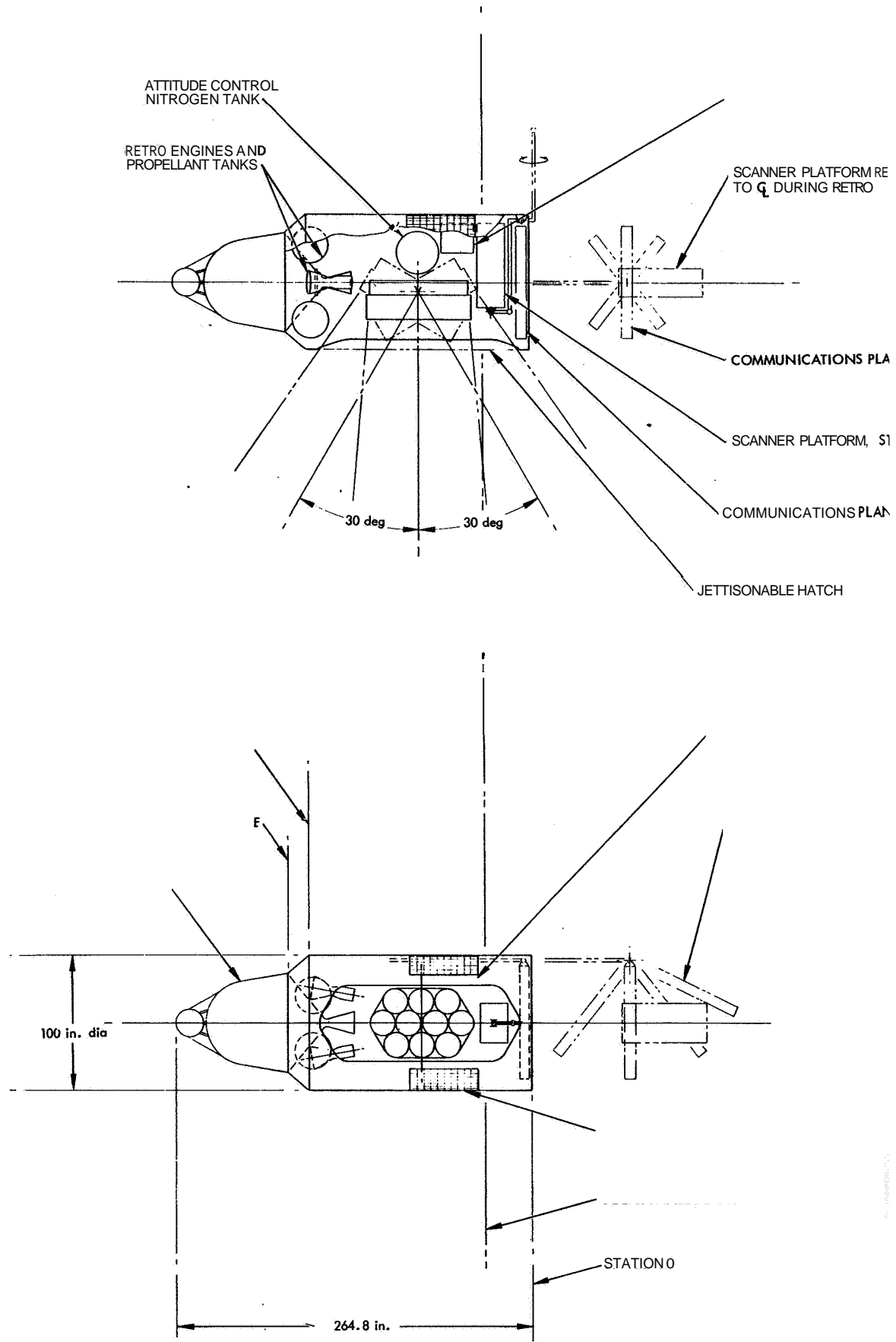


Fig. C. 1-5 Solar-Electric Propulsion Spacecraft Utilizing Rectangular Panel 50 kw Solar Array and Body-Fixed Thruster Array.

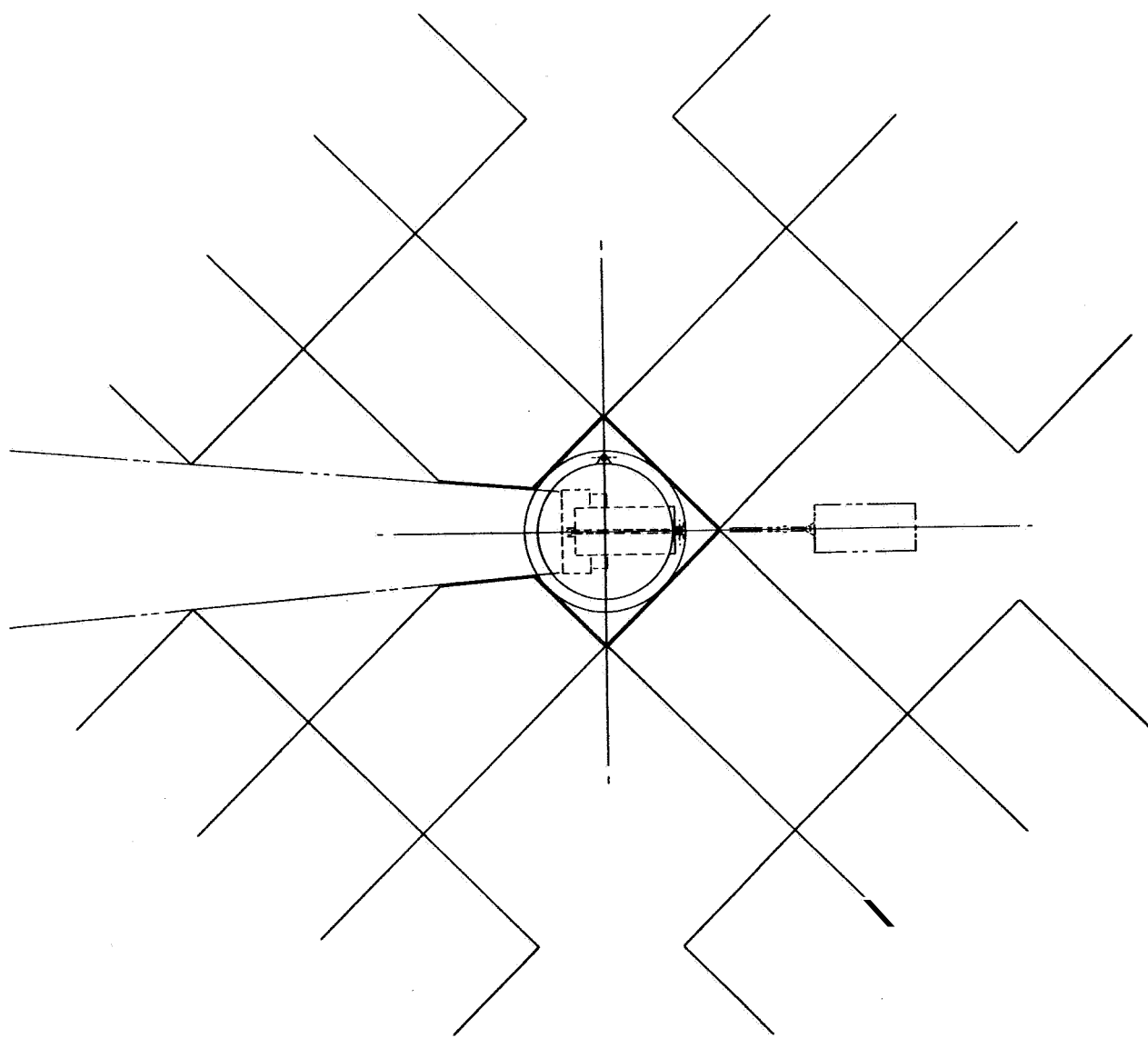
YED

ATED

ARRAY, DEPLOYED

IED

ARRAY, STOWED



C-14

C.2. Scientific Payload

Although it is not the purpose of the present study to select the scientific payload for the mission, it is mandatory that any possible payload candidates be considered insofar as they do have a significant influence on the power requirements and spacecraft general arrangements. The possible scientific payload candidates that currently are being considered for spacecraft designs are identical to those specified in the first "Bi-Monthly Progress Report". Emphasis in the scientific payload area during this study period has been directed towards the determination of the location of magnetometers.

In the previous bi-monthly report the stray magnetic field estimation was based primarily on the contribution of the solar panels. Since that time the solar panel contribution has been revised and the contributions of the remaining parts of the spacecraft have been estimated,

In reality, the magnetic moment must be experimentally measured because there are many influences that cannot be accounted for in estimating a magnetic moment: 1) the influence of slight magnetism in assembly tools and jigs, 2) incomplete deperming of completed spacecraft, and 3) actual shielding capability of some of the more strong magnetic sources -- to name a few.

To determine the proper location of the magnetometers and other magnetically sensitive components in a low field, an estimation of the stray field must be made based upon the fields of all of the spacecraft subsystems. The total magnetic moment estimated has been scaled from

measured magnetic moments of a number of U. S. spacecraft and some of the subsystems. The estimated values are listed in Table C.2-I.

TABLE C.2-I ESTIMATED SPACECRAFT MAGNETIC MOMENT	
Subsystem	Magnetic Moment (pole-cm)
Solar panels	60
Structure	200
Telecommunication (50 watts)	300
Attitude Control Assembly	10
Servo Motors (2)	30
Electric Engines EM (8) (assuming 80% reduction due to clustering)	10^4
Lander Capsule	<u>50</u>
TOTAL	-1.06×10^4

This estimate assumes that permanent magnets are used in the electric engine system. With magnetic shielding around the permanent magnets in the electric engines or if electromagnets are used in the engines the contribution of the electric engines can be reduced to 10^2 or even 10 pole-cm, For this estimate 10^2 will be used. This gives a total of 750 pole-cm as a probable minimum value. The probable maximum is listed in Table C.2-I.

It will be assumed that the sum of all the incremental magnetic fields will produce a dipole moment on the complete spacecraft such that the poles are aligned with the roll axis of the spacecraft. There are two possible directions that a magnetometer can be located in the dipole field--off the end of the dipole (Gaussian A position) or off to the side of the dipole (Gaussian B position).

The expression for the field strength is given for each of the positions as

$$B_A = \frac{2M_T}{d^3}$$

and $B_B = \frac{M_T}{d^3}$

where B is the field strength in gauss
 M_T is magnetic moment in pole-cm
 d is distance in cm.

To keep the field to a minimum it is desirable to place the magnetometers in the Gaussian B position, Solving for the distance d and substituting in the following numbers

$$B_B = 10^{-5} \text{ Gauss}$$

$$M_{T1} = 1.06 \times 10^4 \text{ pole-cm (max)}$$

$$M_{T2} = 750 \text{ pole-cm (min)}$$

gives the following possible distance required for placing the magnetometers.

$$d_1 = 10.2 \text{ meters}$$

$$d_2 = 4.2 \text{ meters}$$

These numbers are for an ambient field of 1 gamma (10^{-5} gauss). The variation for the field strength with distance from the spacecraft is shown as Figure C.2-1 for the estimated maximum and probable minimum magnetic moments.

The likely value of field strength in which the magnetometers must be placed is between 10^{-6} and 10^{-5} gauss for interplanetary magnetic field measurements. Under the conditions presented the distances required vary from 4.2 meters to 10.2 meters for a field strength of 10^{-5} gauss and 9.1 meters to 22 meters for a field strength of 10^{-6} gauss. To reduce the distance required it will be necessary to consider the amount of magnetic shielding required to decrease the total spacecraft magnetic moment.

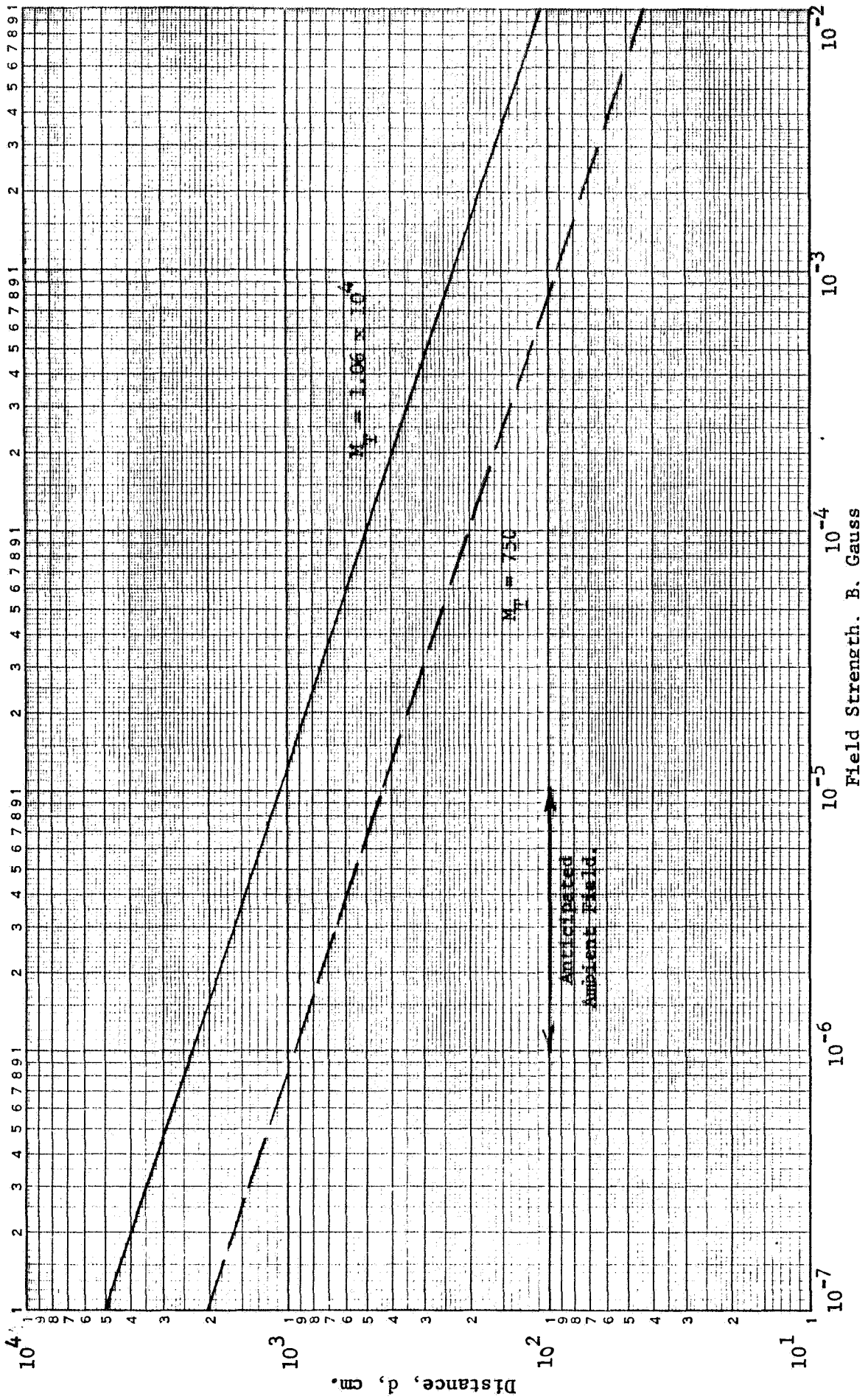


FIGURE C.2-1 Variation of field strength with distance from dipole

C.3 Retro-Propulsion

Although both solid and liquid bi-propellant systems are still under consideration, all configurations discussed herein utilize liquid retro-rocket subsystems to attain a Mars orbit. An N_2O_4/MMH liquid bipropellant combination delivering 315 seconds of specific impulse was used for sizing the liquid systems. All general arrangements presented include a retro-system sized to permit attainment of the design mission Mars orbit - 4,000 KM peri-apsis by 50,000 KM apo-apsis; however, sufficient weight and volume capability are available, for all configurations, to attain any of the orbits presently under consideration. Estimated subsystem weight and tank diameters for both two and four tank systems for these various orbits are as follows:

MARS ORBIT		Retro Subsystem Wt., Lbs.	Tank Diameter, Inches	
<u>Peri-Apsis, KM</u>	<u>Apo-Apsis, KM</u>		<u>(4)</u>	<u>(2)</u>
4,000	50,000	286	15.7	14.8
4,000	20,000	486	20.0	25.2
4,000	10,000	714	23.4	29.5
5,000 circular		1021	26.7	33.6

C.4 Thermal Control

For all of the conceptual spacecraft designs considered during this reporting period, 72 square feet of thermal radiator area is provided for the dissipation of heat generated by the power conditioning equipment (5 KW). This area is predicated on the assumption that the **maximum** temperature of the thermal radiator will be 158^oF (70^oC) which is **the** upper temperature limit of the electrical power conditioning equipment.

Current studies in **this** area are concentrated on determination of thruster module spacing **as** it affects the spacecraft thermal control interface, and the determination of thermal data **as** a function of **modular** switching of the power conditioning equipment for reliability and switching **analysis**

C.5 Spacecraft Attitude Control

A study has been performed to determine the feasibility of reducing the thrust misalignment disturbance torque of the solar electric propulsion vehicle. This function would be implemented by rotating or translating the ion engine bank until the thrust vector is closely aligned to the vehicle center of gravity and net disturbance torques reduced to tolerable levels. The vehicle limit cycling characteristics are measured to determine the necessary corrections, and control torque 'on' and 'off' times are chosen as the best means of measuring and computing disturbance torque magnitude and direction. Two successive corrections are required if a maximum disturbance level exists initially and a 1.5% parameter measurement tolerance is obtainable. The disturbance reduction cycle is shown to be necessary to maintain the required control torque fuel within acceptable weight limits.

A preliminary sizing study for attitude control of the solar electric propulsion vehicle was given in reference (1). A cold gas mechanization was sized based on a disturbance torque resulting from various solar phenomena. Ion engine thrust misalignment can yield a maximum torque of over 100 times greater than the maximum solar disturbance torque used for design in reference (1). Over a one year period this would require that a proportionately greater control impulse be available; hence an unreasonable control system weight (250 pounds x 100 would be required). To eliminate this intolerable weight requirement, the bank of ion engines will be commanded to rotate to point its thrust vector at or near the vehicle center of gravity. The purpose of this study is to determine the commands based upon measurements of limit cycle frequency, period,

etc., and to determine the sensitivity of the commands to parameter measurement errors.

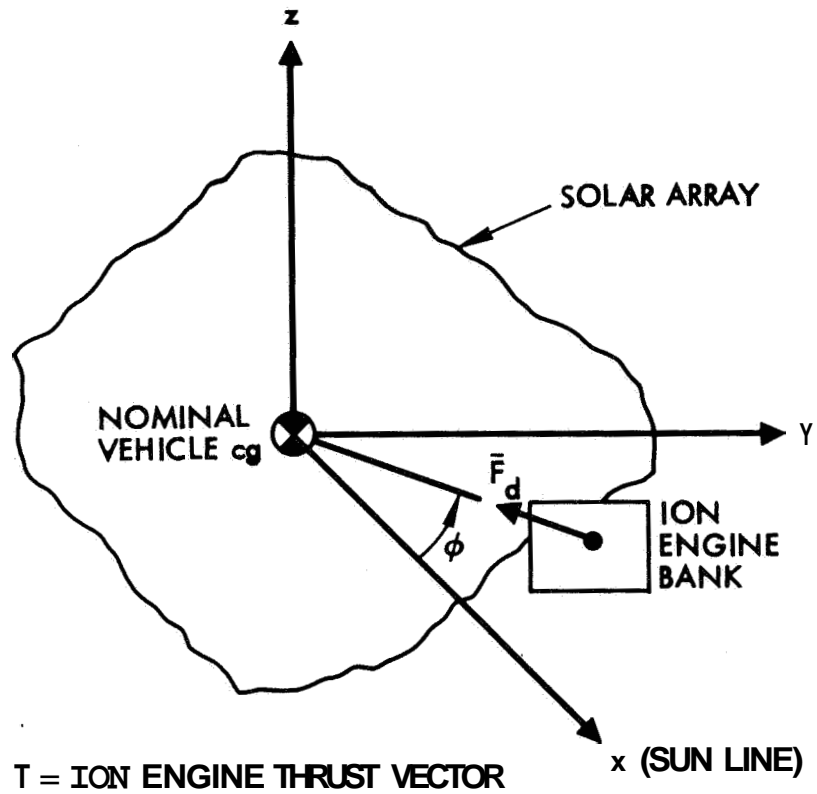
Disturbance Torque

Reference (1) summarizes the various disturbance torques acting on the vehicle. Neglecting ion engine thrust misalignment, the main disturbance source is solar pressure, a worst case approach yielding 1×10^{-3} ft-lbs. of torque for sizing purposes. Additional disturbance torque above this level due to thrust misalignment would require more control fuel than is being carried in the current vehicle design.

Thrust misalignment results because the ion engine thrust vector does not pass through the vehicle c.g. To illustrate the nature of the disturbance torque caused by this misalignment, consider Figures C.5-1,-2 and -3. Figure C.5-1 defines a set of vehicle coordinates. The xy plane is meant to nominally coincide with the trajectory plane. The ion engine bank is rotated an angle ϕ in the xy plane for trajectory control. Nominally the thrust vector \vec{F}_d passes through the design c.g. However, realistically a misalignment exists which can be attributed to:

1. uncertainties in the c.g. position
2. uncertainties in the thrust direction
3. solar heating causing array distortion and consequent c.g. motion.

The misaligned thruster is illustrated in one plane in Figure C.5-2 and a similar misalignment exists out of the plane of the illustration (vehicle xy plane). The distance l_{dz} is defined as the perpendicular distance from the vehicle c.g. to the projection of the net thrust vector in a plane parallel to the xy plane containing the c.g. (illustrated in Figure C.5-2). The distance l_{dy} is defined as the perpendicular



DEFINITION OF COORDINATE AXES

FIGURE C.5-1

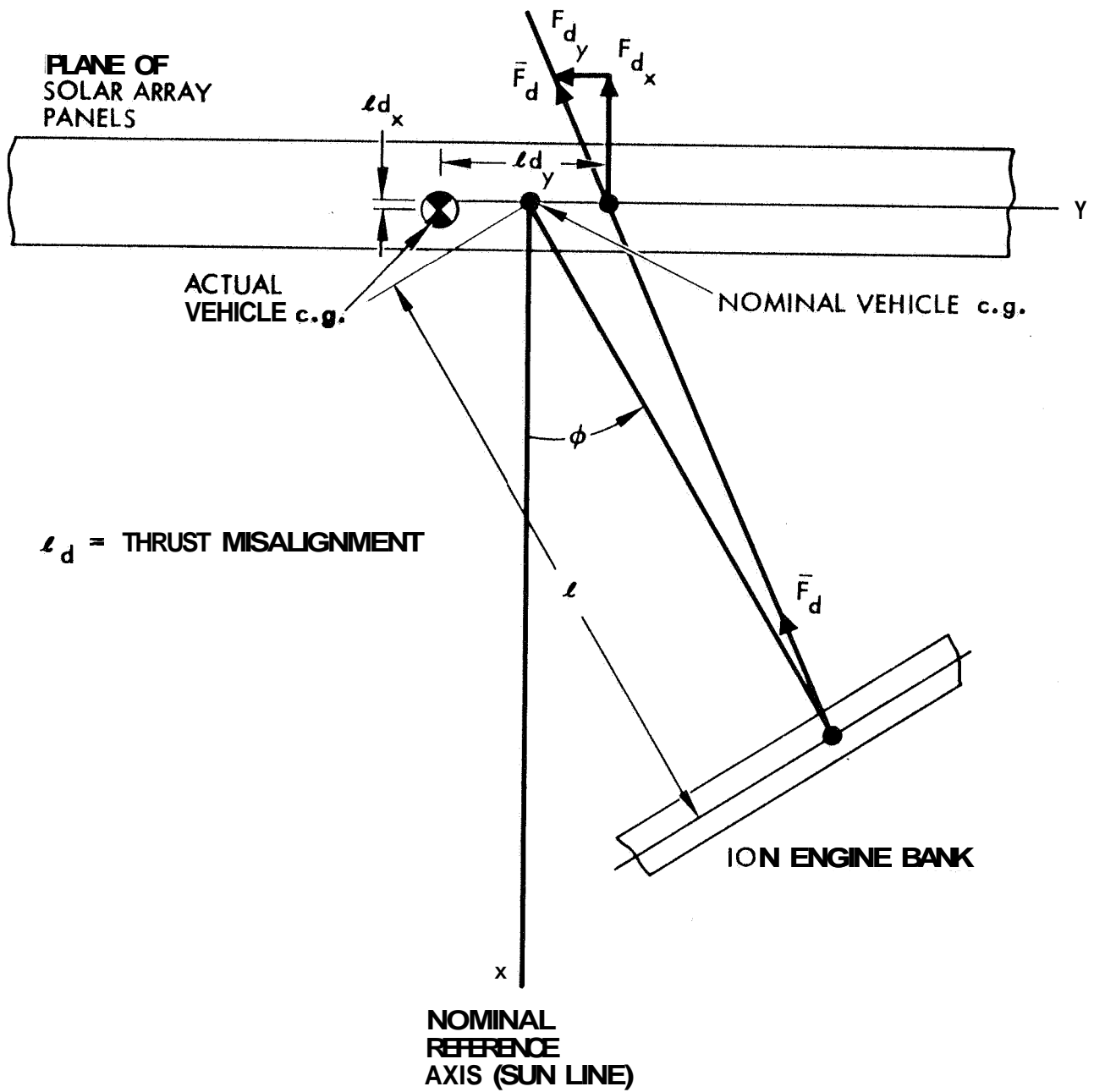


ILLUSTRATION OF THRUST MISALIGNMENT IN ONE PLANE

FIGURE C.5-2

distance from the c.g. to the projection of the net thrust vector in the plane normal to xy which contains the c. g. and the center of force (illustrated in Figure C.5-3).

The resulting torques can be nulled by two degree-of-freedom motion (rotation or translation) of the engine bank; however, depending upon the angle ϕ , the torques may appear in all three vehicle reference axes (xyz). Therefore, the disturbance torques as seen in body reference axes will be given by:

$$T_x \cong F_d l_{dy} \sin \phi \quad (1)$$

$$T_y \cong F_d l_{dy} \cos \phi \quad (2)$$

$$T_z \cong F_d l_{dz} \quad (3)$$

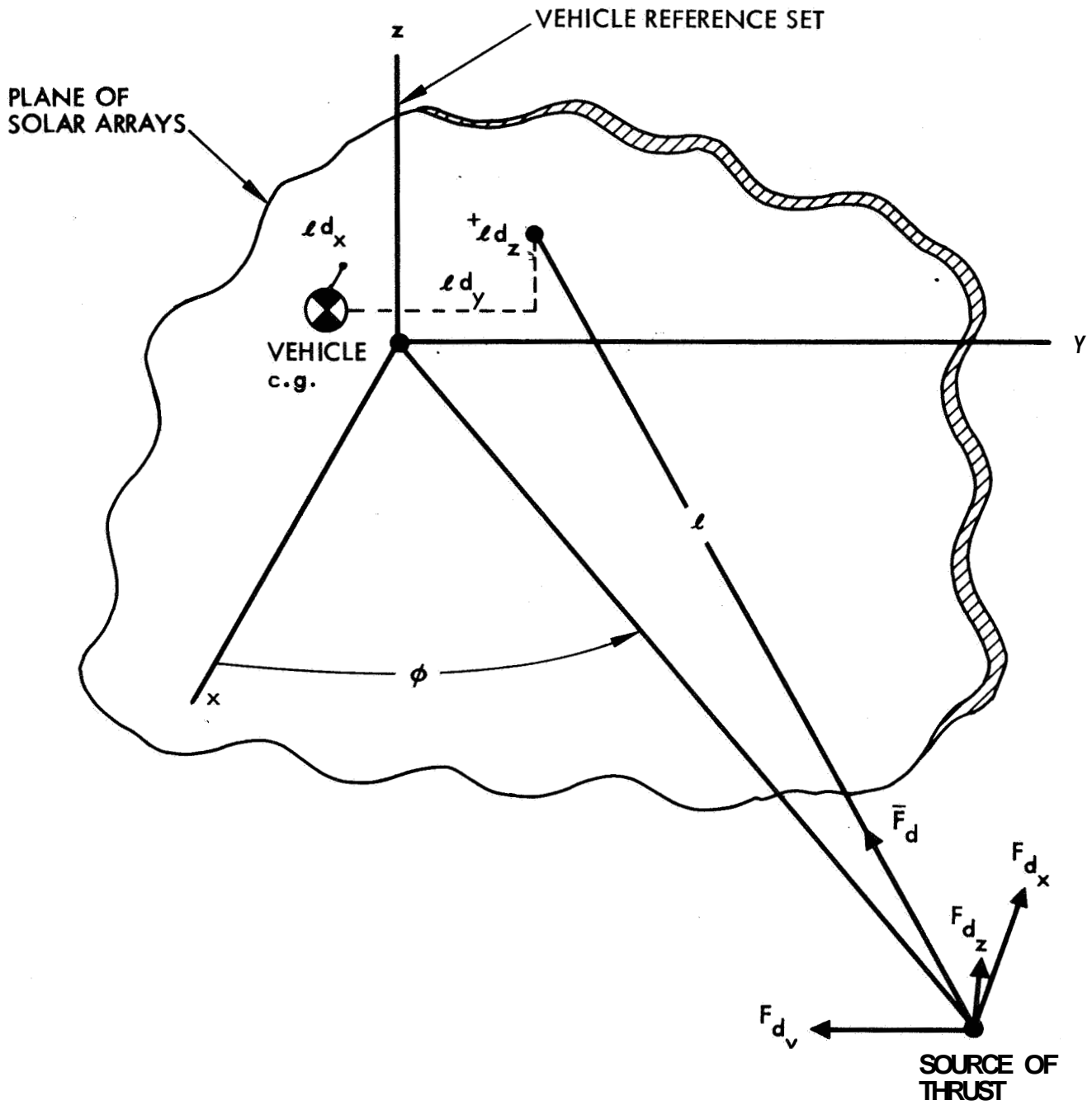
where the assumption has been made that angular thrust misalignment is small compared to the angle ϕ .

If T_x , T_y , T_z can be measured, and the angle ϕ is a known parameter, equations (1), (2) and (3) can be utilized to determine the commanded translation or rotation of the engine bank in the two degrees of freedom. For $\phi \neq 0, \pi/2$ equations (1) and (2) can be averaged in a suitable manner such as to improve the estimate of l_{dy} based upon measurements of T_x , T_y .

Therefore, the relationship between measured disturbance torques and the rotation or translation commands to the engine bank mechanism are:

$$l_{dy} \cong \frac{T_x}{F_d \sin \phi} \cong \frac{T_y}{F_d \cos \phi}$$

$$l_{dz} \cong \frac{T_z}{F_d}$$



3-D MISALIGNMENT DIAGRAM

FIGURE C.5-3

The techniques for determination of T_x , T_y , T_z based upon measured system parameters are discussed in the following paragraphs.

Since angular rates and displacements are small in steady state operation, each of the body axes can be considered independently (uncoupled).

The expected range of misalignment magnitudes perpendicular to the thrust vector are listed in Table C.5-I.

TABLE C.5-I Misalignment Magnitudes	
<u>Contributing Factor</u>	<u>Amount</u>
c. g. location uncertainty	$\pm 3''$
thrust direction uncertainty	$\pm 1''$
solar bending distortion	<u>$\pm 1''$</u>
WORST CASE TOTAL	$\pm 5''$

The worst case total ($\pm 5''$) is assumed to occur in any direction and would result in largest pitch and yaw torques for $\varphi = 0$; or largest roll torque for $\varphi = 90^\circ$. Taking .35 pounds to be a nominal ion engine thrust and combining with the moment arm yields the maximum expected torque in any one channel:

$$(.35 \text{ lb.}) \left(\frac{5}{12} \text{ ft.} \right) = .146 \text{ ft-lbs.}$$

The subsequent description of a disturbance torque reducing procedure is written assuming the thrust remains fixed in magnitude and direction.

If this is not the case the torque reduction procedure is much more difficult to implement and may not be practical. One important factor affected would be cold gas consumption if thrust direction changes require frequency corrections.

Techniques of Measuring and Computing Disturbance Torque

A single control channel mechanization from Reference (1) is repeated in Figure C.5-4. Under a significantly large disturbance torque, a soft duty cycle occurs as discussed in Reference (1) and illustrated by the phase plane of Figure C.5-5. The limit cycle behavior is determined by the control loop characteristics and the disturbance torque magnitude.

The equation for a constant torque trajectory in the phase plane of Figure C.5-5 is given by:

$$(\theta + \theta_d)(T/J) = \frac{1}{2} (\dot{\theta}^2 - \dot{\theta}_o^2) \quad (5)$$

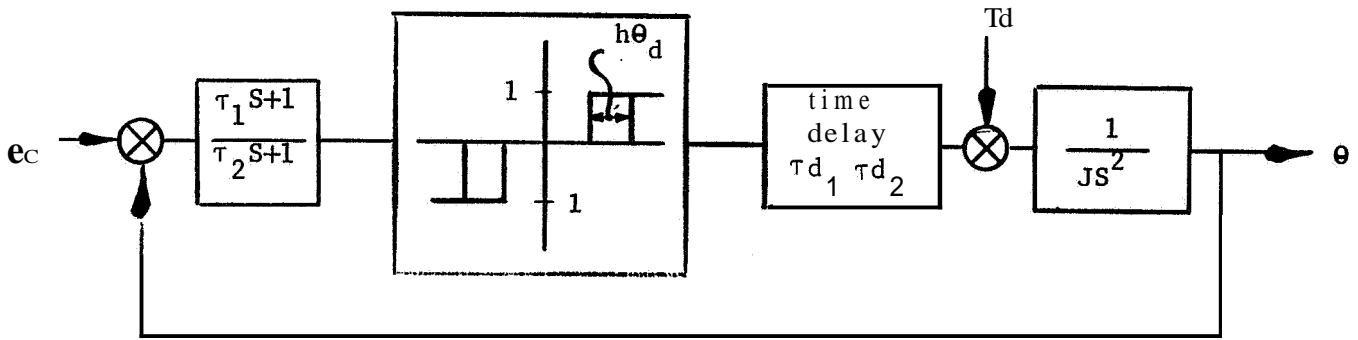
where $\theta = \theta_1 \cong \theta_d$.

The magnitude and sign of T determines the parabola shape. From 0 to 1, $T = T_c + T_d$; from 1 to 2 to 0, $T = T_d$. The time along the phase trajectory is related to θ and $\dot{\theta}$ by:

$$t = \frac{\dot{\theta} - \dot{\theta}_o}{T/J} \quad (6)$$

$$\left\{ \frac{T/J}{2} \right\} t^2 + \dot{\theta}_o t = \theta + \theta_o \quad (7)$$

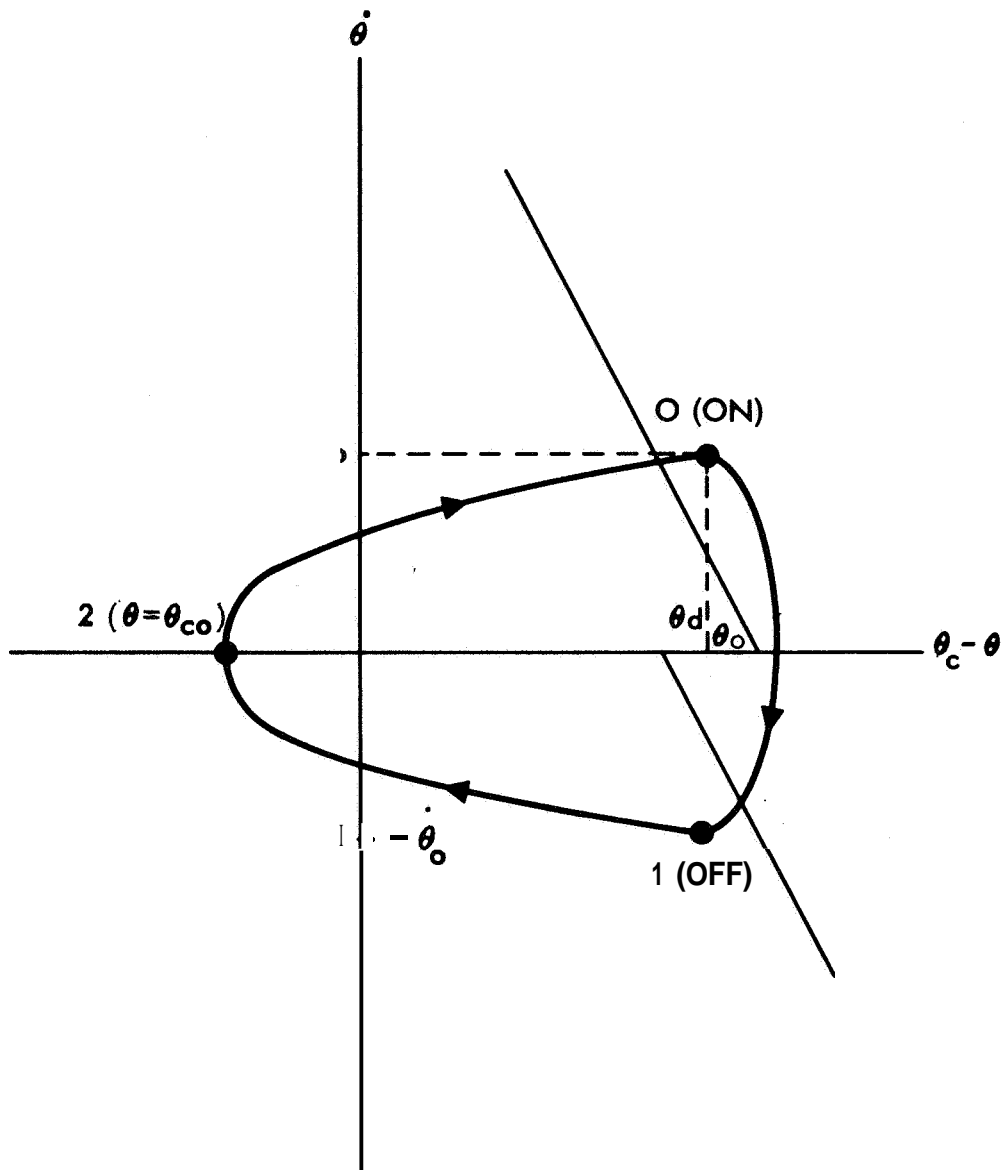
Solution of equations (5), (6), and (7) in terms of measurable parameters leads to equations (8), (9), and (10).



- T_d = $l_d F_d$, disturbance torque
 T_c = $l_c F_c$, control torque
 l_c = control moment arm
 l_d = disturbance moment arm
 F_c = control force
 F_d = disturbance force
 τ_1, τ_2 = lead-lag network time constants
 h = hysteresis (per cent θ_d)
 τ_{d1}, τ_{d2} = 'on', 'off' time delays, respectively
 J = inertia
 e_c = commanded angle (assumed zero for torque adjustment)
 θ_d = dead zone

FIGURE C.5-4

Single Channel Mechanization



SOFT DUTY CYCLE

FIGURE C.5-5

$$T_d = \frac{t_{01} T_c}{t_{120}} \quad (8)$$

t_{01} = time from point '0' to point '1', etc.

$$T_d = \frac{J}{2} \frac{\dot{\theta}_o^2}{\theta_o + \theta_{co}} \quad (9)$$

θ_{co} = crossover angle (See Figure C.5-4)

$$T_d = \frac{2J (\theta_d + \theta_{co})}{t_{12}^2} \quad (10)$$

Each of these equations relates the disturbance torque to known (J, T_c, θ_d) and measurable ($t_{01}, t_{120}, \theta_{co}, \theta_o$) parameters and consequently can be used to compute T_d . Table C.5-II summarizes the three alternatives.

TABLE C.5-II Summary of Measuring Techniques for Disturbance Torque Determination Computation			
No.	Equation	Known	Measured
1	$T_d = \frac{J}{2} \frac{\dot{\theta}_o^2}{\theta_o + \theta_{co}}$	J, θ_d	$\dot{\theta}_o, \theta_{co}$
2	$T_d = \frac{2J (\theta_o + \theta_{co})}{t_{12}^2}$	J, θ_d	t_{12}, θ_{co}
3	$T_d = \frac{T_c t_{01}}{t_{120}}$	T_c	t_{01}, t_{120}

Method (1) requires a measurement to provide $\dot{\theta}_o$ information, necessitating an additional sensor on board. Furthermore, rates are so low for small disturbance levels (10^{-3} degrees/sec) that the feasibility of such a measurement is questionable. The 'on' and 'off' times (t_{01} , t_{12} , and t_{120}) can be measured by using the electrical output of the switching network (see Figure C.5-4). This signal would be in the form of a train of pulses of finite width. The actual control torque contains a transport lag as well as a time constant when responding to a pulse input; hence the measurement would be approximate. The transportation delays are relatively small compared to the pulse width for cold gas, however, the thrust-time characteristics must be known to accurately calibrate the disturbance torque of thrust build-up and delay times are significant compared to the total thrust time.

Method (2) requires a time measurement and a means of determining θ_{eo} from the angular displacement feedback signal or directly from the sensors. This appears to be somewhat more complicated than measuring elapsed times only, as in method (3). Furthermore, times are measured relative to the occurrence of discrete pulse ('ON' and 'OFF' commands) which should lead to a simpler mechanization. Hence method (3) is chosen for disturbance torque estimation,

Disturbance Torque Reduction Procedure

Once the disturbance torque has been computed the disturbance moment arm can be found using equation (11).

$$l_d = \frac{T_d}{F_d} \quad (11)$$

The accuracy of this computation depends on accurate knowledge of F_d . The quantity F_d varies with the distance from the sun, number of ion engines at maximum output, statistical uncertainties in the thrust level, and the angle φ as given by equation (4). From equation (4) there are three equations which can be written for the two unknown quantities l_{dz} and l_{dy} :

$$l_{dz} = \frac{T_{dz}}{F_d} \quad (12a)$$

$$l_{dy} = \frac{T_{dx}}{F_d \sin \varphi} = \frac{T_{dy}}{F_d \cos \varphi} \quad (12b)$$

Hence, a redundant measurement of l_{dx} can be made to achieve greater accuracy. If φ becomes small, the T_{dx} measurement would also be small and the computation would be neglected.

The net disturbance torque must be reduced to .001 foot pound or lower to stay within the same sizing requirements as used in Reference (1). The alternative is additional control fuel for a larger steady state disturbance for the present .001 ft-lbs is assumed to be a suitable number. The problem then is to rotate the ion engine such that a maximum disturbance of .146 ft-lbs, is reduced to .001 ft-lb. by reducing the disturbance moment arm.

If the first adjustment made were performed with .69% accuracy, the function could be accomplished in one step. This type of accuracy is very likely unobtainable, however, so more than one iteration is necessary. If each iteration has an identical expected accuracy the number of iterations required can be found from equation (13).

$$T_{d_o} \sigma^n \leq T_{d_f} \quad (13)$$

- where n = number of iterations
- T_{d_o} = initial disturbance torque
- T_{d_f} = final disturbance torque
- σ = uncertainty in moment arm determination

The physical situation requires that n be an integer. For the specified values of T_{d_o} and T_{d_f} , the number of iterations versus measurement accuracy is shown in Figure C.5-6.

It is expected that the disturbance force will not be known accurately and hence will contribute a large error to the moment arm estimate. However by assuming the force (and the center-of-force) remains constant during the alignment procedure, it can be more accurately computed after the second measurement. To illustrate this improvement technique in one channel assume the first measurement yields a value given by equation (14)

$$\Delta l_d = \frac{T_d}{F_d \text{ (ref)}} = \frac{T_c t_{01}}{F_d \text{ (ref)} t_{120}} \quad (14)$$

$F_d \text{ (ref)}$ is an estimate of the actual force from equation (12) and Δl_d is consequently accurate only to the extent that $F_d \text{ (ref)}$ and the time measurements are accurate.

A command is given to move the thrust vector an amount Δl_d in the yz plane. This correction may be implemented by either a rotation or translation of the ion engine bank. The command must be computed with the angle ϕ accounted for.

After correction, a new disturbance torque,

$$T'_d = \frac{T'_c t'_{01}}{t'_{120}} \quad (15)$$

given by equation (15) can be combined with equations (14), (16), and (17) to yield equation (18).

$$l'_d = l_d - \Delta l_d \quad (16)$$

where l_d = actual initial moment arm
 l'_d = moment arm on second measurement
 Δl_d = first estimate

$$F_d = \frac{T'_d}{l'_d} = \frac{T_d}{l_d} \quad (17)$$

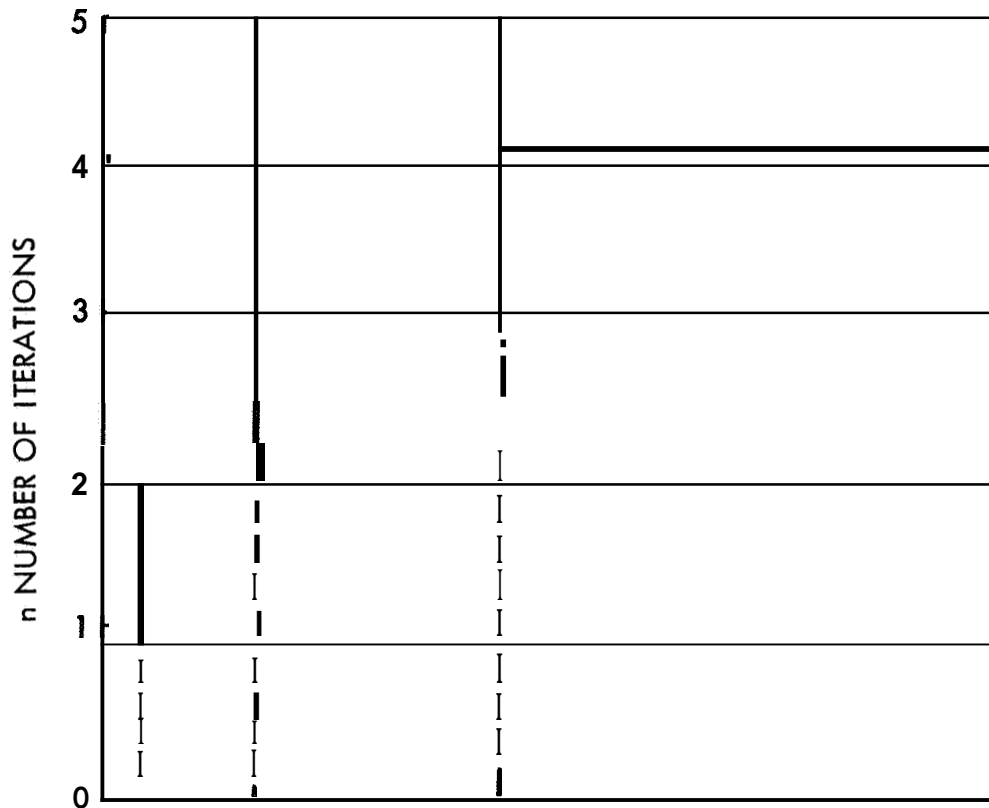
(assuming F_d is constant)

$$F_d = F_d \text{ (ref)} \left[1 - \frac{T'_c}{T_c} \times \frac{t'_{01}}{t'_{120}} \times \frac{t_{120}}{t_{01}} \right] \quad (18)$$

where $T'_c/T_c = \pm 1$

The quantities t_{01} , t_{120} , t'_{01} , t'_{120} are measured before and after the first correction while F_d (ref) is the quantity being updated or refined. The expression T'_c/T_c is present because the control torque may or may not be of the same polarity before and after the iteration. The F_d given by equation (18) is used to compute the moment arm for the second iteration.

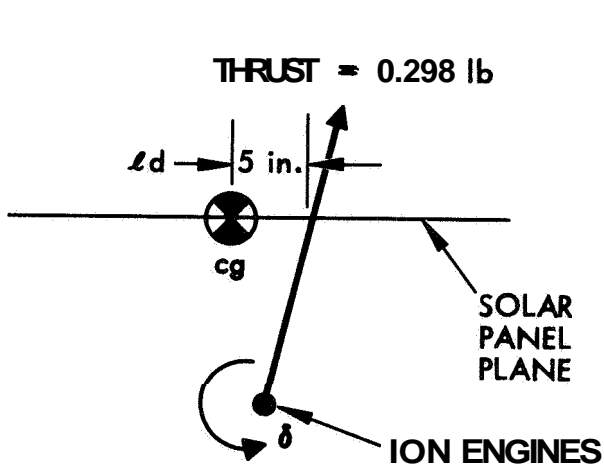
A typical numerical case can be considered to illustrate the procedure. Figure C.5-7(a) shows a maximum misalignment torque initially. From



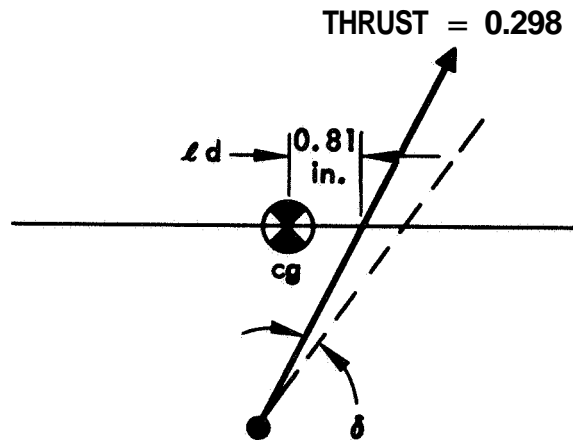
$$\sigma = \frac{\text{MOMENT ARM DETERMINATION ACCURACY ERROR}}{\text{MAGNITUDE}} \times 100\%$$

NUMBERS OF THRUST DIRECTION ITERATIONS VERSUS MEASUREMENT ACCURACY

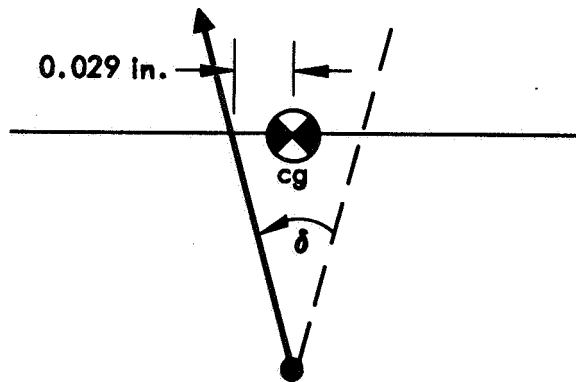
FIGURE C.5-6



(a) INITIAL CONDITION



(b) AFTER FIRST CORRECTION



(c) AFTER SECOND CORRECTION

NOTE: WITHIN ACCEPTABLE STEADY-STATE DISTURBANCE REGION

TYPICAL DISTURBANCE TORQUE REDUCTION PROCEDURE

FIGURE c.5-7

equation (14), Δl_d is computed. The total measurement error is assumed to be 16.5% of which only 1.5% is attributable to random errors. The other part is a systematic, repeatable error such as incorrect estimation of the disturbance force and control torque.

Random errors can occur due to several causes and are dependent on the method of implementation of the measurements. Long sampling intervals if direct telemetry is used can yield such errors, Random variations in ion engine thrust and c.g. location could also affect the accuracy, Measurement and computational errors would occur if on-board control were implemented.

If a reference force of .35 pounds is used then the systematic (15%) error is assumed to occur because the actual force is only .298 pounds, The system would measure a duty cycle (t_{01}/t_{120}) of T_d/T_c as given by equation (19). The factor-985 results from the random error.

$$\frac{t_{01}}{t_{120}} = \frac{T_d}{T_c} = \frac{5}{(.025)(20)} \frac{(.298)}{(.985)} = .2445 \quad (19)$$

Using the reference force (.35 pounds) in equation (13) yields a moment arm estimate Δl_d of 4.19 inches. Hence the angle δ is changed until the moment arm is reduced to .81" as shown in Figure C.5-7 (b). At this point the disturbance has been reduced to .0201 ft-lbs. and the system undergoes a transient response until the steady state duty cycle is approached. A second duty cycle measurement is made with a 1.5% error, yielding a t_{01}/t_{120} of .0408. This time the 1.5% error is taken in the opposite direction to yield a worst case.

Equation (17) can be used to update the reference force. This yields:

$$F_d = (.35) \left[1 - (1)(.0408)/(.2445) \right] = .292 \text{ lbs} \quad (20)$$

The new Δl_d again is computed using equations (14) and (20) for the new reference force to yield: $\Delta l_d = .839$ inches. The next rotation δ to yield a Δl_d of .839 inches results in the error shown by Figure C.5-7(c). The disturbance torque is now reduced to approximately 1×10^{-3} ft-lbs. Slight accuracy improvement would yield a margin of safety since 1×10^{-3} ft-lbs. is the maximum desired level for fuel sizing. However, if the above assumed accuracies (15% systematic and 1.5% random) are not realizable an additional iteration may be required.

Additional Fuel Weight

Reference (2) describes the attitude control transient behavior for a specific set of initial conditions based on the parameters given by Reference (1). Information has not been generated to indicate the transient response for a rapid change in disturbance torque. Based on Reference (2), however, the time taken to return to steady state can be estimated at 5000 seconds. For accurate time measurements and ion engine rotation an additional 3000 seconds are allowed. Hence 7000 seconds (~ 2 hr) is considered to be a realistic estimate of the time per iteration. Of this time, approximately 1400 seconds represents thrust 'ON' time for the first iteration, and 200 seconds for the second iteration. For the nitrogen gas system, this represents 0.8 pounds/adjustment of control fuel usage.

The torque adjusting procedure, if held to 2 or 3 adjustments over a mission yields a small increase in fuel weight, For example:

$$\frac{.8 \text{ lbs.}}{\text{adjustment}} \times \frac{3 \text{ adjustments}}{\text{axis}} \times \frac{3 \text{ axes}}{\text{spacecraft}} = 7.2 \text{ lbs of fuel/mission}$$

Further Comments

The use of the equations for the configuration of Figure C.5-7 implicitly assumed that the distance from the point of force application to the c.g. is large compared to the c.g. offset. Implementation of the torque reducing scheme places definite limitations on the position of the ion engine. If the ion engine is too close to the vehicle c.g. a large angular rotation is required for a given c.g. misalignment. Hence the thrust direction is appreciably changed and orbital control errors may be incurred. On the other hand if the ion engines are too far removed from the vehicle c.g. a very small angle is required for a given moment arm. Tighter angular resolution specifications must then be imposed on the ion engine corrections equipment.

Angular resolution is actually the limitation on how low the disturbance torque can be reduced by this technique. From the standpoint of fuel usage it is desirable to reduce the disturbance as much as possible. If the steady state torque can be reduced to a lower level than .001 ft-lbs. the total control fuel weight may be reduced. However, more fuel per torque reduction cycle **would be** required and a tradeoff is indicated.

REFERENCES:

- 1, **Solar Powered Electric Propulsion Spacecraft - First Bi-Monthly Report, May 1965**
2. **IDC 2223/254, McElvain to Olson. Single Axis Acquisition Analysis for Solar Electric Propulsion Study.**

C.6 Telecommunications

At present, either an 8-ft. diameter parabolic antenna or a 7-ft. diameter planar array appears to offer the most favorable trade-off between desired gain and expected off-axis losses. The planar array appears more attractive due to having the same gain in spite of a smaller aperture, because of the higher illumination efficiency. Further, in this range, the weight appears to be about the same for either system. This trade-off study is continuing.

Emphasis in this study area during the next reporting period will be directed to the exploration of telecommunication interface aspects of electric propulsion (reflection, absorption, noise emission) for the transit phase of the mission.

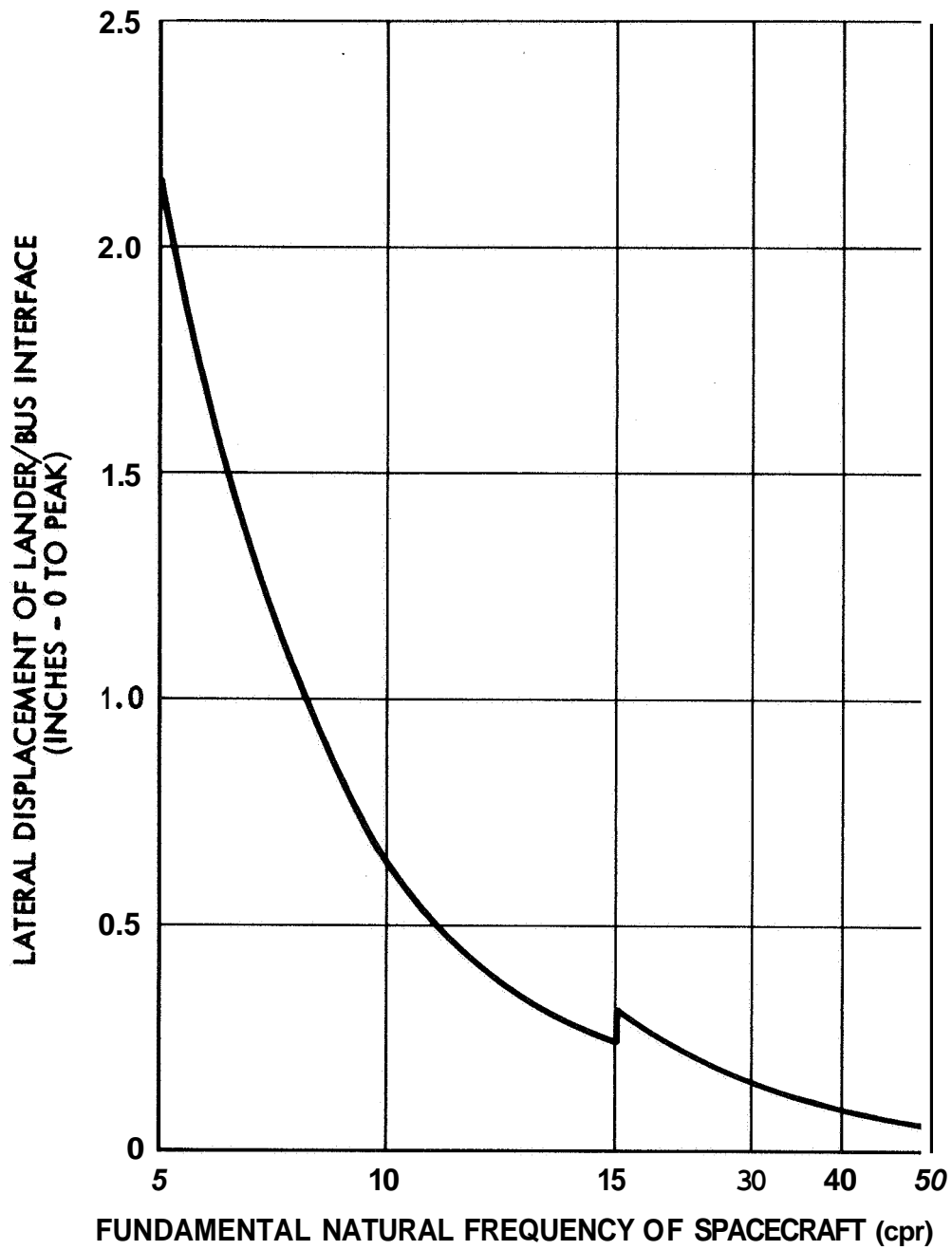
C.7 Structural and Dynamics Analysis

A semi-monocoque structure was suggested for the spacecraft and a thin shelled cylinder was assumed as the primary structure to obtain a 30 degree of freedom dynamic model of the spacecraft in the stowed configuration. For lateral vibration of the field joint and for an assumed 5% of critical damping in the structure, analysis of the model by digital computer program indicated that the amplitude of vibration of the lander/bus interface relative to the field joint would be about 5.5. This was for a natural frequency (about 33 cps) of the stowed spacecraft where the lander experienced relatively large motion.

Using this factor of 5.5, the displacement of the lander/bus interface may be estimated as a function of the natural frequency of the spacecraft for frequencies other than 33 cps. This information is helpful both for sizing the structure and for uncovering any possible interference problems between the solar panels and shroud. Under the action of the lateral sine environment (specified by Figure D-3.2-2) the displacement of the lander/bus interface as a function of frequency is shown in Figure C.7-1.

Results from analysis of this preliminary lateral dynamic model indicated that if a cylindrical type structure is to be used, the lateral fundamental spacecraft natural frequency would probably be in a range from 15 to 25 cps for most efficient design. The stowed solar panels, when simply supported at both ends, may have a fundamental frequency in the same range. Care will be taken in subsequent design to detect, and then avoid, any possible coupling problems between the spacecraft and solar panels.

Because of the large cutout in the structure required for the ion engine exhaust, a space frame may be required in preference to a semi-monocoque. Figure C.7-2 shows a proposed frame which will be investigated.



LATERAL DISPLACEMENT OF LANDER/BUS INTERFACE AS A FUNCTION OF FUNDAMENTAL NATURAL FREQUENCY OF THE SPACECRAFT, UNDER THE ACTION OF LATERAL SINE VIBRATION.

FIGURE C.7-1

Mechanical environment to which the vehicle is subjected has been defined. The mechanical environments specified here satisfy the basic JPL requirements, and they apply to both the Saturn IB/Centaur and Atlas/Centaur launch configurations.

The spacecraft coordinates referred to are defined in Figure C.7-2.

Transportation Loads induced in transportation and ground handling should not exceed the design loads since adequate shock and vibration protection will be provided.

Prelaunch Care should be taken so that erection and attachment loads should not exceed the design loads. Peak values of winds during erection will be less than 50 knots 99 percent of the time; encapsulation may be required during erection.

Boost and Flight The mechanical environment during boost and subsequent operation of the spacecraft consists of a combination of quasi-static acceleration, sinusoidal and random vibration, shock, pressure transients, and acoustic noise. **The** mechanical environment during these phases is defined in Table C.7-1.

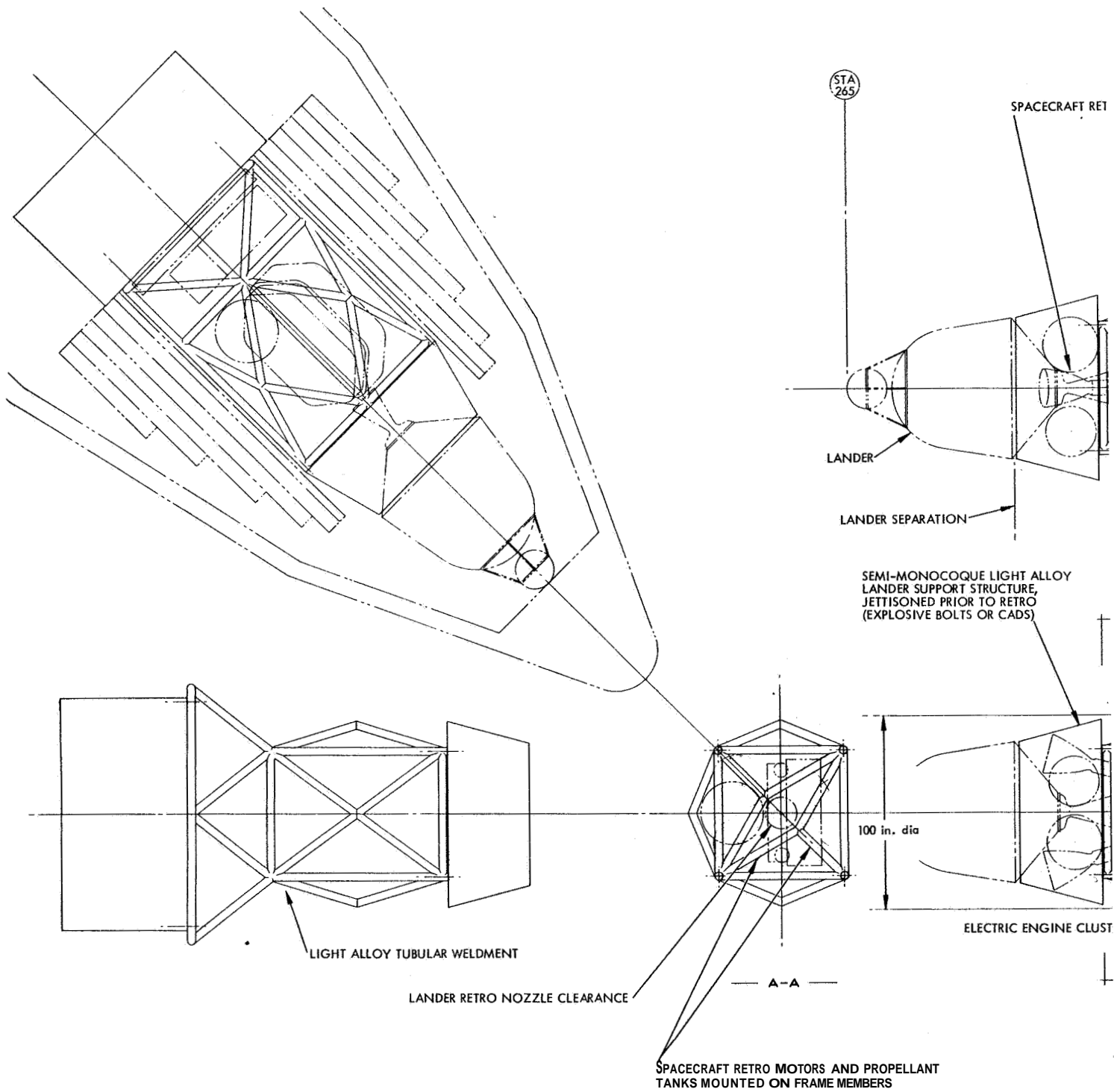
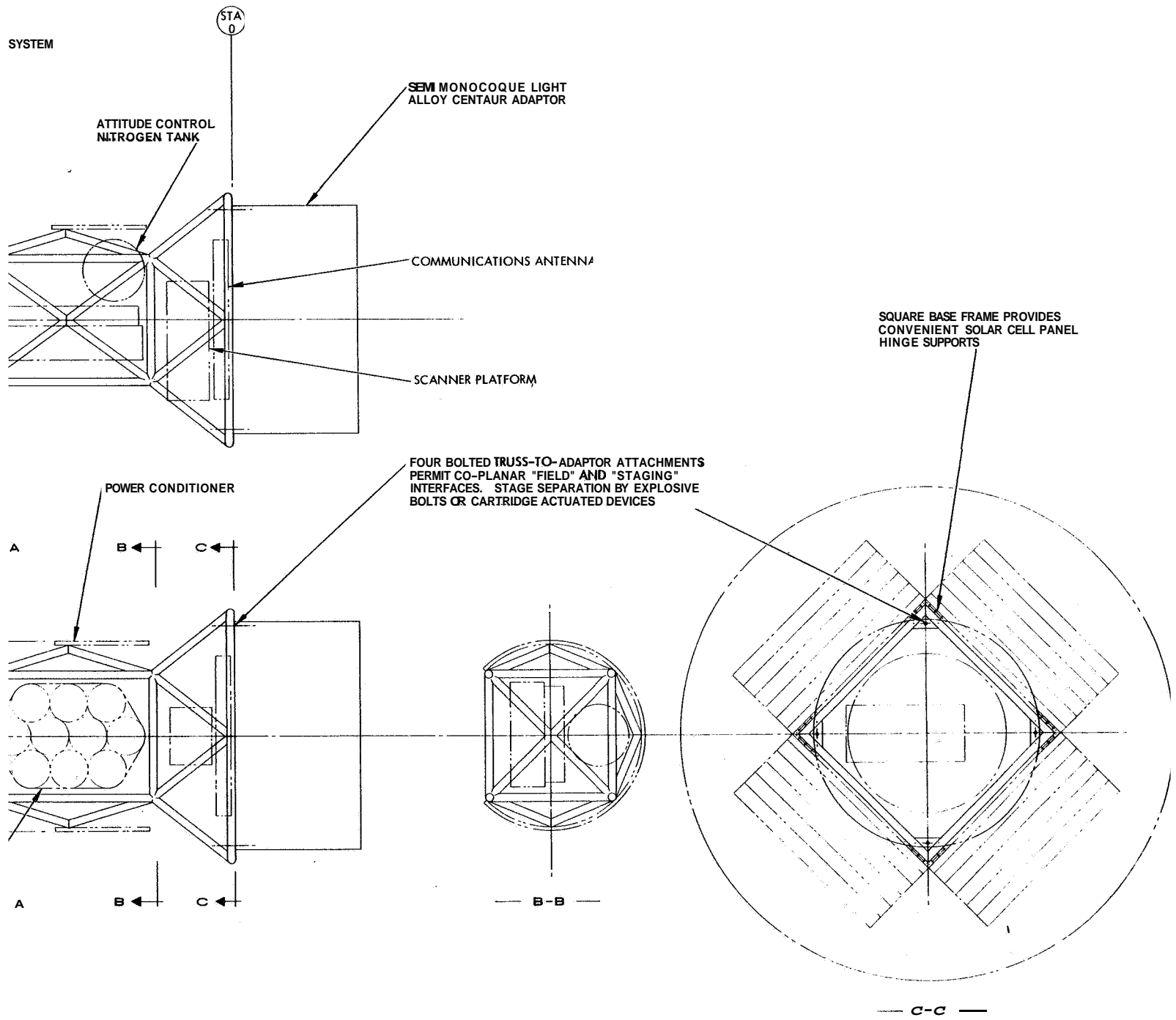


Fig. C.7-2 Solar-Electric Propulsion Spacecraft preliminary Structural Arrangement



C-48

TABLE C.7-1
DEFINITION OF MECHANICAL ENVIRONMENT

	Quasi-Static (g's) (Z - direction)	Quasi-Static (g's) (X-Y direction)	Sine (VFSW) g-rms (Z direction) In Parenthesis	Sine (VFSW) g-rms (X-Y direction) Frequency Range (cps) In Parenthesis	Sine (VFSW) Torsion About Z axis, rad/sec	Random (g ² /cps) White Noise In Parenthesis (c)	Endurance Vibration (sec)	Acoustics	Description of shock and transient loads.
Liftoff (a)	-2.0	2.0	Given in Fig. D-3.2-1	Given in Fig. D-3.2-2	60	0.4 (10-150)	30	Given in Fig. D-3.2-3	Comprehended in random environment
Maximum q (a)	-3.0	1.0	Given in Fig. D-3.2-1	Given in Fig. D-3.2-2	60	0.04 (100-1500)	50	Given in Fig. D-3.2-3	Comprehended in sine and random environment
First Stage Burnout (a)	-6.5	0.5	50% of Fig. D-3.2-1	50% of Fig. D-3.2-2	0	0	0	Given in Fig. D-3.2-3	Comprehended in sine and random environment
Engine Shutdown (a)	0	0	Given in Fig. D-3.2-1	Given in Fig. D-3.2-2	60	0.04 (100-1500)	60	0	6.5 g quasi-static, decreasing instantaneously to zero
TO BE SPECIFIED LATER									
Antenna Deployment									
TO BE SPECIFIED LATER									
Attitude Control	0	0	0	0	0	0	0	0	Vehicle acceleration (f) = 2×10^{-5} rad/sec ² (step function) Min. thrust time = 5 sec Min. coast time = 30 sec.
Ion Engine Fire and Operation (a)	3×10^{-5}	0	0	0	0	0	0	0	Step acceleration = 3×10^{-5} g's
Lander Jettison (d)	0	0	0	0	0	0	0	0	Velocity of separation of lander relative to spacecraft = 5 fps.
Antenna Jettison									
TO BE SPECIFIED LATER									
Retro Engine Fire (b)	+4.0	0.5	0.5 (5-1500)	0.3 (5-1500)	0	0.002 (5-1500)	100	0	Comprehended in random environment
Retro Engine Shutdown (b)	0	0	0.5 (5-1500)	0.3 (5-1500)	0	0.002 (5-1500)	0	0	4 g's quasi static decreasing instantaneously to zero.

(a) Loads applied at Centaur - spacecraft interface, i.e. field joint

(b) Loads applied at retro engine attach points

(c) To be applied in Z and any two orthogonal X-Y directions simultaneously

(d) Applied at lander/bus interface

(e) Environment during second (S-IVB) and third (Centaur) stage boost comprehended

(f) Angular acceleration to be applied about roll pitch and yaw axes

(g) Directed from 0 to 45° to the plane of the array

Note: Pressure transients from all pressure induced forces excepting acoustical loads shall be less than 0.015 psia on any portion of folded array.

PRECEDING PAGE BLANK NOT FILMED.

C.8 System Analysis

From an overall systems viewpoint several problems have been resolved in terms of design specifications.

For example, the dynamic interface between the spacecraft and the solar panels has been specified to the satisfaction of both Boeing and Hughes. Preliminary analysis of vehicle dynamics shows that a control system can be readily designed which will not create significant stress in the solar panels for any panel design except the roll-out version. If the roll-out version is adopted, its fundamental frequency is large enough to require that special attention be given to the automatic control system design. Dynamic interface requirements between spacecraft and solar panels in the stowed condition cause no serious design problems.

In the area of trajectories three dimensional data are **not** yet available. **These** data will permit specifications to be established for the star reference, may modify launch restrictions and affect fuel consumption. Also trajectory data for the case of constant thrust angle with respect to vehicle-sun line must be obtained, This information will affect spacecraft design and may affect control system design. Much of these data will be available within a month.

A study that should be made in this connection is the optimization of a fixed thrust direction.

The degree of subsystem redundancy required for mission success is now under investigation, and is expected to have a dominating effect on the choice of type of attitude control system and, perhaps, on ion thruster arrangements.

The comparison study of types of control systems included in the first progress report is being redone with new data on the spacecraft and system. In addition to these comparisons the method of direct control of the main thruster array position is being detailed as an alternate to the cold gas method for attitude control. Depending on whether the thruster is deployed or not, the engine would be rotated or translated.

At present a separate ion engine control system does not appear attractive on a relative basis because both cold gas control and engine motions are needed anyhow. The ion engine would be a third control system.

An instrument for attitude reference in a plane perpendicular to the ecliptic has been of some concern. The problem was to find a relatively simple instrument such as a canopus tracker having a sufficiently wide field of view to accommodate vehicle motions about its own axis, vehicle motion about the sun, and to find a mounting position on the vehicle where a single star would be in view at all times. It now appears that a canopus tracker can meet the requirements. A remaining item capable of precluding use of a canopus tracker on this vehicle is the amount of reflected light. This has not yet been determined.

During the next period the unsettled problems mentioned above should be solved. However, new system problems have arisen as a result of non-deployment of the thruster array. The resulting major changes in configuration and mass distribution will necessitate among other things (a) a review of dynamics of the spacecraft both during boost and with solar panels deployed, (b) revision of design specifications and (c) re-examination of the control system and its interactions with the spacecraft.

D. SPACECRAFT DESIGN CRITERIA

A preliminary statement of spacecraft design criteria has been formulated and is presented in the following paragraphs.. Inasmuch as spacecraft design analyses to date have indicated the advisability of the use of deployable engine arrays, whereas emphasis in the next reporting period will be directed towards configurations with "body-mounted" (non-deployable) engine arrays, future modifications of these criteria are indicated.

P-1 DESIGN MISSIONS

D-1.1 Launch Vehicle

Both the Atlas/Centaur and the Saturn IB/Centaur launch vehicles shall be considered for the design mission.

D-1.2 Spacecraft

Two preliminary solar-powered electric propulsion spacecraft designs are required. One to accomplish a 1971 Mars orbiter mission utilizing the Atlas/Centaur launch vehicle, and the other utilizing the Saturn IB/Centaur launch vehicle,

D-1.3 Boost Phase

Figure D-1.3-1 defines the earth escape trajectory phase of the mission.

Figure D-1.3-2 indicates the spacecraft distance from the sun, with respect to time for the first 10 days of the mission.

D-1.3.2 Heliocentric Transfer

The omni-directional antennas will be deployed in a sequence such that communication with earth is continuously available after Centaur separation.

Ion Engine turn on at approx. 3 days
 (Effect of Ion Engine assumed negligible
 in first 10 days.)

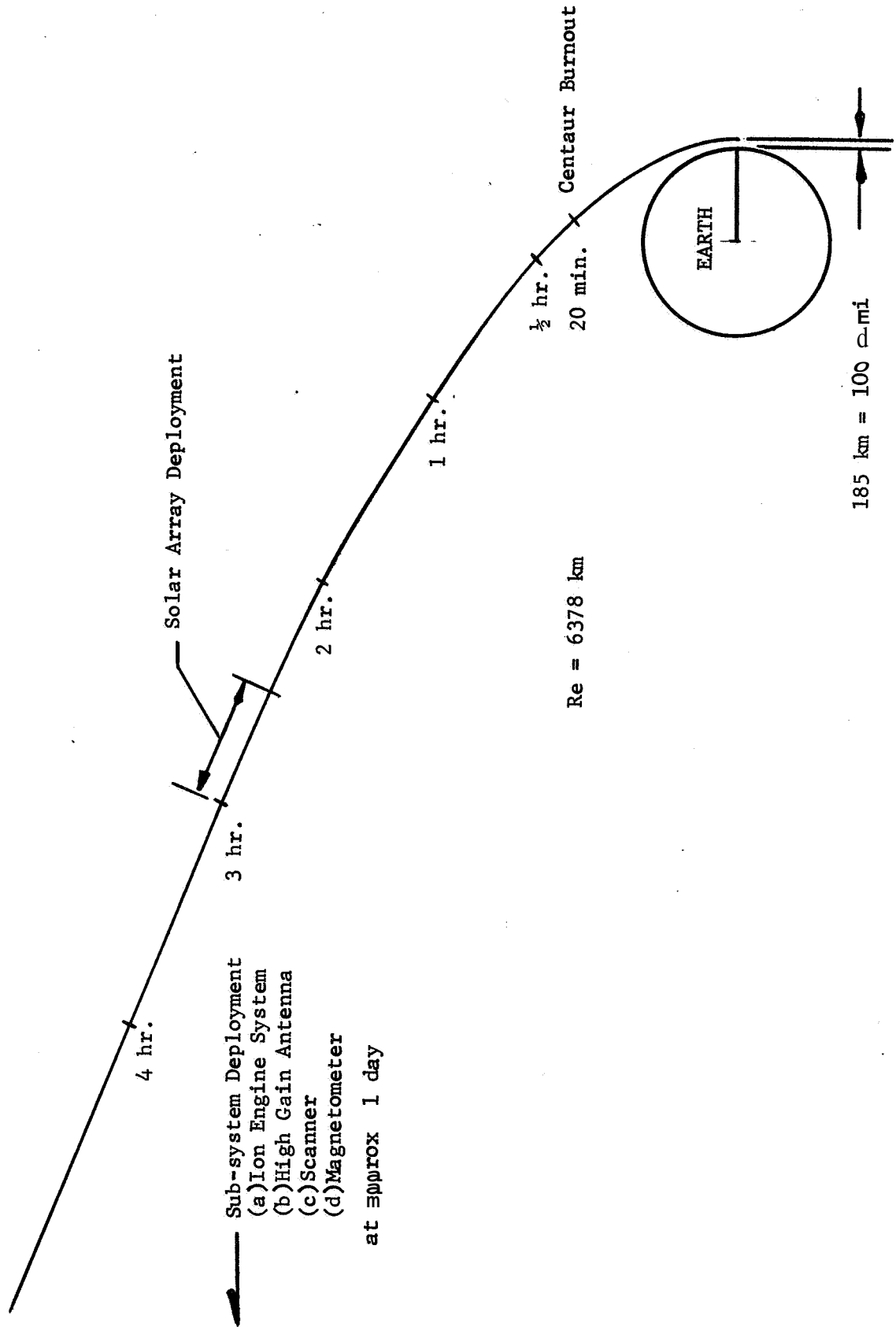
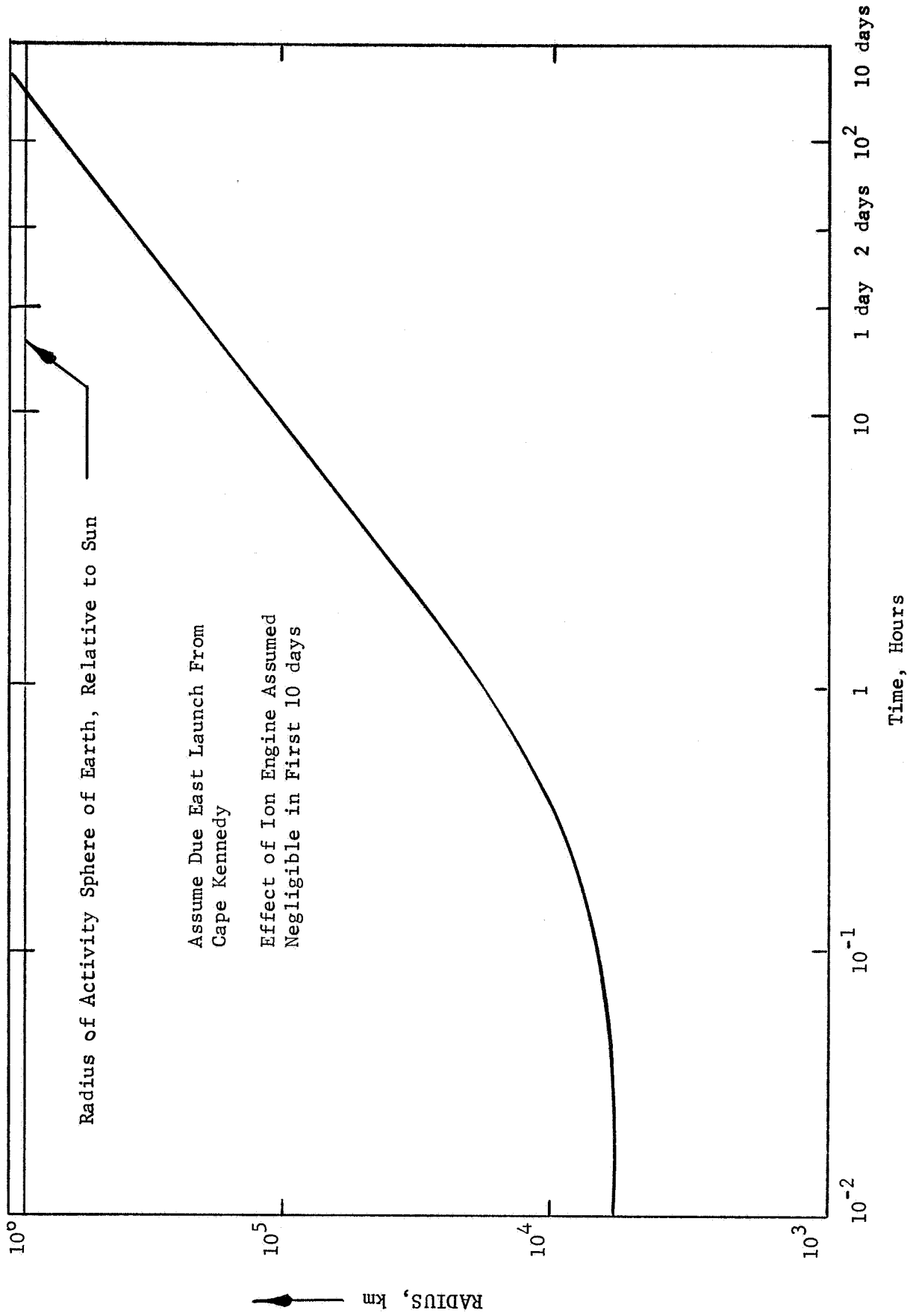


FIGURE D-1.3-1 EARTH ESCAPE TRAJECTORY



RADIAL DISTANCE VS TIME FOR PARABOLIC ESCAPE ($C_3 = 0$)
 FIGURE D-1.3-2

The solar panels shall be in operating condition not later than 3 hours after Centaur separation.

The main thruster assembly, high gain antenna and Mars scanner platform will be deployed in sequence after confirmation of solar panel operation.

The sequence of operations in the vicinity of Mars shall be:

- a. Jettison solar panels, power conditioner and engine
- b. Re-orientation of spacecraft to a launch attitude for the lander.
- c. Launch the Mars lander
- d. Terminal correction if necessary
- e. Retro into orbit about Mars.

D-1.3.3

Mars Orbit

Provision will be made for entry into any one of four Mars orbits, circular at 5,000 KM altitude,

- elliptical with periapsis 4,000 KM - apoapsis 50,000 KM
- 4,000 KM - apoapsis 20,000 KM
- 4,000 KM - apoapsis 10,000 KM

v_{∞} of spacecraft with respect to Mars shall be less than 2,000 fps.

D-2 SPACECRAFT DESIGN CRITERIA

D-2.1 Envelope Requirements

Figures D-2.1-1 and D-2.1-2 define the gross envelope requirements for the solar array and the spacecraft for the Atlas/Centaur and Saturn IB/Centaur launch vehicles respectively. Dynamic and static envelopes as well as permissible center of gravity locations are indicated.

D-2.2 Structural Design Criteria

D-2.2.1 Launch Configuration

The spacecraft including the solar array in the stowed configuration shall be capable of withstanding without structural or mechanical degradation the following structural load environment applied at the field joint (S/C sta. 0).

Sinusoidal Sweep at 1.0 Min/Octave

The variable frequency sinusoidal input shall be as shown in Figures D-3.2-1 and D-3.2-2 respectively.

Random Gaussian Vibration

The random Gaussian vibration shall consist of 50 minutes vibration at $0.4 \text{ g}^2/\text{cps}$ band limited between 100 and 1500 cps.

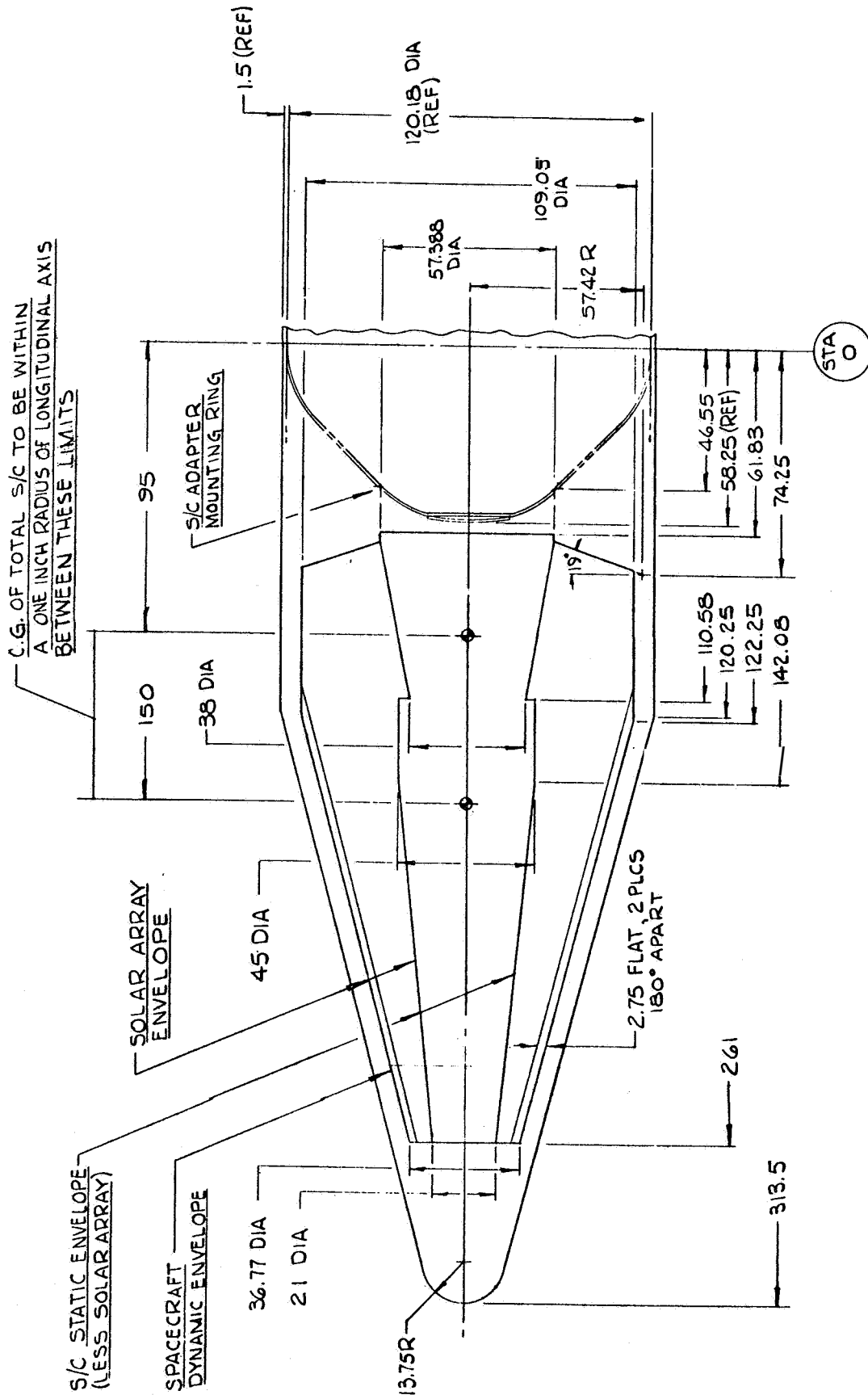


Fig. D. 2. 1-1. Atlas/Centaur Nose Fairing and S/C Dynamic Envelope

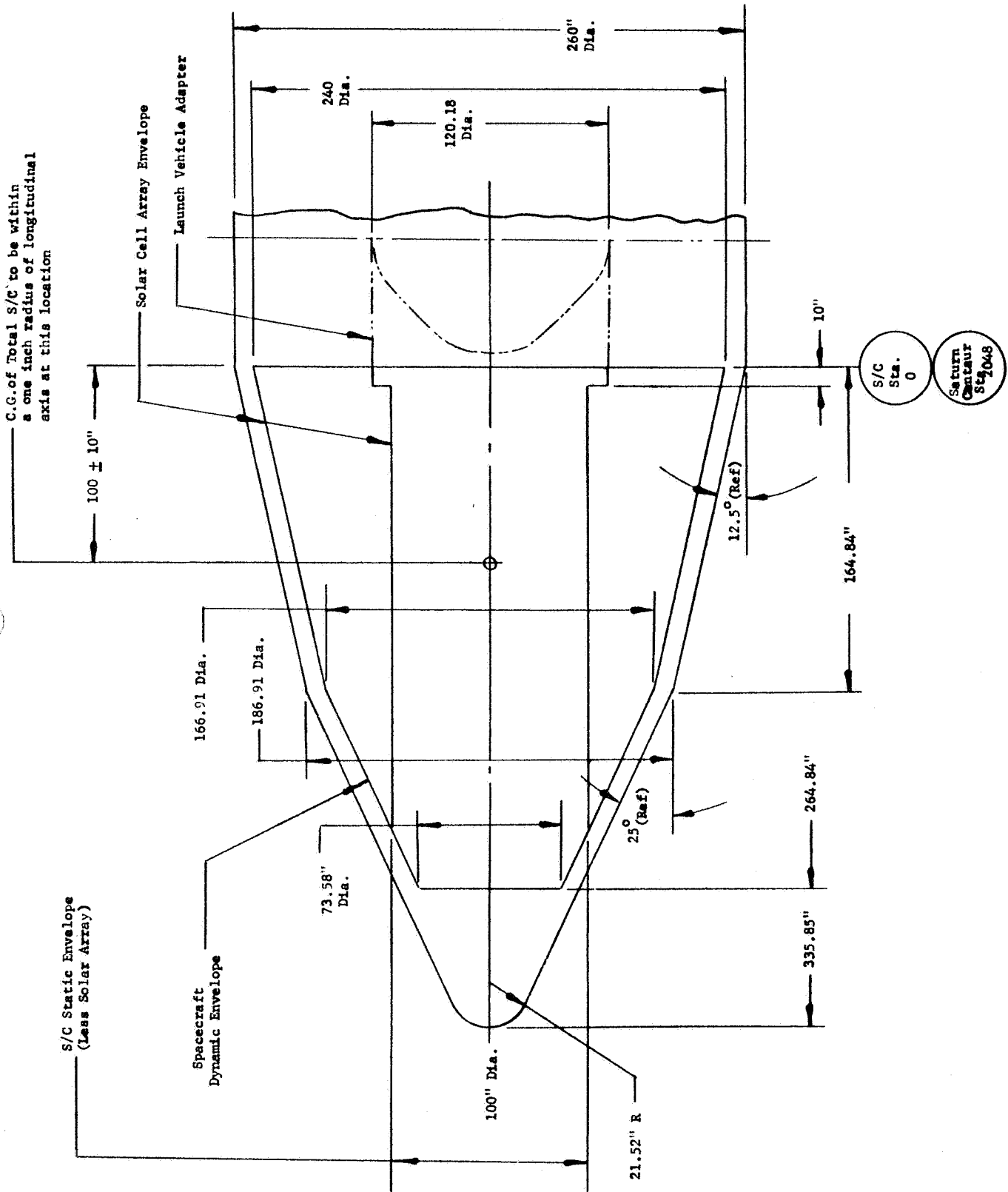


Fig. D.2.1-2. Saturn IB/Centaur Nose Fairing and S/C Envelope

Pressure transients arising from atmospheric out-gassing, shroud ejection, aerodynamic q , and all other pressure induced forces excepting acoustic loads shall be less than .015 psia on any portion of the folded array.

Acoustic Environment is specified in Figure D-3.2-3

Static Environment

The static loads shall consist of a steady-state acceleration of 6.5 "g" directed along the spacecraft longitudinal axis and 0.5 "g" steady-state acceleration directed normal to the spacecraft longitudinal axis.

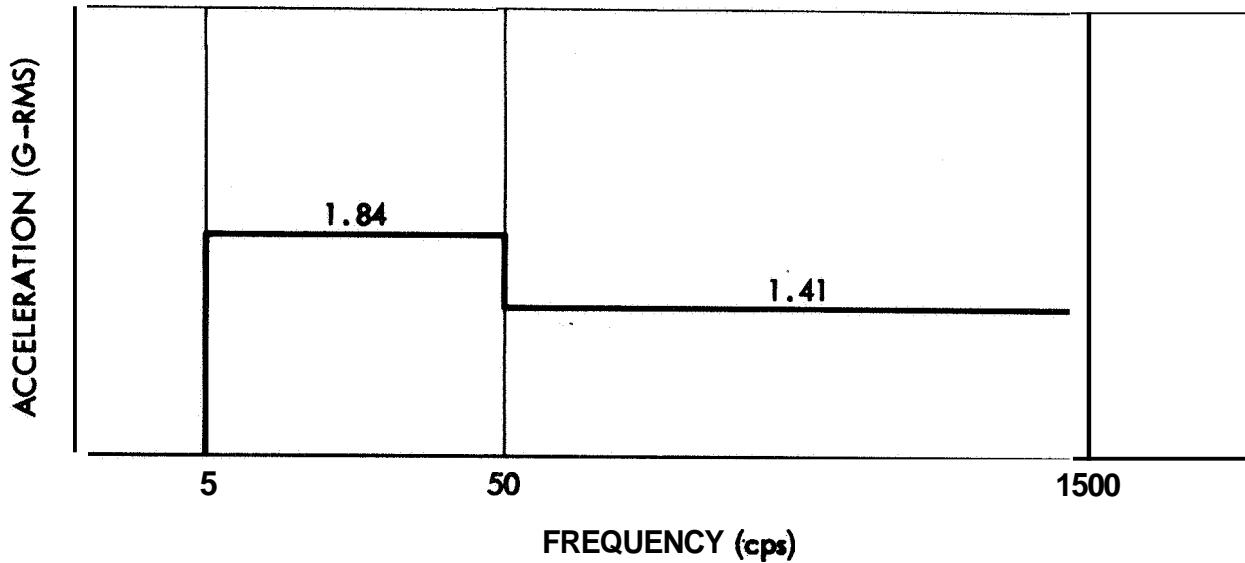
D-2.2.2 Deployed Configuration

The spacecraft in the deployed solar array configuration shall be so designed that no structural degradation will occur due to or during the following conditions.

The thermal gradients that will develop between the Sun and shade sides of the spacecraft due to solar illumination at 140 mw/cm^2 intensity.

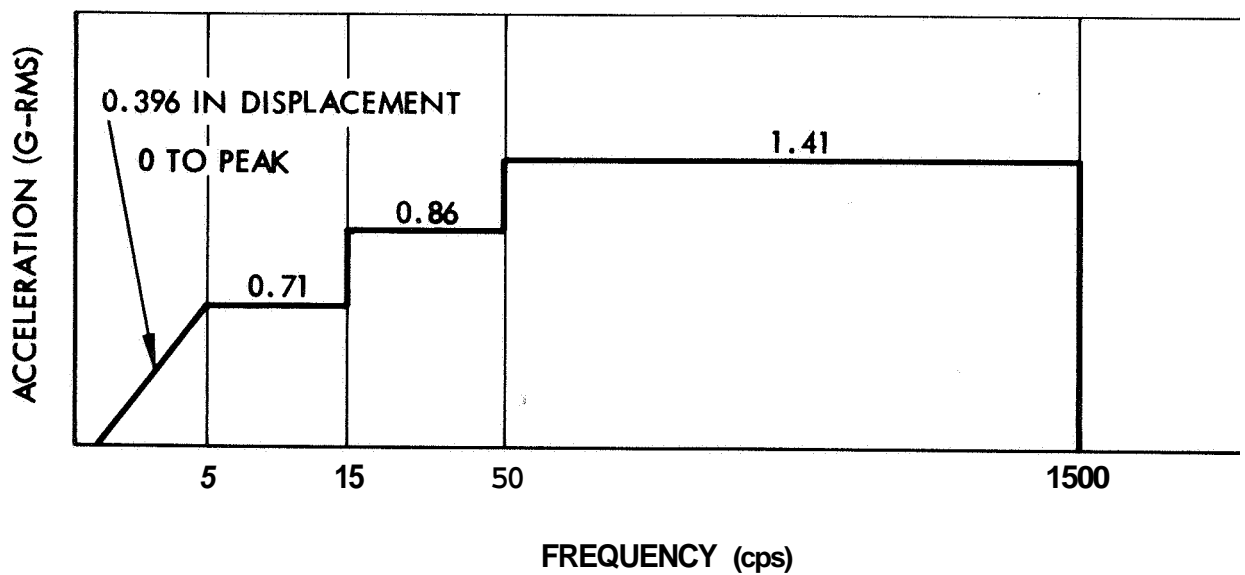
Transient thermal stresses due to repeated entry into, dwell time within, and emergence from planetary shadow with solar intensity of 50 mw/cm^2 , when in a 5000 km circular orbit about Mars,

A steady-state acceleration of 3×10^{-5} "g" directed at 45° to the plane of the array. This loading simulates that imposed by the cruise engines.



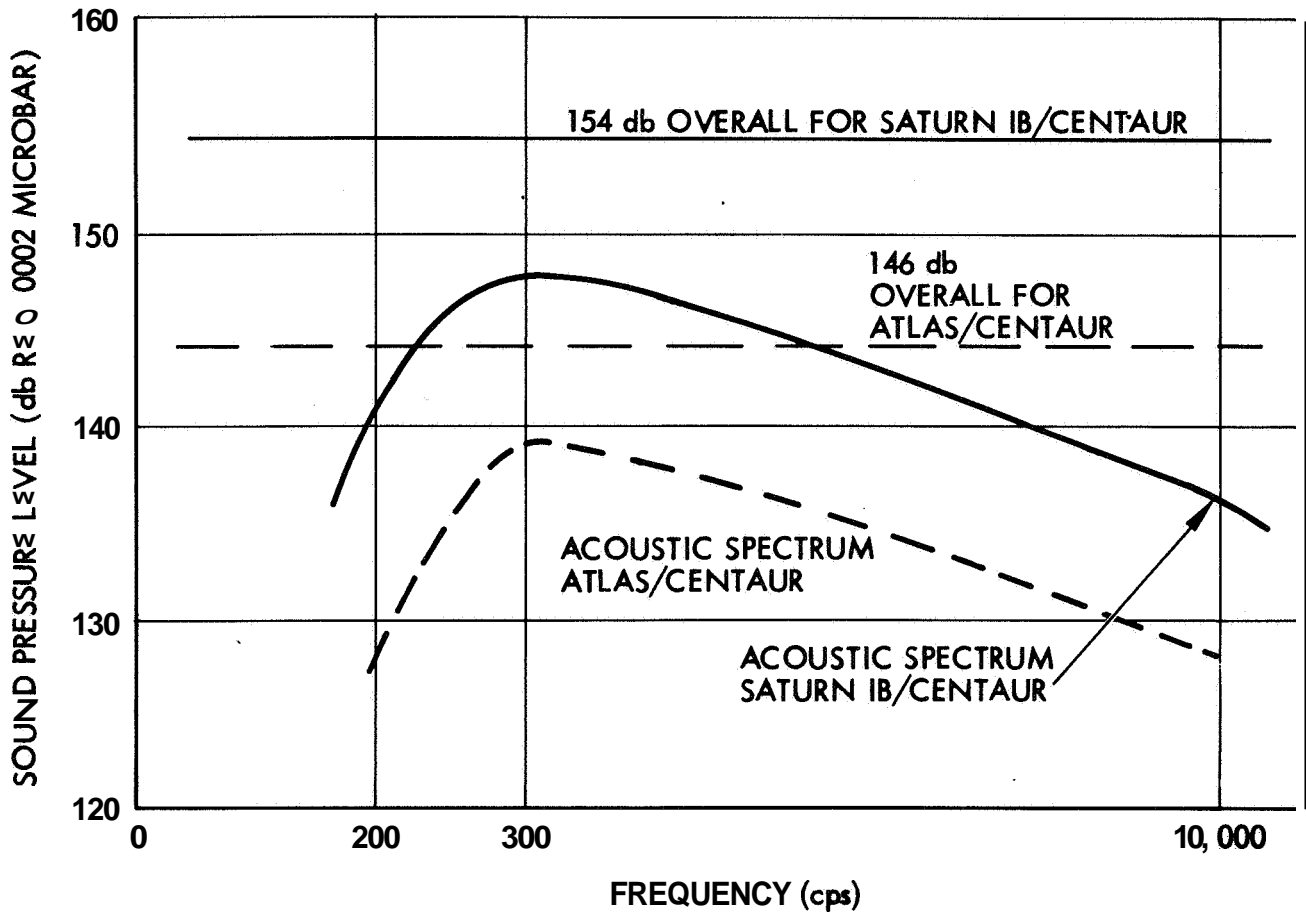
VARIABLE FREQUENCY SINE WAVE, THRUST AXIS (z-Direction)

FIGURE D-3.2-1



VARIABLE FREQUENCY SINE WAVE, LATERAL AXIS (Any x-y Direction)

FIGURE D-3.2-2



ACOUSTIC ENVIRONMENT INSIDE SHROUD

FIGURE D-3.2-3

A steady-state acceleration of four "g's" directed normal to the plane and $\frac{1}{2}$ "g" directed in the plane and normal to the span direction during retro into Mars orbit. (Orbiter configuration-electric propulsion system and lander already jettisoned.)

Control Reference Acquisition Phase

During acquisition the solar array shall withstand a constant angular acceleration of 2×10^{-5} rad/sec² zero angular accelerations as per Figure D-2.2.2-1.

Characteristic vehicle motions during an acquisition phase are shown in Figure D-2.2.2-2 and D-2.2.2-3.

Cruise Phase

The solar array shall withstand a vehicle limit cycle oscillation of approximately the form shown in Figure D-2.2.2-4 for a period of one year.

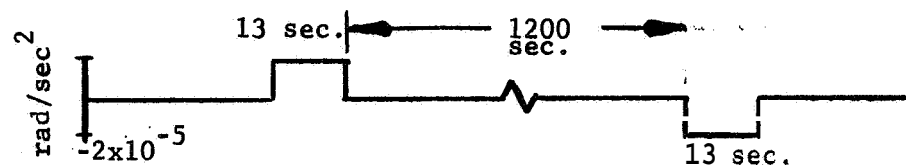


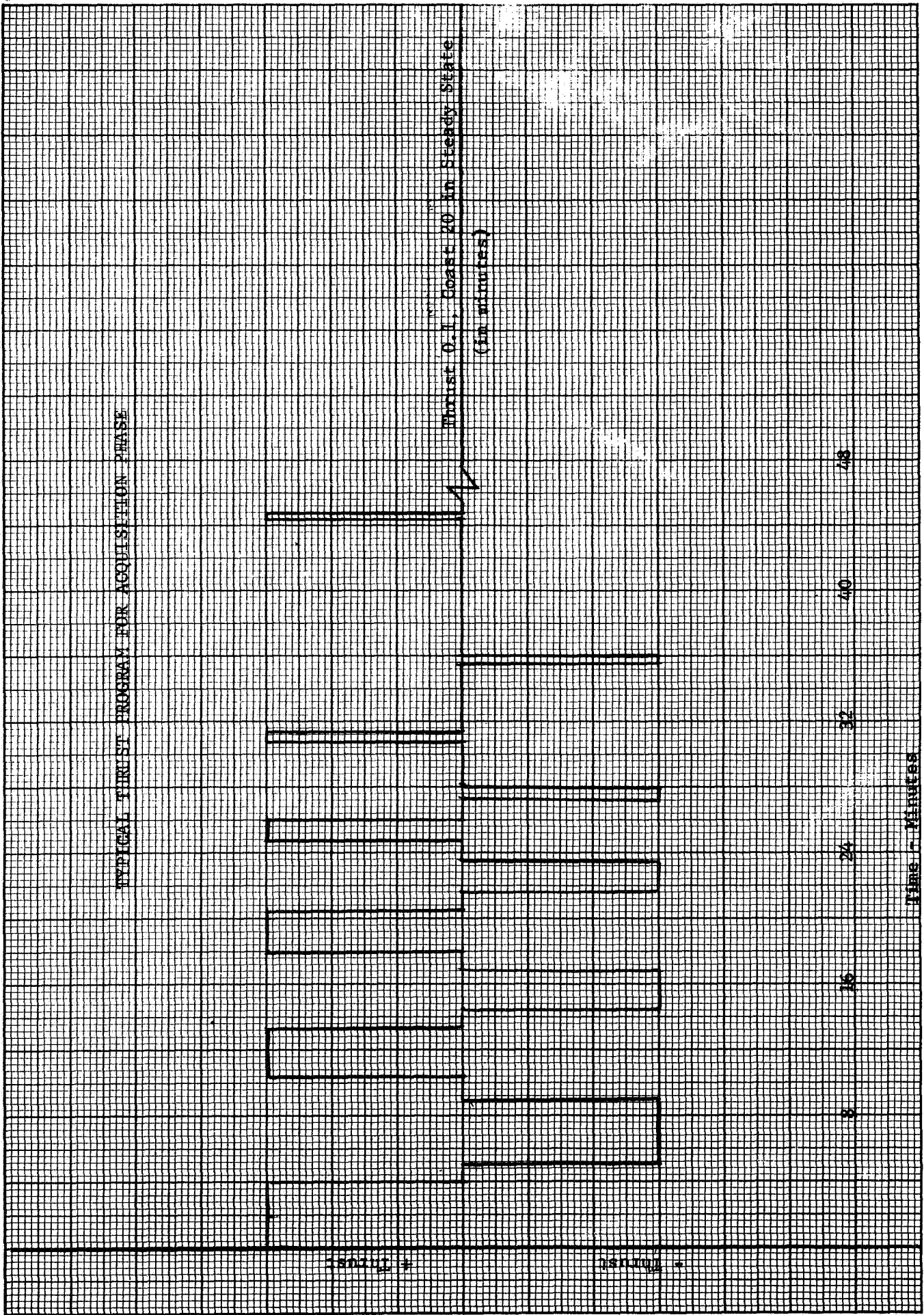
FIGURE D-2.2.2-4

D-2.3 Subsystem Design Criteria

D-2.3.1 Payload (not within the present scope of this program as per JPL instructions).

D-2.3.2 Solar Array

Except for the relevant items noted in D-2.2.1, D-2.2.2 and D-3.1, the Boeing document entitled "Preliminary Criteria and Requirements Statement" dated April 25, 1965 applies.



Time (Minutes)

FIGURE D-2.2.2-1

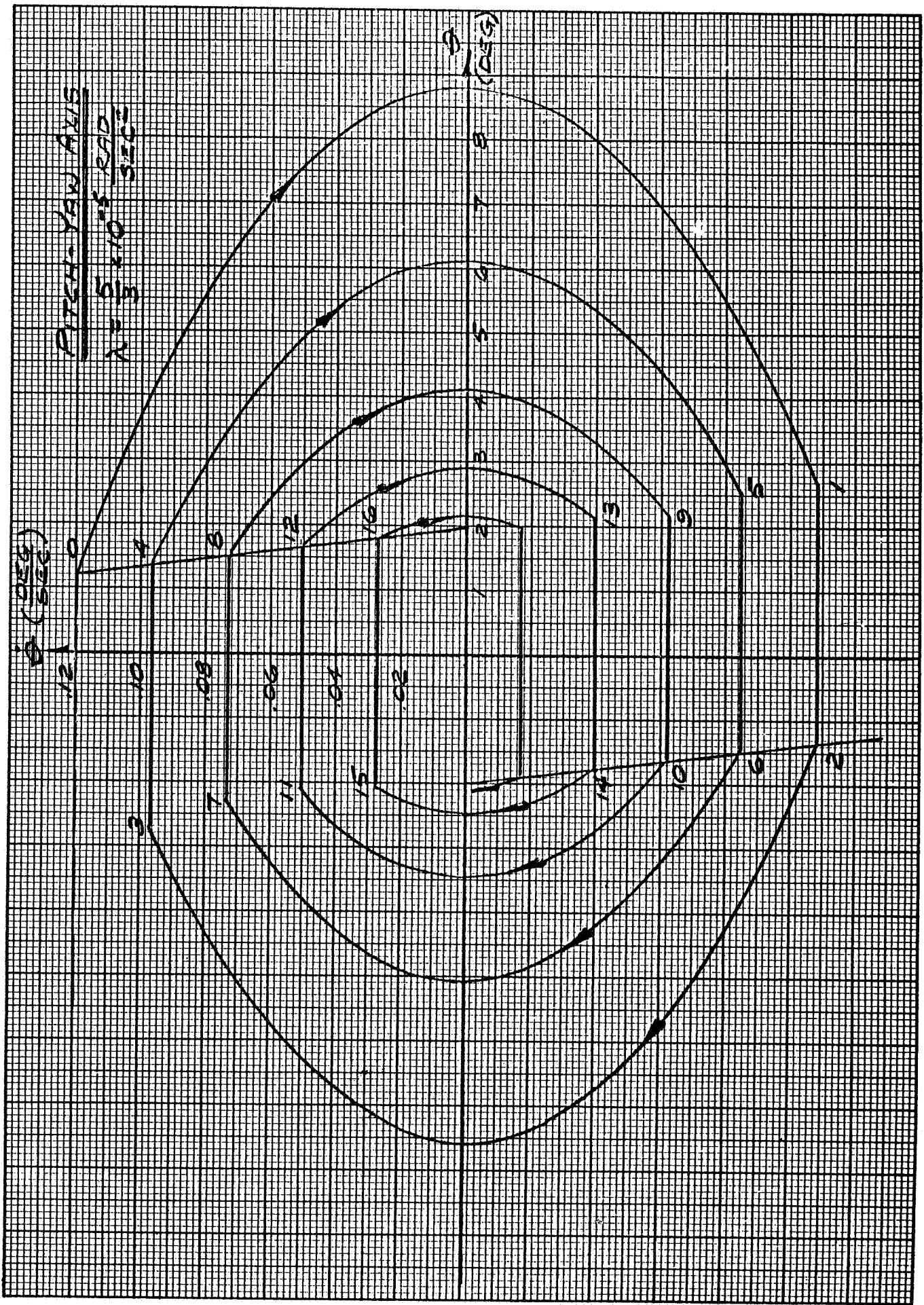


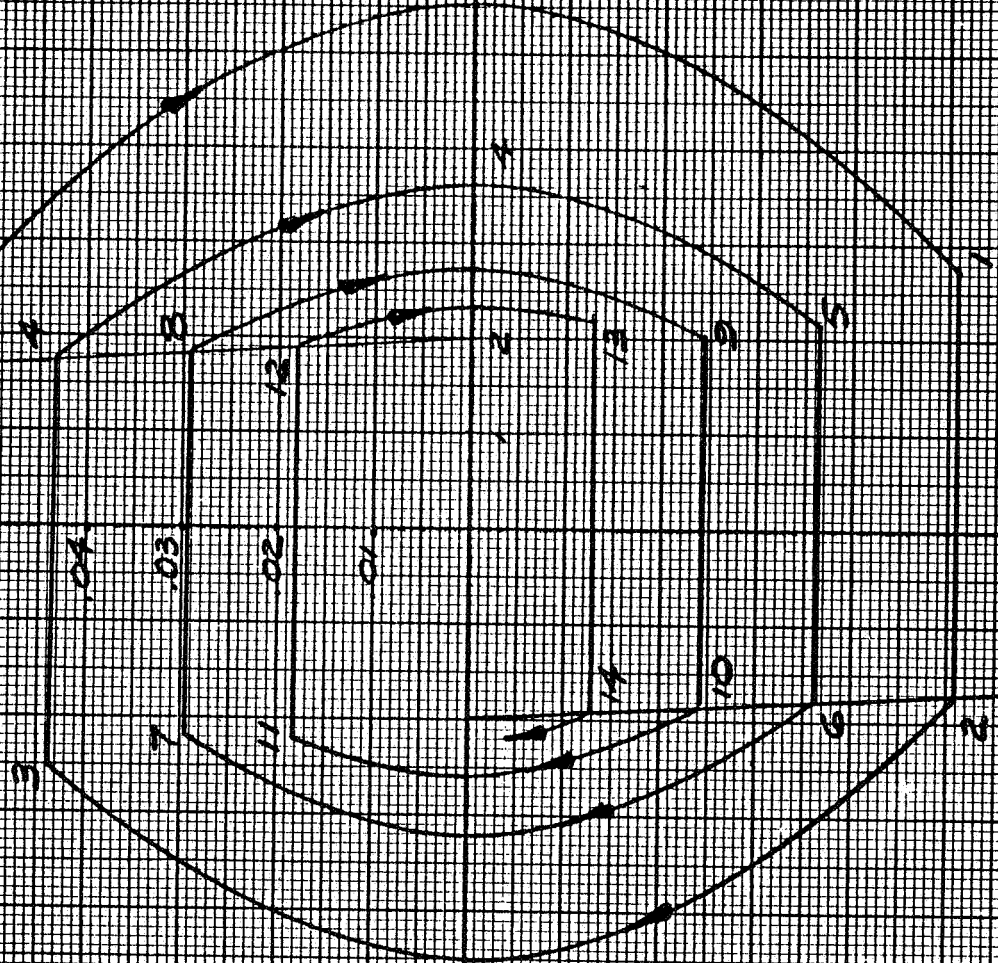
Fig. D. Z 2 Z-Z

ROLL AXIS
 $\lambda = \frac{5}{6} \times 10^{-5} \text{ RAD}$
 $\lambda = \frac{5}{6} \times 10^{-5} \text{ SEC}$

ϕ (COSG)
 (SEC)

.06
 .05
 .04
 .03
 .02
 .01

ϕ (COSG)



D-2.3.3 Telecommunications

Telecommunications between Earth and spacecraft is to be compatible with **DSIF** capability as programmed.

RF power source is to be limited to 50 watts (assumed 1967 state-of-the art).

Fixed parabolic or planar array antennas only are to be considered.

Maximum communication distance to be considered is 350×10^6 km.

Maximum communication time is 530 days (350 days transit and 180 days in ~~Mars~~ orbit).

D-2.3.4 Guidance and Control

On-board guidance and any associated additional instrumentation thereby required will be provided, if necessitated by precision launching of the landing vehicle.

On-board terminal guidance, if any, will utilize instrumentation already on the spacecraft for other purposes insofar as possible.

Three axis control of the spacecraft shall be available at all times after panel deployment.

Application of control forces shall not cause a torque level on the spacecraft exceeding 1 lb. ft.

If control is by means of gas jets, they shall be located at the outer end of the in-board solar panels. The thrust level from these gas jets shall not exceed 0.05 lbs.

Acquisition shall be automatic. Initial acquisition shall be limited by ground command, and must be accomplished from a random spacecraft orientation after solar array deployment. Control shall hold the plane of the solar panels perpendicular to spacecraft - sun line to within $\pm 5^\circ$. Control about the spacecraft sun line (roll) shall be within $\pm 5^\circ$ of a preselected reference.

Spacecraft center of gravity motion shall be sensed by the control system and the thrust vector adjusted by re-positioning the thrusters to compensate for the C. G. travel.

The sun shall serve as reference for two axes. A star reference out of the ecliptic plane shall be used for the roll axis.

The star tracker must be so located that its performance is not restricted by any part of the spacecraft during its operation.

Stray light such as reflections from the solar array must not enter the field of view of the star tracker.

Typical attitude control thrust times for one axis are shown in Figure D-2.2.2-4.

D-2.3.5 Thermal Control System

D-2.3.5.1 Scope

The vehicle thermal control system will provide thermal protection to the electric propulsion engines, the electrical power conditioning equipment, vehicle payload and other spacecraft subsystem equipment. The internal power dissipation of the vehicle payload during the transit phase is assumed to be small compared

with that arising from the power conditioner. The thermal control system for the vehicle will be designed to minimize the thermal interaction between the solar panels and the vehicle.

D-2.3.5.2 Prelaunch

The vehicle shall suffer no degradation of performance when exposed to prelaunch temperatures of 40°F to 120°F .

D-2.3.5.3 Boost Phase

The vehicle shall suffer no degradation when exposed to the following boost environments.

- a. Aerodynamic Heating - A maximum temperature on the inside of the nose fairing of the launch vehicle of 400°F for the severest launch trajectory. (Temperature-Time history forthcoming)
- b. Internal thermal radiation to the vehicle from the heated, nose fairing.
- c. Heat transfer between the vehicle equipment and its structure.
- d. Thermal radiation to free space and irradiation from the sun after nose fairing separation.

D-2.3.5.4 Heliocentric Phase

The vehicle shall suffer no degradation of performance when exposed to the following thermal environments during free-flight:

- a. Heat transfer between vehicle equipment by conduction through the structure and by thermal radiation.
- b. Solar irradiation on sunlit surfaces of $442 \text{ BTU/ft}^2/\text{hr}$.
- c. Thermal radiation to free space.

The thermal control system shall be capable of dissipating internally generated heat at a rate of 5 kilowatts at 1 A.U. from the sun without overheating.

The thermal control system shall keep the temperatures of all components within their respective tolerance at all times,

D-2.3.5.5 The vehicle shall suffer no degradation of performance when subjected to alternate sun and shade during the Mars orbiting phase.

D-2.3.6 Retro Motor Subsystem

The retro motor shall be capable of imparting a velocity increment of 3300 fps to a 7400 lb. spacecraft. This corresponds to 2.3.3.2.

Maximum spacecraft deceleration during retro into Mars orbit shall be 32 ft/sec².

D-2.3.7 Electric Propulsion System
(not yet available)

D-3 INTERFACES

- D-3.1 Array deployment mechanism and hinge attachments to spacecraft shall be so designed that binding does not interfere with deployment, and so that overloading does not result from shock when the array sections arrive at the limit stops.
- D-3.2 Once deployed, the solar array must lock permanently in position.
- D-3.3 The outer sections of the array must be jettisoned without damage to the remainder of the array, before orbiting Mars.
- D-3.4 The base hinges of the solar array shall be considered part of the spacecraft structure.
- D-3.5 The spacecraft shall provide sufficient clearance from exhausts of electric thrusters, control jets and the retro motor to avoid significant damage to the solar panels.
- D-3.6 The spacecraft shall, provide satisfactory view angles for communication with earth and/or with a lander vehicle.
- D-3.7 The solar array shall be designed so that displacements of the vehicle mass center due to thermal gradients and initial deployed position are minimized,
- D-3.8 The configuration of the deployed solar array shall provide adequate clearance adjacent to the spacecraft to permit deployment of spacecraft subsystems.
- D-3.9 Operation of the spacecraft-Centaur adapter separation mechanism shall not cause any damage to the stowed solar array.
- D-3.10 For clearance considerations, deployment of the solar array shall precede deployment of any major spacecraft subsystem.

D-3.11. Magnetometers or magnetic sensitive detectors must be placed at a sufficient distance from the spacecraft to minimize the stray magnetic fields into the noise level of a quiet solar magnetic field.

D-4. GROUND HANDLING AND SUPPORT EQUIPMENT

(Not yet available)